Quantum Transport and Scattering in Dirac Materials and Molecular Systems

by

Chengzhen Wang

A Dissertation Presented in Partial Fulfillment
of the Requirements for the Degree
Doctor of Philosophy

Approved June 2021 by the
Graduate Supervisory Committee:

Ying-Cheng Lai, Chair
Hongbin Yu
Chao Wang
Yuji Zhao

ARIZONA STATE UNIVERSITY

August 2021

ABSTRACT

This dissertation aims to study the electron and spin transport, scattering in two dimensional pseudospin-1 lattice systems, hybrid systems of topological insulator and magnetic insulators, and molecule chain systems.

For pseudospin-1 systems, the energy band consists of a pair of Dirac cones and a flat band through the connecting point of the cones. First, contrary to the conditional wisdom that flatband can localize electrons, I find that in a non-equilibrium situation where a constant electric field is suddenly switched on, the flat band can enhance the resulting current in both the linear and nonlinear response regimes compared to spin-1/2 system. Second, in the setup of massive pseudospin-1 electron scattering over a gate potential scatterer, I discover the large resonant skew scattering called super skew scattering, which does not arise in the corresponding spin-1/2 system and massless pseudospin-1 system. Third, by applying an appropriate gate voltage to generate a cavity in an α-T_3 lattice, I find the exponential decay of the quasiparticles from a chaotic cavity, with a one-to-one correspondence between the exponential decay rate and the Berry phase for the entire family of α-T_3 materials.

Based on the hybrid system of a ferromagnetic insulator on top of a topological insulator, I first investigate the magnetization dynamics of a pair of ferromagnetic insulators deposited on the surface of a topological insulator. The spin polarized current on the surface of topological insulator can affect the magnetization of the two ferromagnetic insulators through proximity effect, which in turn modulates the electron transport, giving rise to the robust phase locking between the two magnetization dynamics. Second, by putting a skyrmion structure on top of a topological insulator, I find robust electron skew scattering against skyrmion structure even with deformation, due to the emergence of resonant modes.

The chirality of molecule can lead to spin polarized transport due to the spin

orbit interaction. I investigate spin transport through a chiral polyacetylene molecule and uncover the emergence of spin Fano resonances as a manifestation of the chiral induced spin selectivity effect.

To my parents, Dewei Wang and Yanzhi Li.

ACKNOWLEDGMENTS

First, I am full of gratitude to my advisor Prof. Ying-Cheng Lai, who gives me guidance about the research direction, has discussion with me about problems I met, and continuously supports me over the past five years. Without Prof. Lai's help, I cannot achieve this. His deep insights and enthusiasm for physics have influenced and inspired me. His regular schedule also inspires me to form good habit. I cannot forget his care for me in everyday life and his help whenever I met difficulties in ASU. And he also gives me so much advice and help in my future career. I have learned a lot and feel very happy under his supervision.

I am also grateful to Prof. Hongya Xu, who was a post-doc in Prof. Lai's group before. He is very knowledgable about the new research and I learned a lot from the discussions with him. I am so fortunate to have him giving me detailed guidance and discussion. And I own too much to Prof. Liang Huang, my master's advisor in Lanzhou University, who keeps in touch with me in my PhD time and offers me help and encourages me when I met problems both in research and life.

I have a good time in our Chaos group, we discuss with and learn from each other, help each other, play and gathering together, many great memories. I thank students in our group, Dr. Lei Ying, Dr. Guanglei Wang, Dr. Lezhi Wang, Dr. Junjie Jiang, Dr. Zhidan Zhao, Mr Chendi Han and Mr Lingwei Kong, and visiting students Dr Huawei Fan, Dr. Yu Meng, Ms. Chun Zhang, Dr. Rui Xiao, Dr. Shijie Zhou and other visiting Professors and students. And I cannot forget their care for me. I also want to thank my roommate Zhongxing Zeng, who is always considerate and gives me help.

I want to give special thanks to my committee members, Prof. Hongbin Yu, Prof. Chao Wang, Prof. Yuji Zhao, as well as the previous committee members Prof. Cun-

Zheng Ning, Prof. Vladimiro Mujica, Prof. Richard Kiehl, Dr. Nicholas D. Rizzo for their precious time as well as invaluable comments and advices.

Finally, I would like to express my deepest thankfulness to my family, especially to my beloved parents, who give all their love to me and support me in all my pursuits.

TABLE OF CONTENTS

Page

CHAPTER Page

CHAPTER Page

CHAPTER Page

CHAPTER Page

LIST OF TABLES

LIST OF FIGURES

Figure Page

Figure Page

Figure Page

Figure Page

Chapter 1

INTRODUCTION

1.1 Electron Transport and Scattering in Pseudospin-1 Dirac-Weyl Systems

Solid state materials, due to the rich variety of their lattice structures and intrinsic symmetries [1, 2], can accommodate quasiparticles that lead to quite unconventional and interesting physical phenomena. The materials and the resulting exotic quasiparticles constitute the so-called "material universe." Such materials range from graphene that hosts Dirac fermions [3] to 3D topological insulators [4, 5] and 3D Dirac and Weyl semimetals [6, 7], in which the quasiparticles are relativistic pseudospin-1/2 fermions. Recently, Dirac-like pseudospin-1 particles have attracted much attention [8, 9, 10, 11, 12, 13, 14, 15, 16, 17, 18, 19, 20, 21, 22, 23, 24, 25, 26, 27, 28, 29, 30, 31, 32, 33], which are associated with a unique type of energy band structure: a pair of Dirac cones with a flat band through the conical connecting point. Materials that can host pseudospin-1 particles include particularly engineered photonic crystals [22, 13, 16, 17, 19], optical dice or Lieb lattices with loaded ultracold atoms [8, 9, 10, 12, 34], and certain electronic materials [14, 15, 20, 21]. In contrast to the Dirac cone system with massless pseudospin-1/2 particles that exhibit conventional relativistic quantum phenomena, in pseudospin-1 systems an array of quite unusual physical phenomena can arise, such as super-Klein tunneling associated with one-dimensional barrier transmission [9, 11, 22], diffraction-free wave propagation and novel conical diffraction [13, 17, 16, 19], unconventional Anderson localization [35, 36, 27], flat-band ferromagnetism [18], unconventional Landau-Zener Bloch Oscillations with flat bands [37], and peculiar topological phases under external

gauge fields or spin-orbit coupling [12, 38, 39, 40, 32].

Quantum transport beyond the linear response and equilibrium regime is of great practical importance, especially with respect to device development. There have been works on nonlinear and non-equilibrium transport of relativistic pseudospin-1/2 particles in Dirac and Weyl materials. For example, when graphene is subject to a constant electric field, the dynamical evolution of the current after the field is turned on exhibits a remarkable minimal conductivity behavior [41]. The scaling behavior of nonlinear electric transport in graphene due to the dynamical Landau-Zener tunneling or the Schwinger pair creation mechanism has also been investigated [42, 43]. Under a strong electrical field, due to Landau-Zener transition a topological insulator or graphene can exhibit a quantization breakdown phenomenon in the spin Hall conductivity [44]. More recently, non-equilibrium electric transport beyond the linear response regime in 3D Weyl semimetals has been studied [45]. In these works, the quasiparticles are relativistic pseudospin-1/2 fermions arising from the Dirac or Weyl system with a conical type of dispersion in their energy momentum spectrum. The aim of Chapter 2 is to present the phenomenon of enhanced non-equilibrium quantum transport of pseudospin-1 particles.

Electronic scattering in Dirac material systems have been extensively studied [46, 47, 48, 49, 50, 51, 52, 53, 54, 55, 56]. For example, a study of the scattering of massless pseudospin-1/2 Dirac electrons by a circular potential barrier revealed [54] that, for a scatterer of small radius, the scattering cross sections are dominated by quantum resonances but, for a large scatterer, the classical picture of reflection and refraction of rays applies, leading to phenomena such as caustics, rainbow, and critical scattering. In massless pseudospin-1 particle scattering from a circular potential barrier, phenomena such as revival resonances, perfect caustics as induced by super-Klein tunneling, and universal low-energy isotropic transport can arise [24], which do

not occur in pseudospin-1/2 scattering systems.

In pseudospin-1/2 or pseudospin-1 materials, opening a gap can lead to intriguing phenomena such as the Anomalous Hall Effect (AHE), a fundamental transport behavior that occurs in solids with a broken time-reversal symmetry in a ferromagnetic phase due to spin-orbit coupling [57]. For example, QAHE (Quantum Anomalous Hall Effect) in graphene was predicted in the presence of Rashba spin-orbit coupling and an exchange field generated by Fe absorbed on top of graphene or by proximity coupling to an antiferromagnetic insulator [58, 59], where the exchange splitting is about 70 meV. AHE in single-layer graphene exchange-coupled to an atomically flat yttrium iron garnet (YIG) ferromagnetic thin film or to a magnetic nanoparticle array was realized in experiments [60, 61]. Light induced AHE in monolayer graphene driven by ultrafast pulses of circularly polarized light was discovered experimentally [62] and explained theoretically [63], whose physical origin lies in light induced topological nontrivial Floquet-Bloch bands. In addition, there were studies on the extrinsic spin Hall effect induced by resonant skew scattering through spin-orbit coupling in graphene decorated by adatoms [64]. For pseudospin-1 systems, there are multiple mechanisms to open a gap: added on-site energy [9], introducing dimerization term [40, 65], intrinsic spin-orbit coupling [12, 65], or staggered flux phases on the kagome lattice [66]. The unconventional topological phases related to the gap was also investigated [40, 12, 65], and anomalous chiral edge states and in-gap edge states were discovered in massive pseudospin-1 systems [30, 31]. Bounded electronic states were found in a gapped pseudospin-1 system with a centrally symmetric potential well and a regularized Coulomb potential induced by the charged impurities [67]. The phenomenon of super-Klein tunneling can occur even for massive pseudospin-1 particles [68]. Unconventional quantum Hall effect was studied in gapped pseudospin-1 systems with an infinite degeneracy of zero-energy Landau levels

lifted into a series of bands [69]. Quantum scattering in massive pseudospin-1 systems have not been systematically studied, especially with respect to skew scattering as related to AHE. The purpose of Chapter 3 is to fill this gap.

Advances in physics, chemistry, materials science and engineering have led to the discoveries of new materials at an extremely rapid pace, e.g., the various two-dimensional Dirac materials [70, 71, 72]. These materials host a variety of quasiparticles with distinct physical characteristics including the Berry phase. Berry phase is a fundamental characteristic of the quasiparticles of the underlying quantum material. When a system is subject to a cyclic adiabatic process, after the cycle is completed, the quantum state returns to its initial state except for a phase difference - the Berry phase [73, 74, 75]. In general, the exact value of the Berry phase depends on the nature of the quasiparticles and hence the underlying material. For example, the Berry phases in monolayer graphene [76, 77] and graphite bilayers [78] are $\pm\pi$ and 2π, respectively. In α-T_3 lattices, for different values of α, the Berry phases associated with the quasiparticles are distinct [79]. To be able to detect Berry phase for a new material would generate insights into its physical properties for potential applications. Conventionally, this can be done using the principle of Aharonov-Bohm interference. For example, an atomic interferometer was realized in an optical lattice to directly measure the Berry flux in momentum space [80]. Graphene resonators subject to an external magnetic field can be used to detect the Berry phase [81, 82]. Specifically, for a circular graphene p-n junction resonator, as a result of the emergence of the π Berry phase of the quasiparticles (Dirac fermions) when the strength of the magnetic field has reached a small critical value, a sudden and large increase in the energy associated with the angular-momentum states can be detected. In photonic crystals, a method was proposed to detect the pseudospin-1/2 Berry phase associated with the Dirac spectrum [83]. In such a system, the geometric Berry phase acquired upon

rotation of the pseudospin is typically obscured by a large and unspecified dynamical phase. It was demonstrated [83] that the analogy between a photonic crystal and graphene can be exploited to eliminate the dynamical phase, where a minimum in the transmission arises as a direct consequence of the Berry phase shift of π acquired by a complete rotation of the pseudospin about a perpendicular axis. In chapter 4, utilizing the α-T_3 lattice as a paradigm, we find that, in the Dirac electron optics regime, the semiclassical decay of the quasiparticles from a chaotic cavity can be effectively exploited for detecting the Berry phase.

1.2 Electron Transport and Scattering in Hybrid Systems of Topological Insulators and Magnetic Structures

TIs are quantum materials with surface states residing in the bulk insulating gap [4, 5]. The edge states are topologically protected and are robust against non-magnetic disorders due to a strong spin-momentum locking. The electron motions on the surface follow the 2D linear dispersion with a single band-touching Dirac point and are described by the Dirac equation. In spite of the strong spin-momentum locking, the surface electronic states are sensitive to magnetic perturbations. That is, the electrons will be scattered off upon encountering a magnetic structure on the surface of the TI.

Quite recently, spin-torque and spin-Hall nano-oscillators [84] have gained attention for their potential applications in various non-Boolean computing [85] including image processing [86], associative memory, pattern recognition [87, 88, 89], and spatiotemporal wave computing [90]. In general, the ability to control and manipulate magnetization dynamics is essential to developing spintronic memory, logic, and sensing nanodevices. A mechanism that has been extensively studied theoretically and experimentally is spin-transfer torque [91, 92], which is based on the transfer of the

spin angular momentum between a spin current flow and the local magnetization of a ferromagnetic layer. The mechanism can be exploited to develop, e.g., switching and steady precession of spin torque oscillators (STOs) [93, 94]. The dynamics of precession of a single STO provide the basis for synchronizing a number of STOs [95, 96, 97], which has applications such as microwave power generation and sensing. Phase locking of two STOs has been achieved experimentally in spin torque devices with multiple nanocontacts, in which the magnetization in all the nanocontact regions can be locked at the same phase via a propagating spin wave [98, 99, 100]. Phase locking of STOs through coupled electrical circuits has also been studied in an array of STO nanopillars that can be electrically connected in series or in parallel [101, 102, 103, 104, 105, 106]. In this case, the AC current produced by each individual oscillators leads to feedback among the STOs, thereby realizing synchronization. In addition, synchronization can be achieved through magnetic dipolar coupling in perpendicular-to-plane polarized STOs [107]. Local synchronization between vortex-based STOs interacting with each other can occur through the mediation of closely spaced antivortices [108]. Recently, spin Hall effect [109, 110, 111, 112] has been exploited to experimentally realize synchronization of STOs driven by a pure spin current through microwave driving [113], and a method to synchronize multiple STOs without requiring any external AC excitation has been proposed [114]. Existing studies on STOs have been focused primarily on nanocontact spin valves and magnetic tunnel junction pillar structures. While the junction structures appear more promising for microwave power generation because of their high junction resistance and larger magnetoresistance, nanocontact spin valves are more promising for mutual phase-locking among multiple STOs because of their better interdevice coupling geometry [98, 99, 100, 115].

The interaction between the topological surface states and magnetic materials in a quasi-one dimensional setting has been studied [116, 117, 118] where, due to the spin-

momentum locking, the exchange coupling between the magnetization and the surface electronic states can lead to intriguing phenomena such as anomalous magnetoresistance and unconventional transport behaviors [119, 120]. The interaction can also lead to nonlinear or even chaotic dynamics in the evolution of magnetization of the FMI [121, 122]. For example, complicated dynamics can emerge in the magnetization switching due to a Hall-current-induced effective anisotropic field [123, 124, 125, 116] and steady self-oscillations can arise in an FMI/TI heterostructure [126, 127, 128]. Motivated by the growing interest in exploiting topological quantum materials for achieving novel charge transport and efficient electrical control of magnetization in spintronics applications, in Chapter 5, we investigate the possibility to realize phase locking of nanoscale magnetic oscillators coupled via some topological mechanism, e.g., through a topologically protected current.

Beside of the the common ferromagnetic insulator, there is another very interesting magnetic structure called skyrmion, which is a particle-like magnetic excitation with a swirling topological 2D spin texture, i.e., the spin at the core and the spin at the perimeter point are in opposite directions [129, 130, 131, 132]. The small size of the skyrmions and the possibility of moving them with electrical currents of small density ($\sim 10^5 \mathrm{A/m}^2$) make them promising candidates for spintronic storage or logic devices [129, 130]. Skyrmions have been experimentally observed in chiral magnets [133, 134] as a result of the competition between the Dzyaloshiskii-Moriya (DM) interactions, Heisenberg exchange, and Zeeman interactions. It has been demonstrated that metallic skyrmions can be driven by spin transfer torque (STT) from the electric current [135, 136, 137]. Optical skyrmion lattices have been achieved in an evanescent electromagnetic field [138]. In addition, the topological spin Hall effect has been demonstrated in which a pure transverse spin current is generated from a skyrmion spin texture [139, 140, 141, 142, 143].

Efforts in improving thermal efficiency and better manipulating skyrmions have led to the "marriage" between skyrmion and TI, where skyrmions arise on the surface of a TI. Electric charging of magnetic vortices on the surface of a TI was investigated [144], and the confinement state in the skyrmion structure on the surface of a TI was discovered, paving the way to driving skyrmion motion using an applied electric field [145]. Electron skew scattering induced by the skyrmion structure on the TI surface was also studied [55]. Quite recently, the combination of two skyrmions with opposite winding numbers, called skyrmionum in an FMI/TI heterostructure was observed in the physical space [146, 147, 148]. Theoretically, fluctuation-induced Néel and Bloch skyrmions on the surface of a TI have been predicted [149]. In Chapter 6, we study the electron scattering from a magnetic skyrmion structure.

1.3 Electron and Spin Transport in Chiral Molecules

When electrons pass through a complex chiral molecule, the phenomenon of chiral-induced spin selectivity (CISS) can arise [150], where the electrons acquire a certain degree of spin polarization due purely to the intrinsic chirality of the molecule itself. The phenomenon opens the possibility of manipulating the spin degree of freedom of electrons in quantum biological systems. CISS has attracted growing attention, both experimentally [151, 152, 153, 154, 155, 156, 157, 158, 159] and theoretically [160, 161, 162, 163, 164, 165, 166, 167, 168, 169, 170, 171, 172, 173]. The phenomenon has been observed in DNA [151, 152, 153], protein(bacteriorhodopsin) [154, 155], oligopeptides [156, 157], and helicenes [158, 159]. CISS is remarkable because the underlying complex molecular system does not possess any intrinsic magnetization that would otherwise affect the spin-dependent responses. Because of the lack of internal magnetism, a theoretical description of CISS must include spin-orbit coupling (SOC) [174]: a weak relativistic effect on the order of a few meV. Consequently,

in order to achieve appreciable spin polarization, some cumulative effect is necessary, which can be achieved in a complex molecule. In particular, during transport through a large molecule, an electron will encounter, visit, and pass through many atoms. At each encounter where the electron orbits the nucleus, the spin-orbit interaction depends on the orbital orientation, which leads to weak spin polarization. For a large chiral molecule such as DNA, there is a preference in the orbital orientation so the effects on the spin polarization from the many atoms on the electron's way through are cumulatively enhanced, leading to the phenomenon of CISS. To understand CISS has remained to be a theoretical challenge. A theorem based on the Onsager reciprocal principle states that the CISS effect vanishes when thermally averaging over all electron states. However, if the incoming electrons are generated optically, as in experiments, this null result will not arise because of the nonthermal character of the electrons [172].

In electronic transport through mesoscopic, solid-state systems, various resonances in experimental quantities such as conductance and scattering cross sections can arise and are described by the universal Fano formula [175, 176]. In terms of spin transport, resonances in the spin polarization arising from the edge of a zigzag graphene nanoribbon was studied using the nonequilibrium Green's function formalism within the framework of density functional theory [177]. Quite recently, a Fano formula characterizing the resonances associated with spin transport was derived [178]. In quantum biology, there were studies of Fano resonances in molecular charge transport [179, 180]. For example, control of electron transport through Fano resonances in molecular wires was investigated using a first-principle approach, where the resonances are induced and can be controlled by the side groups attached to the molecule [181]. Control of quantum interference in T-shaped molecules was investigated theoretically [182], and it was found that a Fano resonance can lead to a giant thermal power [183]. Fano

resonances can also arise from Andreev reflection in molecular wires [184]. Recent experiments have exploited conformal control of quantum interference to modulate single molecule charge transport [185]. In Chapter 7, we investigate spin transport through a chiral polyacetylene molecule and uncover the emergence of spin Fano resonances as a manifestation of the chiral induced spin selectivity (CISS) effect.

1.4 Outline of This Thesis

In Chapter 1, we give the introduction and background for the systems and phenomena we investigate. The aim of Chapter 2 is to present the phenomenon of enhanced non-equilibrium quantum transport of pseudospin-1 particles. In Chapter 3, quantum scattering in massive pseudospin-1 systems is systematically studied, especially with respect to skew scattering as related to AHE. In chapter 4, utilizing the α-T_3 lattice as a paradigm, we find that, in the Dirac electron optics regime, the semiclassical decay of the quasiparticles from a chaotic cavity can be effectively exploited for detecting the Berry phase. In Chapter 5, we investigate the possibility to realize phase locking of two nanoscale magnetic oscillators coupled via the electron on the surface of topological insulator. In Chapter 6, we study the electron skew scattering from a magnetic skyrmion structure. In Chapter 7, we investigate spin transport through a chiral polyacetylene molecule and uncover the emergence of spin Fano resonances as a manifestation of the chiral induced spin selectivity (CISS) effect.

Chapter 2

NONEQUILIBRIUM TRANSPORT IN THE PSEUDOSPIN-1 DIRAC-WEYL SYSTEM

Solid state materials hosting pseudospin-1 quasiparticles have attracted a great deal of recent attention. In these materials, the energy band contains of a pair of Dirac cones and a flat band through the connecting point of the cones. As the "caging" of carriers with a zero group velocity, the flat band itself has zero conductivity. However, in a non-equilibrium situation where a constant electric field is suddenly switched on, the flat band can enhance the resulting current in both the linear and nonlinear response regimes through distinct physical mechanisms. Using the (2+1) dimensional pseudospin-1 Dirac-Weyl system as a concrete setting, we demonstrate that, in the weak field regime, the interband current is about twice larger than that for pseudospin-1/2 system due to the interplay between the flat band and the negative band, with the scaling behavior determined by the Kubo formula. In the strong field regime, the intraband current is $\sqrt{2}$ times larger than that in the pseudospin-1/2 system, due to the additional contribution from particles residing in the flat band. In this case, the current and field follows the scaling law associated with Landau-Zener tunneling. These results provide a better understanding of the role of the flat band in non-equilibrium transport and are experimentally testable using electronic or photonic systems.

2.1 Introduction

In this chapter, we study the transport dynamics of pseudospin-1 quasiparticles that arise in material systems with a pair of Dirac cones and a flat band through their

connecting point. Under the equilibrium condition and in the absence of disorders, the flat band acts as a perfect "caging" of carriers with zero group velocity and hence it contributes little to the conductivity [186, 187, 188]. However, as we will show in this paper, the flat band can have a significant effect on the non-equilibrium transport dynamics. Through numerical and analytic calculation of the current evolution for both weak and strong electric fields, we find the general phenomenon of current enhancement as compared with that associated with non-equilibrium transport of pseudospin-1/2 particles. In particular, for weak field, the interband current is twice as large as that for pseudospin-1/2 system due to the interference between particles from the flat band and the negative band, the scaling behavior of which agrees with that determined by the Kubo formula. For strong field, the intraband current is $\sqrt{2}$ times larger than that in pseudospin-1/2 system, as a result of the additional contribution from the particles residing in the flat band. In this case, the physical origin of the scaling behavior of the current-field relation can be attributed to Landau-Zener tunneling. Our findings suggest that, in general, the conductivity of pseudospin-1 materials can be higher than that of pseudospin-1/2 materials.

2.2 Pseudospin-1 Hamiltonian and Current

We consider a system of 2D noninteracting, Dirac-like pseudospin-1 particles subject to a uniform, constant electric field applied in the x direction. The system is described by the generalized Dirac-Weyl Hamiltonian [24, 10]. The electric field, switched on at $t = 0$, can be incorporated into the Hamiltonian through a time-dependent vector potential [41, 42, 43, 44, 45, 189, 190, 191]: $\boldsymbol{A}(t) = [A(t), 0, 0]$, where $A(t) = -Et\Theta(t)$. The resulting Hamiltonian is

$$H = v_F\{S_x[p_x - qA(t)] + S_y p_y\}, \tag{2.1}$$

where v_F is the Fermi velocity of the pseudospin-1 particle from the Dirac-like cones, $q = -e$ ($e > 0$) is the electronic charge, $\boldsymbol{S} = (S_x, S_y, S_z)$ is a vector of matrices with components

$$S_x = \frac{1}{\sqrt{2}} \begin{bmatrix} 0 & 1 & 0 \\ 1 & 0 & 1 \\ 0 & 1 & 0 \end{bmatrix}, S_y = \frac{1}{\sqrt{2}} \begin{bmatrix} 0 & -i & 0 \\ i & 0 & -i \\ 0 & i & 0 \end{bmatrix}, S_z = \begin{bmatrix} 1 & 0 & 0 \\ 0 & 0 & 0 \\ 0 & 0 & -1 \end{bmatrix}.$$

The three matrices form a complete representation of pseudospin-1 particles, which satisfy the angular momentum commutation relations $[S_l, S_m] = i\epsilon_{lmn} S_n$ with three eigenvalues: $s = \pm 1, 0$, where ϵ_{lmn} is the Levi-Civita symbol. However, they do not follow the Clifford algebra underlying spin-1/2 particles. The corresponding time dependent wave equation reads

$$i\hbar \partial_t \Psi_p(t) = H \Psi_p(t). \tag{2.2}$$

Under the unitary transformation

$$U = \begin{bmatrix} \frac{1}{2} e^{-i\theta} & -\frac{1}{\sqrt{2}} e^{-i\theta} & \frac{1}{2} e^{-i\theta} \\ \frac{\sqrt{2}}{2} & 0 & -\frac{\sqrt{2}}{2} \\ \frac{1}{2} e^{i\theta} & \frac{1}{\sqrt{2}} e^{i\theta} & \frac{1}{2} e^{i\theta} \end{bmatrix}$$

with $\tan\theta = p_y/[p_x - qA(t)]$, we can rewrite Eq. (2.2) in the basis of adiabatic energy as

$$i\hbar \partial_t \Phi_p(t) = \big[S_z \epsilon_p(t) + S_x \sqrt{2} C_0(t)\big] \Phi_p(t), \tag{2.3}$$

where $\Phi_p(t) = U^\dagger \Psi_p(t) = [\alpha_p(t), \gamma_p(t), \beta_p(t)]^T$ and $C_0(t) = \hbar v_F^2 p_y eE/\sqrt{2}\epsilon_p^2(t)$, $\epsilon_p = v_F \sqrt{(p_x - eEt)^2 + p_y^2}$. Initially at $t = 0$, the negative band is assumed to be fully filled: $\Phi_p(t = 0) = [0, 0, 1]^T$. From the equation of motion, we obtain the current operator in the original basis as $J_x = -e\nabla_{\boldsymbol{p}} H = -e v_F S_x$. In the transformed adiabatic

energy base, the current operator is

$$J_x = -ev_F(S_z\cos\theta - S_y\sin\theta). \tag{2.4}$$

We thus have the current density for a certain state as

$$\begin{aligned}\langle J_x\rangle_p(t) = -ev_F\big\{&\cos\theta[|\alpha_p(t)|^2 - |\beta_p(t)|^2] \\ &- \sqrt{2}\sin\theta\mathrm{Re}[i\alpha_p(t)\gamma_p^*(t) + i\gamma_p(t)\beta_p^*(t)]\big\}.\end{aligned} \tag{2.5}$$

In Eq. (2.5), the first term is related to the particle number distribution associated with the positive and the negative bands, which is the intraband or conduction current. The second term in Eq. (2.5) characterizes the interference between particles from distinct bands, which is related to the phenomenon of relativistic Zitterbewegung and can be appropriately called the interband or polarization current.

To assess the contribution of each band (i.e., the positive, flat, or negative) to the interband current, we seek to simplify the current expression. Through some algebraic substitutions, we get

$$\begin{aligned}\partial_t|\alpha_p(t)|^2 &= 2\mathrm{Re}[\alpha_p(t)\partial_t\alpha_p^*(t)], \\ \partial_t|\gamma_p(t)|^2 &= 2\mathrm{Re}[\gamma_p(t)\partial_t\gamma_p^*(t)].\end{aligned}$$

From the Dirac equation (2.3), we have

$$\begin{aligned}\hbar\alpha_p(t)\partial_t\alpha_p^*(t) &= i\epsilon_p\alpha_p(t)\alpha_p^*(t) + iC_0\alpha_p(t)\gamma_p^*(t), \\ \hbar\gamma_p(t)\partial_t\gamma_p^*(t) &= iC_0\gamma_p(t)\alpha_p^*(t) + iC_0\gamma_p(t)\beta_p^*(t),\end{aligned}$$

which gives

$$\begin{aligned}\mathrm{Re}[i\alpha_p(t)\gamma_p^*(t)] &= \frac{\hbar}{2C_0}\partial_t|\alpha_p(t)|^2, \\ \mathrm{Re}[i\gamma_p(t)\beta_p^*(t)] &= \frac{\hbar}{2C_0}\big[\partial_t|\alpha_p(t)|^2 + \partial_t|\gamma_p(t)|^2\big].\end{aligned} \tag{2.6}$$

Using the total probability conservation $|\alpha_p|^2 + |\gamma_p|^2 + |\beta_p|^2 = 1$, we finally arrive at the following current expression

$$\langle J_x \rangle_p(t) = -ev_F \Big\{ \frac{v_F(p_x - eEt)}{\epsilon_p(t)} \big[2|\alpha_p(t)|^2 + |\gamma_p(t)|^2 - 1\big] - \frac{\epsilon_p(t)}{v_F eE} \big(2\partial_t |\alpha_p|^2 + \partial_t |\gamma_p|^2\big) \Big\}, \tag{2.7}$$

where the third term in the first part that is independent of particle distribution vanishes after an integration over the momentum space.

For convenience, in our numerical calculations we use dimensionless quantities, which we obtain by introducing the scale Δ that is a characteristic energy of the system. The dimensionless time, electric field, momentum, energy, and coefficient are

$$\begin{aligned} \tilde{t} &= \Delta t/\hbar, \\ \tilde{E} &= ev_F \hbar E/\Delta^2, \\ \tilde{p} &= v_F p/\Delta, \\ \tilde{\epsilon} &= \sqrt{(\tilde{p}_x - \tilde{E}\tilde{t})^2 + \tilde{p}_y^2}, \\ \tilde{C}_0 &= \tilde{E}\tilde{p}_y/\sqrt{2}[(\tilde{p}_x - \tilde{E}\tilde{t})^2 + \tilde{p}_y^2], \end{aligned}$$

respectively. The dimensionless current $\tilde{J}$ can be expressed in units of $e\Delta^2/v_F\hbar^2\pi^2$.

2.3 Weak Field Regime: Enhancement of Interband Current

In the weak field regime, the intraband current can be ignored compared to interband current due to the less number of conducting particles (see Appendix B or refer to psedospin-1/2 case [42, 43]). In particular, the interband current for a certain state can be expressed as

$$J_p^{inter} = \frac{\epsilon_p(t)}{E}[2\partial_t |\alpha_p|^2 + \partial_t |\gamma_p|^2],$$

where, for pseudospin-1/2 particles, the interband current has only the first term [43]. The additional term $[\epsilon_p(t)/E]\partial_t|\gamma_p|^2$ is unique for pseudospin-1 particles. To reveal the

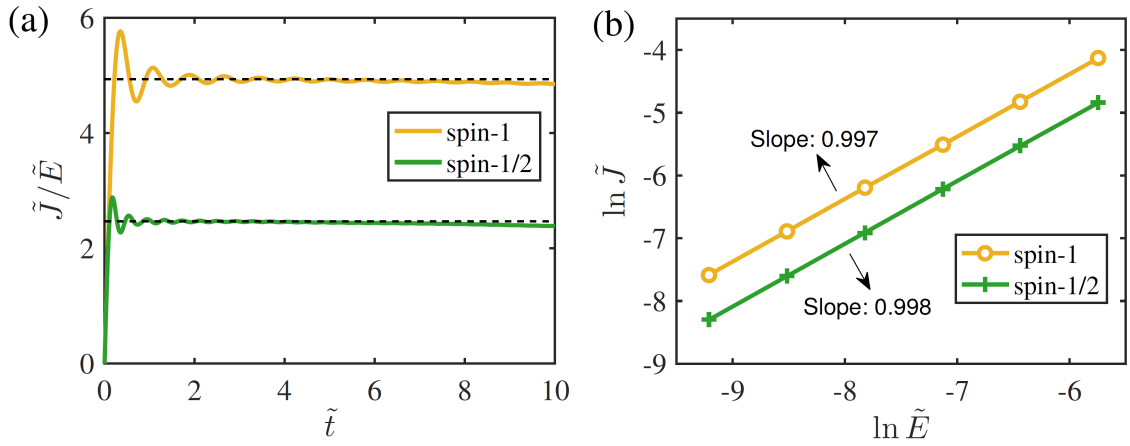

Figure 2.1: Interband current in pseudospin-1 and pseudospin-1/2 systems. (a) Evolution of the total current to electric field ratio $\tilde{J}/\tilde{E}$ with time $\tilde{t}$ for pseudospin-1 and 1/2 systems for a fixed electric field $\tilde{E} = 0.0004$, where the dashed lines denote the theoretical values $\pi^2/2$ and $\pi^2/4$ for the pseudospin-1 and pseudospin-1/2 systems, respectively. The yellow and green lines represent the respective numerical results. (b) The total current $\tilde{J}$ versus the electric field $\tilde{E}$ for time $\tilde{t} = 2$ for the two systems. Comparing with the pseudospin-1/2 system, the interband current in the pseudospin-1 system is greatly enhanced.

scaling behavior of the interband current and to assess the role of the positive and the flat bands in the current, we impose the weak field approximation: $|p| = \sqrt{p_x^2 + p_y^2} \gg eEt$ everywhere except in the close vicinity of the Dirac point, which allows us to obtain an analytic expression for the interband current. Under the approximation, the coefficients ϵ_p and C_0 become $\epsilon_p \approx v_F p$ and $C_0 \approx \hbar p_y eE/(\sqrt{2}p^2)$, which are time independent. Substituting these approximations into Eq. (2.3), we obtain the three components of the time dependent state $\Phi_p(t)$ as

$$\alpha_p(t) = \frac{1}{2}[\cos\omega t + m_0^2(\cos\omega t - 1) - 1], \tag{2.8}$$

$$\beta_p(t) = \frac{1}{2}[\cos\omega t - 2m_0 \sin\omega t - m_0^2[\cos\omega t - 1] + 1], \tag{2.9}$$

$$\gamma_p(t) = \frac{1 + m_0^2}{2C_0}[-i\hbar\omega \sin\omega t - \epsilon_p(\cos\omega t - 1)]. \tag{2.10}$$

The interband current contains two parts:

$$J_p^{\alpha} = 2\frac{\epsilon_p C_0^4 \omega}{E(\epsilon_p^2 + 2C_0^2)^2}(2\sin\omega t - \sin 2\omega t), \tag{2.11}$$

and

$$J_p^\gamma = 2\frac{\epsilon_p C_0^2 \omega}{E(\epsilon_p^2 + 2C_0^2)^2}(\epsilon_p^2 \sin\omega t + C_0^2 \sin 2\omega t), \tag{2.12}$$

which correspond to contributions from the positive and the flat bands, respectively, where $\omega = \sqrt{\epsilon_p^2 + 2C_0^2}/\hbar$. For sufficiently weak field such that the off diagonal term is small compared with the diagonal term in Eq. (2.3), we have $\epsilon_p^2 \gg 2C_0^2$, i.e.,

$$v_F^2 p^2 \gg \frac{p_y^2}{p^2}\frac{\hbar^2 e^2 E^2}{p^2}.$$

In this case, the contribution from the positive band is nearly zero and the flat band contribution is

$$J_p^\gamma \approx 2\frac{\epsilon_p^3 C_0^2 \omega}{E(\epsilon_p^2 + 2C_0^2)^2}\sin\omega t \approx e^2\hbar E\frac{\sin^2\theta}{p^2}\sin\frac{v_F p t}{\hbar}. \tag{2.13}$$

The total positive band contribution over the momentum space is negligibly small, so the flat band contributes dominantly to the total interband current:

$$\begin{aligned} J_{inter} &= \frac{1}{\pi^2\hbar^2}\iint e^2\hbar E\frac{\sin^2\theta}{p}\sin\frac{v_F p t}{\hbar}d\theta dp \\ &= \frac{e^2}{2\hbar}E = \frac{e\Delta^2}{v_F\hbar^2\pi^2}\cdot\frac{\pi^2}{2}\tilde{E}. \end{aligned} \tag{2.14}$$

The dimensionless current is given by

$$\tilde{J} = \frac{\pi^2}{2}\tilde{E}. \tag{2.15}$$

To verify the analytical prediction Eq. (2.14), we calculate the interband current by numerically solving the time dependent Dirac equation (2.3). For comparison, we also calculate the current for the pseudospin-1/2 system both numerically and analytically. The results are shown in Fig. 2.1. For the numerical results in Fig. 2.1(a), the momentum space is defined as $\tilde{p}_x \in [-8, 8]$ and $\tilde{p}_y \in [-8, 8]$ and the integration grid has the spacing 0.0002. In Fig. 2.1(b), we use the same momentum space grid for $\tilde{E} = 0.0001, 0.0002, 0.0004$ but for $\tilde{E} = 0.0008, 0.0016, 0.0032$, the ranges of the

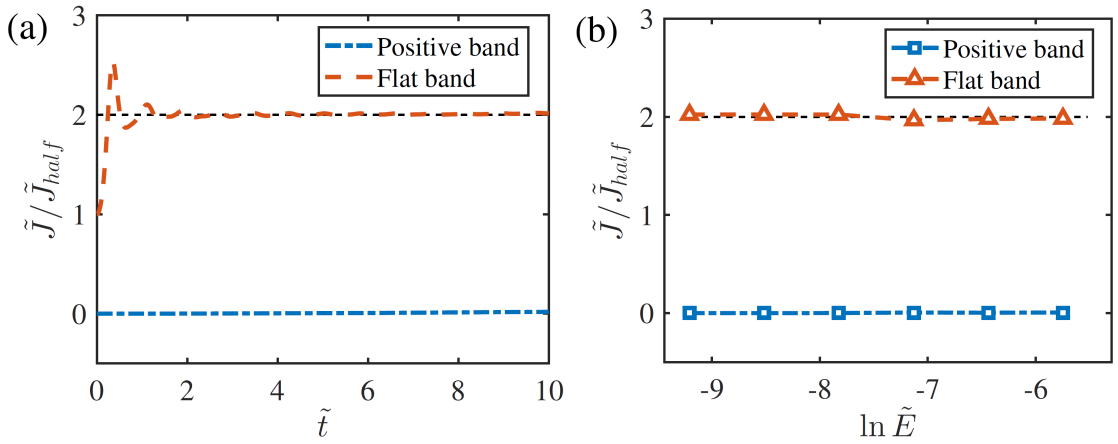

Figure 2.2: Origin of interband current in the pseudospin-1 system. (a) Ratio between interband currents from the pseudospin-1 and pseudospin-1/2 systems as a function of time for electric field strength $\tilde{E} = 0.0004$, (b) the current ratio versus $\tilde{E}$ for fixed time $\tilde{t} = 2$. The black dashed lines are theoretical results, and the red and blue lines are for flat band and positive band, respectively. These results indicate that, for the pseudospin-1 system, the flat band is the sole contributor to the interband current.

momentum space are doubled. From Fig. 2.1(a), we see that the interband current for both pseudospin-1 and pseudospin-1/2 cases are independent of time. That is, after a short transient, the interband current approaches a constant. From Fig. 2.1(b), we see that the current is proportional to the electric field E for both pseudospin-1 and pseudospin-1/2 particles (with unity slope on a double logarithmic scale), but the proportional constant is larger in the pseudospin-1 case. While in the weak field regime, the scaling relation between the interband current and the electric field is the same for pseudospin-1 and pseudospin-1/2 particles, there is a striking difference in the current magnitude. In particular, the interband current for the pseudospin-1 system is about twice that for the pseudospin-1/2 counterpart, as revealed by both the theoretical approximation Eq. (2.14) and the numerical result [corresponding to the dashed and solid lines in Fig. 2.1(a) respectively]. The interband current in the pseudospin-1 system is thus greatly enhanced as compared with that in the pseudospin-1/2 system.

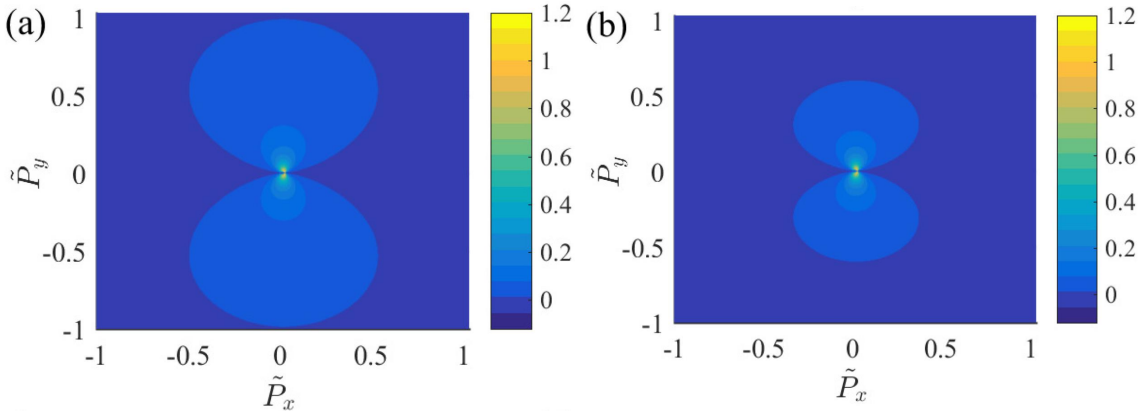

Figure 2.3: Interband current distribution in the momentum space: (a) pseudospin-1 system and (b) pseudospin-1/2 system. The time and electric field strength are $\tilde{t} = 2$ and $\tilde{E} = 0.0128$ respectively.

Intuitively, the phenomenon of current enhancement can be attributed to the extra flat band in the pseudospin-1 system: while the band itself does not carry any current, it can contribute to the interband current. Indeed, the theoretical results in Eqs. (2.11) and (2.12) indicate that the flat band contributes to the total interband current, while the positive band contributes little to the current. To gain physical insights, we numerically calculate three currents: the positive and flat band currents from the pseudospin-1 system, and the current from the pseudospin-1/2 system. Figure 2.2 shows that the ratio of the flat band current and the pseudospin-1/2 current is two, while the ratio between the positive band and pseudospin-1/2 currents is nearly zero, indicating that in the pseudospin-1 system, almost all the interband current originates from the flat band.

To better understand the phenomenon of interband current enhancement in the pseudospin-1 system, we calculate the current distribution for both pseudospin-1 and pseudospin-1/2 systems in the momentum space, as shown in Fig. 2.3. We see that the area in the momentum space with significant current is larger for the pseudospin-1 case, although the current magnitude is almost the same near the Dirac point for both systems. This is indication that the flat band can contribute substantially

more current because the Landau-Zener transition "gap" P_y for the pseudospin-1 system is small compared to that for the pseudospin-1/2 system. Mathematically, with respect to the single state current expression (2.13) for the pseudospin-1 system, the corresponding one state contribution for the pseudospin-1/2 system is

$$J_p^{half} \approx \frac{e^2\hbar E}{2}\frac{\sin^2\theta}{p^2}\sin\left(\frac{2v_F pt}{\hbar}\right). \tag{2.16}$$

The integration of current over the entire momentum space gives the factor 2 of enhancement for the pseudospin-1 system as compared with the pseudospin-1/2 system. This implies that quantum interference occurs mainly between particles from the negative and flat bands due to the small gap between them.

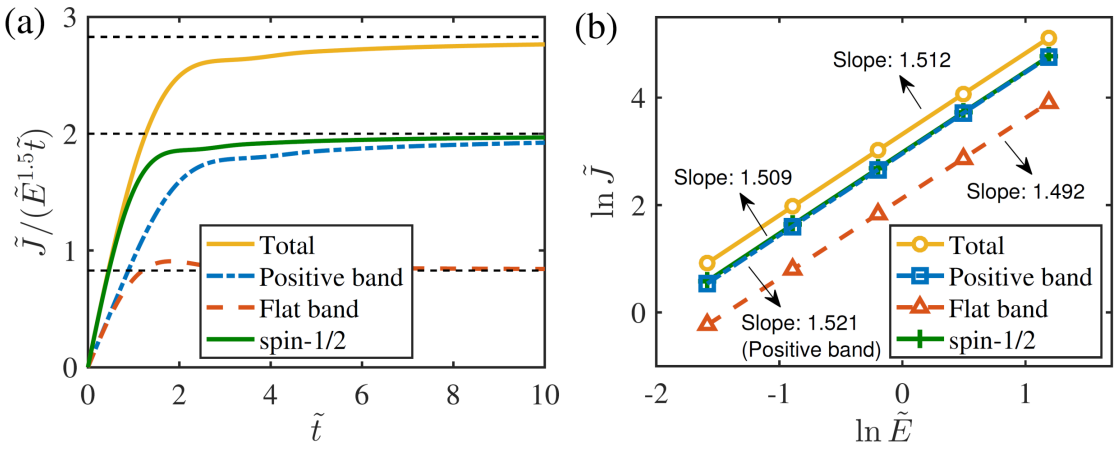

Figure 2.4: Enhancement of intraband current in the strong electric field regime. Intraband current and contributions from distinct bands (a) versus time for $\tilde{E} = 0.8192$, where the black dashed lines represent the analytical values $2(\sqrt{2}-1)$, 2, $2\sqrt{2}$ (from bottom) and (b) versus electric field at time $\tilde{t} = 10$ (for six values of the electric field: $\tilde{E} = 0.2048, 0.4096, 0.8192, 1.6384, 3.2768$.

2.4 Strong Field Regime: Enhancement of Intraband Current

In the strong field regime, the intraband current dominates (see Appendix B) and has the form of the first term in Eq. (2.7). The transition probabilities for the

positive, flat and negative bands are given, respectively, by [192]

$$n_p^+ = \Theta(p_x)\Theta(eEt - p_x)\exp(-\frac{\pi v_F p_y^2}{\hbar eE}), \tag{2.17}$$

$$n_p^0 = \Theta(p_x)\Theta(eEt - p_x) \cdot 2\Big[1 - \exp(-\frac{\pi v_F p_y^2}{2\hbar eE})\Big]\Big[\exp(-\frac{\pi v_F p_y^2}{2\hbar eE})\Big], \tag{2.18}$$

$$n_p^- = \Theta(p_x)\Theta(eEt - p_x)\Big[1 - \exp(-\frac{\pi v_F p_y^2}{2\hbar eE})\Big]^2, \tag{2.19}$$

subject to the momentum constraint: $(p_x, eEt - p_x) \gg |p_y|$. The transition probabilities are essentially the pair production or transition probabilities in the generalized three-level Landau-Zener model. Substituting Eqs. (2.17) and (2.19) into Eq. (2.5) (or equivalently Eq. (2.7)) and integrating its first term over the momentum space, we obtain the positive-band contribution to the intraband current with conducting electrons (or partially filled electrons) populated from the filled bands

$$\begin{aligned} J^+ &= \frac{ev_F}{\hbar^2\pi^2}\iint \frac{v_F(eEt - p_x)}{\epsilon_p(t)} \cdot |\alpha_p(t)|^2 dp_x dp_y \\ &\approx \frac{ev_F}{\hbar^2\pi^2}\int_0^{eEt} dp_x \int_{-p_x}^{p_x} |\alpha_p(t)|^2 dp_y \\ &\approx \frac{ev_F}{\hbar^2\pi^2}\int_0^{eEt} dp_x \int_{-\infty}^{+\infty} |\alpha_p(t)|^2 dp_y \\ &= \frac{e^2}{\hbar\pi^2}\sqrt{\frac{ev_F}{\hbar}}E^{3/2}t \qquad (2.20) \\ &= \frac{e\Delta^2}{v_F\hbar^2\pi^2}\tilde{E}^{3/2}\tilde{t}. \qquad (2.21) \end{aligned}$$

Meanwhile, we get the contribution from the initially filled negative band with holes left by the electrons driven into the positive band and flat band as well

$$J^- = (2\sqrt{2} - 1)\frac{e^2}{\hbar\pi^2}\sqrt{\frac{ev_F}{\hbar}}E^{3/2}t \tag{2.22}$$

$$= \frac{e\Delta^2}{v_F\hbar^2\pi^2}(2\sqrt{2} - 1)\tilde{E}^{3/2}\tilde{t}. \tag{2.23}$$

So, in general, the conducting hole based intraband current J^- can be formally attributed to two parts, i.e.

$$J^- = J^-_{positive} + J^-_{flat}, \tag{2.24}$$

where the first term accounts the holes left by electrons finally driven into the positive band only while the second term is associated with the hole concentration induced by the flat band. Apparently, we have $J^-_{positive} = J^+$. As such, the so-called flat band induced current results from the hole concentration it induces in the dispersive band and reads

$$J^-_{flat} = J^- - J^+ = \frac{e\Delta^2}{v_F\hbar^2\pi^2} 2(\sqrt{2}-1)\tilde{E}^{3/2}\tilde{t}. \tag{2.25}$$

With both the conducting electrons and corresponding holes taken into account, the dispersive positive band based current is obtained as

$$J_{positive} = J^+ + J^-_{positive} = 2 \cdot \frac{e^2}{\hbar\pi^2}\sqrt{\frac{ev_F}{\hbar}}E^{3/2}t \tag{2.26}$$

$$= 2 \cdot \frac{e\Delta^2}{v_F\hbar^2\pi^2}\tilde{E}^{3/2}\tilde{t}, \tag{2.27}$$

which alone is the same amount as the total current generated for the pseudospin-1/2 system in strong field regime. The total intraband current in the presence of the flat band (for the pseudospin-1 system with an additional flat band) is

$$J^{intra} = J^+ + J^- = J_{positive} + J^-_{flat}$$

$$= 2\sqrt{2}\frac{e^2}{\hbar\pi^2}\sqrt{\frac{ev_F}{\hbar}}E^{3/2}t \tag{2.28}$$

$$= \frac{e\Delta^2}{v_F\hbar^2\pi^2} 2\sqrt{2}\tilde{E}^{3/2}\tilde{t}. \tag{2.29}$$

The intraband current scales with the electrical field as $E^{3/2}$ and scales linearly with time, which are the same as those for the pseudospin-1/2 system [43]. However, for the pseudospin-1 system, the magnitude of the intraband current is larger: there

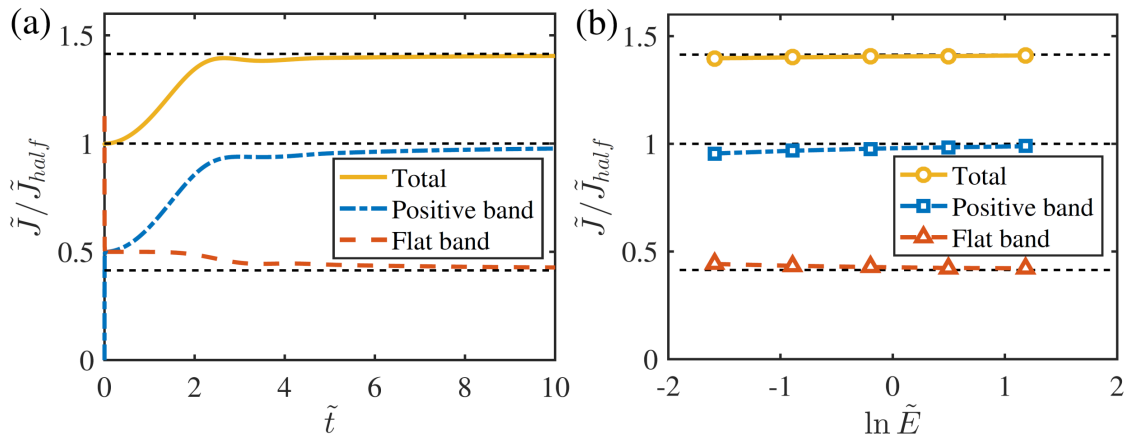

Figure 2.5: Further evidence of enhancement of intraband current in the pseudospin-1 system. (a) The ratio of the intraband currents in the pseudospin-1 and pseudospin-1/2 systems versus time $\tilde{t}$ for $\tilde{E} = 0.8192$. (b) The current ratio versus $\tilde{E}$ for $\tilde{t} = 10$.

is an enhancement factor of $\sqrt{2}$ as compared with the pseudospin-1/2 system. Since the positive band contribution is the same as for the pseudospin-1/2 system, the enhancement is due entirely to the flat band contribution.

We now provide numerical evidence for the phenomenon of intraband current enhancement in the pseudospin-1 system. Figures 2.4(a) and 2.4(b) show the intraband current versus time $\tilde{t}$ and electric field strength $\tilde{E}$, respectively, where the momentum space grid is $p_x \in [-16, 16]$ and $p_y \in [-16, 16]$ with spacing 0.002 in (a) and the momentum space range is increased according to the increase in the electric field strength in (b). We see that the intraband current scales with E as $E^{3/2}t$ - the same as for the pseudospin-1/2 system [43, 42]. There is good agreement between the numerical results and the theoretical predictions Eqs. (2.21-2.29).

To provide further confirmation of the enhancement of the intraband current, we calculate the ratio between the currents from the pseudospin-1 and pseudospin-1/2 systems versus time for certain electric field, as shown in Fig. 2.5(a). The ratio versus the electric field for a given time is shown in Fig. 2.5(b). We see that, in the long time regime, under a strong electric field the total intraband current for the pseudospin-

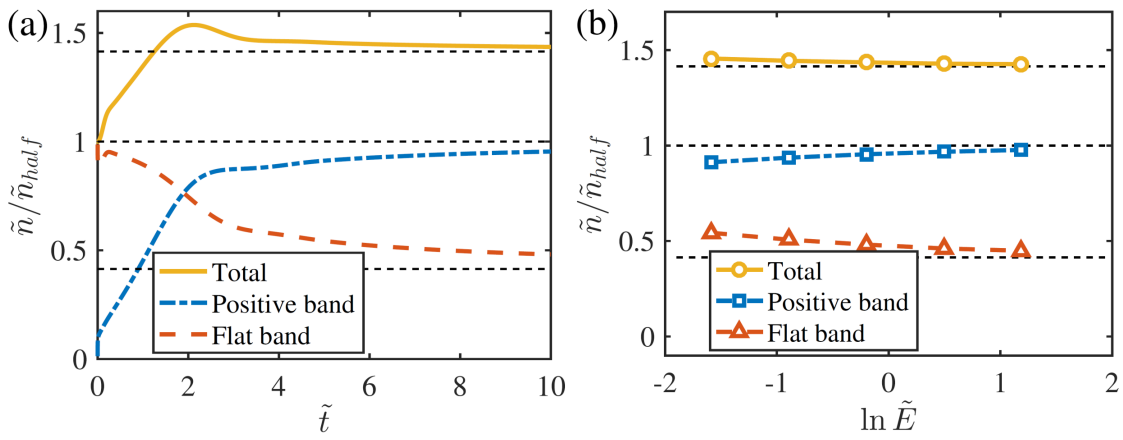

Figure 2.6: Numerical evidence of pair creation mechanism for the intraband current. The ratio of particle number distribution for pseudospin-1 and pseudospin-1/2 systems (a) versus time $\tilde{t}$ for $\tilde{E} = 0.8192$ and (b) versus $\tilde{E}$ for $\tilde{t} = 10$.

1 system is about $\sqrt{2}$ times the current of the pseudospin-1/2 system. However, the positive band currents are approximately the same for both systems. The extra current in the pseudospin-1 system, which is about 0.4 times the contribution from the positive band, is originated from the flat band. These numerical results agree well with the theoretical predictions. The physical mechanism underlying the intraband current enhancement is the Schwinger mechanism or Landau-Zener tunneling. Note that, in Fig. 2.5, the transition of an electron from the negative to the flat bands does not contribute to the intraband current, as the process leaves behind a hole in the negative band that contributes to the net current.

If the intraband current is generated by pair creation through Landau-Zener tunneling, the number of created particles should be consistent with the current behaviors. To test this, we numerically calculate the particle number distribution in different bands and plot the ratio between the numbers of particles for pseudospin-1 and pseudospin-1/2 systems versus time and the electric field, as shown in Fig. 2.6. For the pseudospin-1 system, the number of particles created in the positive band is approximately the same as that created in the upper band in the pseudospin-1/2

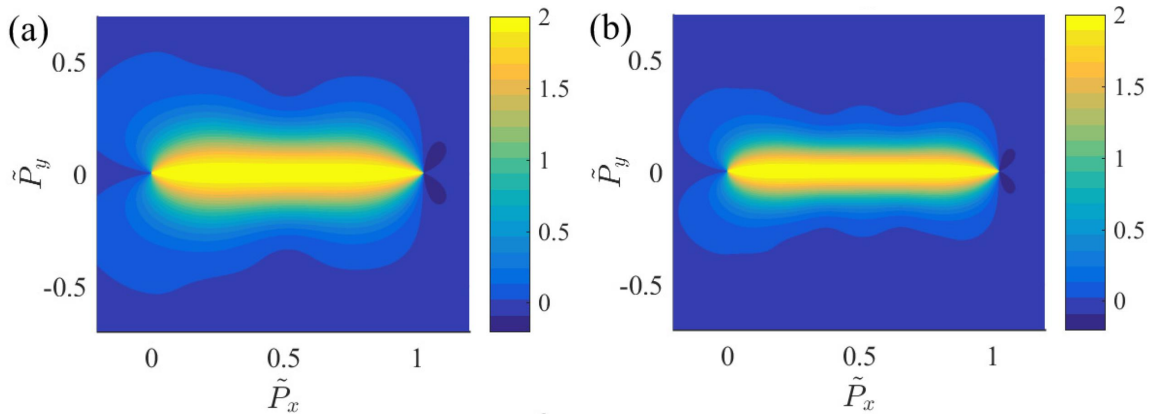

Figure 2.7: Current density distribution in the momentum space. (a,b) For pseudospin-1 and pseudospin-1/2 systems, respectively, the distributions of the current density in the momentum space for $\tilde{t} = 20$ and $\tilde{E} = 0.0512$. When the momentum gap value P_y is large, the flat band can enhance the current.

system, and the number of particles in the flat band is only about half of that in the positive band. Note that, for the positive band, it is necessary to count the particle number twice as both electrons and holes contribute to the transport current. However, for the flat band, only holes contribute to the current. We see that, for each band, the particle number distribution is consistent with the current distribution, providing strong evidence that the intraband current results from pair creation in the negative band. In fact, under the strong field approximation, the intraband current is the particle distributions in the positive and flat bands multiplying by the constant ev_F, as current is due to electron and hole transport.

We also calculate the current density distribution in the momentum space for a fixed time and electric field strength, as shown in Fig. 2.7. We see that the current distribution range in the P_y direction is wider for the pseudospin-1 system than for the pseudospin-1/2 system. However, the current distribution near $P_y = 0$ is approximately the same for the two systems, and the current decays in the p_y direction. In addition, there is a current cut-off about $\tilde{p}_x = \tilde{E}\tilde{t}$ along the p_x axis. All these features of the current density distribution can be fully explained by the theoretical formulas

(2.17-2.19). The general result is that the flat band can enhance the current when the "gap" P_y is large.

2.5 Current-Electric Field Characteristics for Pseudospin-1 System

In general, for carriers following a given multi-band dispersion relation such as the particular three band profile investigated in this work, contributions to the current are always from two parts i.e. the intraband current and interband current. Physically, the intraband current is proportional to the number of the electrons (holes) within an unfilled (occupied) band while the interband current is subject to the rate of change of the number characterizing the interband interference. It follows from Eq. (2.7) that the former is quantified by the transition amplitudes while the latter depends on their rate of change. In the weak driving field, the transition amplitudes (probabilities) between the occupied band and the empty band and hence the number of electron-hole generation are always so small that the resulting intraband current is rather weak, while their rate of change leading to the interband current have a different scenario. By calculation, it quantitatively turns out that the particle generation number based intraband current is negligible compared with its rate of change based interband current at weak field and becoming dominant as the field strength increasing. So, in weak field regime, the interband current dominates, while in strong field case, the interband current is overwhelmed by intraband ones, as the scaling factor of current-field relation changing from 1 to 1.5. The numerical results are shown in Fig. 2.8.

2.6 Discussions and Outlook

In our linear dispersion model, the interband current will be overwhelmed by intraband current with increasing electric field or evolution time. When it comes to

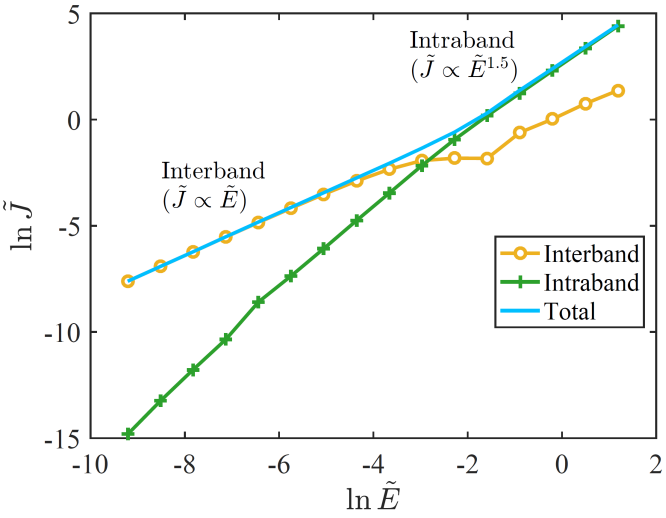

Figure 2.8: Current-electric field characteristics of pseudospin-1 system at $\tilde{t} = 5$. The dominant contribution to the total current changes from interband to intraband, with the scaling factor of the current-field relation changing from 1 to 1.5.

the real materials, the effective Dirac-like Hamiltonian description only works around the degeneracy (Dirac) point as it should be, which will intrinsically impose a time upper bound on the valid simulation. Since the models we consider do not provide a channel of dissipation, the time range of applicability of our model in lattice model is essential. The time range is approximately the time required for the electric field to shift the momentum across the Brillounin zone, i.e., $\Delta p_x = eEt \approx \hbar/a$ with a being characteristic lattice constant, so in real materials, our results valid up to the time scale $t \sim \frac{\hbar}{eEa}$, which is similar to the time scale of pseudospin-1/2 model applied to graphene and in which the Bloch oscillation set in with period $t_B \sim \frac{\hbar}{eEa}$ [42]. So, under the time restriction $\tilde{E}\tilde{t} < \frac{\hbar v_F}{\Delta a}$ (in dimensionless form as used in this paper), our results can be obtained experimentally by tuning the characteristic energy Δ of the designed system.

If the whole band structure for real materials is taken into account, basically Bloch oscillations will set in under external electric fields when $t \gtrsim t_B$, i.e., the electron distribution oscillates along a certain range of lattice sites. For that case, the

present Dirac-like Hamiltonian is incapable while a full tight-binding Hamiltonian $H_{TB}(\boldsymbol{p})$ characterizing the multiband structure associated with a particular lattice configuration is expected to work, e.g. for the Dice or T_3 lattice with intersite distance a and hopping integral t, it reads

$$H_{TB}^{(dice)}(\boldsymbol{p}) = \begin{bmatrix} 0 & h_{\boldsymbol{p}} & 0 \\ h_{\boldsymbol{p}}^* & 0 & h_{\boldsymbol{p}} \\ 0 & h_{\boldsymbol{p}}^* & 0 \end{bmatrix}, \tag{2.30}$$

$$h_{\boldsymbol{p}} = -t\left(1 + 2\exp\left(3ip_y a/2\right)\cos(\sqrt{3}p_x a/2)\right). \tag{2.31}$$

It has been argued in a previous work [42] based on a two-band tight-binding model for the honeycomb lattice that, at these later times around t_B, Bloch oscillations appear. Similar investigations on the later time behavior and the Bloch oscillation issue in such a generalized three band system with the extra flat band are still much less. We note that in a recent letter [37], a strikingly tunable/engineered Bloch oscillation with the flat band under some perturbation is reported in a quasi-one dimensional diamond lattice. It is interesting and open how it will behave in a more intricate two dimensional case.

For a particular lattice configuration associated with real materials, band anisotropy say the trigonal warping will generally arise when entering the energy range relatively far from the Dirac-like points at the later times. In that case, interesting direction dependent transport behavior is very likely. Some concrete lessons of driving direction resolved Bloch oscillation and Zener tunneling can be learned from existing studies for the two-band systems with a so-called 'semi-Dirac' spectrum (a hybrid of the linear and quadratic dispersion) [193, 194]. It is still unclear how it particularly looks like in the presence of the flat band and relevant dispersion anisotropy, which we think itself deserves further studies beyond the current Dirac-like approximate expansion.

2.7 Conclusion

We investigate non-equilibrium transport of quasiparticles subject to an external electric field in the pseudospin-1 systems arising from solid state materials whose energy band structure constitutes a pair of Dirac cones and a flat band through the conical connecting point. Since the group velocity for carriers associated with the flat band is zero, one may naively think that the flat band would give no contribution to the current. However, we find that the current in the pseudospin-1 system is generally enhanced as compared with that in the counterpart (pseudospin-1/2) system. In particular, in the weak field regime, for both systems the interband current dominates and is proportional to the electric field strength and is independent of time. However, the interference between quasiparticles associated with the flat and the negative bands in the pseudospin-1 system leads to an interband current whose magnitude is twice the current in the pseudospin-1/2 system. In the strong field regime, for both types of system the intraband current dominates and scales with the electric field strength as $E^{3/2}$ and linearly with time. We find that the current associated with carrier transition from the negative to the positive bands is identical for both types of system, but the flat band in the pseudospin-1 system contributes an additional term to the current, leading to an enhancement of the total intraband current. The general conclusion is that, from the standpoint of generating large current, the presence of the flat band in the pseudospin-1 system can be quite beneficial. Indeed, the interplay between the flat band and the Dirac cones can lead to interesting physics that has just begun to be understood and exploited.

2.8 Supplementary Notes

2.8.1 Analytic Calculation of the Interband Current

In the weak field regime, we can expand Eq. (2.3) as

$$i\hbar\partial_t\alpha_p(t) = \epsilon_p\alpha_p(t) + C_0\gamma_p(t), \tag{2.32}$$

$$i\hbar\partial_t\gamma_p(t) = C_0[\alpha_p(t) + \beta_p(t)], \tag{2.33}$$

$$i\hbar\partial_t\beta_p(t) = -\epsilon_p\beta_p(t) + C_0\gamma_p(t). \tag{2.34}$$

Applying the time differential operator $i\hbar\partial_t$ to Eqs. (2.32) and (2.34), we get

$$i\hbar\partial_t(i\hbar\partial_t\alpha_p(t)) = \epsilon_p i\hbar\partial_t\alpha_p(t) + C_0 i\hbar\partial_t\gamma_p(t), \tag{2.35}$$

$$i\hbar\partial_t(i\hbar\partial_t\beta_p(t)) = -\epsilon_p i\hbar\partial_t\beta_p(t) + C_0 i\hbar\partial_t\gamma_p(t), \tag{2.36}$$

and, hence,

$$-\hbar^2\partial_t^2\alpha_p(t) - \hbar^2\partial_t^2\beta_p(t) = [\alpha_p(t) + \beta_p(t)][\epsilon_p^2 + 2C_0^2]. \tag{2.37}$$

From Eqs. (2.32) and (2.34), we have

$$i\hbar\partial_t\alpha_p(t) - i\hbar\partial_t\beta_p(t) = \epsilon_p[\alpha_p(t) + \beta_p(t)]. \tag{2.38}$$

Defining $x_p(t) = \alpha_p(t) + \beta_p(t)$, and $y_p(t) = \alpha_p(t) - \beta_p(t)$, we get, from Eqs. (2.37) and (2.38), respectively, the following relations:

$$\frac{d^2x_p}{dt^2} + \frac{\epsilon_p^2 + 2C_0^2}{\hbar^2}x_p = 0, \tag{2.39}$$

$$\frac{dy_p}{dt} = \frac{\epsilon_p}{i\hbar}x_p. \tag{2.40}$$

Solving Eq. (2.39), we get

$$x_p(t) = A\cos\omega t + B\sin\omega t,$$

where A and B are constant, and $\omega = \sqrt{(\epsilon_p^2 + 2C_0^2)/\hbar^2}$. Using the initial condition that the negative band is fully filled: $(\Phi_p(t=0) = [0,0,1]^T)$, we have $x_p(t=0) = A = 1$. From Eq. (2.40), we have

$$y_p(t) = \frac{\epsilon_p}{i\hbar\omega}[\sin\omega t - B\cos\omega t] + d.$$

Using the initial condition, we get $y_p(t=0) = -m_0 B + d = -1$, where $m_0 = \epsilon_p/(i\hbar\omega)$, $d = m_0 B - 1$, which leads to

$$\alpha_p(t) = \frac{1}{2}(x+y) = \frac{1}{2}[\cos\omega t + B\sin\omega t + m_0(\sin\omega t - B\cos\omega t + B) - 1],$$
$$\beta_p(t) = \frac{1}{2}(x-y) = \frac{1}{2}[\cos\omega t + B\sin\omega t - m_0(\sin\omega t - B\cos\omega t + B) + 1].$$

Substituting the expressions of $\alpha_p(t)$ and $\beta_p(t)$ into Eqs. (2.32) and (2.34), we obtain an expression for $\gamma_p(t)$. Using $\gamma_p(t=0) = 0$, we have $B = -m_0$ and, hence,

$$\alpha_p(t) = \frac{1}{2}[\cos\omega t + m_0^2(\cos\omega t - 1) - 1], \tag{2.41}$$
$$\beta_p(t) = \frac{1}{2}[\cos\omega t - 2m_0\sin\omega t - m_0^2[\cos\omega t - 1] + 1], \tag{2.42}$$
$$\gamma_p(t) = \frac{1+m_0^2}{2C_0}[-i\hbar\omega\sin\omega t - \epsilon_p(\cos\omega t - 1)]. \tag{2.43}$$

Chapter 3

SUPER SKEW SCATTERING IN TWO-DIMENSIONAL DIRAC MATERIAL SYSTEMS WITH A FLAT BAND

The phenomenon of super scattering was previously found to arise in massless pseudospin-1 two-dimensional Dirac material systems with a flat band. Here we report the phenomenon of *super skew scattering* of massive pseudospin-1 quasiparticles, which does not arise in the corresponding massless system. In particular, the scatterer is electrically generated with a certain geometric shape, and the mass is induced by gap opening between the Dirac cones. Even for a circular scatterer, the occurrence of resonant states inside it can induce a sizable anomalous Hall current, which is associated with the gap opening. The striking finding is that, a significant reduction in the scatter size and/or the potential height does nothing to weaken the skew scattering and, for certain resonant states, even tends to strengthen the scattering. This phenomenon of *super skew scattering* in Dirac materials with a flat band is in stark contrast to the scattering of massive pseudospin-1/2 quasiparticles from the same configuration, where skew scattering is significantly weaker and a reduction in the scatterer strength can quickly diminish it. The phenomenon is established analytically for the case of a circular scatterer in the framework of continuum Hamiltonian, and is found to be robust for an elliptical scatterer, which is solved numerically by adopting the multiple-multipole method to massive pseudospin-1 scattering. Calculations of the electronic transport properties in the Lieb lattice system reveal the occurrence of a large anomalous Hall current as well, paving the way for experimental observation and test of super skew scattering. Because of the "skew" nature that is absent in massless pseudospin-1 systems, the phenomenon of super skew scattering

in massive systems can be exploited for applications in novel electronic or photonic Hall devices.

3.1 Introduction

Notwithstanding the existing work, quantum transport and scattering in massive pseudospin-1 systems have not been systematically studied, especially with respect to skew scattering as related to AHE. The purpose of this Chapter is to fill this gap. In particular, we investigate massive pseudospin-1 wave scattering from a finite size electrostatic potential barrier (realized by a proper gate voltage in experiments) in the deep subwavelength regime where the scatterer size is smaller than the wavelength. We find the occurrence of resonant modes inside the potential domain, associated with which is a quite appreciable skew scattering (Hall) current. The peak Hall current value obeys a scaling law with the potential properties. To test the robustness of the Hall current, we numerically study an elliptic potential barrier and find that the resonance-induced scattering peaks persist. In fact, due to breaking of the rotational symmetry, two sets of peaks emerge. For comparison, we also study the scattering of massive pseudospin-1/2 particles but find a vanishingly small Hall current as the result of absence of any resonant states. To test the feasibility of experimental observation of this "super-skew-scattering" phenomenon uncovered using a continuum Hamiltonian for pseudospin-1 wave scattering, we employ a finite size Lieb lattice device with a barrier generated by a gate potential, where gap opening is induced through the mechanisms of dimerization or spin-orbit coupling. We find that the resonant states leading to a large Hall current peak persist, which is particularly pronounced in the dimerization case. These findings have potential applications in AHE based devices.

3.2 Scattering Hamiltonian and Analytic Cross Sections for a Circular Potential

The 2D scattering system of massive pseudospin-1 quasiparticle from a scalar potential barrier of a given geometric shape is schematically illustrated in Fig. 3.1. The barrier shape is defined by the potential function $V(\boldsymbol{r})$, where $\boldsymbol{r}$ represents the position in the plane. The continuum massive pseudospin-1 Hamiltonian with a single Dirac point can be written as

$$H = \hbar v_F \boldsymbol{S} \cdot \boldsymbol{k} + \Delta S_z + V(\boldsymbol{r}), \tag{3.1}$$

where v_F is the magnitude of the group velocity associated with the Dirac cone, $\boldsymbol{k} = (k_x, k_y)$ denotes the wave vector, and Δ is the size of the energy gap between the flat and upper (lower) bands. The vector of matrices, $\boldsymbol{S} = (S_x, S_y)$, along with the third matrix S_z, forms a complete representation of spin-1 quasiparticles with the angular momentum commutation relations: $[S_l, S_m] = i\epsilon_{lmn} S_n$. The free-space energy-momentum dispersion relations in the presence of the energy gap Δ and a constant scalar potential V are

$$E = V, \tag{3.2}$$

$$E = \pm\sqrt{\hbar^2 v_F^2 (k_x^2 + k_y^2) + \Delta^2} + V, \tag{3.3}$$

as illustrated in Fig. 3.1(a).

The scattering process can be fully characterized by a number of cross sections: the differential, total, transport and skew cross sections, denoted as $d\sigma/d\theta$, σ, σ_{tr} and σ_{skew}, respectively. For the case of a circular, constant potential barrier, these cross sections of pseudospin-1 system can be calculated analytically. In particular, let V and R be the height and radius of the 2D potential barrier, respectively. The potential function is given by

$$V(\boldsymbol{r}) = V\Theta(R - r), \tag{3.4}$$

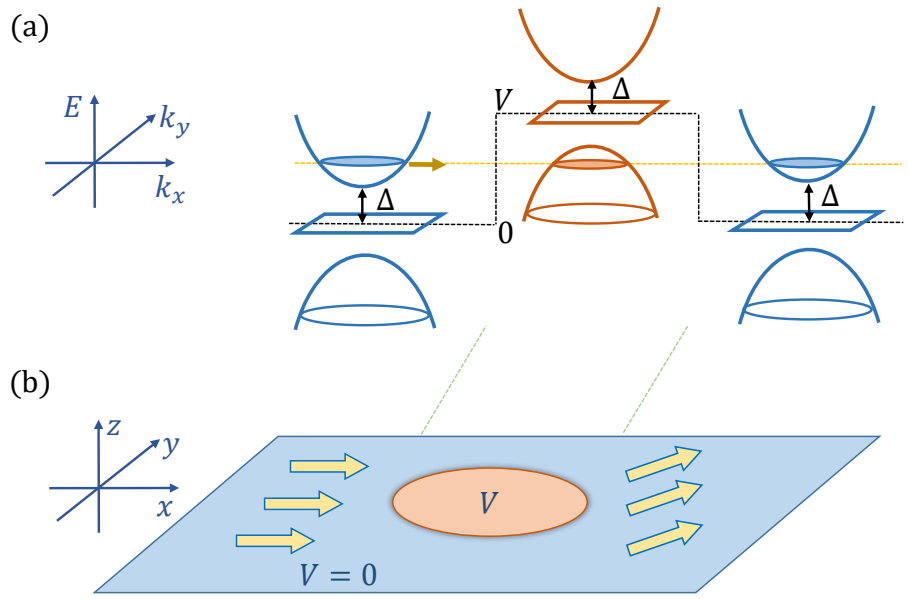

Figure 3.1: Schematic illustration of massive pseudospin-1 particle scattering. (a) The energy-momentum dispersion relations in distinct spatial regions. (b) 2D scattering from a scatterer formed by a scalar gate potential.

where Θ is the Heaviside function. The generalized Pauli matrices S_x, S_y, and S_z for spin-1 quasiparticles are

$$S_x = \frac{1}{\sqrt{2}} \begin{pmatrix} 0 & 1 & 0 \\ 1 & 0 & 1 \\ 0 & 1 & 0 \end{pmatrix}, \quad S_y = \frac{1}{\sqrt{2}} \begin{pmatrix} 0 & -i & 0 \\ i & 0 & -i \\ 0 & i & 0 \end{pmatrix}, \tag{3.5}$$

and

$$S_z = \begin{pmatrix} 1 & 0 & 0 \\ 0 & 0 & 0 \\ 0 & 0 & -1 \end{pmatrix}. \tag{3.6}$$

The Hamiltonian matrix in the polar coordinates is

$$H = -\frac{\hbar v_F}{\sqrt{2}} \cdot \begin{pmatrix} \frac{-\sqrt{2}(\Delta+V)}{\hbar v_F} & e^{-i\theta}(i\partial_r + \frac{1}{r}\partial_\theta) & 0 \\ e^{i\theta}(i\partial_r - \frac{1}{r}\partial_\theta) & \frac{-\sqrt{2}V}{\hbar v_F} & e^{-i\theta}(i\partial_r + \frac{1}{r}\partial_\theta) \\ 0 & e^{i\theta}(i\partial_r - \frac{1}{r}\partial_\theta) & \frac{-\sqrt{2}(-\Delta+V)}{\hbar v_F} \end{pmatrix}, \tag{3.7}$$

Because of the circular geometry of the electric potential scatterer, the total angular momentum

$$l = -i\hbar\partial_\theta + \hbar S_z (= 0, \pm 1, \pm 2, \ldots$$

is conserved. The partial wave component corresponding to l is

$$\psi_l(\boldsymbol{r}) = \begin{pmatrix} u_1 e^{i(l-1)\theta} \\ u_2 e^{ij\theta} \\ u_3 e^{i(l+1)\theta} \end{pmatrix}, \tag{3.8}$$

which enables a reduction of the Dirac equation $H\psi = E\psi$ to the following radial differential equation:

$$\frac{-\hbar v_F}{\sqrt{2}} \begin{pmatrix} \frac{-\sqrt{2}(\Delta+V-E)}{\hbar v_F} & i(\frac{\partial}{\partial r} + \frac{l}{r}) & 0 \\ i(\frac{\partial}{\partial r} - \frac{l-1}{r}) & \frac{-\sqrt{2}(V-E)}{\hbar v_F} & i(\frac{\partial}{\partial r} + \frac{l+1}{r}) \\ 0 & i(\frac{\partial}{\partial r} - \frac{l}{r}) & \frac{-\sqrt{2}(-\Delta+V-E)}{\hbar v_F} \end{pmatrix} \cdot \begin{pmatrix} u_1 \\ u_2 \\ u_3 \end{pmatrix} = 0. \tag{3.9}$$

The corresponding eigenfunction is

$$\psi_l = C \begin{pmatrix} s_\tau F^\tau_{l-1}(k_\tau r) e^{-i\theta} \\ i\sqrt{2}\nu_\tau F^\tau_l(k_\tau r) \\ t_\tau F^\tau_{l+1}(k_\tau r) e^{i\theta} \end{pmatrix} e^{il\theta}, \tag{3.10}$$

where

$$k_\tau = \sqrt{(E - V_\tau)^2 - \Delta^2}/\hbar v_F, \tag{3.11}$$

$$s_\tau = -(\Delta - V_\tau + E)\hbar v_F k_\tau, \tag{3.12}$$

$$\nu_\tau = (\Delta + V_\tau - E)(\Delta - V_\tau + E), \tag{3.13}$$

$$t_\tau = -(\Delta + V_\tau - E)\hbar v_F k_\tau, \tag{3.14}$$

with $\tau =$ I or II denoting the exterior or interiors regions of the potential barrier, respectively. In the exterior region of the potential barrier, $F^I_l(k_I r) = H_l(k_I r)$ is the

Hankel function of the first kind. In the potential region, $F_l^{II}(k_{II}r) = J_l(k_{II}r)$ is the Bessel function. Employing the method of partial wave decomposition, we can write the incident wave in the spinor spherical wave basis as

$$\Psi_{in} = \frac{N}{\sqrt{2}} \sum_l i^{l-1} \begin{pmatrix} s_I J_{l-1}(k_I r) e^{-i\theta} \\ i\sqrt{2}\nu_I J_l(k_I r) \\ t_I J_{l+1}(k_I r) e^{i\theta} \end{pmatrix} e^{il\theta}, \tag{3.15}$$

and the reflected wave as

$$\Psi_{ref} = \frac{N}{\sqrt{2}} \sum_l i^{l-1} A_l \begin{pmatrix} s_I H_{l-1}(k_I r) e^{-i\theta} \\ i\sqrt{2}\nu_I H_l(k_I r) \\ t_I H_{l+1}(k_I r) e^{i\theta} \end{pmatrix} e^{il\theta}, \tag{3.16}$$

with $J_l(x)$ and $H_l(x)$ being the Bessel and Hankel functions of the first kind, respectively. The transmitted wave inside the potential region is

$$\Psi_{tr} = \begin{pmatrix} \psi_1^{II} \\ \psi_2^{II} \\ \psi_3^{II} \end{pmatrix} = \frac{N}{\sqrt{2}} \sum_l i^{l-1} B_l \begin{pmatrix} s_{II} J_{l-1}(k_{II} r) e^{-i\theta} \\ i\sqrt{2}\nu_{II} J_l(k_{II} r) \\ t_{II} J_{l+1}(k_{II} r) e^{i\theta} \end{pmatrix} e^{il\theta}. \tag{3.17}$$

The total wavefunction outside the scattering region ($r > R$) is given by

$$\begin{aligned} \Psi_I = \Psi_{in} + \Psi_{ref} &= \begin{pmatrix} \psi_1^I \\ \psi_2^I \\ \psi_3^I \end{pmatrix} \\ &= \frac{N}{\sqrt{2}} \sum_l i^{l-1} \begin{pmatrix} s_I [J_{l-1}(k_I r) + A_l H_{l-1}(k_I r)] e^{-i\theta} \\ i\sqrt{2}\nu_I [J_l(k_I r) + A_l H_l(k_I r)] \\ t_I [J_{l+1}(k_I r) + A_l H_{l+1}(k_I r)] e^{i\theta} \end{pmatrix} e^{il\theta}. \end{aligned} \tag{3.18}$$

Utilizing the boundary conditions

$$\psi_2^I(R, \theta) = \psi_2^{II}(R, \theta), \tag{3.19}$$

$$\psi_1^I(R, \theta) + \psi_3^I(R, \theta) = \psi_1^{II}(R, \theta) + \psi_3^{II}(R, \theta), \tag{3.20}$$

we can obtain the coefficients A_l and B_l with the formula given in Appendix 3.6.1.

In the far field, i.e., $r \gg R$, the spinor wave function can be written as

$$\Psi_I = N \begin{pmatrix} -\frac{s_I}{\sqrt{2}} \\ -\nu_I \\ \frac{t_I}{\sqrt{2}} \end{pmatrix} e^{ikr\cos\theta} + N \begin{pmatrix} -\frac{s_I}{\sqrt{2}} e^{-i\theta} \\ -\nu_I \\ \frac{t_I}{\sqrt{2}} e^{i\theta} \end{pmatrix} \frac{f(\theta)}{\sqrt{r}} e^{ikr}. \tag{3.21}$$

The reflected wave can be simplified as

$$\Psi_{ref} = N \sum_l -i^l A_l \sqrt{\frac{2}{\pi k_I r}} e^{i(k_I r - \frac{l\pi}{2} - \frac{\pi}{4})} \begin{pmatrix} -\frac{s_I}{\sqrt{2}} e^{-i\theta} \\ -\nu_I \\ \frac{t_I}{\sqrt{2}} e^{i\theta}, \end{pmatrix} e^{il\theta} \tag{3.22}$$

where we have used the approximate formula for the Hankel function of the first kind for $x \gg 1$:

$$H_\nu(x) \approx \sqrt{\frac{2}{\pi x}} e^{i(x - \frac{\nu\pi}{2} - \frac{\pi}{4})}. \tag{3.23}$$

This way, we obtain an explicit form for the function $f(\theta)$ as

$$f(\theta) = -\frac{e^{-i\pi/4}}{\sqrt{2\pi k}} \sum_{l=-\infty}^{\infty} 2A_l e^{il\theta}. \tag{3.24}$$

The differential, total, transport, and skew cross sections are given by

$$\frac{d\sigma}{d\theta} = |f(\theta)|^2 = \frac{2}{\pi k} |\sum_l A_l e^{il\theta}|^2, \tag{3.25}$$

$$\sigma = \int_0^{2\pi} |f(\theta)|^2 d\theta = \frac{4}{k} \sum_l |A_l|^2, \tag{3.26}$$

$$\begin{aligned} \sigma_{tr} &= \int_0^{2\pi} |f(\theta)|^2 (1 - \cos\theta) \\ &= \sigma - \frac{4}{k} \sum_l \Re[A_l A_{l+1}^*], \end{aligned} \tag{3.27}$$

$$\begin{aligned} \sigma_{skew} &= \int_0^{2\pi} d\theta |f(\theta)|^2 \sin\theta \\ &= \frac{4}{k} \sum_l \Im[A_l^* A_{l+1}], \end{aligned} \tag{3.28}$$

respectively, with $k = \sqrt{E^2 - \Delta^2}/\hbar v_F$.

3.3 Emergence of Super Skew Scattering

3.3.1 Circular Scatterer

Far Field Behavior

We first study a circular scatterer whose scalar potential barrier is defined by Eq. (3.4). As shown in Sec. 3.2, due to the circular symmetry, the Dirac-Weyl equation can be analytically solved to yield the various scattering cross sections. For example, the skew scattering cross section is given by Eq. (3.28), which is determined by the coefficients A_l in the partial wave expansion. The formulas for these coefficients are quite sophisticated, posing an obstacle to understand the basic scattering physics.

To gain insights, we focus on the weak scattering regime where the size of the scatterer is smaller than the electron wavelength: $k_I R \ll 1$, $VR/\hbar v_F \ll 1$, and $k_{II} R \ll 1$. In this regime, the formulas for A_l and then for σ_{skew} can be simplified. Figure 3.2(a) shows σ_{skew} versus the incident electron energy for $VR = 0.256$ (with radius $R = 1$) and normalized mass $R\Delta = 0.064$. The choice of the value of VR can be arbitrary in a wide range to give qualitatively similar results. We set $R\Delta = VR/4$ for convenience. It can be seen that σ_{skew} exhibits three resonant peaks, one wide but relatively low and the two others narrow but high, for energy about $V_0/2$, indicating strong skew scattering near this energy value. The occurrence of skew scattering is indicative of the emergence of AHE for massive pseudospin-1 electrons scattered by an electric gate potential. In contrast, for pseudospin-1/2 scattering from the same configuration, no such resonant peaks in σ_{skew} arise and its overall values are much smaller than those for pseudospin-1 scattering in the entire energy interval, as shown in Fig. 3.2(b).

Associated with the wider resonant peak in Fig. 3.2(a), the skew scattering is

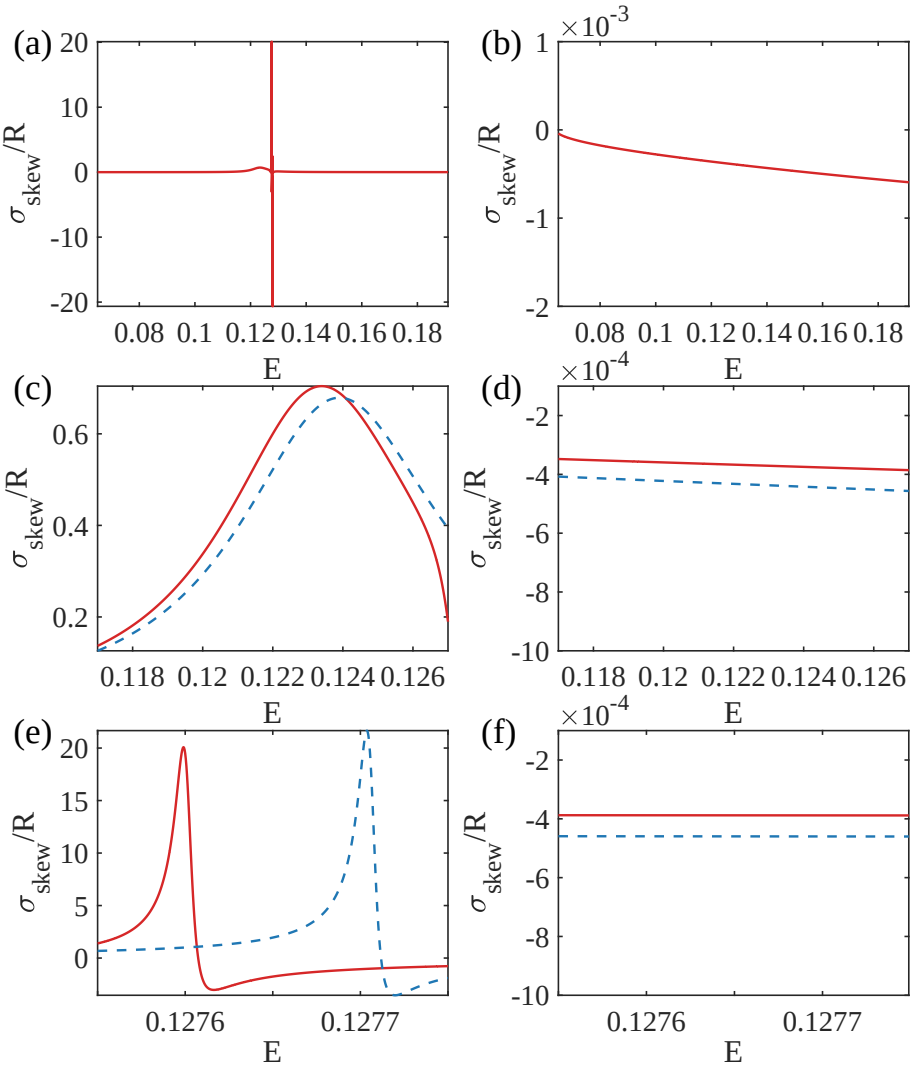

Figure 3.2: Contrasting behaviors arising from the scattering of massive pseudospin-1 and that of pseudospin-1/2 quasiparticles from a circular gate potential scatterer in the Klein tunneling regime where the particle energy is about half of the potential height. The mass of the quasiparticles is $\Delta = 0.064$ and the gate potential is $V = 0.256$. (a) Skew scattering cross section σ_{skew} for massive pseudospin-1 quasiparticles versus incident energy, where resonant peaks arise. (b) The corresponding plot for pseudospin-1/2 scattering, where no resonant peaks occur and the values of σ_{skew} are much smaller than those in (a) in the entire energy range. (c) Magnification of the first resonant peak in (a), where the red solid and blue dashed curves are the numerical and analytic results, respectively. (d) The corresponding magnification for pseudospin-1/2 scattering with the same legends as in (c). (e) Magnification of the second resonant peak in (a). (f) The corresponding magnification for pseudospin-1/2 scattering.

mainly contributed to by the interference between the $l = 0$ and $l = 1$ states. Focusing on the corresponding terms in Eq. (3.28), we get

$$\sigma_{skew} \approx \frac{4}{k}\Im[A_0 A_1^*] \approx \pi k R^2 \frac{V^2}{E^2}\frac{(V-E)(E-\Delta)+2\Delta E}{V(E+\Delta)}, \tag{3.29}$$

which is plotted as the dashed curve in Fig. 3.2(c), where the peak value is over 0.6. This analytic prediction agrees reasonably well with the numerical curve. The second (narrow and higher) peak in Fig. 3.2(a) is due to the interference between the $l = 1$ and $l = 2$ states. Focusing on this particular interference channel, we get

$$\sigma_{skew} \approx \frac{4}{k}\Im[A_1 A_2^*] \approx -\frac{4}{\pi}\frac{V-E+\Delta}{V}\frac{\ln\frac{\gamma kR}{2}}{k}, \tag{3.30}$$

with $\ln\gamma \approx 0.577$ being the Euler's constant, which is plotted as the blue dashed curve in Fig. 3.2(e). In comparison with the numerical curve (red solid), we observe a close resemblance between them, with a small difference in the peak position. In this case, the peak value of σ_{skew} is quite large, which is strong evidence for the emergence of super skew scattering. The details of the derivation and approximation of the analytic scattering formulas are given in Appendix 3.6.1.

For scattering of massive pseudospin-1/2 quasiparticles, the analytic formula for the skew scattering cross section is (details in Appendix 3.6.2)

$$\sigma_{skew} = \frac{4}{k}\sum_l \Im[A_l A_{l+1}^*] \approx \frac{4}{k}\Im[A_0 A_1^*] = -\frac{\pi^2}{8}\frac{V^3\Delta}{k}(E^2-\Delta^2), \tag{3.31}$$

which agrees well with the numerical result, as shown in Figs. 3.2(d) and 3.2(f) for the same energy intervals as in Figs. 3.2(c) and 3.2(e), respectively. In stark contrast to the scattering of pseudospin-1 quasiparticles, there are no resonant peaks and the value of σ_{skew} is about 4×10^{-4}, which is over three orders of magnitude smaller than those of the former.

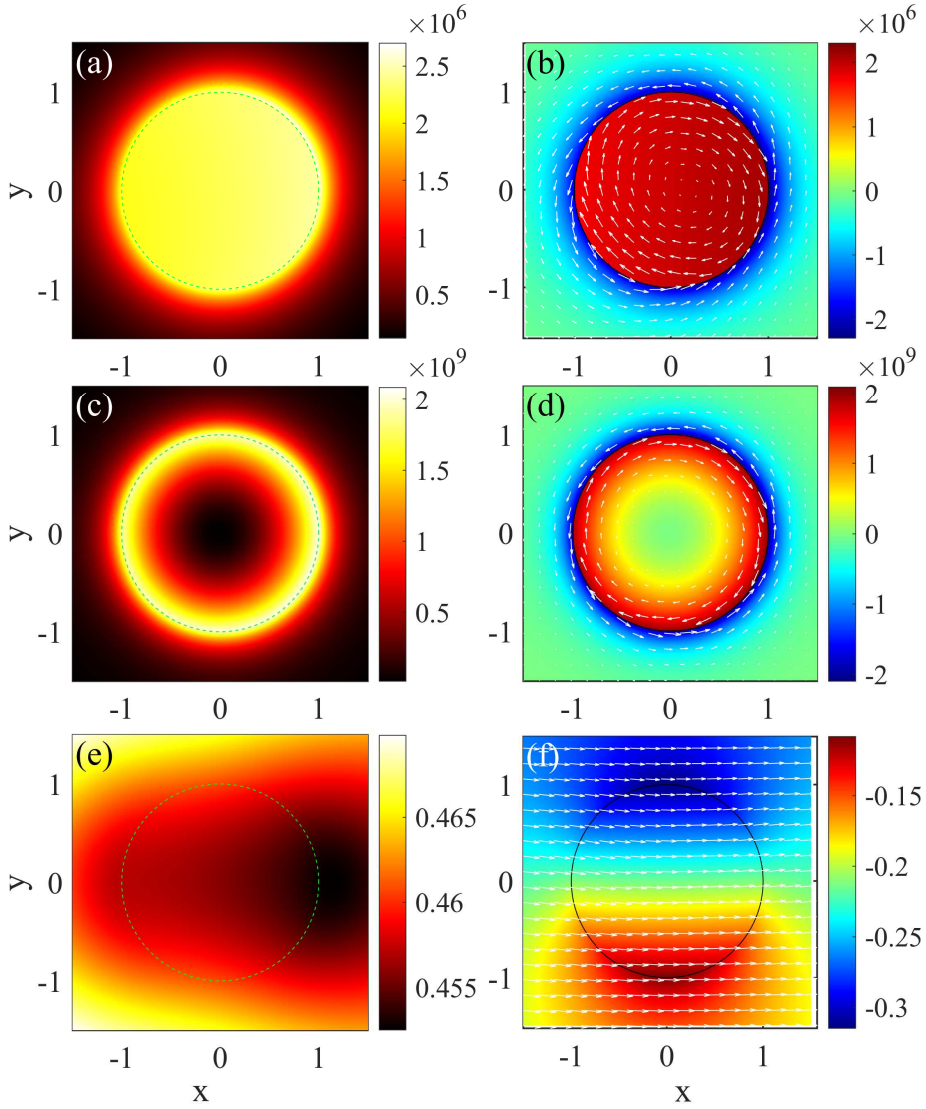

Figure 3.3: Resonant state and current distribution for massive pseudospin-1 scattering from a circular potential barrier. (a) Probability density distribution of the first pseudospin-1 resonant state for $E = 0.1234$, and (b) the current density and spin-z density distributions, where the in-plane current is labeled by the white arrows and the out-of-plane pseudospin-z component is represented by the color map. (c) Probability density distribution for the second resonant state for $E = 0.1276$. (d) The corresponding current density and spin-z density distributions, with the same legends as in (b). (e) Probability density distribution of pseudospin-1/2 system for energy $E = 0.128$, and (f) the corresponding current and spin-z density distributions.

Near-field Scattering Behavior

To reveal the near-field behavior, we calculate the probability and current distributions of the states corresponding to the first (wide) and second (narrow) resonant peaks in Fig. 3.2(a). The probability distribution can be written as $P = \Psi^\dagger \Psi$, where $\Psi = (\psi_1, \psi_2, \psi_3)^T$ is the wavefunction for points inside and outside the potential area, respectively, as given by Eqs. (3.17) and (3.18). The probability current operator is $\hat{\boldsymbol{J}} = \nabla_{\boldsymbol{p}} H = v_F(S_x, S_y)$, so the probability current density can be obtained as

$$\begin{aligned} \boldsymbol{J} &= (J_x, J_y) \\ &= v_F\sqrt{2}[Re(\psi_1^*\psi_2 + \psi_2^*\psi_3), Im(\psi_1^*\psi_2 + \psi_2^*\psi_3)]. \end{aligned} \tag{3.32}$$

The probability density distribution of the spin-z component is given by

$$\langle \sigma_z \rangle = |\psi_1|^2 - |\psi_3|^2. \tag{3.33}$$

The results for the first peak are shown in Figs. 3.3(a) and 3.3(b) for the peak in Fig. 3.2(c) for energy $E = 0.1234$. It can be seen that the quasiparticles are mainly confined inside the potential area with a clockwise current, and the spin-z component is positive inside and negative outside. By further investigating the wavefunction form in Eqs. (3.17) and (3.18), we find that the main contribution to this probability distribution is the partial component of the angular momentum channel $l = 1$. As a result, the probability distribution is approximately circularly symmetric. The corresponding results for the second peak are shown in Figs. 3.3(c) and 3.3(d) for $E = 0.1276$. This resonance state is mostly confined about the edge area of the potential with a clockwise current inside and a counterclockwise current outside, and the spin-z component has different signs inside and outside the barrier. Moreover, the electron density is much larger than that associated with the first resonant state. We find that the main contribution to this state comes from the

partial component of $l = 2$. In contrast, for pseudospin-1/2 quasiparticles, there is neither concentration of the probability density in the potential region nor that for the current, as shown in Figs. 3.3(e) and 3.3(f), indicating an absolute absence of any resonant scattering behavior. This lack of resonance is further confirmed by checking the partial component contributions, where a number of low angular momentum states contribute to this probability distribution. That is, pseudospin-1/2 quasiparticles effectively "see" no potential with near zero scattering.

Emergence of Super Skew Scattering - Scaling of Skew Cross Section with Scatterer Strength

The analytical formulas for the skew scattering cross section for pseudospin-1 and pseudospin-1/2 quasiparticles [Eqs. (3.29-3.31)], together with the numerical support in Fig. 3.2, suggest certain scaling relationship between the cross section and the strength parameter VR of the scatterer. Figure 3.4 shows, on a log-log plot, the peak value of the effective skew scattering cross section σ_{skew}/R versus V_0R for three cases: pseudospin-1/2 scattering (blue) and resonant scattering associated with the first (red) and second (green) resonances in pseudospin-1 scattering [in Figs. 3.2(c) and 3.2(e), respectively]. Note that there are no peaks in the skew scattering cross section for pseudospin-1/2 particle, so we choose the energy to be $E = V/2$. In all three cases, there is a reasonably good agreement between the analytic predictions and the numerical results. For pseudospin-1/2 scattering (blue), the maximum value of σ_{skew}/R decreases rapidly as the strength of the scatterer is reduced: $\sigma_{skew}/R \sim (VR)^5$, which is characteristic of conventional quantum or light scattering. However, corresponding to the first resonance of pseudospin-1 scattering (red), the decrease in the value of the skew cross section is much slower with $\sigma_{skew}/R \sim VR$, indicating persistent super skew scattering when the scatterer is continuously weakened. The

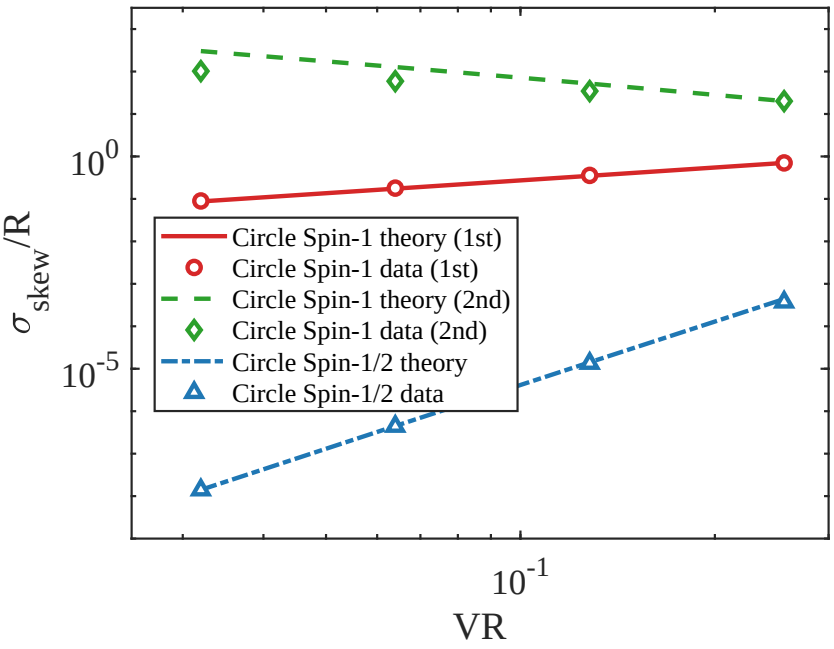

Figure 3.4: Scaling of the resonant skew scattering cross section peak value with the strength of the circular scatterer. The red circles and green diamonds represent the numerical results for the first and second resonances of pseudospin-1 scattering, and the blue triangles are the corresponding results for pseudospin-1/2 scattering. The lines of the same colors are the theoretical predictions (not fittings). As the strength of the scatterer is weakened, the maximum value of the skew cross section decreases fast for pseudospin-1/2 scattering, but not so for pseudospin-1 scattering. In fact, for the second resonance peak in pseudospin-1 scattering (green), the skew scattering tends to intensify slightly as the scatterer becomes weaker. This scaling behavior signifies the emergence of super skew scattering of pseudospin-1 quasiparticles.

surprising phenomenon occurs for the second resonance of pseudospin-1 scattering (green), where skew scattering tends to intensify even as the scatterer strength is reduced, implying the presence of a large anomalous Hall current. A summary of the scaling of the peak value of skew and transport scattering cross section with the scatterer strength VR is given in Table 3.1 of Appendix 3.6.3.

3.3.2 Elliptic Scatterer

To test the robustness of resonant skew scattering for pseudospin-1 quasiparticles against geometric deformations, we consider an elliptical potential barrier. In this

case, the scattering cross sections cannot be obtained analytically, and we use the multiple multipole method developed for treating the scattering of spin-1 and spin-1/2 particles from scatterers of an arbitrary geometric shape [30, 56].

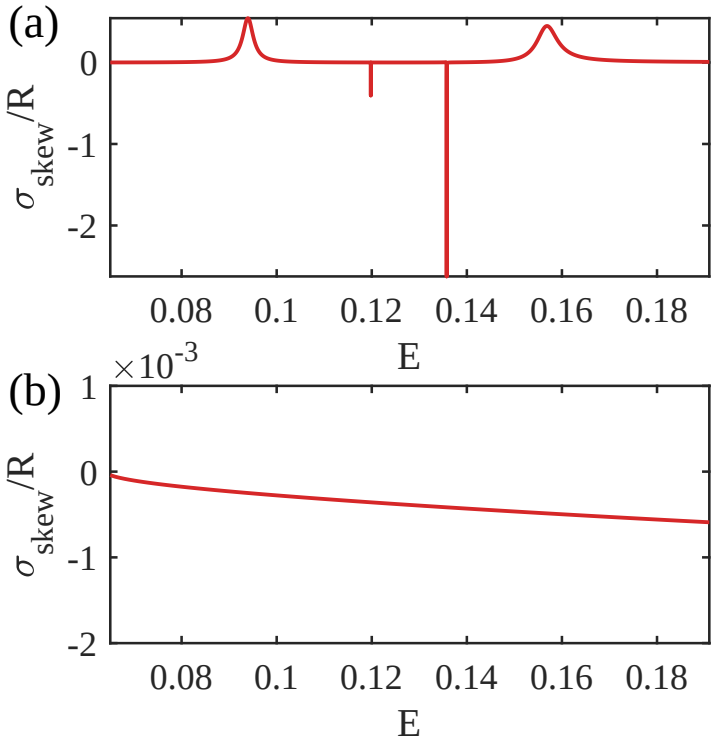

Figure 3.5: Skew cross section versus energy E for scattering of massive Dirac quasiparticles from an elliptic gate potential barrier: (a) pseudospin-1 and (b) pseudospin-1/2. The uniform mass value is $\Delta = 0.064$ and the gate potential is $V = 0.256$ inside the elliptic barrier.

Far-field behavior. For comparison, we use the same values of the potential and mass as for the case of a circular scatterer: $V = 0.256$ and $\Delta = 0.064$, and set the area of the ellipse to be identical to that of the circle. Here, the ratio of the semi-minor axis b to the semi-major axis a is set to 0.6. The incident plane wave comes from the left to the right along the major axis of the ellipse. As shown in Fig. 3.5(a), for pseudospin-1 scattering, four resonant peaks arise in the pertinent energy interval: two wide and two narrow peaks, where one pair of wide-narrow peaks have their energy less than

$V/2$ and the other pair larger than $V/2$. This should be compared with the case of a circular scatterer where the pair of resonant peaks have their energies approximately equal to $V/2$. The difference in the locations of the resonances notwithstanding, the occurrence of skew resonant scattering is robust against geometric deformations of the scatterer.

For pseudospin-1/2 scattering, no resonant peak exists in the skew scattering cross section, as shown in Fig. 3.5(b), which is similar to the case of a circular scatterer.

Near-field behavior. Figure 3.6 shows the distributions of the probability, current, and the out-of-plane component of the pseudospin for the four resonant states in Fig. 3.5(a) and for the corresponding pseudospin-1/2 scattering. The probability distribution for the first, wide resonant state is shown in Fig. 3.6(a), where the electron is uniformly distributed inside the potential region. Figure 3.6(b) shows that the current exhibits a vortex structure and is in the counterclockwise direction along the right and left edges of the barrier. It is this unidirectional current distribution that leads to the AHE. Figure 3.6(b) also shows that the z-component of the pseudospin is positive inside the barrier and negative outside. The probability distribution of the fourth wide resonant state is similar to that of the first state, as shown in Fig. 3.6(g), where the quasiparticles concentrate inside the barrier. The current is still counterclockwise, which forms vortices around the up and down parts of the barrier, as shown in Fig. 3.6(h). In addition, the z-component of pseudospin is negative inside the barrier region, in contrast to that associated with the first resonance. The corresponding results for the second and the third narrow resonance peaks are shown in Figs. 3.6(c-f), where the directions of the current for the two cases are the same. For the second peak, the current vortices occur at the four edges of the barrier (up, down, left, and right), while for the third peak, the vortices are in the up-left/right

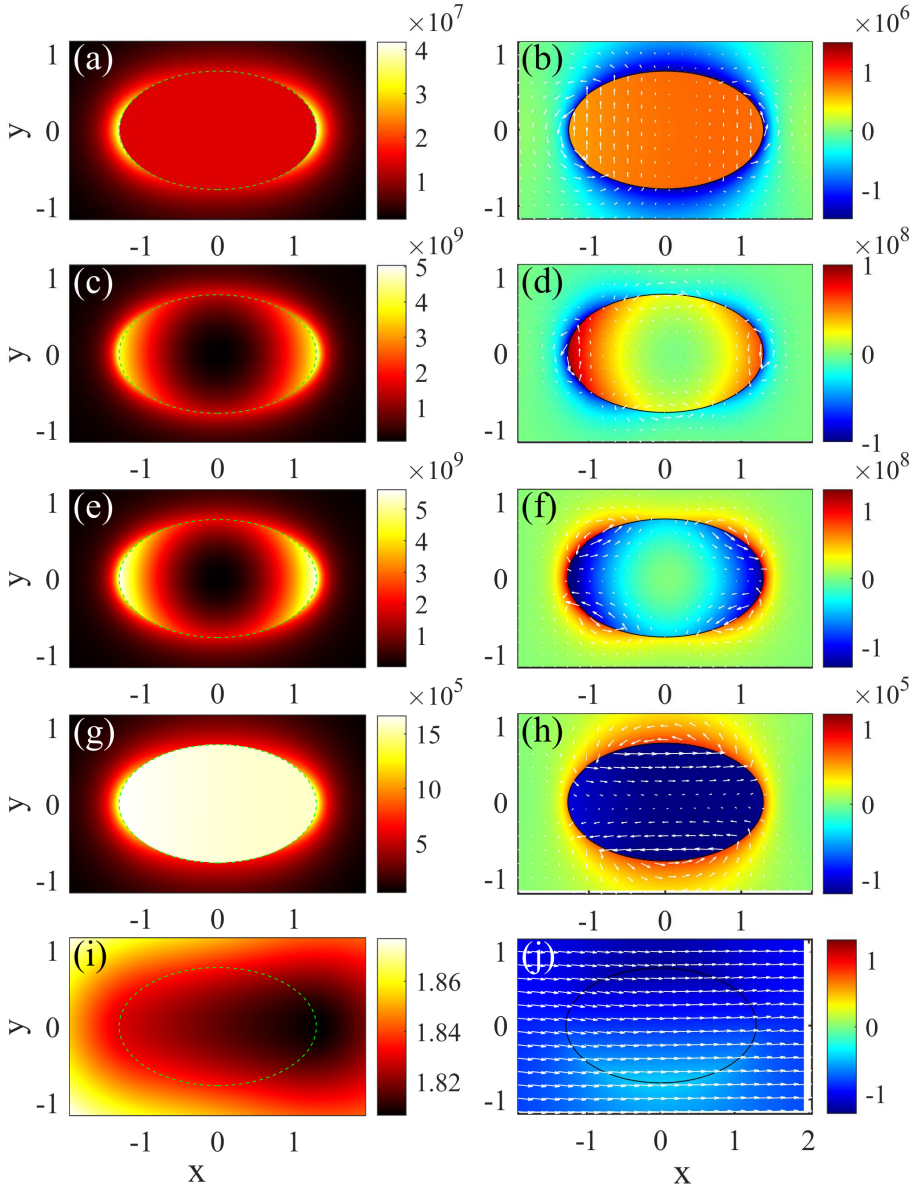

Figure 3.6: Resonant state and current distribution for massive pseudospin-1 scattering from an elliptical potential barrier. (a,c,e,g) Probability density distribution for the pseudospin-1 resonant state for $E = 0.094$, 0.1198, 0.1357, and 0.1569, respectively. (b,d,f,h) The corresponding current density and spin-z density distributions, where the in-plane current is labeled with the arrows and the out-of-plane z component of the pseudospin is color represented. (i) Probability density distribution for pseudospin-1/2 scattering from an elliptical scatterer for $E = 0.128$ and (j) the corresponding current and pseudospin-z distributions.

and down-left/right corners. The pseudospin-z directions are opposite for the two narrow resonance states. For pseudospin-1/2 scattering, no resonant states occur, nor do current vortices, as shown in Figs. 3.6(i) and 3.6(j), leading to near zero values of the skew scattering cross section.

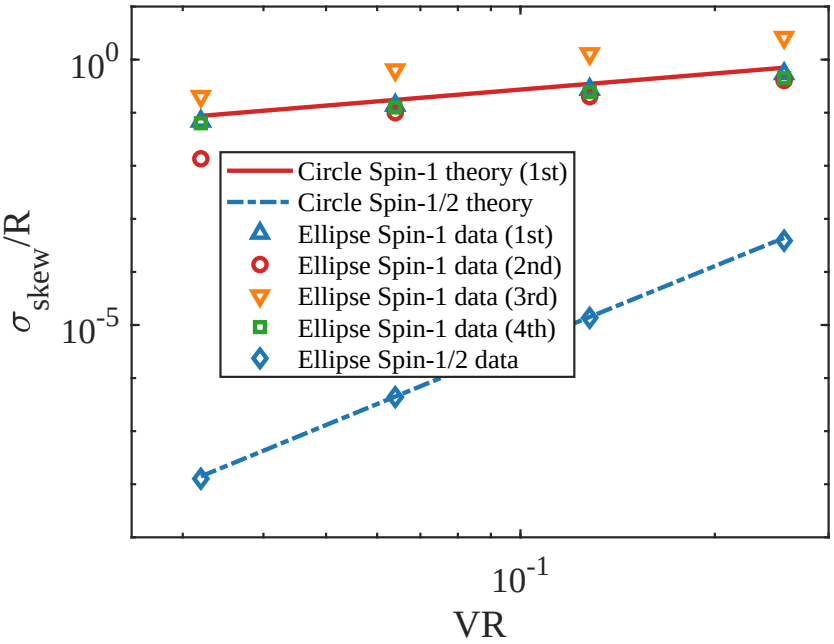

Figure 3.7: Scaling of the peak value of skew scattering cross section with the strength of an elliptical electrical potential scatterer. The cross section is normalized by R, the radius of the circle with the same area as the ellipse, and the scatterer strength is VR ($R = 1$). The blue up-triangles, red circles, orange down-triangles, and green squares are the data points associated with the four skew scattering resonances in Fig. 3.5(a), respectively, from small to large energies. The red, green and blue lines are the theoretical results for circular scatterer, which serve as a reference. For pseudospin-1 quasiparticles, for all four resonant states, as the scatterer strength is reduced, the maximum value of the skew cross section decreases little, signifying super skew scattering. For pseudospin-1/2 quasiparticles (blue diamonds and dashed line), the maximum decreases rapidly and algebraically with the scatterer strength, which is typical of conventional quantum or light scattering.

Persistence of super skew scattering. Figure 3.7 shows the peak values of the four skew scattering resonances in Fig. 3.5(a) versus the scatterer strength. The data points from the four resonant states are nearly identical and, as the scatterer

is weakened (by reducing the barrier height or its size, or both), the decrease in the peak cross section values roughly follow the scaling of $\sigma_{skew}/R \sim VR$, similar to the behavior of the first peak in the circular-potential case, which is indicative of super skew scattering that persists even when the circular potential barrier is deformed. In contrast, for pseudospin-1/2 quasiparticles, the maximum value of the skew cross section is small and decreases rapidly with the scatterer strength, as for the case of a circular barrier in Fig. 3.4. It is worth noting that skew scattering is robust against not only deformations of the scatterer shape, but also variations in the incident angles due to the resonant vortices formed about the potential area. (Further evidence is provided in Appendix 3.6.4.)

3.4 Skew Resonant Scattering and Anomalous Hall Effect in Experimental Massive Pseudospin-1 Lattice Systems

The results in Secs. 3.2 and 3.3 are from the effective, continuum Hamiltonian model for pseudospin-1 scattering where the system size is infinite. In experiments, pseudospin-1 systems are typically realized through lattices, e.g., photonic, electronic, or cold-atom lattices of finite size. To anticipate the theoretical and numerical results in Secs. 3.2 and 3.3 to occur in real physical systems, a prerequisite is to study if resonant skew scattering can arise in a finite lattice system. To be concrete, herein we study massive pseudospin-1 transport in a paradigmatic flat-band system: the Lieb lattice, as shown in Fig. 3.8(a). The relation between the single Dirac cone Hamiltonian of a Lieb lattice and that of a dice lattice can be found in Appendix 3.6.5.

For an idealized Lieb lattice, the energy bands consist of a pair of vertex-touching Dirac cones and a flat band through the touching point, so the quasiparticles are of the massless pseudospin-1 type. When a gap opens between the two Dirac cones, the quasiparticles become massive. There are two methods to open up such a gap. The

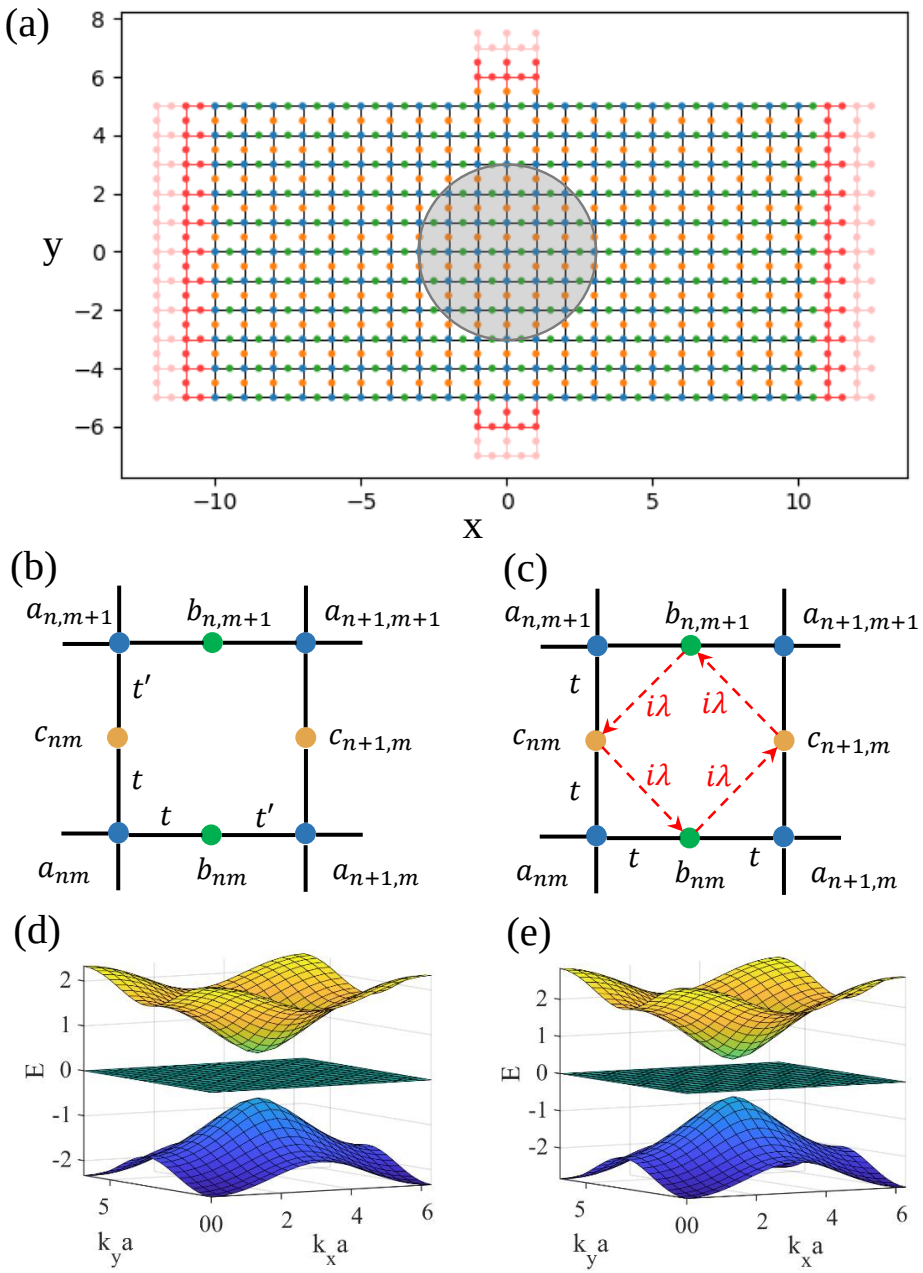

Figure 3.8: Schematic illustration of an experimentally feasible, finite size lattice system for massive pseudospin-1 scattering. (a) General Lieb lattice structure. (b,c) Two mechanisms to generate massive pseudospin-1 quasiparticles: (b) dimerization and (c) imaginary next-nearest-neighbor interaction. (d,e) Band structures for the dimerized and imaginary next-nearest neighbor hopping Lieb lattices, respectively.

first one is through dimerization, which staggers different hopping amplitudes along the a-b and a-c directions, as shown in Fig. 3.8(b). The difference in the coupling strength breaks the C_4 symmetry of the lattice, leading to a gap opening. This is the 2D Su-Schrieffer-Heeger (SSH) model [40, 65] with the following tight-binding Hamiltonian:

$$H = \sum_{n,m} t a^+_{n,m} b_{n,m} + t' a^+_{n,m} b_{n-1,m} + t a^+_{n,m} c_{n,m} + t' a^+_{n,m} c_{n,m-1} + h.c. \tag{3.34}$$

where t and t' are the nearest neighbor coupling energies, $\{a^+_{n,m}, b^+_{n,m}, c^+_{n,m}\}$ and $\{a_{n,m}, b_{n,m}, c_{n,m}\}$ are the creation and annihilation operators for the localized states $|a_{n,m}\rangle$, $|b_{n,m}\rangle$, $|c_{n,m}\rangle$ of each atom, with n, m being the cell indices. In the momentum representation, the Hamiltonian is described by the following 3×3 matrix:

$$H = \tag{3.35}$$
$$\begin{pmatrix} 0 & te^{i\frac{k_x a}{2}} + t'e^{-i\frac{k_x a}{2}} & te^{i\frac{k_y a}{2}} + t'e^{-i\frac{k_y a}{2}} \\ te^{-i\frac{k_x a}{2}} + t'e^{i\frac{k_x a}{2}} & 0 & 0 \\ te^{-i\frac{k_y a}{2}} + t'e^{i\frac{k_y a}{2}} & 0 & 0 \end{pmatrix}.$$

The corresponding energy-momentum dispersion relation is

$$E_\pm(\boldsymbol{k}) = \pm\sqrt{4tt'\cos^2\frac{k_x a}{2} + 4tt'\cos^2\frac{k_y a}{2} + 2(t-t')^2}, \tag{3.36}$$

$$E_0(\boldsymbol{k}) = 0, \tag{3.37}$$

where $E_\pm$ are the energies of the upper and lower bands, respectively, E_0 is the flat band energy of the Lieb lattice, and a is lattice constant. Near the Dirac point $\boldsymbol{k} = (\frac{\pi}{a}, \frac{\pi}{a})$, the gap is the smallest with $\Delta = \sqrt{2}|t - t'|$. In the vicinity of the gap, the quasiparticles are described by the generalized, spin-1 Dirac-Weyl equation. The band structure is illustrated in Fig. 3.8(d).

The second method to open up a gap for the Lieb lattice is to introduce a purely imaginary next-nearest neighbor (NNN) hopping term [12, 65] between atoms b and

c with coupling strength λ , as shown in Fig. 3.8(c). Such interactions can be created via a magnetic flux [66] or spin-orbit coupling with only one spin component [12, 195]. The tight-binding Hamiltonian is

$$\begin{aligned} H = & \sum_{n,m} t a^{+}_{n,m} b_{n,m} + t a^{+}_{n,m} b_{n-1,m} + t a^{+}_{n,m} c_{n,m} \\ & + t a^{+}_{n,m} c_{n,m-1} - i\lambda c^{+}_{n,m} b_{n,m} - i\lambda b^{+}_{n-1,m} c_{n,m} \\ & - i\lambda c^{+}_{n,m-1} b_{n-1,m} - i\lambda b^{+}_{n,m} c_{n,m-1} + h.c., \end{aligned} \tag{3.38}$$

and the momentum space Hamiltonian is

$$H = \begin{pmatrix} 0 & 2t\cos\frac{k_x a}{2} & 2t\cos\frac{k_y a}{2} \\ 2t\cos\frac{k_x a}{2} & 0 & -i4\lambda\sin\frac{k_x a}{2}\sin\frac{k_y a}{2} \\ 2t\cos\frac{k_y a}{2} & i4\lambda\sin\frac{k_x a}{2}\sin\frac{k_y a}{2} & 0 \end{pmatrix}, \tag{3.39}$$

with the energy-momentum dispersion relation given by

$$E_{\pm}(\boldsymbol{k}) = \pm\sqrt{4t^2[\cos^2\frac{k_x a}{2} + \cos^2\frac{k_y a}{2}] + 16\lambda^2\sin^2\frac{k_x a}{2}\sin^2\frac{k_y a}{2}}, \tag{3.40}$$

$$E_0(\boldsymbol{k}) = 0. \tag{3.41}$$

At the Dirac point, the gap size is $\Delta = 4\lambda$ and the corresponding band structure is schematically shown in Fig. 3.8(e).

We employ the Kwant package [196] to calculate the transport properties of massive pseudospin-1 particles on a finite Lieb lattice. We set the device length (in the horizontal direction) to be 80 lattice units and width (in the vertical direction) to be 40 units. The left and right leads have the same width as the device. To measure the Hall current, we set up two leads (up and down) with the width of two units. A circular gate potential is applied to the top of the device, whose radius is 10 units, with the potential height $V = 0.01$. The gap size is $\Delta = 0.0025$. The incident electron energy (normalized by the hopping energy t) varies from 0.0026 to 0.0099. The

electrons come from the left lead, scatter from the device defined by the potential step, and leave the device through the right lead.

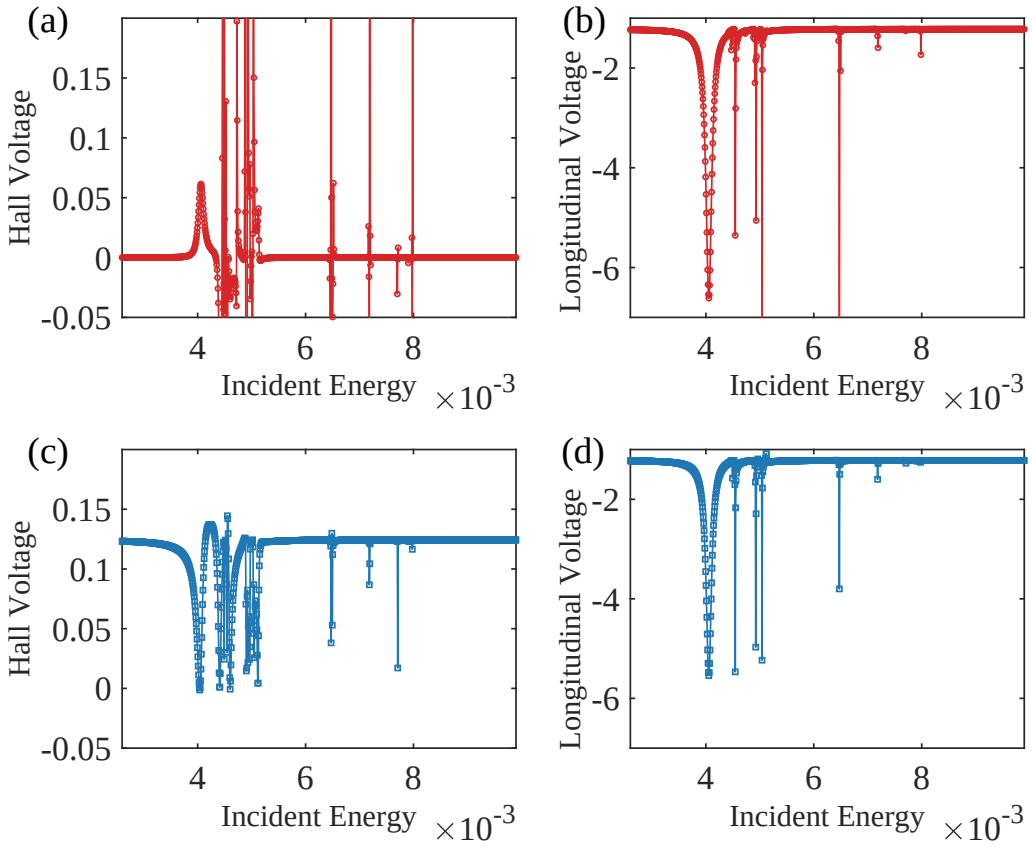

Figure 3.9: Hall and longitudinal voltages of massive pseudospin-1 particles through a finite Lieb lattice device defined by an externally applied electrical potential. (a,b) Hall and longitudinal voltages versus the incoming electron energy for the dimerization gap-opening mechanism, respectively. (c,d) The corresponding results for the imaginary NNN hopping gap-opening mechanism.

Figures 3.9(a) and 3.9(b) show, for the dimer structure Lieb lattice, the Hall and longitudinal voltages versus the incident electron energy. The Hall voltage exhibits a large number of wide and narrow peaks, indicating the occurrence of Hall current (the Hall effect is anomalous because of the absence of any external magnetic field). The corresponding results for the imaginary NNN hopping Lieb lattice are shown in Figs. 3.9(c) and 3.9(d), where there are valleys below the constant Hall voltage, resulting from breaking of the time-reversal symmetry and the finite size effect.

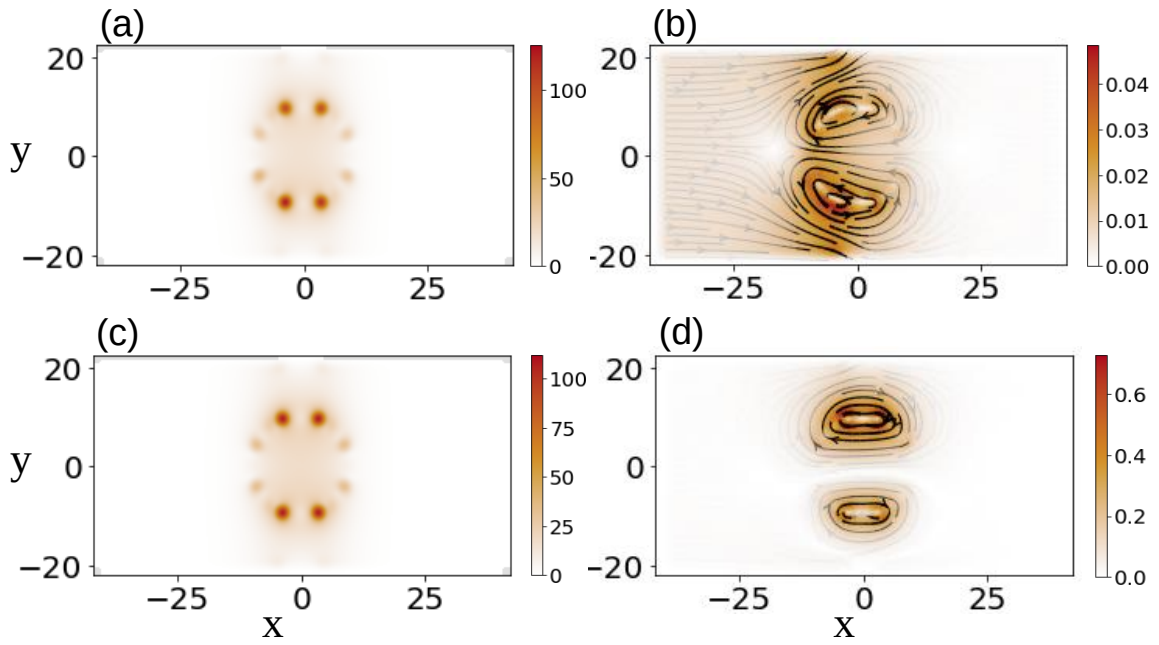

Figure 3.10: Density and current distribution associated with resonant states. (a,b) Dimerization Lieb lattice with incident electron energy $E = 0.00406$. (c,d) Imaginary NNN hopping Lieb lattice with incident energy $E = 0.00404$.

We calculate the probability density and current distribution associated with the peak resonant state for incidence energy of $E = 0.0406$ (dimerization lattice) and $E = 0.0404$ (imaginary NNN hopping lattice). For the dimerized lattice scattering system, there is a concentration of pseudospin-1 electrons about the edge of the potential region, as shown in Fig. 3.10(a). Associated with the resonant state, there are current vortices around the top and bottom edges of the potential, as shown in Fig. 3.10(b), where the currents in the top and bottom vortices have opposite directions, signifying conservation of time-reversal symmetry. The corresponding results for the imaginary NNN hopping Lieb lattice are shown in Figs. 3.10(c) and 3.10(d). In this case, the currents associated with the top and bottom vortices have the same direction, as shown in Fig. 3.10(d), which is indicative of a broken time-reversal symmetry.

The results in Figs. 3.9 and 3.10 affirm that skew resonant scattering leading to anomalous Hall current can arise in experimentally realizable lattice systems hosting

massive pseudospin-1 quasiparticles.

3.5 Discussion

The phenomenon of superscattering in Dirac material systems has been theoretically predicted [26]. Specifically, in the subwavelength regime where the size of the scatterer is smaller than the wavelength, extraordinarily large values of the scattering cross section can arise even when the scatterer strength as measured by the product of its size with the potential height becomes arbitrarily small. This phenomenon occurs in two-dimensional Dirac material systems in which the quasiparticles are of the *massless* pseudospin-1 type, defying the conventional wisdom that wave scattering as characterized by the cross section should weaken continuously as the scatterer strength is reduced. The physical mechanism underlying superscattering was found [26] to be the emergence of a class of localized resonant modes inside the scatterer [24]. The energy band structure of the Dirac materials that host massless pseudospin-1 quasiparticles consists of a pair of Dirac cones with a flat band through the conical connecting point - the Dirac point, without gap opening. In experiments or real applications, various perturbations can be present which open a gap at the Dirac point, rendering *massive* the quasiparticles. The questions are whether the phenomenon of superscattering can persist and whether there are features that do not occur in the massless case.

Our study of massive pseudospin-1 scattering from an electrostatic potential barrier reveals the phenomenon of super skew scattering. Our method consists of two steps. First, for theoretical interest, we consider an effective continuum Hamiltonian system, in which an externally applied electrical field generates a potential barrier of either a circular or a deformed shape. In the former case, the wavefunctions and the relevant scattering cross sections can be solved analytically from the generalized spin-1 Dirac-Weyl equation through the approach of partial wave decomposition. Analytic

and numerical results provide evidence for the occurrence of skew resonant scattering. The remarkable finding is the phenomenon of super skew scattering in which a decrease in the size and/or potential height of the scatterer does not lead to a reduction in the skew scattering cross section. When the circular scatterer is deformed so that the cross sections can be calculated only numerically, we find that the phenomenon of super skew scattering persists. We emphasize that skew scattering resonances and super scattering belong to the type of exotic physics unique to pseudospin-1 Dirac material systems with a flat band. In fact, we have demonstrated that such behaviors do not arise in pseudospin-1/2 systems (e.g., graphene).

Skew scattering is synonymous with AHE. In experiments, massive pseudospin-1 Dirac material systems are realized by finite size lattices and the Hall current is usually measured. We have thus studied a Lieb lattice system incorporating two distinct mechanisms to induce a band gap so that quasiparticles are of the pseudospin-1 type with a finite mass. We find that skew resonant scattering and anomalous Hall current can arise in the lattice systems, paving the way for experimentally observing and characterizing these phenomena. It should be noted the band topology can affect the transport behavior in a finite lattice system (See 3.6.6).

The phenomenon of resonant skew scattering in massive pseudospin-1 systems can be exploited for applications in Hall devices. For example, the skew scattering direction (or the direction of the anomalous Hall current) depends on the polarity of the applied electrical potential: by switching its polarity, the Hall current will be reversed. This may find applications in quantum sensing. Further, our work has revealed that, when the geometric shape of the scattering region is deformed from a perfect circle, a pair of wide resonant peaks with opposite z component of the pseudospin can arise for different incident energy. Tuning the incident energy can thus be used to control the direction of pseudospin.

We remark that, while adding mass to spin-1 fermions does not suppress the Klein tunneling effect, our work has revealed a key difference between the massless and massive cases: there is superscattering in the former but there is super skew scattering in the latter as induced by the gap opening. The main contribution of our work is an understanding of the skew scattering cross section resonances as a function of the incident energy through uncovering a scaling law characteristic of super skew scattering. The physical origin of the skew scattering resonances has also been elucidated in terms of certain angular momentum channels. Beyond the previously published massless, circular-scatterer case, the present work extends the study of massive spin-1 skew scattering to an elliptic shaped scatterer - a numerically challenging feat that we achieve by generalizing the multiple multipole method to massive spin-1 scattering. This is evidence that the phenomenon of super skew scattering is robust against geometric deformation of the scatterer. Another feature going beyond the previous work on massless spin-1 scattering is that, in the present work, electron transport in a finite Lieb lattice device has been studied to confirm that the phenomenon of super skew scattering can arise in experimentally feasible systems. Taken together, the results of this paper provide new insights into the relativistic quantum scattering of spin-1 particles with potential applications to anomalous Hall devices.

3.6 Supplementary Notes

3.6.1 Simplification of Pseudospin-1 Skew Scattering Formula

Using the partial wave decomposition method, we get the coefficient A_l and B_l for the scattering wave as

$$A_l = -\frac{A_l^1 - A_l^2}{A_l^3 - A_l^4}, \tag{3.42}$$

$$B_l = \frac{B_l^1 - B_l^2}{B_l^3 - B_l^4}, \tag{3.43}$$

where

$$A_l^1 = \nu_I J_l(k_I R)[s_{II} J_{l-1}(k_{II} R) + t_{II} J_{l+1}(k_{II} R)], \tag{3.44}$$

$$A_l^2 = \nu_{II} J_l(k_{II} R)[s_I J_{l-1}(k_I R) + t_I J_{l+1}(k_I R)], \tag{3.45}$$

$$A_l^3 = \nu_I H_l(k_I R)[s_{II} J_{l-1}(k_{II} R) + t_{II} J_{l+1}(k_{II} R)], \tag{3.46}$$

$$A_l^4 = \nu_{II} J_l(k_{II} R)[s_I H_{l-1}(k_I R) + t_I H_{l+1}(k_I R)], \tag{3.47}$$

$$B_l^1 = \nu_I H_l(k_I R)[s_I J_{l-1}(k_I R) + t_I J_{l+1}(k_I R)], \tag{3.48}$$

$$B_l^2 = \nu_I J_l(k_I R)[s_I H_{l-1}(k_I R) + t_I H_{l+1}(k_I R)], \tag{3.49}$$

$$B_l^3 = \nu_I H_l(k_I R)[s_{II} J_{l-1}(k_{II} R) + t_{II} J_{l+1}(k_{II} R)], \tag{3.50}$$

$$B_l^4 = \nu_{II} J_l(k_{II} R)[s_I H_{l-1}(k_I R) + t_I H_{l+1}(k_I R)], \tag{3.51}$$

and

$$\begin{aligned} &s_\tau = \hbar v_F k_\tau (V_\tau - \Delta - E),\ t_\tau = -\hbar v_F k_\tau (V_\tau + \Delta - E), \\ &\nu_\tau = -(V_\tau + \Delta - E)(V_\tau - \Delta - E),\ k_\tau = \sqrt{\frac{(E - V_\tau)^2 - \Delta^2}{\hbar^2 v_F^2}}, \end{aligned} \tag{3.52}$$

with $\tau =$ I or II, corresponding to the region outside or inside the scatterer, respectively. For simplicity, we denote $x_1 = k_I R$ and $x_2 = k_{II} R$. The weak scattering

regime can then be characterized by $x_1 \ll 1$ and $x_2 \ll 1$. For angular momentum $l = 0$, we have

$$\begin{aligned}
A_0 &= -\frac{\nu_I J_0(x_1)[s_{II}J_{-1}(x_2) + t_{II}J_1(x_2)] - \nu_{II}J_0(x_2)[s_I J_{-1}(x_1) + t_I J_1(x_1)]}{\nu_I H_0(x_1)[s_{II}J_{-1}(x_2) + t_{II}J_1(x_2)] - \nu_{II}J_0(x_2)[s_I H_{-1}(x_1) + t_I H_1(x_1)]} \\
&\approx -\frac{\nu_I[s_{II}(-\frac{x_2}{2}) + t_{II}\frac{x_2}{2}] - \nu_{II}[s_I(-\frac{x_1}{2}) + t_I\frac{x_1}{2}]}{\nu_I[1 + i\frac{2}{\pi}\ln\frac{\gamma x_1}{2}][s_{II}(-\frac{x_2}{2}) + t_{II}\frac{x_2}{2}] - \nu_{II}[s_I(-\frac{x_1}{2} + i\frac{2}{\pi}\frac{1}{x_1}) + t_I(\frac{x_1}{2} - i\frac{2}{\pi}\frac{1}{x_1})]} \\
&= -\frac{\frac{\nu_I}{2}x_2(t_{II} - s_{II}) - \frac{\nu_{II}}{2}x_1(t_I - s_I)}{\frac{\nu_I}{2}x_2(t_{II} - s_{II})[1 + i\frac{2}{\pi}\ln\frac{\gamma x_1}{2}] - \frac{\nu_{II}}{2}x_1(t_I - s_I)[1 - i\frac{4}{\pi}\frac{1}{x_1^2}]} \\
&\approx -\frac{\pi x_1^2}{\pi x_1^2 - i\frac{4E}{V} + i2\frac{V-E}{V}x_1^2\ln\frac{\gamma x_1}{2}},
\end{aligned} \tag{3.53}$$

where Eq. (3.52) have been used in Eq. (3.53) to yield the final approximate results.

For angular momentum $l = 1$ with the corresponding coefficient A_1, we have

$$\begin{aligned}
A_1 &= -\frac{\nu_I J_1(x_1)[s_{II}J_0(x_2) + t_{II}J_2(x_2)] - \nu_{II}J_1(x_2)[s_I J_0(x_1) + t_I J_2(x_1)]}{\nu_I H_1(x_1)[s_{II}J_0(x_2) + t_{II}J_2(x_2)] - \nu_{II}J_1(x_2)[s_I H_0(x_1) + t_I H_2(x_1)]} \\
&\approx -\frac{\frac{\nu_I x_1}{2}[s_{II} + t_{II}\frac{x_2^2}{8}] - \frac{\nu_{II}x_2}{2}[s_I + t_I\frac{x_1^2}{8}]}{\nu_I[\frac{x_1}{2} - i\frac{2}{\pi}\frac{1}{x_1}][s_{II} + t_{II}\frac{x_2^2}{8}] - \frac{\nu_{II}x_2}{2}[s_I(1 + i\frac{2}{\pi}\ln\frac{\gamma x_1}{2}) + t_I(\frac{x_1^2}{8} - i\frac{4}{\pi}\frac{1}{x_1^2})]} \\
&\approx -\frac{\pi x_1^2}{\pi x_1^2 + i[4\frac{E-\Delta}{E+\Delta}\frac{V-2E}{V} + 2\frac{V+\Delta-E}{V}x_1^2\ln\frac{\gamma x_1}{2}]}.
\end{aligned} \tag{3.54}$$

For A_{-1} with angular momentum $l = -1$, we have

$$\begin{aligned}
A_{-1} &= \frac{-\nu_I J_{-1}(x_1)[s_{II}J_{-2}(x_2) + t_{II}J_0(x_2)] + \nu_{II}J_{-1}(x_2)[s_I J_{-2}(x_1) + t_I J_0(x_1)]}{\nu_I H_{-1}(x_1)[s_{II}J_{-2}(x_2) + t_{II}J_0(x_2)] - \nu_{II}J_{-1}(x_2)[s_I H_{-2}(x_1) + t_I H_0(x_1)]} \\
&\approx -\frac{\frac{\nu_I x_1}{2}[t_{II} + s_{II}\frac{x_2^2}{8}] - \frac{\nu_{II}x_2}{2}[t_I + s_I\frac{x_1^2}{8}]}{\nu_I[\frac{x_1}{2} - i\frac{2}{\pi}\frac{1}{x_1}][t_{II} + s_{II}\frac{x_2^2}{8}] - \frac{\nu_{II}x_2}{2}[t_I(1 + i\frac{2}{\pi}\ln\frac{\gamma x_1}{2}) + s_I(\frac{x_1^2}{8} - i\frac{4}{\pi}\frac{1}{x_1^2})]} \\
&\approx -\frac{\pi x_1^2}{\pi x_1^2 + i[4\frac{E+\Delta}{E-\Delta}\frac{V-2E}{V} + 2\frac{(V-\Delta-E)}{V}x_1^2\ln\frac{\gamma x_1}{2}]}.
\end{aligned} \tag{3.55}$$

For A_2 corresponding to the angular momentum $l = 2$, we have

$$A_2 = -\frac{\nu_I J_2(x_1)[s_{II} J_1(x_2) + t_{II} J_3(x_2)] - \nu_{II} J_2(x_2)[s_I J_1(x_1) + t_I J_3(x_1)]}{\nu_I H_2(x_1)[s_{II} J_1(x_2) + t_{II} J_3(x_2)] - \nu_{II} J_2(x_2)[s_I H_1(x_1) + t_I H_3(x_1)]}$$

$$\approx$$

$$\frac{-\frac{\nu_I x_1^2}{8}[s_{II}\frac{x_2}{2} + t_{II}\frac{x_2^3}{48}] + \frac{\nu_{II} x_2^2}{8}[s_I \frac{x_1}{2} + t_I \frac{x_1^3}{48}]}{\nu_I \frac{x_1^2}{8}[s_{II}\frac{x_2}{2} + t_{II}\frac{x_2^3}{48}] - \frac{\nu_{II} x_2^2}{8}[s_I \frac{x_1}{2} + t_I \frac{x_1^3}{48}] - i\frac{4}{\pi}\frac{\nu_I}{x_1^2}[s_{II}\frac{x_2}{2} + t_{II}\frac{x_2^3}{48}] + i\frac{\nu_{II} x_2^2}{8}[\frac{2}{\pi}\frac{s_I}{x_1} + \frac{16}{\pi}\frac{t_I}{x_1^3}]} \tag{3.56}$$

$$\approx -\frac{\pi x_1^4}{\pi x_1^4 + i[32\frac{E-\Delta}{E+\Delta}\frac{V-2E}{V} - 4x_1^2\frac{V-E+\Delta}{V}(1 - \frac{1}{3}\frac{V-E+\Delta}{E+\Delta})]}. \tag{3.57}$$

For A_{-2}, we have

$$A_{-2} =$$

$$\frac{-\nu_I J_{-2}(x_1)[s_{II} J_{-3}(x_2) + t_{II} J_{-1}(x_2)] + \nu_{II} J_{-2}(x_2)[s_I J_{-3}(x_1) + t_I J_{-1}(x_1)]}{\nu_I H_{-2}(x_1)[s_{II} J_{-3}(x_2) + t_{II} J_{-1}(x_2)] - \nu_{II} J_{-2}(x_2)[s_I H_{-3}(x_1) + t_I H_{-1}(x_1)]} \tag{3.58}$$

$$\approx -\frac{\pi x_1^4}{\pi x_1^4 + i[32\frac{E+\Delta}{E-\Delta}\frac{V-2E}{V} - 4x_1^2\frac{V-E-\Delta}{V}(1 - \frac{1}{3}\frac{V-E-\Delta}{E-\Delta})]}. \tag{3.59}$$

The reflection amplitude can be obtained as

$$f(\theta) = -e^{-i\pi/4}\sqrt{\frac{2}{\pi k}}\sum_{l=-\infty}^{\infty} A_l e^{il\theta}. \tag{3.60}$$

The differential cross section is given by

$$\frac{d\sigma}{d\theta} = |f(\theta)|^2 = \frac{2}{\pi k}|\sum_{l=-\infty}^{\infty} A_l e^{il\theta}|^2. \tag{3.61}$$

The transport cross section is

$$\sigma_{tr} = \int_0^{2\pi} d\theta |f(\theta)|^2(1 - \cos\theta) = \frac{4}{k}\sum_l \big[|A_l|^2 - \Re(A_l A_{l+1}^*)\big]. \tag{3.62}$$

The skew scattering cross section has the form

$$\sigma_{skew} = \int_0^{2\pi} d\theta |f(\theta)|^2 \sin\theta = \frac{4}{k}\Im\big[\sum_l A_l^* A_{l-1}\big]. \tag{3.63}$$

For the first resonant state in Fig. 3.2, the probability density distribution is confined inside the circular potential region. The transport cross section is dominated by the $l = 1$ term:

$$\sigma_{tr} \approx \frac{4}{k}|A_1|^2 \approx \frac{4}{k} = \frac{4}{\sqrt{E^2 - \Delta^2}}, \tag{3.64}$$

and skew scattering is the result of interference between the $l = 0$ and $l = 1$ states. We have

$$\sigma_{skew} \approx \frac{4}{k}\Im[A_0 A_1^*] \approx \pi k \frac{V^2}{E^2}\frac{(V - E)(E - \Delta) + 2\Delta E}{V(E + \Delta)}. \tag{3.65}$$

For the second resonant state in Fig. 3.2, the $l = \pm 1$ and $l = 2$ states contribute to the transport cross section. We have

$$\sigma_{tr} = \frac{4}{k}\left[|A_{-1}|^2 + |A_1|^2 + |A_2|^2\right] \approx \frac{8}{k}. \tag{3.66}$$

In this case, skew scattering is due to the interference between the $l = 1$ and $l = 2$ states. We have

$$\sigma_{skew} \approx \frac{4}{k}\Im[A_1 A_2^*] \approx -\frac{4}{\pi}\frac{V - E + \Delta}{V}\frac{\ln\frac{\gamma k}{2}}{k}. \tag{3.67}$$

3.6.2 Massive Pseudospin-1/2 Scattering from a Circular Potential Scatterer

For massive pseudospin-1/2 scattering [56], the reflection coefficient is

$$A_l = -\frac{\tau_1 J_l(x_1) J_{l-1}(x_2) - \tau_2 J_{l-1}(x_1) J_l(x_2)}{\tau_1 H_l(x_1) J_{l-1}(x_2) - \tau_2 H_{l-1}(x_1) J_l(x_2)}, \tag{3.68}$$

where $l = j + \frac{1}{2}$, with $j = \pm\frac{1}{2}, \pm\frac{3}{2}, \ldots$, $x_1 = k_1 R$, $x_2 = k_2 R$, and

$$\tau_1 = -\frac{\hbar v_F k_1}{E - \Delta},\ \tau_2 = -\frac{\hbar v_F k_2}{E - V - \Delta},$$

$$k_1 = \sqrt{\frac{E^2 - \Delta^2}{\hbar^2 v_F^2}},\ k_2 = \sqrt{\frac{(E - V)^2 - \Delta^2}{\hbar^2 v_F^2}},$$

with (x_1, τ_1, k_1) and (x_2, τ_2, k_2) being quantities corresponding to the area outside and inside the circular potential scatterer, respectively. In the weak scattering regime ($x_1 \ll 1$ and $x_2 \ll 1$), we have A_0 for $j = -1/2$ as

$$\begin{aligned} A_0 &= -\frac{\tau_1 J_0(x_1)J_{-1}(x_2) - \tau_2 J_{-1}(x_1)J_0(x_2)}{\tau_1 H_0(x_1)J_{-1}(x_2) - \tau_2 H_{-1}(x_1)J_0(x_2)} \\ &\approx -\frac{-\pi\tau_1 x_1 x_2 + \pi\tau_2 x_1^2}{-\pi\tau_1 x_1 x_2 + \pi\tau_2 x_1^2 - i[4\tau_2 + 2\tau_1 x_2 x_1 \ln\frac{\gamma x_1}{2}]} \\ &= \frac{-\pi V(E+\Delta)\sqrt{\frac{V-E-\Delta}{V-E+\Delta}}}{\pi V(E+\Delta)\sqrt{\frac{V-E-\Delta}{V-E+\Delta}} - i\big[4\sqrt{\frac{V-E-\Delta}{V-E+\Delta}} - 2\sqrt{\frac{E+\Delta}{E-\Delta}}\sqrt{(V-E)^2-\Delta^2}x_1 \ln\frac{\gamma x_1}{2}\big]}. \end{aligned} \tag{3.69}$$

Similarly, for $j = 1/2$, we have

$$\begin{aligned} A_1 &= -\frac{\tau_1 J_1(x_1)J_0(x_2) - \tau_2 J_0(x_1)J_1(x_2)}{\tau_1 H_1(x_1)J_0(x_2) - \tau_2 H_0(x_1)J_1(x_2)} \\ &\approx -\frac{-\pi\tau_2 x_1 x_2 + \pi\tau_1 x_1^2}{-\pi\tau_2 x_1 x_2 + \pi\tau_1 x_1^2 - i[4\tau_1 + 2\tau_2 x_2 x_1 \ln\frac{\gamma x_1}{2}]} \\ &= -\frac{\pi V\sqrt{E^2-\Delta^2}}{\pi V\sqrt{E^2-\Delta^2} + i\big[-4\sqrt{\frac{E+\Delta}{E-\Delta}} + 2(V-E-\Delta)x_1 \ln\frac{\gamma x_1}{2}\big]}. \end{aligned} \tag{3.70}$$

The relevant coefficient-dependent quantities can be approximated as

$$\begin{aligned} |A_0|^2 &\approx \frac{\pi^2 V^2}{16}(E+\Delta)^2, \\ |A_1|^2 &\approx \frac{\pi^2 V^2}{16}(E+\Delta)^2, \\ \Re[A_0 A_1^*] &\approx \frac{\pi^2 V^2}{16}(E^2-\Delta^2), \\ \Im[A_0 A_1^*] &\approx -\frac{\pi^3 V^3 \Delta}{32}(E^2-\Delta^2). \end{aligned}$$

The transport cross section is

$$\begin{aligned} \sigma_{tr} &= \frac{4}{k}\sum_l \big[|A_0|^2 + |A_1|^2 - \Re(A_l A_{l+1}^*)\big] \\ &\approx \frac{4}{k}\big[|A_0|^2 + |A_1|^2 - \Re(A_0 A_1^*)\big] \\ &= \frac{\pi^2}{4}\frac{V^2}{k}[E^2 + 3\Delta^2]. \end{aligned} \tag{3.71}$$

The skew scattering cross section has the form

$$\sigma_{skew} = \frac{4}{k}\sum_{l}\Im[A_l A_{l+1}^*] \approx \frac{4}{k}\Im[A_0 A_1^*] = -\frac{\pi^2}{8}\frac{V^3\Delta}{k}(E^2-\Delta^2). \tag{3.72}$$

3.6.3 Transport Cross Sections

The results in the main text are for the skew cross sections. Here we present results for the transport cross sections in various cases. Figure 3.11 shows the behavior of the transport cross section for the same setting as in Fig. 3.2, and also shows the scaling of the peak transport cross section with the scatterer strength. It can be seen that there are super scattering associated with electron transport, similar to the massless case [26]. The scaling behavior of skew and transport cross sections with respect to circular scatterer strength is summarized in Table 3.1. The results are based on Eqs. (3.64), (3.65), (3.66), (3.67), (3.71) and (3.72).

Note that these formulas are valid in certain potential range. The scattering cross section should be zero when there is no potential. The corresponding results for the elliptic scatterer are shown in Figs. 3.12, where the phenomenon of super scattering persists.

Table 3.1: Summary of the Scaling of the Peak Value of Skew and Transport Scattering Cross Sections with the Scatterer Strength VR.

	Spin-1 (1st)	Spin-1 (2nd)	Spin-1/2
σ_{skew}/R	VR	$\frac{\ln(\gamma VR)}{VR}$	$(VR)^5$
σ_{tr}/R	$(VR)^{-1}$	$(VR)^{-1}$	$(VR)^3$

3.6.4 *Effect of Varying Incident Angle for the Case of an Elliptical Scatterer*

For the elliptical scatterer, a different incident direction may affect the scattering cross sections. Surprisingly, we find that resonant skew scattering persists and changes little for different incident angles, as exemplified in Figs. 3.13(a) and 3.13(b), in spite of large variations in the transport cross section. The current distribution reveals that the vortices are similar for different incident angles, giving rise to robust vortices (or resonance) that lead to robust super skew scattering, as shown in Fig. 3.14.

3.6.5 *Unitary Transformation Between the Effective Hamiltonians of Single Dirac-cone Dice and Lieb Lattices*

In Secs. 3.2 and 3.3, the effective Hamiltonian is derived from the a single Dirac cone dice lattice. In Sec. 3.4, the phenomenon of super skew scattering is observed in the single Dirac cone Lieb lattice. From a theoretical point of view, there exists a unitary transformation between the effective Hamiltonians of the single Dirac cone dice and Lieb lattices. Thus, in principle, results from the effective Hamiltonian of the single Dirac cone dice lattice are expected to hold when the effective Hamiltonian is one from the Lieb lattice. The results in Secs. 3.2-3.4 thus demonstrate the generality of the phenomenon of super skew scattering across the two lattice systems. Here we present this unitary transformation.

For the dice lattice, the effective Hamiltonian is given by

$$H^d = \hbar v_F \boldsymbol{S}^d \cdot \boldsymbol{k} + \Delta S_z + V(\boldsymbol{r}), \tag{3.73}$$

with

$$S_x^d = \frac{1}{\sqrt{2}} \begin{pmatrix} 0 & 1 & 0 \\ 1 & 0 & 1 \\ 0 & 1 & 0 \end{pmatrix}, \quad S_y^d = \frac{1}{\sqrt{2}} \begin{pmatrix} 0 & -i & 0 \\ i & 0 & -i \\ 0 & i & 0 \end{pmatrix}, \tag{3.74}$$

and

$$S_z^d = \begin{pmatrix} 1 & 0 & 0 \\ 0 & 0 & 0 \\ 0 & 0 & -1 \end{pmatrix}. \tag{3.75}$$

For the Lieb lattice, the effective Hamiltonian is

$$H^L = \hbar v_F \boldsymbol{S}^L \cdot \boldsymbol{k} + \Delta S_z + V(\boldsymbol{r}), \tag{3.76}$$

with

$$S_x^L = \begin{pmatrix} 0 & 1 & 0 \\ 1 & 0 & 0 \\ 0 & 0 & 0 \end{pmatrix}, \quad S_y^L = \begin{pmatrix} 0 & 0 & 1 \\ 0 & 0 & 0 \\ 1 & 0 & 0 \end{pmatrix}, \tag{3.77}$$

and

$$S_z^L = \begin{pmatrix} 0 & 0 & 0 \\ 0 & 0 & -i \\ 0 & i & 0 \end{pmatrix}. \tag{3.78}$$

Consider the following unitary matrix:

$$U = \begin{pmatrix} 0 & 1 & 0 \\ \frac{1}{\sqrt{2}} & 0 & \frac{1}{\sqrt{2}} \\ \frac{i}{\sqrt{2}} & 0 & -\frac{i}{\sqrt{2}} \end{pmatrix}, \tag{3.79}$$

which satifies $U^\dagger U = I$. The unitary transformation for the S-matrix can be expressed as

$$U^\dagger S_x^L U = S_x^d, \tag{3.80}$$

$$U^\dagger S_y^L U = S_y^d, \tag{3.81}$$

$$U^\dagger S_z^L U = S_z^d. \tag{3.82}$$

The effective Hamiltonians from the two lattice systems can thus be connected by the unitary transformation

$$U^{\dagger} H^{L} U = H^{d}, \tag{3.83}$$

with the current operator defined as

$$\hat{\boldsymbol{J}} = \nabla_{\boldsymbol{p}} H. \tag{3.84}$$

The conclusion is that the far field scattering behavior and near field probability and current distributions are identical for the single Dirac-cone dice and Lieb lattices.

3.6.6 Topological Effect on Super Skew Scattering

In Sec. 3.4, two gap-opening methods are employed for the Lieb lattice system: exploiting the dimerization term and adding a purely imaginary next-nearest neighbor hopping term. The topological properties of these two types of lattices are different. The dimerization lattice is topologically trivial while the lattice system with the imaginary NNN hopping is topologically nontrivial. A detailed discussion of the topological properties of these two cases can be found in Ref. [64]. For the finite device in our study, we calculate the energy band for a strip that is finite in the y direction and infinite along the x direction, as shown in Fig. 3.15. It can be seen that there is an empty gap for the dimerization lattice, while there is an edge mode for the imaginary NNN hopping lattice about $k_x = \pm\pi/a$. There is indication that the topology can have some effect on skew scattering for transport inside the energy band gap. In particular, as shown in Figs. 3.9(a) and 3.9(c), there is zero Hall voltage away from the resonance for the dimerization lattice, but there is a finite Hall voltage for the imaginary NNN hopping lattice when the energies are away from the resonance so it becomes a resonant valley. While the focus of this paper is on super skew scattering, the effect of topology deserves further attention.

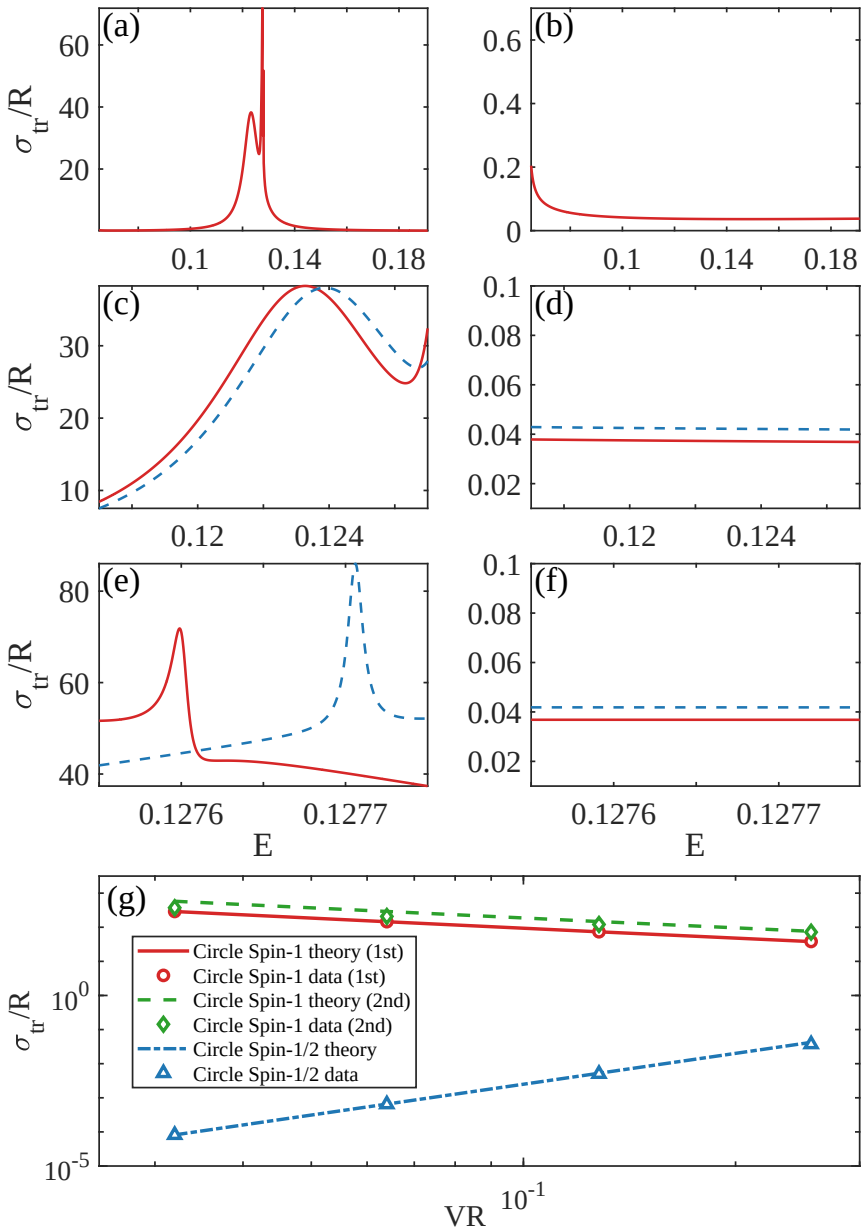

Figure 3.11: Resonant transport cross section for massive pseudospin-1 scattering from a circular potential barrier in the Klein tunneling regime. The parameter values are the same as those in Fig. 3.2. (a) σ_{tr} for massive pseudospin-1 quasiparticles versus the incident energy. There are resonant peaks, corresponding to these in Fig. 3.2. (b) The corresponding plot for pseudospin-1/2 scattering, where no resonant peaks occur and the values of σ_{tr} are much smaller than those in (a) in the entire energy range. (c) Magnification of the first resonant peak in (a), where the red and blue dashed curves are the numerical and theoretical results, respectively. (d) The corresponding magnification for pseudospin-1/2 scattering with the same legends as in (c). (e) Magnification of the second resonant peak in (a). (f) The corresponding magnification for pseudospin-1/2 scattering. (g) Scaling of the resonant transport cross section peak value with the strength of the scatterer. The symbols are numerical data and the lines are the corresponding theoretical predictions.

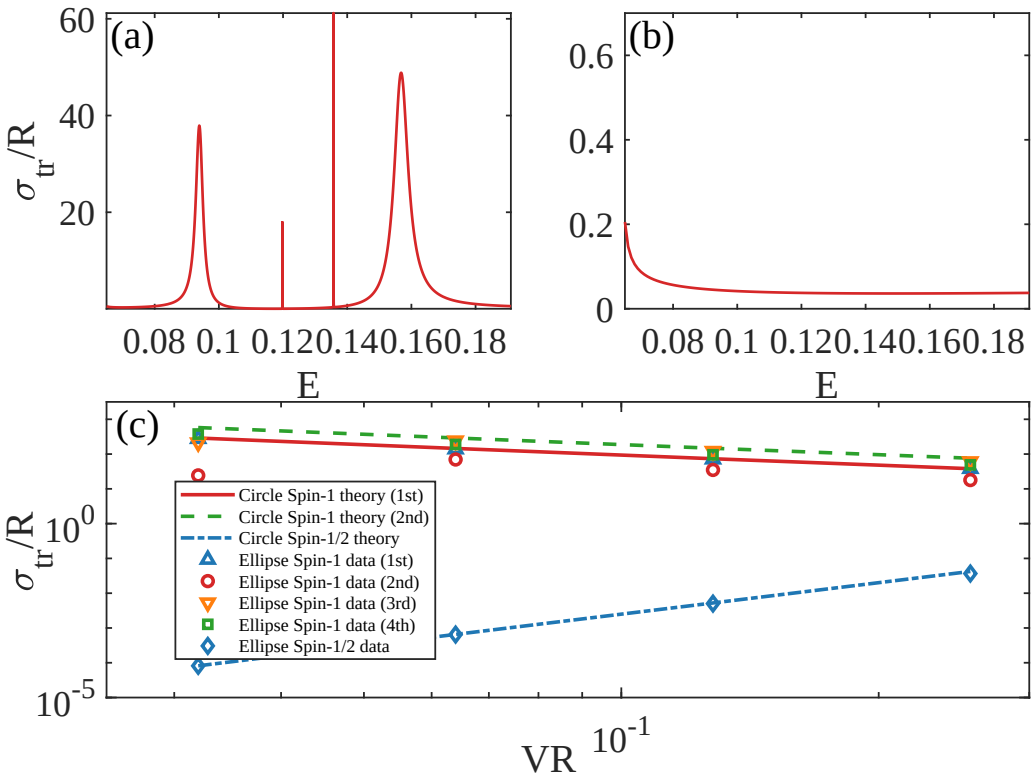

Figure 3.12: Resonant transport cross section versus energy for scattering from an elliptical potential. (a) Pseudospin-1 system (b) Pseudospin-1/2 system. The parameter values are the same as those in Fig. 3.5. (c) Scaling of the resonant transport cross section peak value with the strength of the elliptical scatterer. Legends are the same as those in Fig. 3.7.

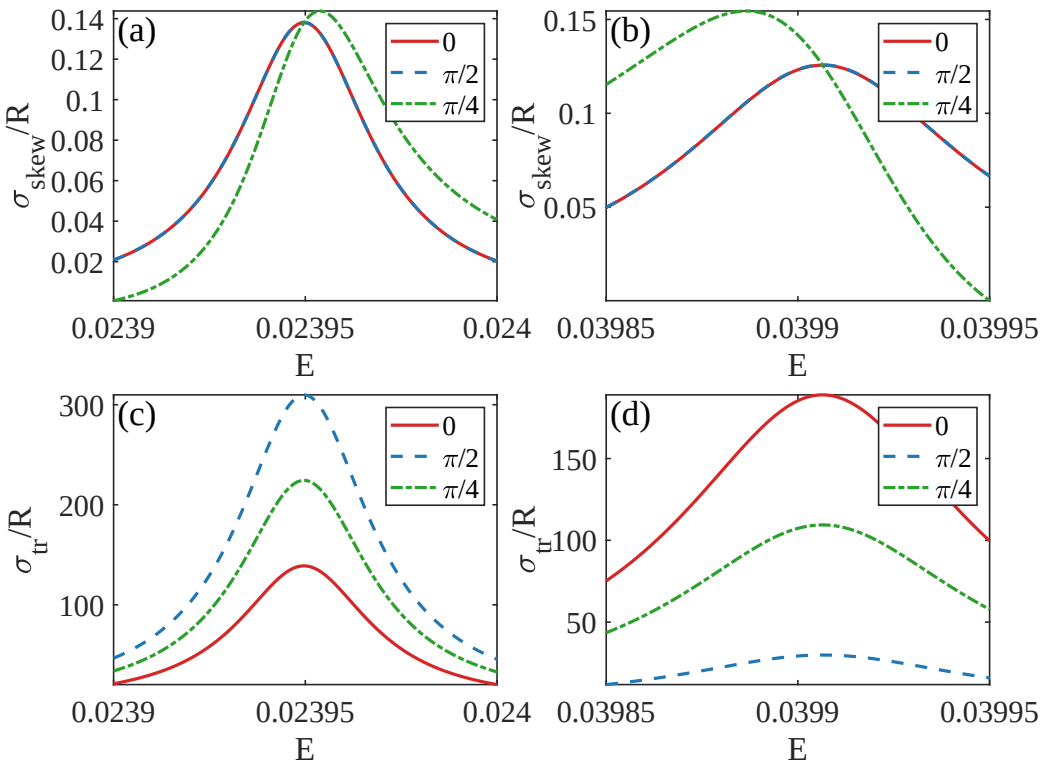

Figure 3.13: Resonant skew and transport scattering cross sections for an elliptical scatterer for different incident angles. (a) Resonant skew scattering cross section for the first peak in Fig. 3.5. The red solid, blue dashed, and green dash-dotted curves are for the incident angles of 0 (along positive x direction), $\pi/2$ (along positive y direction), and $\pi/4$ (with respect to positive x direction), respectively. (b) The corresponding results for the fourth resonant peak in Fig. 3.5. (c) Resonant transport scattering cross section for the first peak in Fig. 3.12. The red solid, blue dashed, and green dash-dotted curves are for the incident angles of 0, $\pi/2$, and $\pi/4$, respectively. (d) The corresponding results for the fourth resonant peak in Fig. 3.12.

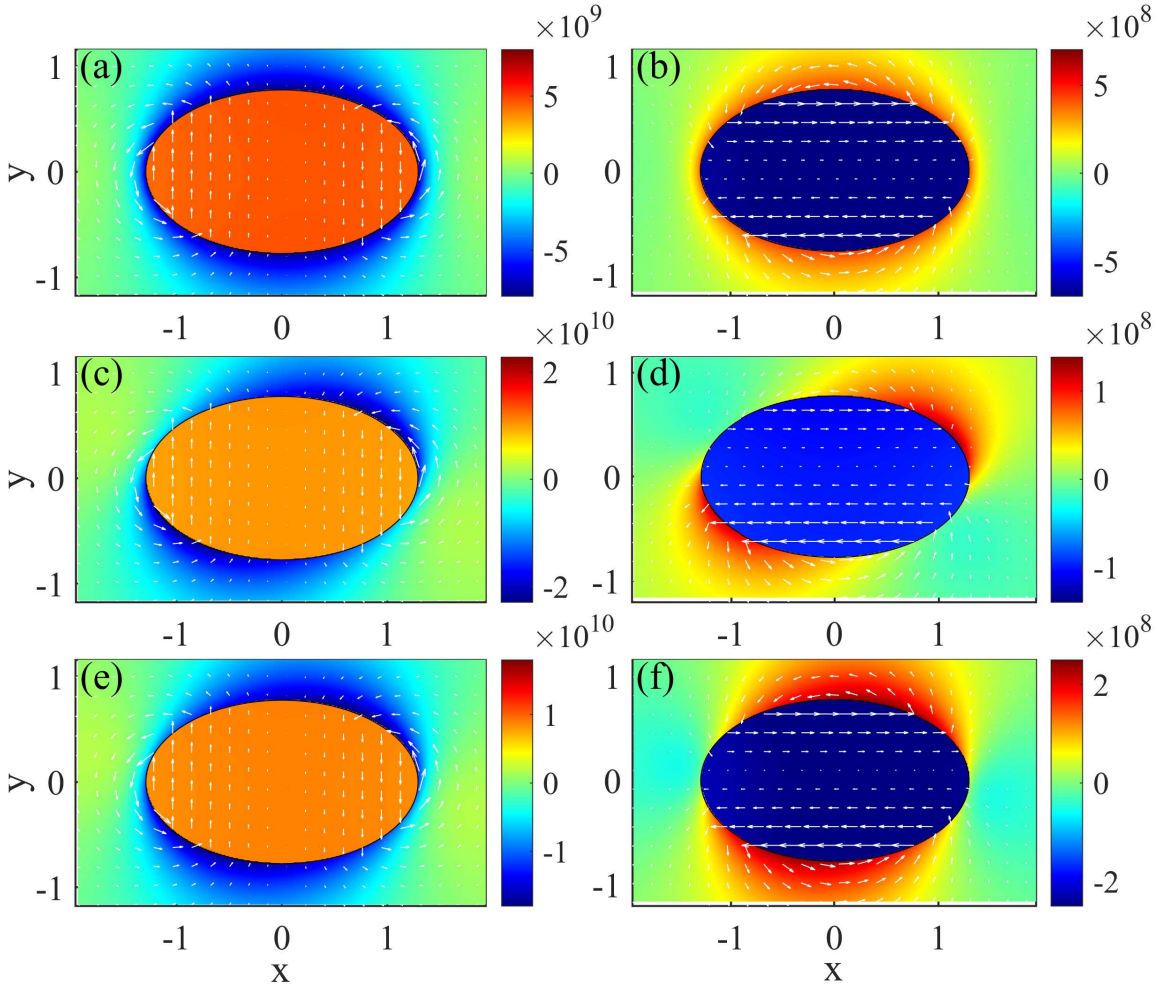

Figure 3.14: In-plane current density and pseudospin-z distribution for different incident angles. (a,c,e) Results for the first resonant state in Fig. 3.5 for incident angle 0, $\pi/2$ and $\pi/4$. (b,d,f) Results for the fourth resonant state in Fig. 3.5 for the same set of incident angles.

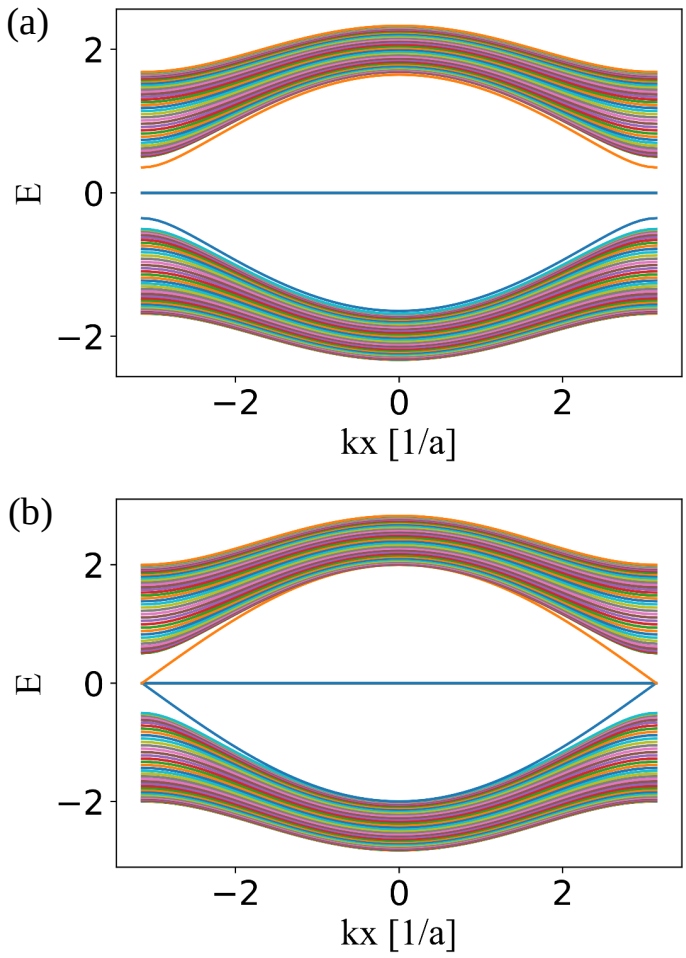

Figure 3.15: Energy band structures of Lieb lattice under two gap-opening mechanisms. The lattice system is a strip that has the width of 40 lattice constants in the y direction and is infinite along the x direction. (a) Dimerization Lieb lattice and (b) Imaginary NNN hopping Lieb lattice. Here, for the illustrative purpose, the band gap size is chosen to be relatively large.

Chapter 4

CHAOS BASED BERRY PHASE DETECTOR

The geometric or Berry phase, a characteristic of quasiparticles, is fundamental to the underlying quantum materials. The discoveries of new materials at a rapid pace nowadays call for efficient detection of the Berry phase. Utilizing α-T_3 lattice as a paradigm, we find that, in the Dirac electron optics regime, the semiclassical decay of the quasiparticles from a chaotic cavity can be effectively exploited for detecting the Berry phase. In particular, we demonstrate a one-to-one correspondence between the exponential decay rate and the geometric phase for the entire family of α-T_3 materials. This chaos based detection scheme represents an experimentally feasible way to assess the Berry phase and to distinguish the quasiparticles.

4.1 Introduction

In this chapter, we report a striking phenomenon in 2D Dirac materials, which leads to the principle of chaos based detection of Berry phase. To be concrete, we consider the entire α-T_3 material family. An α-T_3 material can be synthesized by altering the honeycomb lattice of graphene to include an additional atom at the center of each hexagon which, for $\alpha = 1$, leads to a T_3 or a dice lattice that hosts pseudospin-1 quasiparticles with a conical intersection of triple degeneracy in the underlying energy band [197, 8, 9, 66, 11, 198, 199, 200, 201, 202, 203, 15, 204, 17, 205, 18, 206, 19, 21, 1, 207, 208, 209, 210, 211, 212, 213]. An α-T_3 lattice is essentially an interpolation between the honeycomb lattice of graphene and a dice lattice, where the normalized coupling strength α between the hexagon and the central site varies between zero and one [34, 214, 79, 215, 216, 217], as shown in Fig. 4.1(a). Theoretically, pseudospin-1

quasiparticles are described by the Dirac-Weyl equation [8, 9, 1]. Suppose we apply an appropriate gate voltage to generate an external electrostatic potential confinement or cavity of α-T_3 lattice. The mechanism for Berry phase detection arises in the short wavelength or semiclassical regime, where the classical dynamics are relevant and can be treated according to ray optics with reflection and transmission laws determined by Klein tunneling - the theme of the emergent field of Dirac electron optics (DEO) [47, 218, 219, 220, 221, 222, 223, 224, 225, 226, 53, 227, 54, 228, 229, 230, 231, 232, 233, 234, 235, 84, 236, 237, 238, 239, 82, 240, 241, 242]. If the shape of the cavity is highly symmetric, e.g., a circle, the classical dynamics of the quasiparticles are integrable. However, if the cavity boundaries are deformed from the integrable shape, chaos can arise. We focus on the energy regime $V_0/2 < E < V_0$ in which Klein tunneling is enabled, where V_0 is the height of the potential [Fig. 4.1(b)], so that the relative effective refractive index n inside the cavity falls in the range $[-\infty, -1]$. As a result, there exists a critical angle for total internal reflections. For different values of the material parameter α, the physical characteristics of the quasiparticles, in particular the values of the Berry phase, are different. Our central idea is then that, for a fixed cavity shape, the semiclassical decay laws for quasiparticles corresponding to different values of α would be distinct. If the classical cavity dynamics contain a regular component, the decay laws will be algebraic [243, 244, 245, 246, 247], but we find that the differences among them will not be statistically significant enough to allow lattices of different values of α to be distinguished. However, when the cavity is deformed so that the classical dynamics are fully chaotic, the decay law becomes exponential [248]. The striking phenomenon is that the exponential decay rate for different values of α can be statistically distinguished to allow the Berry phase of the quasiparticles to be unequivocally detected, leading to the birth of chaos based Berry phase detectors. We note that in microcavity optics, classical chaos can be exploited

to generate lasing with a high quality factor and good emission directionality at the same time [249, 250, 251, 252, 253, 254, 255, 256, 257, 258, 259].

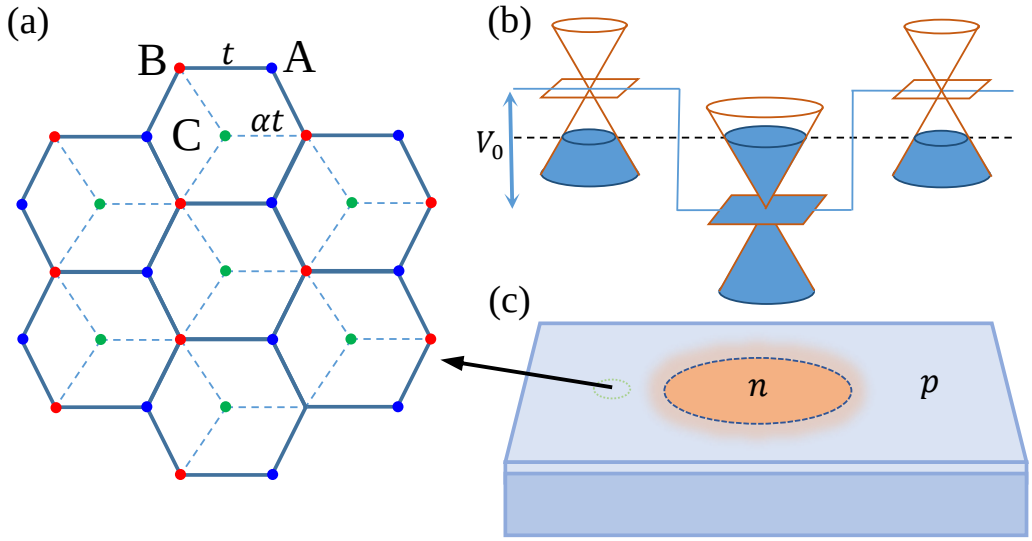

Figure 4.1: Schematic illustration of an α-T_3 cavity and the energy dispersion relation. (a) α-T_3 lattice structure. (b) The electron and hole energy dispersion relations in different spatial regions. (c) A possible scheme of experimental realization of the cavity through an applied gate voltage. The amount of the voltage is such that the quasiparticles are in the Klein-tunneling regime.

4.2 Hamiltonian and Dirac Electron Optics

The α-T_3 lattice system has the advantage of generating a continuous spectrum of quasiparticles with systematically varying Berry phase through the tuning of the value of the parameter α in the unit interval. At the two opposite ends of the spectrum, i.e., $\alpha = 0, 1$, the quasiparticles are pseudospin-1/2 Dirac fermions and pseudospin-1 Dirac-Weyl particles, respectively. As illustrated in Fig. 4.1, the lattice has three nonequivalent atoms in one unit cell, and the interaction strength is t between A and B atoms and αt between B and C atoms, where t is the nearest neighbor hopping energy of the graphene lattice. A cavity of arbitrary shape can be realized by applying an appropriate gate voltage through the STM technique [228, 82, 260], as shown in Fig. 4.1(c). We consider circular and stadium shaped cavities that exhibit inte-

grable and chaotic dynamics, respectively, in the classical limit [261]. The low-energy Hamiltonian for the α-T_3 system about a K point in the hexagonal Brillouin zone is [34, 216] $\hat{H} = \hat{H}_{kin} + V(x)\hat{I}$, where $\hat{H}_{kin}$ is the kinetic energy, $V(x)$ is the applied potential that forms the cavity, and I is the 3×3 identity matrix. The coupling strength α can be conveniently parameterized as $\alpha = \tan\psi$. The kinetic part of the rescaled Hamiltonian (by $\cos\psi$) is

$$\hat{H}_{kin} = \begin{bmatrix} 0 & f_k \cos\psi & 0 \\ f_k^* \cos\psi & 0 & f_k \sin\psi \\ 0 & f_k^* \sin\psi & 0 \end{bmatrix}, \tag{4.1}$$

where $f_k = v_F(\xi k_x - i k_y)$, v_F is the Fermi velocity, $\boldsymbol{k} = (k_x, k_y)$ is the wave vector, and $\xi = \pm$ is the valley quantum number associated with K and K', respectively. In the semiclassical regime where the particle wavelength is much smaller than the size of the cavity so that the classical dynamics are directly relevant, the DEO paradigm can be instated to treat the particle escape problem, which is analogous to decay of light rays from a dielectric cavity. In DEO, the essential quantity is the transmission coefficient of a particle through a potential step, which can be obtained by wavefunction matching as [216]

$$T = \frac{4ss'\cos\theta\cos\phi}{2 + 2ss'\cos(\theta+\phi) - \sin^2 2\psi(s\sin\theta - s'\sin\phi)^2}, \tag{4.2}$$

where $s = \pm$ and $s' = \pm$ with the plus and minus signs denoting the conduction and valence band, respectively, and incident and transmitted angles are ϕ and θ, respectively. Imposing conservation of the component of the momentum tangent to the interface, we get $\sin\theta = (E/|E - V_0|)\sin\phi$. For more details about the electron transmission through a potential step, one can refer Appendix 4.5.1. Our focus is on the survival probability of the quasiparticles from an α-T_3 cavity for the entire material spectrum: $0 \leq \alpha \leq 1$.

We set the amount of the applied voltage such that the energy range of the quasiparticles is $V_0/2 < E < V_0$ (the Klein tunneling regime). In the optical analog, the corresponding relative effective refractive index inside the cavity is $n = E/(E - V_0)$ and that outside of the cavity is $n = 1$. Due to Klein tunneling, the range of relative refractive index in the cavity is negative: $-\infty < n < -1$. As a result, a critical angle exists for the tunneling of electrons through a simple static electrical potential step, which is $\sin\phi_c = (V_0 - E)/E$ and is independent of the α value [216]. This behavior is exemplified in the polar representation of the transmission in Fig. 4.2(a), which shows that the value of the transmission increases with α. As the value of α is varied in the unit interval, the critical angle remains unchanged.

4.3 Results

Algebraic Decay of α-T_3 Quasiparticles from a Circular (Integrable) Cavity

The classical phase space contains Kolmogorov-Arnold-Moser (KAM) tori and an open area through which particles (rays) escape. Initializing an ensemble of particles (e.g., 10^7) in the open area, the survival probability time distribution (SPTD) is given by

$$P_{sv}(t) = \int_0^L ds \int_{-p_c}^{p_c} dp I(s,p) R(p)^{N(t)}, \tag{4.3}$$

where L is the boundary length, $p_c = \sin\phi_c = 1/|n|$ with ϕ_c the critical angle for total internal reflection, $R(p) = 1 - T$ is the reflection coefficient for the α-T_3 quasiparticles with transmission T defined in Eq. (4.2), $N(t) = t/(2\cos\phi)$ is the number of bounces off the boundary, and $I(s,p) = |n|/2L$ is the uniform initial distribution. Consider a circle of unit radius, using the length of the ray trajectory as the time scale, we can

rewrite Eq. (4.3) as

$$P_{sv}(t) = |n| \int_0^{\phi_c} d\phi \cos\phi \exp[-\frac{t}{2\cos\phi} \ln(\frac{1}{R})], \tag{4.4}$$

with

$$R^{-1} = 1 + \frac{-4\cos\theta\cos\phi}{2 + 2\cos(\theta-\phi) - \sin^2 2\psi(\sin\theta + \sin\phi)^2} \tag{4.5}$$

From the particle transmission plot in Fig. 4.2(a), we can see the particles near the critical angle ϕ_c can survive for a longer time and can contribute to the long time behavior. As a result, we can expand the $\ln(\frac{1}{R})$ term about the critical angle ϕ_c by defining a new variable χ with $\phi = \phi_c - \chi$, and use the approximations $\chi \to 0$, we have

$$\ln(\frac{1}{R}) \approx \frac{4\sqrt{2|n|\cos\phi_c}\cos\phi_c}{2 + [2|n| - \sin^2 2\psi(|n|+1)^2 \sin^2\phi_c]} \cdot \chi^{1/2}. \tag{4.6}$$

Substituting Eq. (4.6) into Eq. (4.4), we obtain the SPTD as

$$\begin{aligned} P_{sv} &= \frac{1}{4} t^{-2} \{2 + [2|n| - \sin^2 2\psi(|n|+1)^2] \frac{1}{|n|^2}\}^2 \\ &= C(n,\psi) t^{-2} \end{aligned} \tag{4.7}$$

This indicates that the quasiparticles decay algebraically from the cavity and the value of the decay exponent is two, regardless of the value of α. For certain value of $|n|$, as the value of α changes from zero to one, the decay coefficient $C(n,\psi)$ decreases, as shown in Fig. 4.2(b). The numerical calculation for SPTD in the circular cavity is performed via taking 10^7 random initial points in the open region of the phase space. We then trace each point with reflection coefficient $R(p)$ when bouncing from the boundary, and sum the surviving probabilities between t and $t + \Delta$ with $\Delta = 1$ with the initial probability being 1 at $t = 0$. We can see from Fig. 4.2(b) that both theoretical and numerical results show an algebraic behavior in the long time, with exponent equals to 2.

Experimentally, to distinguish the nature of the quasiparticles and to detect the Berry phase, the decay coefficient is not a desired quantity to measure as it reflects the short time behavior of the decay process. In fact, it not only depends the nature of the material (as determined by the value of α) but also on the detailed system design. The long time behavior of the decay is characterized by the algebraic decay exponent, which does not depend on the details of the experimental design and, hence, it can possibly be exploited for Berry phase detection. However, for an integrable cavity, the algebraic decay exponent remains constant as the value of α is changed, as shown in Fig. 4.2(b). It is thus not feasible to distinguish the quasiparticles by their long time behavior, ruling out integrable cavities as a potential candidate for detecting the Berry phase.

Exponential Decay of α-T_3 Quasiparticles from a Chaotic Cavity

For the stadium cavity, the classical dynamics are chaotic, leading to random changes in the direction of the propagating ray. In this case, the survival probability of the quasiparticles in the cavity decays exponentially with time, as shown in Fig. 4.2(c), where the long time behavior is determined by the exponential decay rate. The striking phenomenon is that the decay rate increases monotonically as the value of the material parameter α is increased from zero to one, suggesting the possibility of using the exponential decay rate to distinguish the α-T_3 materials and to detect the intrinsic Berry phase. The difference in the decay rate can be further demonstrated by calculating its dependence on the absolute value $|n|$ for different values of α, as shown in Fig. 4.3(a). For small values of $|n|$, the difference in the decay rate is relatively large, indicating a stronger ability to discern the α-T_3 quasiparticles. For large values of $|n|$, the difference in the decay rate is somewhat reduced. This is expected because, as the value of $|n|$ is increased from one, the transmission for the materials at the

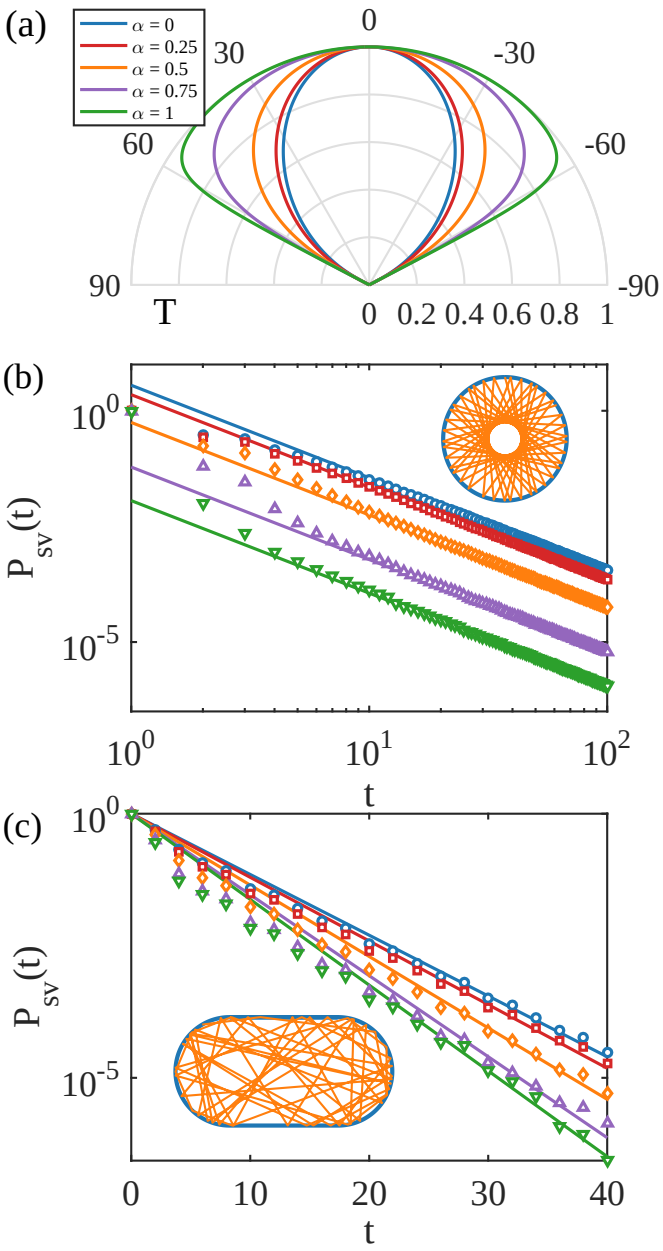

Figure 4.2: Semiclassical decay of quasiparticles from a cavity in an α-T_3 lattice. For particle energy $E = 0.53V_0$ (within Klein tunneling regime) and relative refractive index $n = -1.1277$ inside of the cavity, (a) transmission T across a potential step as a function of incident angle ϕ for a number of equally spaced α values. (b) SPTD for the circular (integrable) cavity on a double logarithmic plot, where the blue circles, red squares, orange diamonds, purple up-triangles, and green down-triangles are numerical results for the five α values in (a), respectively, and the solid lines are the theoretical predictions. The decay is algebraic but the decay exponent is a constant independent of the value of α. (c) SPTD for a stadium shaped (chaotic) cavity of semicircle radius one and straight edge of length two on a semi-logarithmic plot. The color legends are the same as in (b). In this case, the decay is exponential and its rate depends on the value of α. Measuring the exponential decay rate then gives the value of α and the corresponding Berry phase of the underlying material lattice system.

two ends of the α-T_3 spectrum, namely graphene and pseudospin-1 lattice, decreases continuously. For $|n| \to \infty$, the transmission tends to zero. This result indicates that, the optimal regime to discern the quasiparticles for α-T_3 occurs for $|n|$ above one but not much larger, corresponding to the regime where the particle energy is slightly above half of the potential height.

In general, for a given value of α, the exponential decay rate is inversely proportional to n, which can be argued, as follows [262, 263]. For $P_{sv}(t) \sim \exp(-\gamma t)$, we have $dP_{sv}(t)/dt \sim -\gamma \cdot P_{sv}(t) \sim -(\langle T(p)\rangle/\langle d\rangle) \cdot P_{sv}(t)$, where $\langle T(p)\rangle$ and $\langle d\rangle$ are the average transmission and the distance between two consecutive collisions in the chaotic cavity. The decay rate can then be obtained in terms of the steady probability distribution $P_s(s,p)$ as:

$$\gamma = \langle T(p)\rangle/\langle d\rangle = \langle d\rangle^{-1} \int_0^L ds \int_{-1}^1 dp P_s(s,p) T(p) \tag{4.8}$$

Explicitly, in the Klein tunneling regime $V_0/2 < E < V_0$ ($-\infty < n < -1$), we can derive an analytical expression for the exponential decay rate based on a simple model of the steady probability distribution (SPD) for the stadium-shaped cavity that generates fully developed chaos in the classical limit [262]. We assume that the SPD is a uniform distribution over the whole phase space except the open regions related to the linear segments of the stadium boundary. Then the decay rate can be expressed in terms of the steady probability distribution:

$$\gamma = \frac{2\pi R}{2(\pi A/L)(L - 2l/|n|)} \int_{-1/|n|}^{1/|n|} dp T(p), \tag{4.9}$$

where $T(p)$ is the transmission coefficient defined in Eq. (4.2), the average path length of ray trajectory segments between two successive bounces is $\langle d\rangle = \pi A/L$, with $A = \pi R^2 + 2Rl$ and $L = 2\pi R + 2l$ being the area and boundary length of the stadium, respectively. Substituting the expressions $\sin\theta = |n|p$, $\cos\theta = -\sqrt{1 - \sin^2\theta} =$

$-\sqrt{1-n^2p^2}$, $\sin\phi = p$, $\cos\phi = \sqrt{1-p^2}$ into the expression of $T(p)$ in the main text, we get

$$T = 4\sqrt{1-p^2}\sqrt{1-n^2p^2}/[2+2\sqrt{1-p^2}\sqrt{1-n^2p^2} \\ +2|n|p^2 - \sin^2 2\psi(n^2p^2+p^2+2|n|p^2)]. \tag{4.10}$$

In the limit $|n| \approx 1$, imposing change of variable $x = n^2p^2$ to get $dp = dx/(2|n|\sqrt{x})$, we can write the decay rate in terms of variable x as

$$\begin{aligned}\gamma &= \frac{2\pi R}{2(\pi A/L)(L-2l/|n|)}\int_0^1 \frac{dx}{\sqrt{x}}T(x) \\ &= \frac{2\pi R}{2(\pi A/L)(L-2l/|n|)}\int_0^1 \frac{dx}{\sqrt{x}}(1-x)(1-\sin^2 2\psi\cdot x)^{-1} \\ &= \frac{2\pi R}{2(\pi A/L)(L-2l/|n|)}B(1/2,2)F(1,1/2;5/2;\sin^2 2\psi) \\ &\approx \frac{2\pi R}{2(\pi A/L)(L-2l/|n|)}\frac{4}{3}\cdot(1+\frac{1}{5}\sin^2 2\psi+...),\end{aligned} \tag{4.11}$$

where $B(x,y) = \Gamma(x)\Gamma(y)/\Gamma(x+y)$ is the beta function and $F(\alpha,\beta;\gamma;z)$ is the Gauss hypergeometric function.

For the $|n| \gg 1$ regime, we use the change of variable $x = np$ to simplify the decay rate integral. The decay rate becomes

$$\gamma = \frac{4\pi R}{2(\pi A/L)L|n|}\int_0^1 \frac{4\sqrt{1-x^2}}{2+2\sqrt{1-x^2}-\sin^2(2\psi)x^2}, \tag{4.12}$$

which is inversely proportional to the absolute value of the refractive index $|n|$. More importantly, the decay rate depends on the material parameter α monotonically ($\alpha = \tan\psi$, with α increasing from zero to one). We note that, the theoretical results in Fig. 4.2(c) is obtained by doing the integration formula (4.9) directly. The approximation used to derive Eqs. (4.11) and (4.12) here is to facilitate an analytic demonstration of the scaling of the decay rate with n. The formulas also reveal that the decay rate increases monotonically with α.

Numerically, we choose stadium shape with the semicircle radius to be 1 and the straight long edge being 2 in length. In the calculation, we use a random ensemble of 10^7 initial points spread over the whole phase space and trace the survival probability with time, which is scaled as the length of trajectory as in the circular case. The numerical results are consistent with the theoretical cases based on SPD approximation, as shown in Fig. 4.2(c).

Detection of Berry Phase

The Berry phase associated with an orbit in the conical bands is given by [79]

$$\phi_{\xi}^{B} = \pi\xi\cos(2\psi) = \pi\xi(\frac{1-\alpha^2}{1+\alpha^2}). \tag{4.13}$$

For the flat band, the Berry phase is

$$\phi_{0,\xi}^{B} = -2\pi\xi\cos(2\psi) = -2\pi\xi(\frac{1-\alpha^2}{1+\alpha^2}). \tag{4.14}$$

We take $\xi = \pm 1$ for the K and K' valleys, respectively. For $\xi = 1$, the dependence of the Berry phase on α is shown in Fig. 4.3(b). As the value of α is increased from zero to one, the Berry phase decreases monotonically from π to zero. At the same time, the exponential decay rate increases monotonically. There is then a one-to-one correspondence between the decay rate and the Berry phase for the entire spectrum of α-T_3 materials, justifying a semiclassical chaotic cavity as an effective Berry phase detector.

4.4 Conclusion

To summarize, we uncover a phenomenon in relativistic quantum chaos that can be exploited to detect the Berry phase of two-dimensional Dirac materials. In particular, for the spectrum of α-T_3 materials, in the semiclassical regime, the decay of the

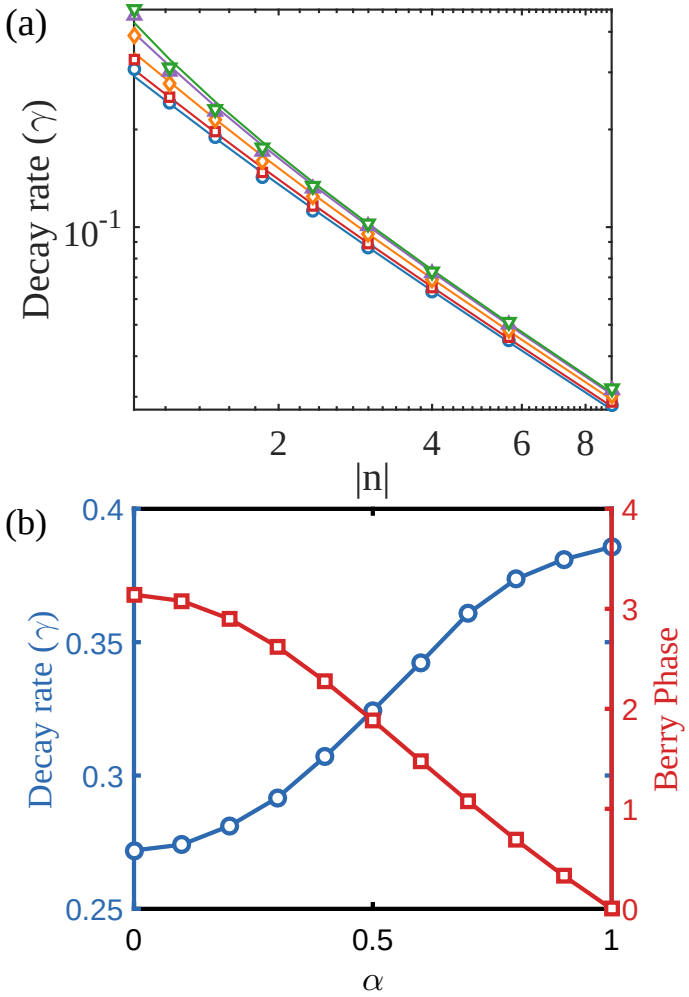

Figure 4.3: Dependence of the semiclassical exponential decay rate from a chaotic cavity on the effective refractive index and the detection of the Berry phase. (a) For $\alpha = 0, 0.25, 0.5, 0.75, 1$, the decay rate versus the refractive index, where the blue circles, red squares, orange diamonds, purple up-triangles and green down-triangles are the respective numerical results and the dashed curves are theoretical predictions. (b) For $E/V_0 = 0.53$, detection of Berry phase (red squares) based on the decay rate (blue circles). As the value of α is changed from zero to one, there is a one-to-one correspondence between the exponential decay rate and the Berry phase.

quasiparticles from a chaotic cavity depends on the intrinsic material parameter. Experimentally, the cavity can be realized through a gate voltage, where locally the boundary of the cavity is effectively a potential step. When the Fermi energy of the quasiparticles is above half but below the potential height, the system is in the Klein tunneling regime, rendering applicable Dirac electron optics. In this case, the

relative effective refractive index inside the cavity is between negative infinity and minus one, so a critical angle exists for the semiclassical ray dynamics. Because of the close interplay between Klein tunneling and the value of the Berry phase, measuring the quasiparticle escape rate leads to direct information about the Berry phase and for differentiating the α-T_3 materials. Our analysis and calculation have validated this idea - we have indeed found a one-to-one correspondence between the exponential decay rate and the value of the Berry phase. In terms of basic physics, our finding builds up a connection, for the first time, between classical chaos and Berry phase. From an applied standpoint, because of the fundamental importance of Berry phase in determining the quantum behaviors and properties of materials, our work, relative simplicity notwithstanding, provides an effective and experimentally feasible way to assess the Berry phase for accurate characterization of the underlying material. This may find broad applications in materials science and engineering where new nanomaterials are being discovered at a rapid pace, demanding effective techniques of characterization.

4.5 Supplementary Notes

4.5.1 The Band Structure and Wave-vectors Across the Potential Step

In order to give a clear understanding of the optic-like decay behavior of electrons from a cavity formed by electro-static gate potential, we schematically depict the electron band structure and the wave-vectors across the potential step in the transmission process, as shown separately in the first row and second row in Fig. 4.4. Besides, we give a clear classification of the different refractive index regimes, corresponding to different potential values compared to the Fermi energy. These regimes can be divided into cases with the positive and negative refractive index and that with and

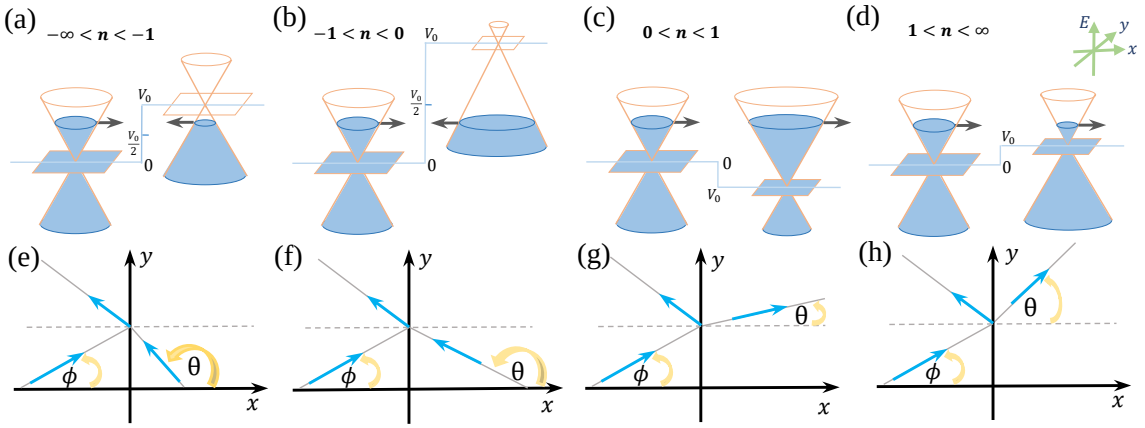

Figure 4.4: Schematic plot of the band structures and wave-vectors across potential step with different refractive indexes. The first row gives the band structures of the electrons across the potential step with different gate potential values and fixed Fermi energy, thus different refractive index for each setup. The black arrows denote the wavevector directions (only depicting the x direction case). For negative refractive index regimes, the wave-vector along x direction is opposite. The second row shows the wave-vectors of the electrons with the incident angle labeled as ϕ and the transmitted angle as θ.

without critical angles. In our setup, we always choose the incident electron in them conduction band, i.e., with positive Fermi energy, and vary the potential V_0. When V_0 is larger than the Fermi energy, the transmitted electron is in the valence band. In this case, the wave-vector is in opposite direction along x direction and the same direction along y direction, while keeping the velocity direction unchanged, leading to negative refractive index.

Explicitly, for the gate potential in the range $V_0/2 < E < V_0$, the refractive index denoted as $n = \frac{E}{E-V_0}$ falls in the regime $-\infty < n < -1$. There are critical angle in this case, corresponding to $\sin\theta = 1 = \frac{E}{|E-V_0|}\sin\phi_c$. And the transmission angle can be obtained in terms of incident angle ϕ as

$$\begin{aligned}\theta &= \pi - \tan^{-1}\frac{\sin\phi \cdot E/V_0}{\sqrt{(1-E/V_0)^2 - (\sin\phi \cdot E/V_0)^2}} \\ &= \pi + \tan^{-1}\frac{n\sin\phi}{\sqrt{1-(n\sin\phi)^2}}.\end{aligned} \tag{4.15}$$

where we have utilized $\sin\theta = \frac{E}{|E-V_0|}\sin\phi$ and $\cos\theta = -\sqrt{1-\sin^2\theta}$. The band

structure and angles corresponding to wave-vectors are shown in Fig. 4.4 (a), (e).

In the regime where the potential satisfies $0 < E < V_0/2$, the refractive index satisfies $-1 < n < 0$. As a result, there is no critical angle in this case. The transmission angle can be obtained in the same form as Eq. (4.15) and the schematic plot of the band structure and wave-vector angles are shown in Fig. 4.4 (b), (f).

For the case where $V_0 < 0 < E$, the refractive index is in the range $0 < n < 1$, which is positive refractive index due to the incidence and transmission electron both in the conduction band. The is no critical angle in this case. And the transmission angle can be obtained as

$$\begin{aligned}\theta &= \tan^{-1} \frac{\sin\phi \cdot E/V_0}{\sqrt{(1 - E/V_0)^2 - (\sin\phi \cdot E/V_0)^2}} \\ &= \tan^{-1} \frac{n \sin\phi}{1 - (n \sin\phi)^2}.\end{aligned} \tag{4.16}$$

where we used the relation $\sin\theta = \frac{E}{E-V_0} \sin\phi$ and $\cos\theta = \sqrt{1 - \sin^2\theta}$. This schematic band structure and angles related to wave-vectors are depicted in Fig. 4.4 (c), (g).

In the regime where $0 < V_0 < E$, the refractive index is in the range $1 < n < \infty$ with the incidence and transmission electrons both in the conduction band. And there is critical angle in this case, with $\sin\theta = 1 = \frac{E}{E-V_0} \sin\phi_c$. The transmission angle can be obtained in the same form as in Eq. (4.16). And the band structures and the wave-vectors can be seen in Fig. 4.4 (d), (h).

4.5.2 Survival Probability Distribution of α-T_3 Quasiparticles in Different Energy Regimes

For completeness, we derive the decay law of the survival probability of α-T_3 quasiparticles and obtain the decay rate in other energy regimes. We demonstrate that the decay in these regimes is not easy to be used to detect berry phase. For the regimes where there are not critical angles, the decay is very fast, which is not

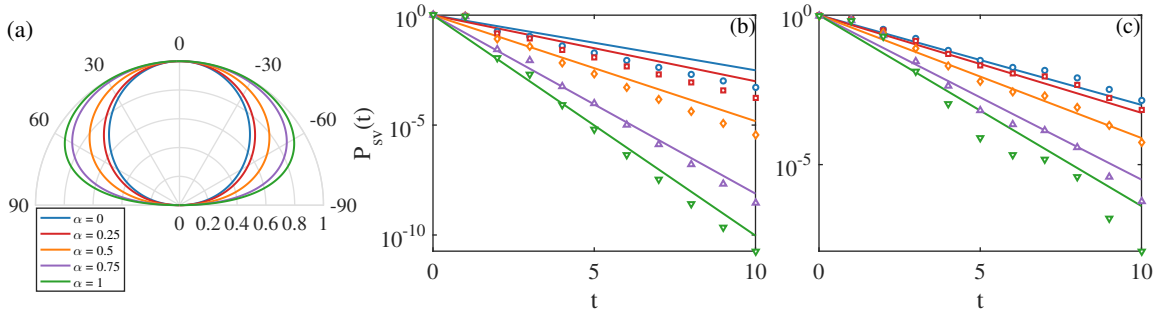

Figure 4.5: Survival probabilities from integrable and chaotic cavities for $0 < E < V_0/2$. For $E/V_0 = 1/3$ and $n = -0.5$, (a) transmission versus the incident angle on a polar plot, (b) decay of the survival probability from a circular (integrable) cavity with time, and (c) decay of the survival probability from a stadium shaped (chaotic) cavity.

feasible to detect Berry phase. For the regime there is critical angle, the decay rate for different particles follow similar curve, making them not easy to distinguish.

The $0 < E < V_0/2$ Regime

In this energy regime, the refractive index $n = E/(E - V_0)$ of the cavity is in the range $-1 < n < 0$. In this regime, there exists no critical angle for rays inside the cavity. Figure 4.5(a) shows that the transmission is nonzero for all angles and it increases with decreasing α values. In this case, the decay of quasiparticles is exponential and it does not depend on the nature of the classical dynamics, i.e., integrable or chaotic, as shown in Fig. 4.5.

A theoretical explanation of the features in Fig. 4.5 is as follows. Due to the absence of a critical angle for Dirac electron optical rays in the energy range $0 < E < V_0/2$, the survival probability from a circular (integrable) is mainly determined by the ray behavior about $\phi = \pi/2$. Letting $\phi = \pi/2 - x$, where x is a small angle

deviation from $\pi/2$, and using the approximations

$$\sin\phi \approx \sin\phi_c - \cos\phi_c \cdot x,$$

$$\cos\phi \approx \cos\phi_c + \sin\phi_c \cdot x,$$

$$\sin\theta \approx |n| \cdot (\sin\phi_c - \cos\phi_c \cdot x),$$

$$\cos\theta \approx -\sqrt{1 - n^2 \cdot (\sin\phi_c - \cos\phi_c \cdot x)^2},$$

we get

$$\ln R^{-1} = \frac{4x\sqrt{1-n^2}}{2 + 2|n| - \sin^2(2\psi)(1+|n|)^2}. \tag{4.17}$$

where $R = 1 - T$ with T being the transmission coefficient defined in Eq. (4.2) in the main text. The survival probability can be expressed as

$$P_{sv} = \exp\{-\frac{2\sqrt{1-n^2}}{2 + 2|n| - \sin^2(2\psi)(1+|n|)^2} \cdot t\} \tag{4.18}$$

For a chaotic cavity, the angle distribution is random, leading to an exponential behavior of the survival probability. We can obtain the expression for the decay rate γ by approximating P_{sv} as

$$P_{sv}(t) \approx \langle 1 - T(p)\rangle^{t/\langle d\rangle} = \exp\{\ln[1 - \langle T(p)\rangle](t/\langle d\rangle)\}. \tag{4.19}$$

The decay rate can be expressed as

$$\gamma = -\frac{1}{\langle d\rangle} \ln[1 - \langle T(p)\rangle]. \tag{4.20}$$

For either the integrable or the chaotic cavity, the exponential decay rate depends on the material parameter α which, in principle, can be used to detect the Berry phase. However, due to the lack of a critical angle in this energy range, experimentally it would be difficult to confine the quasiparticles. Indeed, comparing with the exponential decay from a chaotic cavity in the Klein tunneling regime ($V_0/2 < E < V_0$) as treated in the main text, here the decay is much faster.

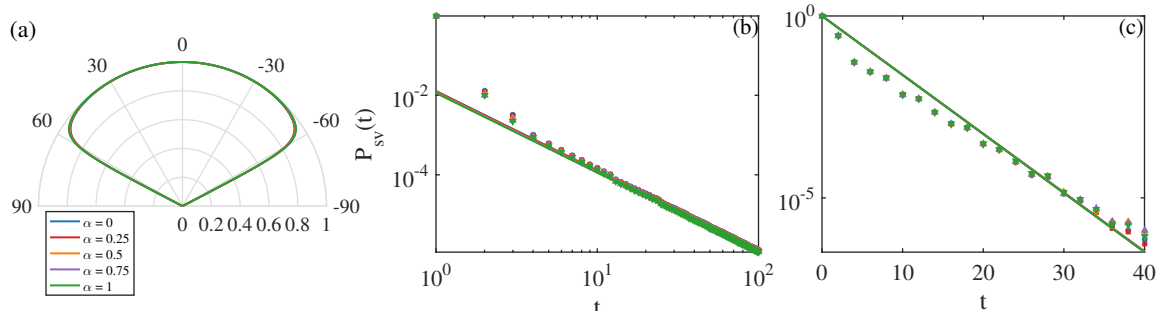

Figure 4.6: Survival probabilities from integrable and chaotic cavities for $0 < V_0 < E$. For $E/V_0 = 8.8309$ ($n = 1.1277$), (a) polar representation of the transmission with respect to the incident angle, (b) decay with time of the survival probability from a circular (integrable) cavity, and (c) decay of survival probability from a stadium shaped (chaotic) cavity.

The $0 < V_0 < E$ Regime

For the energy range $0 < V_0 < E$ with the refractive index $n = E/(E - V_0)$ of the cavity in the range $1 < n < \infty$, the survival probability with time exhibits an algebraic decay from an integrable cavity and an exponential decay from a chaotic cavity, which is characteristically similar to the decay behaviors in the Klein tunneling regime ($V_0/2 < E < V_0$) treated in the main text. A difference is that, for $0 < V_0 < E$, the dependence of the transmission on the material parameter α is much weaker in the sense that, as the value of α is increased from zero to one, the transmission barely changes. It is thus practically difficult to distinguish the quasiparticles for different materials. These behaviors are shown in Fig. 4.6, where the analytical fitting is calculated in the same way as in the main text.

The $V_0 < 0 < E$ Regime

In the energy regime $V_0 < 0 < E$ with the refractive index $n = E/(E - V_0)$ of the cavity in the range $0 < n < 1$, the decay of the survival probability is similar to that in the $0 < E < V_0/2$ regime. In particular, regardless of the nature of the classical dynamics (integrable or chaotic), the survival probability exhibits an exponential

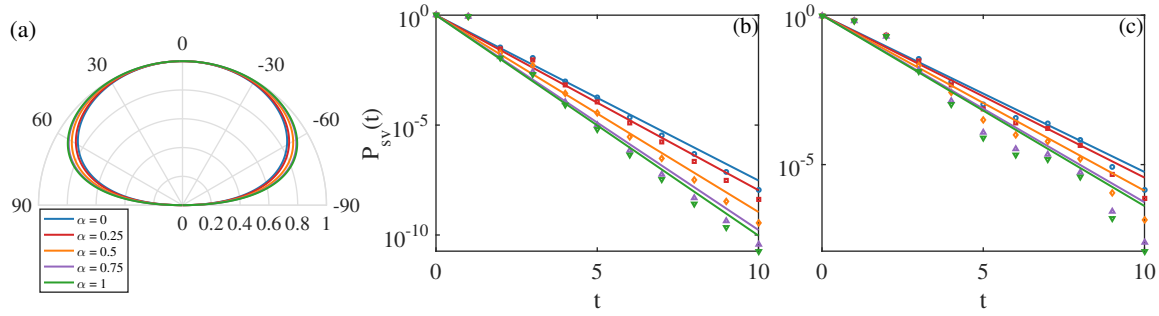

Figure 4.7: Survival probability from integrable and chaotic cavities in the $V_0 < 0 < E$ energy regime. For $E/V_0 = -1$ ($n = 0.5$), (a) a polar representation of the transmission versus the incident angle, (b) decay of survival probability from a circular (integrable) cavity, and (c) decay of survival probability from a stadium shaped (chaotic) cavity.

decay with time, as shown in Fig. 4.7. Again, comparing with the energy regime of Klein tunneling, the decay is much faster here, making experimental detection of Berry phase difficult.

4.5.3 Comparison Between the Decay of Survival Probability for Pseudospin-1/2 and Pseudospin-1 Quasiparticles

The best studied material in the α-T_3 family is graphene, corresponding to $\alpha = 0$. There is also a growing interest in the material at the other end of the spectrum: $\alpha = 1$ for which the quasiparticles are of the pseudospin-1 nature. We offer a comparison of the decay behavior of the quasiparticles at these two extreme cases.

In the energy range $0 < E < V_0/2$ [corresponding to negative refractive index: $-1 < n = E/(E - V_0) < 0$], there is no critical angle for total internal reflection. For both integrable and chaotic cavities, the survival probability decays exponentially with time, with no qualitative difference. As the absolute value of the refractive index is increased, the range of angle for transmission is large for pseudospin-1 quasiparticles, but the range is smaller for pseudospin-1/2 quasiparticles. For integrable cavities, the difference is somewhat larger.

In the energy range for Klein tunneling: $V_0/2 < E < V_0$ ($-\infty < n < -1$), a critical angle arises, above which there are total internal reflections. For an integrable cavity, the survival probability decays algebraically with time, but the decay is exponential for a chaotic cavity. In the integrable case, the algebraic decay exponents have approximately identical values for the pseudospin-1 and pseudospin-1/2 particles. However, for a chaotic cavity, the decay of pseudospin-1 quasiparticles is much faster than that of pseudospin-1/2 quasiparticles. Chaos can thus be effective in detecting the Berry phase to distinguish the two types of quasiparticles. In fact, as demonstrated in the main text, chaos in the Klein tunneling regime can be effective for detecting the Berry phase across the entire material spectrum of the α-T_3 family.

In the energy range of $V_0 < E$ ($1 < n < \infty$), a critical angle exists. The decay behavior of the survival probability is algebraic for an integral cavity and exponential for a chaotic cavity. The difference in the transmission versus the incident angle is small for pseudospin-1 and pseudospin-1/2 quasiparticles, leading to a similar value of the algebraic decay coefficient in the integrable case and a similar exponential decay law in the chaotic case. In this energy range, to use the decay behavior to discern the quasiparticles would be practically difficult.

In the energy range $V_0 < 0 < E$ ($0 < n < 1$), there is no critical angle, and the decay behavior is exponential for both integrable and chaotic cavities. As the energy is increased, the difference in the decay behaviors of pseudospin-1 and pseudospin-1/2 quasiparticles diminishes, ruling out the possibility of exploiting the decay for detection of Berry phase.

Finally, we note a symmetry related phenomenon: for spin-1 quasiparticles the behavior of the survival probability is identical for positive and negative refractive index regimes, as a result of symmetry in the expression of the transmission coefficient.

Chapter 5

PHASE LOCKING OF A PAIR OF FERROMAGETIC NANO-OSCILLATORS ON A TOPOLOGICAL INSULATOR

We investigate the magnetization dynamics of a pair of ferromagnetic insulators (FMIs) deposited on the surface of a topological insulator (TI). Due to the nonlinear nature of the underlying dynamics, the FMIs can exhibit oscillatory behaviors even under constant applied voltage. The motion of the surface electrons of the TI, which obeys relativistic quantum mechanics, provides a mechanism to couple the FMIs. In particular, the spin polarized current of the TI surface electrons can affect the magnetization of the two FMIs, which in turn modulates the electron transport, giving rise to a hybrid relativistic quantum/classical nonlinear dynamical system. We find robust phase and anti-phase locking between the magnetization dynamics. As driving the surface electrons of a TI only needs extremely low power, our finding suggests that nano FMIs coupled by a spin polarized current on the surface of TI have the potential to serve as the fundamental building blocks of unconventional, low-power computing paradigms.

5.1 Introduction

In this chapter, motivated by the growing interest in exploiting topological quantum materials for achieving novel charge transport and efficient electrical control of magnetization in spintronics applications, we investigate whether it is possible to realize phase locking of nanoscale magnetic oscillators coupled via some topological mechanism, e.g., through a topologically protected current. This has the potential to lead to highly efficient, low power nano-oscillators as the fundamental building

blocks of unconventional computing paradigms. To be concrete, we consider the prototypical setting of a pair of ferromagnetic insulators (FMIs) on the surface of a three-dimensional (3D) topological insulator (TI). A 3D TI possesses an insulating bulk but hosts chiral metallic channels on its surface, where electrons are described as massless Dirac fermions with spin-momentum locking [4, 5], resulting in large spin-charge conversion efficiency [264, 265, 266, 267]. The locking provides an effective mechanism to control the FMI magnetization [268, 269], and a large figure of merit for charge spin conversion has been experimentally realized [270, 271]. For a single FMI deposited on the top of a 3D TI, the exchange coupling between the magnetization and the surface state of TI can lead to nonlinear magnetization evolution but the spin-momentum locking of the surface current of the TI is preserved, and this can lead to phenomena such as anomalous magnetoresistance, unconventional transport behaviors [119, 120], and magnetization switching due to Hall current induced effective anisotropy field [123, 124, 125]. Quite recently, steady self oscillations in the FMI/TI heterostructure were uncovered [126, 127] and explained [128], and a number of nonlinear dynamical behaviors were studied [121, 122]. Here, we apply a DC voltage to the TI and place the two FMIs on the top of the TI in series. We first consider the case where the distance between the two FMIs is larger than the de Broglie wavelength so that direct quantum interference between the two FMIs can be neglected. As a result, the surface electronic states provide the only mechanism that couples the two FMIs. We calculate the average spin of the electron flow in each heterostructure interface by solving the quantum transmission. The effective spin field, when combined with the magnetic anisotropy of the FMIs, can lead to self oscillations of the magnetization vectors of the FMIs, *even when the external driving is DC*. The oscillations in turn can modulate the electron transmission periodically, effectively making the current time varying. The resulting AC current provides the

needed coupling between the two FMIs for phase locking. We then study the case where there is quantum interference between the two FMIs and find robust phase locking. The topologically coupled FMI system thus represents a class of highly efficient, low power nanoscale coupled oscillators, which can potentially serve as the fundamental building blocks for unconventional computing paradigms.

5.2 Model and Solution Method

Figure 5.1 shows schematically the system configuration of two FMIs deposited on the top of a TI [272, 273], which can be realized using material combinations such as Bi_2Se_3/YIG ($Y_3Fe_5O_{12}$) [274], Bi_2Te_3/GdN [275], Bi_2Se_3/EuS [117, 276], and Bi_2Se_3/$Cr_2Ge_2Te_4$ [277] (For more details about experimental realization, one can refer Appendix 5.4). The dynamical variable of each FMI is its macroscopic magnetization vector $\boldsymbol{M}$. For the TI, a topologically protected spin polarized current flows through the surface, where the spin is perpendicular to the current flow direction. The spin and magnetization are coupled via the proximity interaction. The magnetization can affect the spin distribution and hence the electron transport behavior. Simultaneously, the average spin will act as an effective magnetic field to influence the dynamics of the FMIs. Even with constant voltage driving, the magnetization vectors of the FMIs can exhibit oscillations. Intuitively, because the spin polarized current is common to both FMIs, it serves a kind of coupling between the two FMIs. Specifically, the magnetization of the first FMI can affect the current, which in turn alters the effective magnetic field acting on the second FMI, impacting its dynamics, and vice versa. As a result, phase locking is possible.

To develop a computational model, we assume that the magnetization precession period is much longer than the time it takes for electronic transport to transmit through the FMI/TI interface. For simplicity, first we ignore the quantum interference

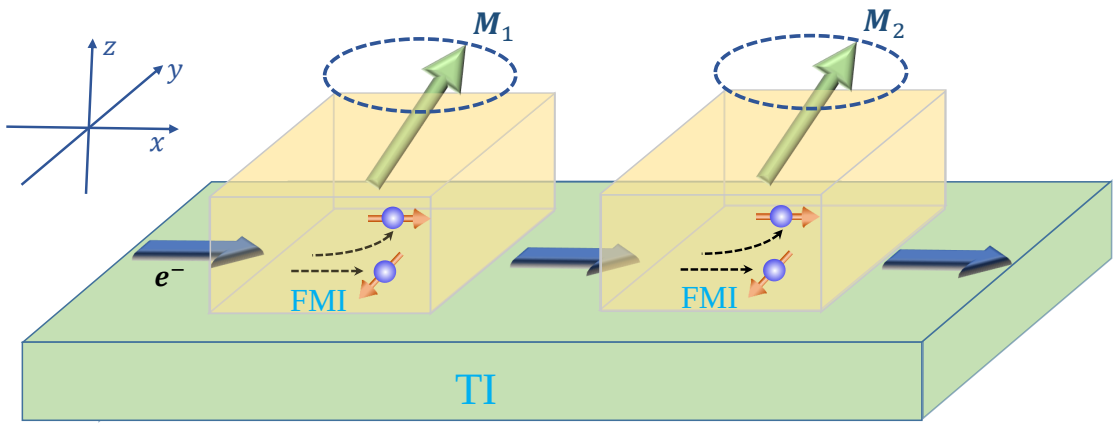

Figure 5.1: Schematic illustration of two FMIs on the top of a TI. The two yellow blocks represent the FMIs and the green block underneath is the TI. The green arrows in the yellow blocks are the magnetization vectors $\boldsymbol{M}$, the blue arrows on the surface of green blocks represent certain electron incident direction in magnetic free region. And the small red arrows with the electron (blue sphere) denote the spin direction, the black arrows indicate the electron motion direction.

effect or any other direct interaction between the two FMIs (later we will discuss the case with quantum interference in the second part of section III). We solve the time-independent Dirac equation for the electrons at the two interfaces separately, taking into account the proximity effect. In particular, the low-energy electronic behavior of the TI surface states is described by the effective Dirac Hamiltonian [126]

$$H = \hbar v_F(\boldsymbol{\sigma} \times \boldsymbol{k}) \cdot \hat{\boldsymbol{z}} - \xi \boldsymbol{M} \cdot \boldsymbol{\sigma} - U, \tag{5.1}$$

where $\boldsymbol{p} = \hbar \boldsymbol{k} = -i\hbar(\partial_x, \partial_y, 0)$ is the two-dimensional (2D) electron momentum operator, $\boldsymbol{\sigma} = (\sigma_x, \sigma_y, \sigma_z)$ are the Pauli matrices for electron spin, $\hat{\boldsymbol{z}} = (0, 0, 1)$ is the unit vector normal to the TI surface, and v_F is the electron Fermi velocity, as shown in Fig. 5.1. The second term in Eq. (5.1) represents the energy of exchange interaction between an electron and the proximate FMI, with ξ being the coupling coefficient. The last term is the external bias applied to the interface regions. Note that we treat

the two FMI/TI heterostructures separately in the case without quantum interference, i.e., we solve Eq. (5.1) by taking $\boldsymbol{M} = \boldsymbol{M}_1$ in the first heterostructure region and match the wavefunctions in the incidence, heterostructure, and transmitted area for the first one without any influence of the second heterostructure. And we treat the second heterostructure in the same way with no influence from the first one. The calculation of electron transmission through one FMI/TI heterostructure can be find in Appendix 5.6.2. For the case with quantum interference, we solve Eq. (1) for two FMIs on TI heterostructures as a whole (details refer the second part of section III and Appendix 5.6.3).

The energy eigenvalues of Eq. (5.1) are

$$E_{\pm} = \pm\sqrt{(v_F p_x + \xi M_y)^2 + (v_F p_y - \xi M_x)^2 + \xi^2 M_z^2} - U,$$

where the "$\pm$" signs correspond to the conduction (+) and valence (−) bands, and $\boldsymbol{p} = \hbar\boldsymbol{k}$ is the electron momentum. We see that the in-plane (x, y) magnetization components can lead to a displacement in the momentum space. Especially, the momentum displacement in the y direction can lead to a Hall current in that direction. Besides, the perpendicular component of the magnetization vector can open up a gap between the Dirac cones, contributing an additional Hall current in y. The first kind of Hall current plays the role of effective anisotropy, while the second kind is responsible for anti-damping. The two kinds of Hall current can lead to self oscillations of magnetization [126, 127, 128].

For each FMI, the conductance through one FMI/TI heterostructure can be calculated from the Landauer-Buttiker formalism [120, 126]:

$$G = \frac{Ee^2 L_w}{2\pi^2\hbar^2 v_F}\int_{-\frac{\pi}{2}}^{\frac{\pi}{2}} T_{\boldsymbol{M}}(E,\theta)\cos\theta d\theta. \tag{5.2}$$

where E is electron Fermi energy, $T_{\boldsymbol{M}}(E,\theta) = |t|^2$ is the transparency through one FMI/TI barrier, θ is the electron incident angle in the (x, y) plane, $-e$ is the electron

charge. For two coupled FMIs, their conductances G_1 and G_2 determine the voltage partition between them:

$$V_1 = \frac{G_2}{G_1 + G_2} V \quad \text{and} \quad V_2 = \frac{G_1}{G_1 + G_2} V. \tag{5.3}$$

The current density is given by

$$J_x = \frac{V_1 G_1}{L_w} = \frac{E e^2 V_1}{2\pi^2 \hbar^2 v_F} \int_{-\frac{\pi}{2}}^{\frac{\pi}{2}} T_{\boldsymbol{M}}(E, \theta) \cos\theta d\theta. \tag{5.4}$$

From the current definition $\hat{J} = -e\nabla_{\boldsymbol{p}} H = -e v_F(-\hat{\sigma}_y, \hat{\sigma}_x)$ [125, 126], we can get the mean spin polarization density for the first FMI as

$$\langle \sigma_y \rangle_1 = J_x / e v_F, \tag{5.5}$$

$$= \frac{E e V_1}{2\pi^2 \hbar^2 v_F^2} \int_{-\frac{\pi}{2}}^{\frac{\pi}{2}} T_{\boldsymbol{M}}(E, \theta) \cos\theta d\theta, \tag{5.6}$$

Utilizing the equality $T_{\boldsymbol{M}}(E, \theta) \cos\theta = -\psi^\dagger \sigma_y \psi$ (ψ is the electron wavefunction, more details about the spin density derivation, see Appendix 5.6.2), we can rewrite the above equation as

$$\begin{aligned} \langle \sigma_y \rangle_1 &= -\frac{E e V_1}{2\pi^2 \hbar^2 v_F^2} \int_{-\frac{\pi}{2}}^{\frac{\pi}{2}} \psi^\dagger \sigma_y \psi d\theta, \\ &= -\frac{E e V_1}{2\pi^2 \hbar^2 v_F^2 d} \int_0^d \int_{-\frac{\pi}{2}}^{\frac{\pi}{2}} \psi^\dagger \sigma_y \psi d\theta dx \end{aligned} \tag{5.7}$$

There are three spin components for each electron at specific position with certain incident angle, which is ($\psi^\dagger \sigma_x \psi$, $\psi^\dagger \sigma_y \psi$, $\psi^\dagger \sigma_z \psi$). So once we know the y component spin density, the other components can be obtained by replacing $\psi^\dagger \sigma_y \psi$ in Eq.(8) by $\psi^\dagger \sigma_x \psi$ and $\psi^\dagger \sigma_y \psi$ for the factor before the integral in Eq. (8) is related to electron density. So, we can get

$$\langle \sigma_x \rangle_1 = -\frac{E e V_1}{2\pi^2 \hbar^2 v_F^2 d} \int_0^d \int_{-\frac{\pi}{2}}^{\frac{\pi}{2}} \psi^\dagger \sigma_x \psi d\theta dx, \tag{5.8}$$

$$\langle \sigma_z \rangle_1 = -\frac{E e V_1}{2\pi^2 \hbar^2 v_F^2 d} \int_0^d \int_{-\frac{\pi}{2}}^{\frac{\pi}{2}} \psi^\dagger \sigma_z \psi d\theta dx. \tag{5.9}$$

Note that we can also first get the electron density and then get the spin density expression above. The detailed discussion can be find in Appendix 5.6.2. The mean spin density for the second FMI can be obtained in a similar way. The effective magnetic field is then given by

$$\boldsymbol{B}_{spin} = -\langle \frac{\partial H}{\partial \boldsymbol{M}} \rangle \frac{A_0}{V_0} = \frac{\xi}{a} \langle \boldsymbol{\sigma} \rangle, \tag{5.10}$$

where $\langle \boldsymbol{\sigma} \rangle$ is the mean spin density of the electron flow.

In addition to the effective magnetic field contribution from the electron spin, there is another term that stems from the magnetic anisotropy of the material. We assume that the magnetic layer has the z hard axis and the x easy axis; this corresponds to anisotropy parameters $K_z > K_y > K_x = 0$ and the density of magnetic free energy [126]

$$\begin{aligned} F(\boldsymbol{M}) &= F_{an} + F_{spin} \\ &= K_x n_x^2 + K_y n_y^2 + K_z n_z^2 - \boldsymbol{M} \cdot \boldsymbol{B}_{spin}(\boldsymbol{M}), \end{aligned} \tag{5.11}$$

where $\boldsymbol{n} = (n_x, n_y, n_z) = \boldsymbol{M}/|\boldsymbol{M}|$. The effective magnetic field by material anisotropy can be obtained via $\boldsymbol{B}_{an} = -\partial F_{an}/\partial \boldsymbol{M}$.

The LLG equation for magnetization dynamics of the two coupled FMIs can be written as

$$\frac{d\boldsymbol{n}_1}{dt} = -\gamma \boldsymbol{n}_1 \times \boldsymbol{B}_{eff}^{(1)}(\boldsymbol{n}_1, \boldsymbol{n}_2) + \alpha \boldsymbol{n}_1 \times \frac{d\boldsymbol{n}_1}{dt}, \tag{5.12}$$

$$\frac{d\boldsymbol{n}_2}{dt} = -\gamma \boldsymbol{n}_2 \times \boldsymbol{B}_{eff}^{(2)}(\boldsymbol{n}_1, \boldsymbol{n}_2) + \alpha \boldsymbol{n}_2 \times \frac{d\boldsymbol{n}_2}{dt}, \tag{5.13}$$

where the normalized vectors of magnetization are defined as $\boldsymbol{n}_1 = \boldsymbol{M}_1/|\boldsymbol{M}_1|$, $\boldsymbol{n}_2 = \boldsymbol{M}_2/|\boldsymbol{M}_2|$ ($|\boldsymbol{M}_1| = |\boldsymbol{M}_2|$ in this paper), γ is the gyromagnetic ratio, and α is the Gilbert damping constant. $\boldsymbol{B}_{eff}^{(1)}$ and $\boldsymbol{B}_{eff}^{(2)}$ are the effective magnetic field for the first and second FMI respectively with $\boldsymbol{B}_{eff}^{(1)} = \boldsymbol{B}_{spin}^{(1)} + \boldsymbol{B}_{an}^{(1)}$, and $\boldsymbol{B}_{eff}^{(2)} = \boldsymbol{B}_{spin}^{(2)} + \boldsymbol{B}_{an}^{(2)}$.

The anisotropy induced effective magnetic field $\boldsymbol{B}_{an}^{(1)}$ and $\boldsymbol{B}_{an}^{(2)}$ are different for these two FMIs, which will lead to different oscillation frequencies for the two FMIs when applying the same voltage on them separately. The spin induced effective magnetic field of the first heterostructure is $\boldsymbol{B}_{spin}^{(1)} = \frac{\xi}{a}\langle\boldsymbol{\sigma}\rangle_1 \sim V_1$, and V_1 is determined by the conductance of both heterostructures via voltage partition with the same longitudinal current along x direction. And the conductance of the two heterostructures is of course related to the magnetization $\boldsymbol{M}_1$ and $\boldsymbol{M}_2$. Similarly, the spin induced effective magnetic field in the second heterostructure is $\boldsymbol{B}_{spin}^{(2)} \sim V_2$, which is also related to $\boldsymbol{M}_1$ and $\boldsymbol{M}_2$ in the same way as the first one. Thus, the magnetization of the two FMIs are coupled together via the same current going through them. The iterative calculation procedure is as following: Utilizing magnetization $\boldsymbol{M}_1$ and $\boldsymbol{M}_2$ of the two FMIs, we solve the Hamiltonian Eq. (5.1) separately to get the corresponding electron wavefunctions in these two heterostructures. Based on wavefunctions, we can calculate the electron conductance (Eq. (5.2)) and average spin. Because the common x direction current goes through these two heterostructures, we need to do the voltage partition (Eq. (5.3)). This common current coupled the two FMIs together. Then we can get the spin density (Eq. (5.7)-(5.9)) and thus the effective magnetic field by spin which can affect the magnetization dynamics. A schematic illustration of this procedure is illustrated in Appendix 5.6.1.

Our simulation parameters are the following. Each magnet is assumed to have the dimension of d (length)$\times L_w$ (width) $\times a$ (thickness) $= 40 \times 90 \times 2.2$ nm^3, with hard-axis anisotropy coefficients $K_y = 2.0 \times 10^5$ erg/cm^3 and $K_z = 2.5 \times 10^5$ erg/cm^3 along the y and z axis, respectively. The initial magnetization is $M_0 = 1200$ Oe. The Gilbert damping factor is $\alpha = 0.01$. For the TI layer, the Fermi velocity of the electron is $v_F = 4.6 \times 10^7$ cm/s. The exchange energy term is $\xi M_0 = 40$ meV.

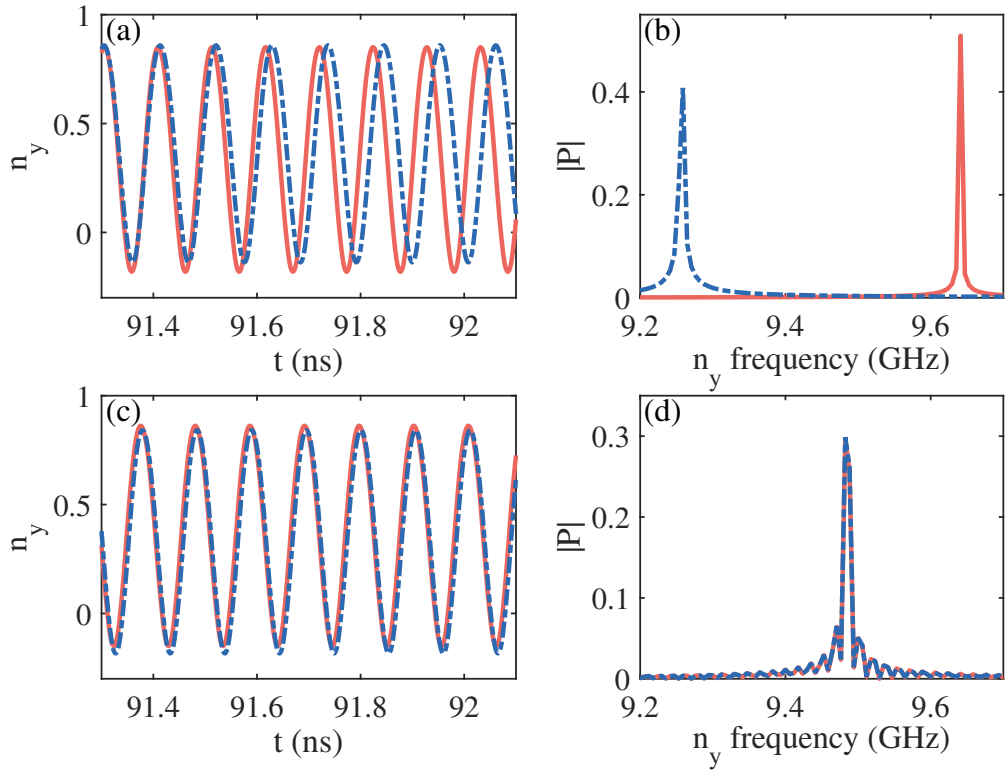

Figure 5.2: Phase locking between the magnetization vectors of two FMIs. (a) Time evolution of y components of the magnetization vectors of the two isolated FMIs under the same applied voltage of 40 mV. The electron energy is 100 meV. The red solid and blue dashed lines denote the y component of the magnetization of the first and second FMI, respectively. (b) Fourier spectra of the time series in (a). (c,d) The corresponding results under coupling through the surface current of the TI under applied voltage of 80 mV. There is phase locking.

5.3 Results

Phase Locking in the Absence of Quantum Interference

To uncover phase locking for a pair of coupled FMIs in a general setting, we assume that the FMIs have different values of anisotropy: one with the values listed above, the other having an additional anisotropy in the x direction with the value of the anisotropy coefficient being $K_x = 0.0955 \times 10^5$ erg/cm^3. Nonidentical values of the anisotropy lead to different oscillation frequencies for the two FMIs under the same applied voltage. We first consider the case of isolated FMIs by applying the same

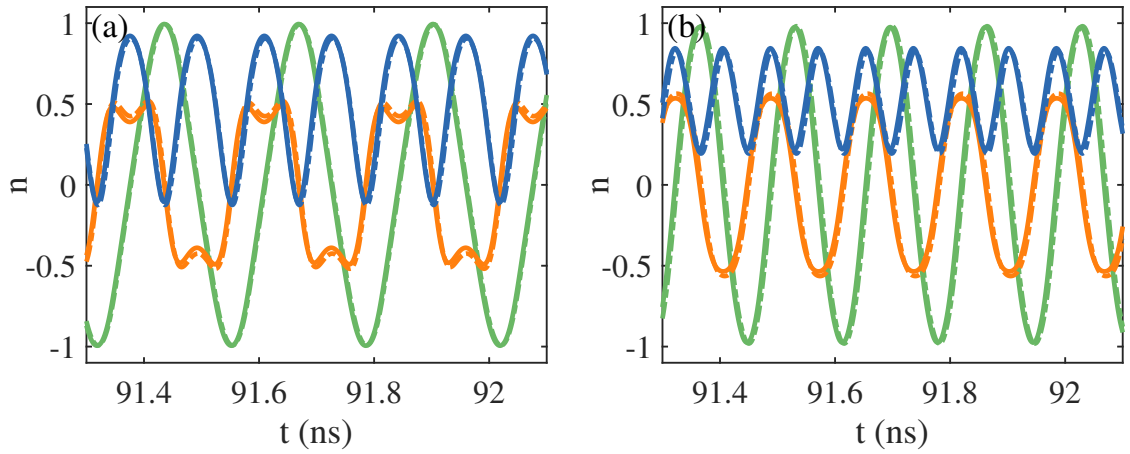

Figure 5.3: Robustness of phase locking for different parameter settings. (a) For $K_y = 1.5\times10^4$ erg/cm^3 (the anisotropy coefficient in y), phase locking between the two FMIs. Note that the value of K_y in Fig. 5.2 is $K_y = 2 \times 10^4$ erg/cm^3. The red, blue and green curves denote the n_x, n_y and n_z components, respectively. The solid and dashed curves are for the first and second FMIs, respectively. The applied voltage is 100 mV and the electron energy is 100 meV. (b) Phase locking behavior when the damping factor is increased to 0.02 (from the value of 0.01 in Fig. 5.2). The applied voltage is 140 mV and the electron energy is 100 meV.

DC voltage on the two FMIs separately. Figure 5.2(a) shows that the magnetization vectors of the isolated FMIs exhibit oscillations at difference frequencies, where the solid red and dotted blue lines correspond to the first and second FMI, respectively. Note that the two magnetization components deviate within 1 ns (containing several oscillation periods), signifying a difference in their frequencies due to the difference in the anisotropy. The frequency difference can also be seen from the Fourier spectra, as shown in Fig. 5.2(b). For the second FMI with an additional value of anisotropy along the x axis, the frequency is lower than that of the first one. We next introduce coupling by placing the two FMIs in series on a TI and letting the current go through the two FMIs, as illustrated in Fig. 5.1. The separation between the two FMIs is sufficiently large so that any direct quantum interference between the two FMIs can be neglected. We apply the voltage of 80 mV. The magnetization oscillations will make the current oscillate in time through the proximity effect, i.e., modulation of the transmission

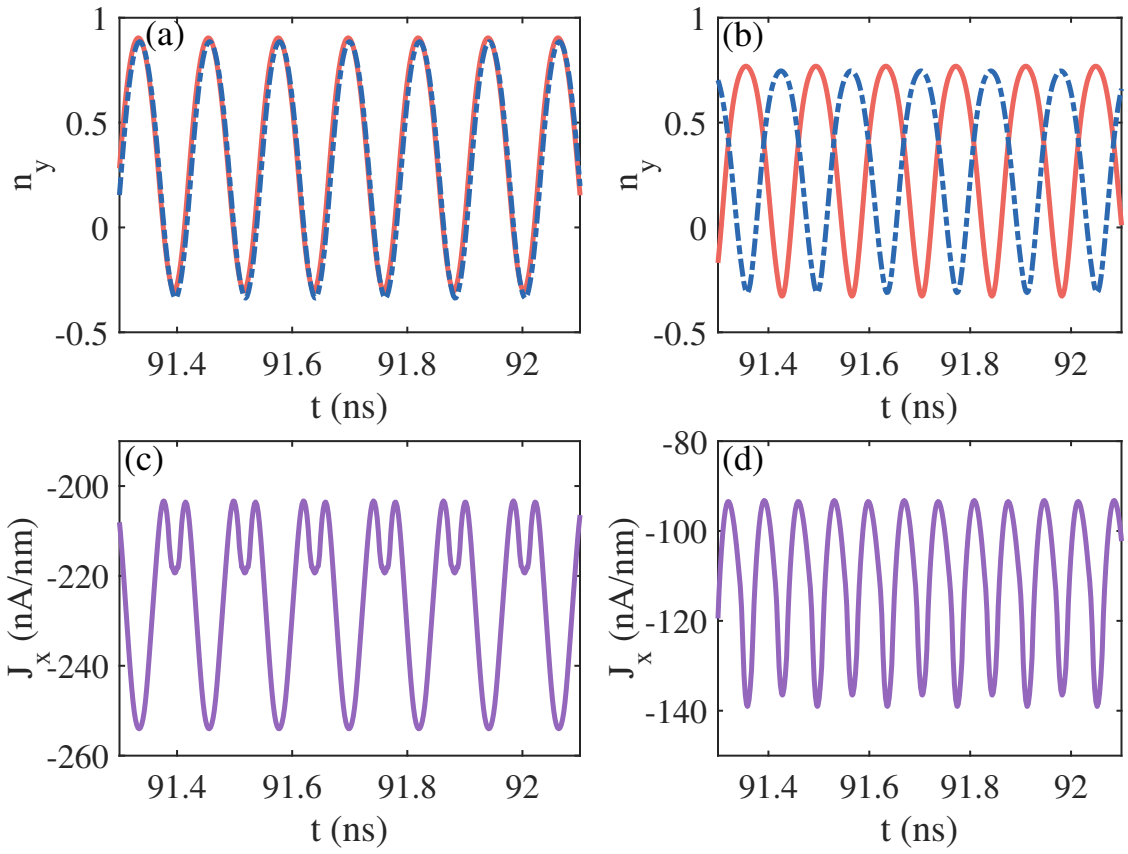

Figure 5.4: Phase and anti-phase locking between a pair of coupled FMIs. (a) Phase locking between the y components of the magnetization vectors for $V_0 = 110$ mV and $E = 60$ meV. (b) Anti-phase locking for $V_0 = 190$ mV and $E = 30$ meV. (c,d) The corresponding evolutions of the surface current of the TI for cases (a,b), respectively. Other parameters are the same as those in Fig. 5.2(c).

of electrons. The current induces interaction between the two FMIs by an effective magnetic field due to electron spin, leading to phase locking, as shown in Fig. 5.2(c), where the y components of the magnetization vectors of the two FMIs evolve with time at the same pace. Phase locking can be further demonstrated by the Fourier spectra, as shown in Fig. 5.2(d), where the two oscillatory time series have essentially the same peak frequency. We have examined a large number of combinations of the parameters such as the amount of anisotropy and damping factor and found robust phase locking in all cases, as exemplified in Fig. 5.3.

We also find persistent phase locking in wide ranges of the applied voltage and

electron Fermi energy. For example, Figs. 5.4(a,b) demonstrate phase locking for two cases where the applied voltage and electron energy are (110 mV, 60 meV) and (190 mV, 30 meV), respectively, with other parameters being the same as those in Fig. 5.2(c). Note that in Fig. 5.4(a), the magnetization vectors of the two FMIs are in phase, while there is anti-phase locking between them in Fig. 5.4(b). The corresponding surface current oscillations in the TI are shown in Figs. 5.4(c,d). In each case, the primary frequency of the current oscillations is the same as that of the magnetization oscillations. To our knowledge, the demonstrated phase and anti-phase locking behavior enabled by the proximity induced torques in the FMI/TI systems has not been reported before.

To examine more closely the different phase and anti-phase locking behaviors in Fig. 5.4, we plot the 3D trajectories of the magnetization unit vector. Figures 5.5(a,b) correspond to the cases in Fig. 5.4(a,b), respectively. The red and blue trajectories are for the two FMIs, and the red and blue dots denote the position of the magnetization vector at a certain time. For case (a), the trajectories almost coincide with each other and the magnetization vectors (red and blue dots) are at the same location for any time, and the frequency of the y component is twice those of the n_x and n_z components, as illustrated in insets (c,d). For case (b), the trajectories are close to each other but the magnetization vectors are dominated by the z component and have opposite phases at the time instants t_0 and t_1. In this case, the frequencies of the three components are the same. We also plot the trajectory of one FMI in the spherical coordinate, as shown in Fig. 5.6, where the components of the magnetization vector are $n_x = \cos\theta\cos\phi$, $n_y = \cos\theta\sin\phi$, and $n_z = \sin\theta$. The spherical coordinate trajectory in Fig. 5.6(a) corresponds to the case in Fig. 5.5(a), where the magnetization vector circulates about the minimum energy point. In Fig. 5.6(b), the trajectory is along the edge.

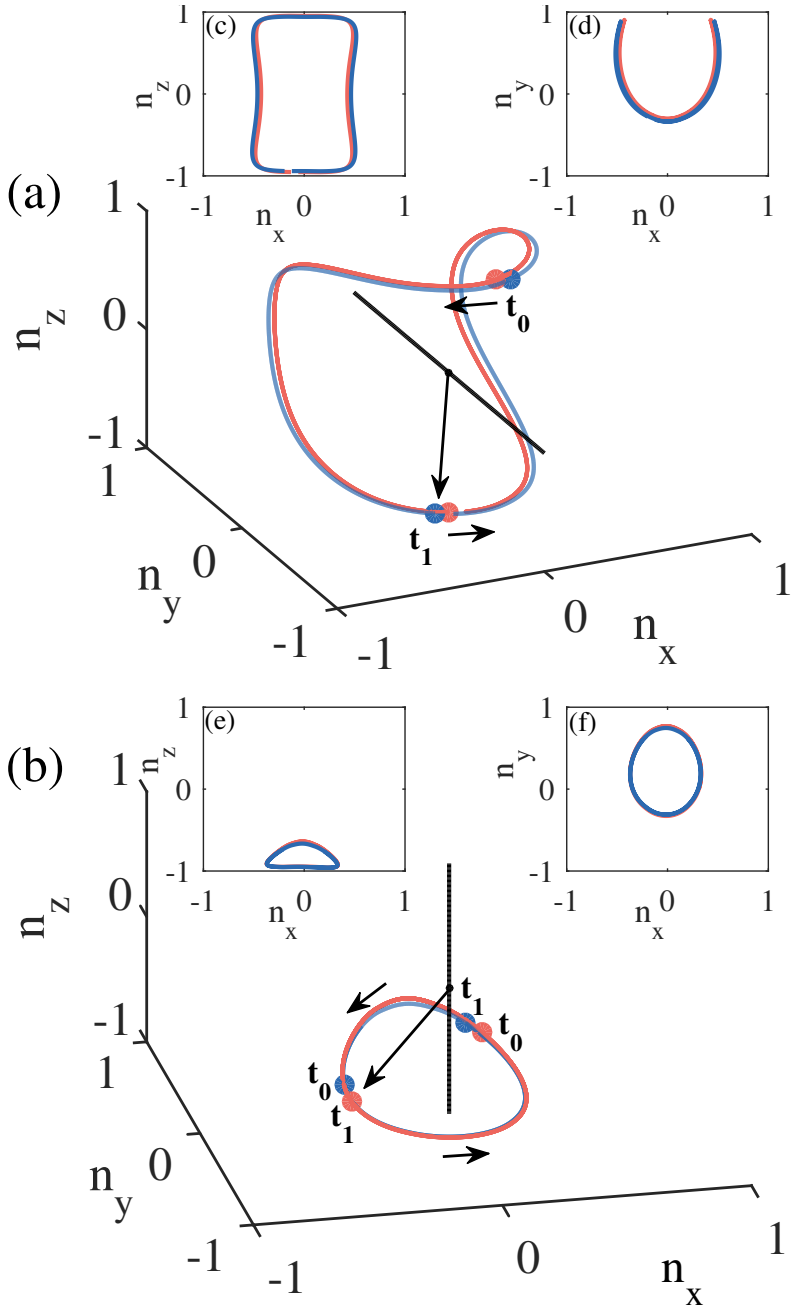

Figure 5.5: Trajectories of the magnetization unit vectors. (a) Trajectories (red and blue for the two FMIs, respectively) in the 3D magnetization space corresponding to Fig. 5.4(a). The black arrow denotes the trajectory evolution direction. The insets (c,d) correspond to the projections of the trajectory on the $n_x - n_z$ and $n_x - n_y$ planes, respectively. (b) Trajectories corresponding to Fig. 5.4(b).

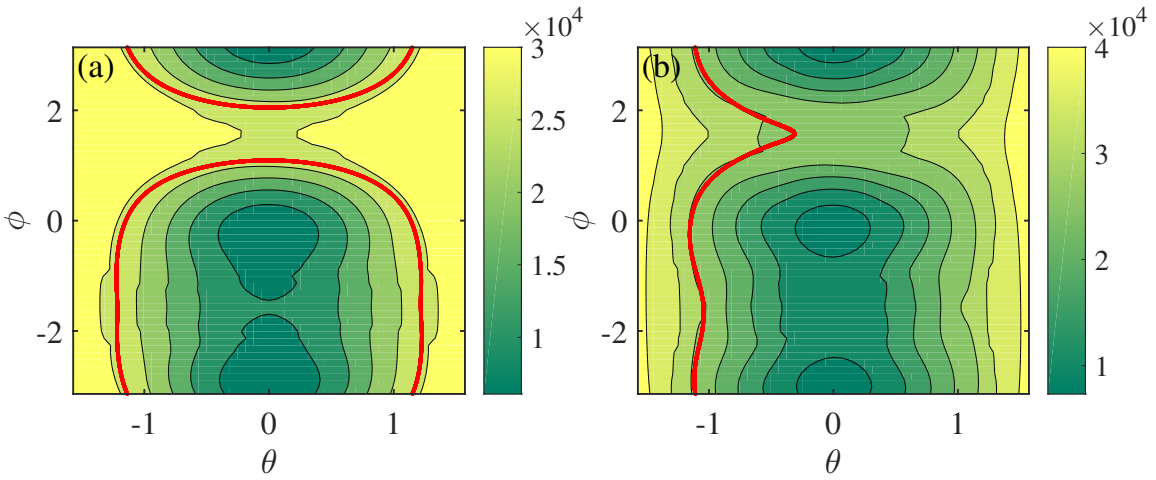

Figure 5.6: Magnetization trajectories in the spherical coordinate with respect to energy distribution. The red curve is the trajectory of the magnetization vector. Darker background color indicates lower energy value. The applied voltage is 55 meV for (a) and 95 meV for (b), whereas the electron energy is 60 meV for (a) and 30 meV for (b).

The difference in the trajectories is closely related to the relative value of the electron and exchange coupling energies. As illustrated in Fig. 5.7, when the magnetization vector is along the z direction, the exchange coupling energy is 40 meV, opening up a gap in the energy band. For the case where the electron energy is above the bottom of the upper band (e.g., for energy value of about 60 meV), the in-plane electron spin component is large, especially along the y axis. The value of the out-of-plane spin component is limited by the small exchange coupling energy in comparison with the electron energy. This has been confirmed by the effective magnetic field value from the average spin, as shown in Fig. 5.8(a). It can be seen that the absolute value of the effective magnetic field is stable and large along the y axis, whereas the z component exhibits large oscillations. The effective magnetic field by anisotropy makes the magnetization vector circulate about the y axis. When the electron energy is decreased to, say, 30 meV (an energy value inside the gap), the electron will experience a strong barrier if the z component of the magnetization vector is non-zero, leading to a large out-of-plane spin component that in turn

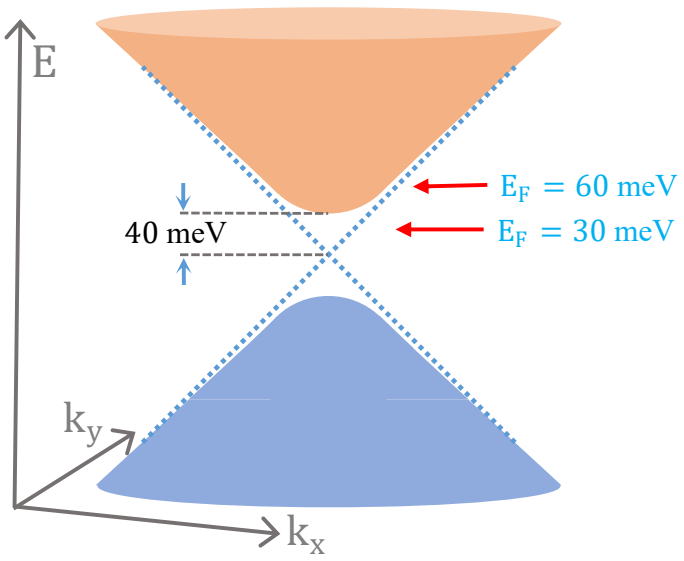

Figure 5.7: Electron energy band structure for the case where the magnetization vector is in the z direction.

acts as an effective magnetic field in the z direction. As a result, the total effective magnetic field is large in the z direction, causing the magnetization vector to precess dominantly about the z axis. This picture is confirmed by the effective magnetic field value experienced by the electron, as shown in Fig. 5.8(b), where the z component of the field is quite large.

When there is coupling between the two oscillators by the electron current in the TI, the magnetization vector will be mostly in-plane. In this case, the anti-damping torque will assume relatively small values if there is anti-phase locking between the two magnetization vectors. As a result, in-phase locking will induce large fluctuations in both y and z components, as can be seen from Fig. 5.8(a), where the lower values of the y component correspond to a large absolute value in the z direction. On the contrary, if the out-of-plane spin component dominates, an anti-damping torque will arise, thereby reducing the total current fluctuations.

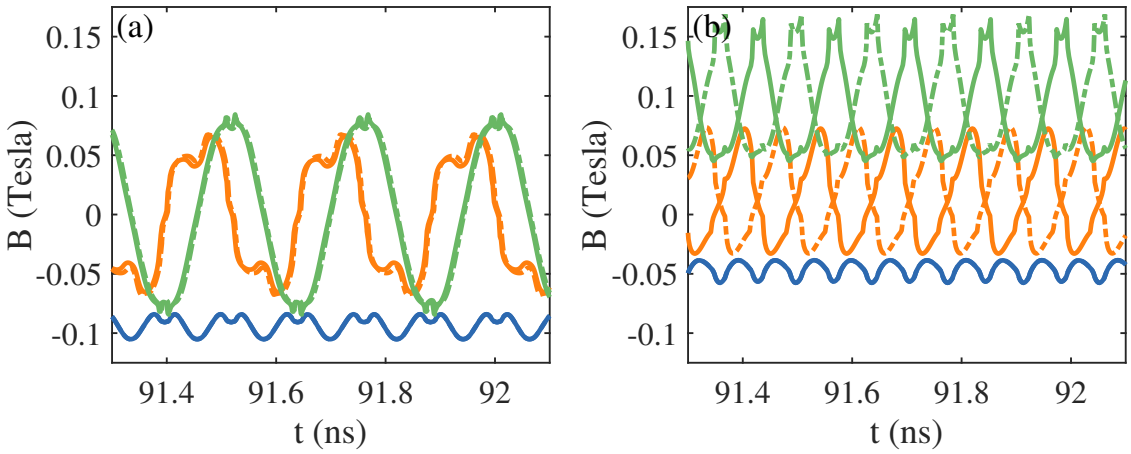

Figure 5.8: Effective magnetic field by spin. The red, blue and green curves denote the effective magnetic field in the x, y and z directions, respectively. The solid and dashed lines are for the two FMIs. The two cases are: (a) $E = 60$ meV (above the bottom of the upper band, the upper horizontal red arrow in Fig. 5.7) and (b) $E = 30$ meV (in the gap, the lower horizontal red arrow in Fig. 5.7).

Effect of Quantum Interference on Phase Locking

Having uncovered the phenomena of phase and anti-phase locking in a pair of FMIs coupled by the spin polarized surface current of the TI, we address the issue of quantum interference and investigate its effect on the phase locking dynamics. To take into account quantum interference, we treat the two FMIs as a single tunneling system and calculate the probability of quantum tunneling through the whole system.

Consider a surface electron in the TI moving toward the interface region. As shown in Fig. 5.9, there are five subregions of interest: (I) the "free" region to the left of the interface between the first FMI and TI, (II), the interface region itself, (III) the region between the two interfaces, (IV) the second interface region, and (V) the "free" region to the right of the region IV. Let θ be the incident angle of the electron from region I to region II. The spinor wavefunctions in the five regions are shown in Appendix 5.6.3. Matching the wavefunctions at the boundaries, we can get all the coefficients and hence the wavefunction in the whole 2D space. The average

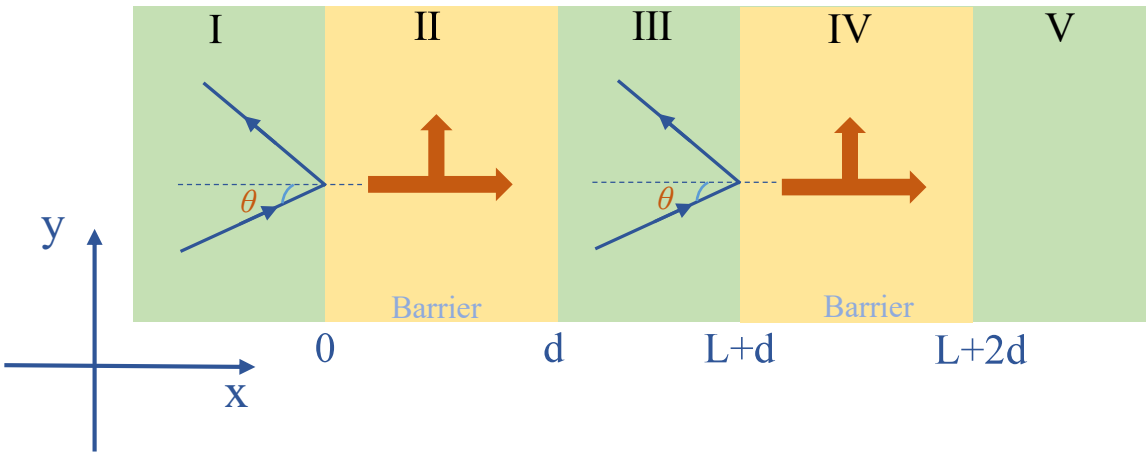

Figure 5.9: A schematic illustration of distinct quantum transport regions for calculating the effective coupling field. The distance between the two FMIs is $L = d = 40$ nm.

spin polarization in each subregion and the corresponding effective magnetic field can then be calculated, as in Eqs. (5.4)-(5.13).

Figure 5.10 shows the representative magnetization dynamics of the two FMIs when quantum interference is taken into account, for $V_0 = 50$ mV and $E = 100$ meV. The three components of the magnetization vector are represented by different colors, and the solid and dashed lines are for the first and second FMI, respectively. The magnetization vectors exhibit oscillations and there is phase locking. We vary the external voltage and the electron energy in quite large ranges, and also change the anisotropy value. In all cases, persistent phase locking is observed.

5.4 Indication on Experimental Realization of Phase Locking

One commonly used TI/FMI heterostructure is Bi_2Se_3/YIG (yttrium iron garnet) heterostructure [274, 278, 279] which has been used for investigating the effect of exchange interaction between FMI and TI surface states on the magnetization dynamics of YIG recently [279]. Among the different types of anisotropies in YIG thin film, the shape anisotropy dominates. And the hard axis (perpendicular to the film plane

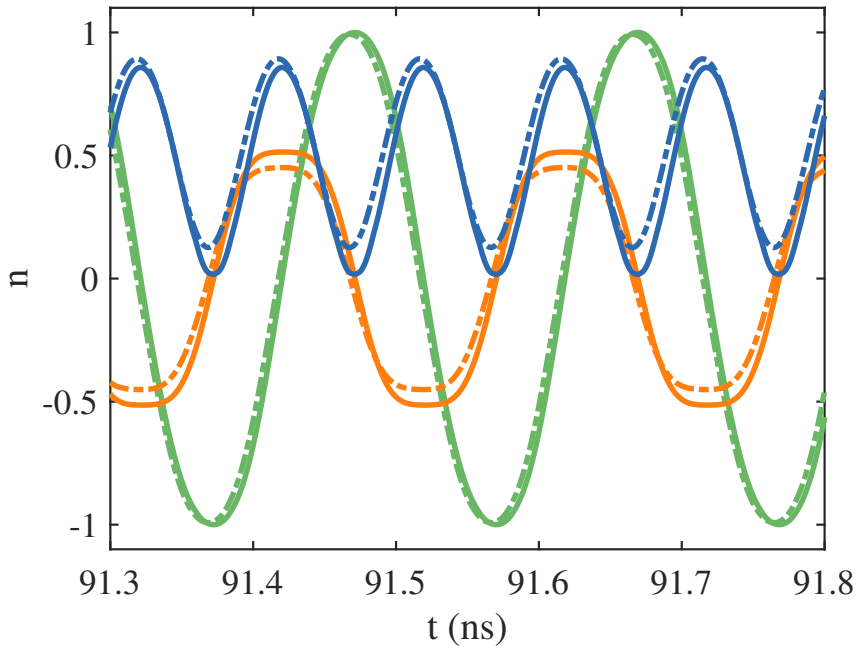

Figure 5.10: Phase locking between the two coupled FMIs in the presence of quantum interference. The applied voltage is 50 mV and the electron energy is 100 meV. The red, blue and green curves denote n_x, n_y and n_z, respectively. The solid and dashed lines are for the FMI in region II and IV, respectively.

denoted as z direction here) anisotropy coefficient for YIG is in the order of $K_z \sim 10^5$ erg/cm^3 corresponding to the thickness d of the film ranging from several nm to tens of nm [279, 278]. The magnetocrystalline anisotropy coefficient is smaller than that of shape anisotropy, which is about $K \sim 2.5 \times 10^4$ erg/cm^3 and can produce hard axis in plane favoring magnetization along the $\langle 111 \rangle$ axis [278]. And the magnetization value is usually in the order of 1000 Oe [279, 278]. Another popular heterostructure Bi_2Se_3/EuS [117, 280, 118, 281] is also widely investigated and the recent progress about the magnetoresistance and even current-induced magnetization switching is reported [281]. The hard axis anisotropy is in the range of $10^4 - 10^5$ erg/cm^3 for EuS [280, 118]. And the magnetization is also in the order of 1000 Oe [118]. The anisotropy value of these two materials are comparable to the value we take in the model ($K_z = 2.5 \times 10^5$ erg/cm^3) and have the potential to realize auto-oscillation and

then phase locking based on the recent experimental progress.

Although we use specific anisotropy values to illustrate the phase locking phenomena in our paper, we can show that there is tunability of the anisotropy values in certain range to fit the real materials. First, if we fix the value of anisotropy in z direction, we can also achieve phase locking by changing y direction anisotropy and applied voltage in a wide range. As an example, we take the z direction anisotropy coefficient to be $K_z = 2.5\times10^5$ erg/cm^3, then we change the y direction anisotropy coefficient K_y and the voltage. We can see phase locking can be achieved in a wide range of K_y value and voltage range. We plot the phase diagram of phase locking in Fig. 5.11 based on numerical calculation with K_y and V as variables and $K_z = 2.5 \times 10^5$ erg/cm^3, electron Fermi energy $E = 100$ meV. The yellow area Fig. 5.11 roughly shows the parameter range for phase locking.

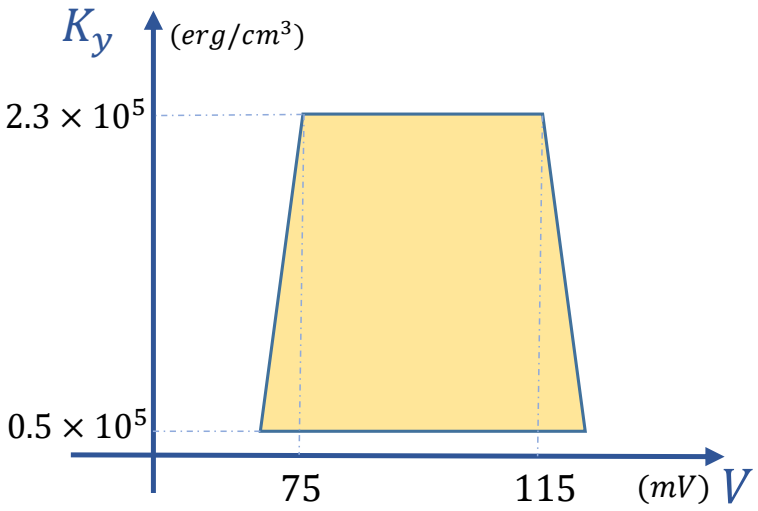

Figure 5.11: The parameter range for phase locking. Fixing the K_z value, we can get a wide range of voltage and K_y values for phase locking.

Furthermore, we can show the K_z value can also be tunned based on the analysis of LLG equation. We can get an equivalent equation to LLG equation called Landau-

Lifshitz (LL) equation by using the cross product of $\boldsymbol{n}$ on the left side

$$\boldsymbol{n} \times \frac{d\boldsymbol{n}}{dt} = -\gamma \boldsymbol{n} \times (\boldsymbol{n} \times \boldsymbol{B}_{eff}) - \alpha \frac{d\boldsymbol{n}}{dt}, \tag{5.14}$$

and take it into the LLG equation, we get the equivalent form

$$\frac{d\boldsymbol{n}}{dt} = -\frac{\gamma}{1+\alpha^2} \boldsymbol{n} \times \boldsymbol{B}_{eff} - \frac{\gamma\alpha}{1+\alpha^2} \boldsymbol{n} \times (\boldsymbol{n} \times \boldsymbol{B}_{eff}). \tag{5.15}$$

where we can see increasing the effective magnetic field is equivalent to decreasing the time period of magnetization oscillations. Specificly, we know that $\boldsymbol{B}_{eff} = \boldsymbol{B}_{spin} + \boldsymbol{B}_{an}$, with the spin induced effective magnetic field proportional to the applied voltage, i.e., $\boldsymbol{B}_{spin} \sim V$ and the anisotropic magnetic field proportional to the anisotropy coefficient, i.e., $\boldsymbol{B}_{an} \sim K$. Thus if we change the material anisotropy say by several times, then we just need to change the voltage the same times to ensure the value of $\boldsymbol{B}_{eff}$ also changes the same times. This will not affect the phase locking and only the magnetization dynamics period or time scale can be affected. Thus, in theory, we can have a large range of tunability of the anisotropy.

In addition to the range of anisotropy, we need to restrict the anisotropy difference of two nanocontact to be less than 10% of K_z value. If the anisotroopy difference of these two nanocontacts is too large, synchronization cannot be realized.

5.5 Conclusion

To summarize, motivated by the need for nanoscale oscillators for developing potential unconventional computing paradigms, we have studied the oscillatory dynamics and phase locking of a pair of FMI oscillators coupled through the spin-polarized current on the surface of an TI. The dynamics of the whole system are of the hybrid type [122]: a combination of classical nonlinear and relativistic quantum dynamics, with the following underlying physics. For each heterostructure interface between the

FMI and TI, there is an average spin of the electron flow, which can be solved via the transmission through the interface. The average spin acts as an effective field which, when combining with the magnetic anisotropy of the FMI, leads to self oscillations of the magnetization of each individual, uncoupled FMI. The self oscillations in turn modulate the electron transmission periodically, making the surface current of the TI time varying. The AC current generates the coupling of the two FMIs. As a result, stable phase or anti-phase locking between the two FMIs emerges, regardless of whether quantum interference is absent or present. The locking phenomenon is robust as it occurs in wide ranges of the external applied voltage and electron energy. To our knowledge, this is the first demonstration of phase locking due to proximity effect induced torques in FMI/TI systems, justifying further investigation of these systems in terms of their possible role in serving as the fundamental building block of unconventional computing paradigms.

In an experimental setup, if the two FMIs are far from each other (e.g., $>$ 100 nm), scattering from impurities will destroy the coherence between the states of the two FMIs. In this case, our non-coherent approach is applicable. If the two FMIs are close to each other (e.g., within 100 nm), coherence cannot be ignored, rendering necessary our quantum coherence based treatment. Another very important direct interaction between two FMIs that can affect the phase locking is the dipole-dipole interaction [107] for which the energy can be written in the following form

$$H_{dip} = -\frac{\mu_0}{4\pi|\boldsymbol{r}|^3}[3(\boldsymbol{m}_1 \cdot \hat{\boldsymbol{r}})(\boldsymbol{m}_2 \cdot \hat{\boldsymbol{r}}) - \boldsymbol{m}_1 \cdot \boldsymbol{m}_2], \tag{5.16}$$

where μ_0 is vacuum permeability, $\boldsymbol{r}$ is the distance between two effective point dipoles, $\hat{\boldsymbol{r}}$ is a unit vector parallel to the line joining the centers of the two dipoles, and $\boldsymbol{m}_{1,2} = \boldsymbol{M}_{1,2} \cdot V$, V is the volume of the FMI stripe. And for one FMI, the effective magnetic field it feels from another is in this form $\boldsymbol{B}_{1,2} = -\frac{\partial H}{\partial \boldsymbol{M}_{1,2}}$. Using the parameters in this

paper, and set the two magnetization in the same direction (minimum energy) we can roughly get the energy density $H/V \approx 2\times10^4$ erg/cm^3 if we take the distance $|\boldsymbol{r}| = 20$ nm. This is about one order of magnitude smaller than the z direction anisotropy coefficient, which is $K_z = 2.5 \times 10^5$ erg/cm^3. So, if we keep the edge distance of these two FMIs larger than 20 nm, the dipole-dipole interaction can be ignored. If the two FMIs are too near to each other with dipole-dipole energy comparable to the system energy, we should take the dipole-dipole interaction into account. The effect of inclusion of dipole-dipole interaction into our current system on phase locking is an interesting topic deserved for further investigation.

5.6 Supplementary Notes

5.6.1 Iterative Calculation Procedure for Coupled Magnetization Dynamics

In Fig. 5.12 we give a schematic procedure for calculating the magnetization dynamics without quantum interference (Fig. 5.12 (a)) and with quantum interference (Fig. 5.12 (b)). The definition of all the corresponding quantities can be find in section 7.2 of the paper.

5.6.2 Electron Spin Density Calculation in One FMI/TI Heterostructure

For one FMI/TI heterostructure (area I, II, III of Fig. 5.9), we can write the wavefunctions in the incident area, heterostructure interface and the transmitted area as following [125],

$$\begin{aligned}\psi_1(x \le 0) =& \frac{1}{\sqrt{2}} \begin{pmatrix} ie^{-i\theta} \\ 1 \end{pmatrix} e^{ik_F x \cos\theta} \\ &+ \frac{r}{\sqrt{2}} \begin{pmatrix} -ie^{i\theta} \\ 1 \end{pmatrix} e^{-ik_F x \cos\theta}\end{aligned} \tag{5.17}$$

$$\psi_2(0<x<d) = A\cdot\begin{pmatrix}\hbar v_F(\tilde{k}_y+i\tilde{k}_x)\\ E+U-\xi M_z\end{pmatrix}e^{i(\tilde{k}_x+\xi M_y/\hbar v_F)x} + B\cdot\begin{pmatrix}\hbar v_F(\tilde{k}_y-i\tilde{k}_x)\\ E+U-\xi M_z\end{pmatrix}e^{i(-\tilde{k}_x+\xi M_y/\hbar v_F)x} \tag{5.18}$$

$$\psi_3(x\geq d) = \frac{t}{\sqrt{2}}\begin{pmatrix}ie^{-i\theta}\\ 1\end{pmatrix}e^{ik_F x\cos\theta} \tag{5.19}$$

where r and t are the reflection and transmission coefficients, $E+U=\hbar v_F k_F$, $k_x=k_F\cos\theta$, $k_y=k_F\sin\theta$, $\hbar v_F\tilde{k}_x=\sqrt{(E+U)^2-(\xi M_z)^2-(\hbar v_F\tilde{k}_y)^2}$, and $\hbar v_F\tilde{k}_y=\hbar v_F k_y-\xi M_x$. Besides, for simplicity, we have denoted $A=\frac{a}{\sqrt{2(E+U)(E+U-\xi M_z)}}$, $B=\frac{b}{\sqrt{2(E+U)(E+U-\xi M_z)}}$ with a, b the corresponding coefficients. Matching the wavefunctions on the boundary between different parts, we can get the corresponding coefficients, r, a, b, and t. Note that we ignore the spatial factor $1/\sqrt{LW}$ in the wavefunction above with L, W the size parameter of the 2D device. For one electron, the spin y component in the transmitted region III can be obtained via the wavefunction (Eq. (5.19)) average

$$\psi_3^\dagger\sigma_y\psi_3 = -|t|^2\cos\theta, \tag{5.20}$$

We define the transmission probability $T(E,\theta)=|t|^2$, thus we have $T\cos\theta=-\psi_3^\dagger\sigma_y\psi_3$, by which we have established the relation between electron transmission in x direction and the spin y component value in the transmitted region (free region). Next, we will prove that this relation (spin-momentum locking) is also valid in the FMI/TI heterostructure region, i.e., $\psi_2^\dagger\sigma_y\psi_2=\psi_3^\dagger\sigma_y\psi_3$ independent of position x. To verify this, we write the spin value in terms of the wavefunction (Eq. (5.18)) in the

heterostructure region at position x as following

$$\begin{aligned}\psi_2^\dagger\sigma_y\psi_2 = -2\beta\cdot\Big[&|A|^2\Im(\alpha_1)\exp(-2\Im(\tilde{k}_x)x)\\&+|B|^2\Im(\alpha_2)\exp(2\Im(\tilde{k}_x)x)\Big]\\&+2\beta\cdot\Re\Big[iA^*B\cdot(\alpha_2-\alpha_1^*)\exp(-2i\Re(\tilde{k}_x)x)\Big]\end{aligned}\tag{5.21}$$

where we denote $\alpha_1 = \hbar v_F(\tilde{k}_y + i\tilde{k}_x)$, $\alpha_2 = \hbar v_F(\tilde{k}_y - i\tilde{k}_x)$ and $\beta = E + U - \xi M_z$, $\Re(\cdot)$ and $\Im(\cdot)$ represent the real part and imaginary part of a certain number respectively. Now, we can further simplify the expression of Eq. (5.21). From the formulas above, we know $\tilde{k}_y$ is real and $\tilde{k}_x$ can be real or pure imagniary depending on M_z and k_y ($\hbar v_F\tilde{k}_x = \sqrt{(E+U)^2 - (\xi M_z)^2 - (\hbar v_F\tilde{k}_y)^2}$). To evaluate the value of $\psi_2^\dagger\sigma_y\psi_2$, we first assume $\tilde{k}_x$ is real. Then we can get the second part on the right hand side of Eq. (5.21) is 0, and $\exp(-2\Im(\tilde{k}_x)x) = \exp(2\Im(\tilde{k}_x)x) = 1$. We have

$$\psi_2^\dagger\sigma_y\psi_2 = -2\beta\hbar v_F\tilde{k}_x(|A|^2 - |B|^2),\tag{5.22}$$

which is independent of the position x. Then we suppose $\tilde{k}_x$ is pure imaginary, then the first part on the right hand side of Eq. (5.21) is zero, because $\Im(\alpha_1) = \Im(\alpha_2) = 0$. Using $\exp(-2i\Re(\tilde{k}_x x)) = 1$, we have

$$\psi_2^\dagger\sigma_y\psi_2 = 4\beta\Re(A^*B\tilde{k}_x).\tag{5.23}$$

which is also independent of position x. Because the wavefunction matching at the boundary, we can get the relation $T(E,\theta)\cos\theta = -\psi_3^\dagger\sigma_y\psi_3 = -\psi_2^\dagger\sigma_y\psi_2$ in the heterostructure region.

Thus, the current density along x direction (Eq. (5.4)) can be written in terms of spin average, i.e.,

$$J_x = \frac{V_1G_1}{L_w} = -\frac{Ee^2V_1}{2\pi^2\hbar^2v_F}\int_{-\frac{\pi}{2}}^{\frac{\pi}{2}}\psi_2^\dagger\sigma_y\psi_2 d\theta.\tag{5.24}$$

Utilizing the current definition in free area $\hat{J} = -e\nabla_{\boldsymbol{p}} H = -ev_F(-\hat{\sigma}_y, \hat{\sigma}_x)$, we can get the mean spin density

$$\begin{aligned}\langle\sigma_y\rangle_1 &= \frac{J_x}{ev_F} = -\frac{EeV_1}{2\pi^2\hbar^2 v_F^2}\int_{-\frac{\pi}{2}}^{\frac{\pi}{2}} \psi_3^\dagger \sigma_y \psi_3 d\theta, \\ &= -\frac{EeV_1}{2\pi^2\hbar^2 v_F^2}\int_{-\frac{\pi}{2}}^{\frac{\pi}{2}} \psi_2^\dagger \sigma_y \psi_2 d\theta, \\ &= -\frac{EeV_1}{2\pi^2\hbar^2 v_F^2 d}\int_0^d \int_{-\frac{\pi}{2}}^{\frac{\pi}{2}} \psi_2^\dagger \sigma_y \psi_2 d\theta dx. \end{aligned} \tag{5.25}$$

For each incident particle with certain angle and certain energy, the spin value at each point x in the heterostructure is $(\psi_2^\dagger\sigma_x\psi_2, \psi_2^\dagger\sigma_y\psi_2, \psi_2^\dagger\sigma_z\psi_2)$. So we can also do angle and position average for σ_x and σ_z like σ_y, and finally multiply the factor related to electron density, as in Eq. (5.25). Thus the x and z components spin density in the heterostructure region can be obtained by substituting $\psi_2^\dagger\sigma_y\psi_2$ with $\psi_2^\dagger\sigma_x\psi_2$ and $\psi_2^\dagger\sigma_z\psi_2$ in Eq. (5.25)

$$\langle\sigma_x\rangle_1 = -\frac{EeV_1}{2\pi^2\hbar^2 v_F^2 d}\int_0^d \int_{-\frac{\pi}{2}}^{\frac{\pi}{2}} \psi^\dagger \sigma_x \psi d\theta dx, \tag{5.26}$$

$$\langle\sigma_z\rangle_1 = -\frac{EeV_1}{2\pi^2\hbar^2 v_F^2 d}\int_0^d \int_{-\frac{\pi}{2}}^{\frac{\pi}{2}} \psi^\dagger \sigma_z \psi d\theta dx. \tag{5.27}$$

For the general Rashba Hamiltonian, we can also get the effective spin density using the idea above but in a more straight forward manner. The general Rashba Hamiltonian with exchange interaction has the form [282, 283, 284]

$$H = \frac{\hbar^2}{2m}k^2 + \alpha(\boldsymbol{\sigma}\times\boldsymbol{k})\cdot\hat{z} - \xi\boldsymbol{M}\cdot\boldsymbol{\sigma}, \tag{5.28}$$

where $\hbar\boldsymbol{k} = -i\hbar(\partial_x, \partial_y, 0)$ is the two-dimensional electron momentum operator, α parametrizes the spin-orbit coupling, ξ is the exchange coupling strength between conduction electron and the magnetization. We can also write the wavefunctions in the incident, heterostructure and transmitted area, and matching wavefunctions at the boundary to get the corresponding coefficients. We just give the transmitted wave

in the following form [285] which is essential for spin density calculation

$$\phi_t = \frac{t}{\sqrt{2}} \exp(i\boldsymbol{k}\cdot\boldsymbol{r}) \cdot \begin{pmatrix} i \cdot s\exp(-i\theta) \\ 1 \end{pmatrix} \tag{5.29}$$

with t the transmission coefficient, $s = \pm 1$, $\exp(-i\theta) = (k_x - ik_y)/\sqrt{k_x^2 + k_y^2}$. The current operator for x direction in the transmitted area is defined as

$$\hat{J}_x = -e\nabla_{p_x} H = -e(\frac{p_x}{m} - \frac{\alpha}{\hbar}\hat{\sigma}_y). \tag{5.30}$$

So for one electron, the current with certain incident angle is

$$\begin{aligned} j_x = \phi_t^\dagger \hat{J}_x \phi_t &= -e\Big[\frac{p_x}{m}|t|^2 + s\cdot\frac{\alpha}{\hbar}|t|^2\cos\theta\Big] \\ &= -e\Big[\frac{\hbar k}{m} + \frac{s\alpha}{\hbar}\Big]|t|^2\cos\theta \end{aligned} \tag{5.31}$$

Thus the current with all angle average is in the form

$$j_x^{ave} = \frac{-e}{\pi}\cdot\Big[\frac{\hbar k}{m} + \frac{s\alpha}{\hbar}\Big]\int_{-\frac{\pi}{2}}^{\frac{\pi}{2}} T_{\boldsymbol{M}}(E,\theta)\cos\theta d\theta. \tag{5.32}$$

From the Landauer-Buttiker formalism, the conductance is

$$G = \frac{Ee^2 L_w}{2\pi^2\hbar^2 v_F}\int_{-\frac{\pi}{2}}^{\frac{\pi}{2}} T_{\boldsymbol{M}}(E,\theta)\cos\theta d\theta. \tag{5.33}$$

And the current density is

$$J_x = \frac{V_1 G_1}{L_w} = \frac{Ee^2 V_1}{2\pi\hbar^2 v_F}\cdot\frac{1}{\pi}\int_{-\frac{\pi}{2}}^{\frac{\pi}{2}} T_{\boldsymbol{M}}(E,\theta)\cos\theta d\theta. \tag{5.34}$$

So, the incident electron density can be expressed as

$$n = \frac{J_x}{j_x^{ave}} = -\frac{EeV_1}{2\pi\hbar^2 v_F}\cdot\frac{1}{\frac{\hbar k}{m} + \frac{s\alpha}{\hbar}}. \tag{5.35}$$

Once we know the current density, we can calculate the spin average over different incident angles and position, for example, the σ_y component can be written as

$$\begin{aligned} \langle\sigma_y\rangle_1 &= n\cdot\frac{1}{\pi d}\int_0^d\int_{-\frac{\pi}{2}}^{\frac{\pi}{2}} \psi^\dagger\sigma_y\psi d\theta dx \\ &= -\frac{EeV_1}{2\pi^2\hbar^2 v_F d}\cdot\frac{1}{\frac{\hbar k}{m} + \frac{s\alpha}{\hbar}}\int_0^d\int_{-\frac{\pi}{2}}^{\frac{\pi}{2}} \psi^\dagger\sigma_y\psi d\theta dx, \end{aligned} \tag{5.36}$$

If we take $m \to \infty$, $\alpha = \hbar v_F$, $s = 1$, we can get the spin density for TI case in Eq. (5.25). In summary, the surface state of TI corresponds to the $m \to \infty$ limit of 2D Rashba Hamiltonian, in which case the spin-momentum locking efficiency is maximum.

Another type of 2D Rashba systems can be graphene based heterostructures, e.g. graphene/Ni(111) and graphene/transition metal dichalcogenide. For such systems, the electron dynamics is governed by the 2D Dirac-Rashba Hamiltonian and turns out to show great in-plane spin polarization, which is perpendicular to electron momentum and proportional to the group velocity [286]. As such, like the surface electron states of topological insulators considered, an in-plane voltage induced charge current will lead to spin density along the perpendicular direction and hence corresponding torque that can be the driven source for magnetization in adjacent magnetic insulators. Then, similar inter-coupling dynamics (between electron transport and magnetization) can be established by adapting/generalizing the current formalism.

5.6.3 Solutions of Quantum Tunneling of Dirac Electrons Through Double FMI Barriers

The spinor wavefunctions in the five regions in Fig. 5.9 can be written as

$$\psi_1(x \leq 0) = \frac{1}{\sqrt{2}} \begin{pmatrix} ie^{-i\theta} \\ 1 \end{pmatrix} e^{ik_F x \cos\theta} + \frac{r}{\sqrt{2}} \begin{pmatrix} -ie^{i\theta} \\ 1 \end{pmatrix} e^{-ik_F x \cos\theta}$$

$$\psi_2(0 < x \leq d) = \frac{1}{\sqrt{2(E+U_1)(E+U_1-M_{z1})}} \cdot \left[a \begin{pmatrix} \hbar v_F(\tilde{k}_{y1} + i\tilde{k}_{x1}) \\ E + U_1 - M_{z1} \end{pmatrix} e^{i(\tilde{k}_{x1} + m_{y1}/\hbar v_F)x} + b \begin{pmatrix} \hbar v_F(\tilde{k}_{y1} - i\tilde{k}_{x1}) \\ E + U_1 - M_{z1} \end{pmatrix} e^{i(-\tilde{k}_{x1} + m_{y1}/\hbar v_F)x} \right]$$

$$\psi_3(d < x < L + d) = \frac{c}{\sqrt{2}} \begin{pmatrix} ie^{-i\theta} \\ 1 \end{pmatrix} e^{ik_F x \cos\theta} + \frac{d}{\sqrt{2}} \begin{pmatrix} -ie^{i\theta} \\ 1 \end{pmatrix} e^{-ik_F x \cos\theta}$$

$$\psi_4(L + d < x < L + 2d) = \frac{1}{\sqrt{2(E+U_2)(E+U_2-M_{z2})}} \cdot \left[f \begin{pmatrix} \hbar v_F(\tilde{k}_{y2} + i\tilde{k}_{x2}) \\ E + U_2 - M_{z2} \end{pmatrix} e^{i(\tilde{k}_{x2} + m_{y2}/\hbar v_F)x} + g \begin{pmatrix} \hbar v_F(\tilde{k}_{y2} - i\tilde{k}_{x2}) \\ E + U_2 - M_{z2} \end{pmatrix} e^{i(-\tilde{k}_{x2} + m_{y2}/\hbar v_F)x} \right]$$

$$\psi_5(L + 2d < x) = \frac{t}{\sqrt{2}} \begin{pmatrix} ie^{-i\theta} \\ 1 \end{pmatrix} e^{ik_F x \cos\theta}$$

where r is the reflection coefficient in region I, t is the transmission coefficient in region V, a, b, c, d, f, and g are the corresponding coefficients in regions II, III, and

IV. Other quantities are

$$\begin{aligned} E &= \hbar v_F k_F, \\ k_y &= k_F \sin\theta, \\ \hbar v_F \tilde{k}_{x1} &= \sqrt{E^2 - m_{z1}^2 - (\hbar v_F \tilde{k}_y)^2}, \\ \hbar v_F \tilde{k}_{x2} &= \sqrt{E^2 - m_{z2}^2 - (\hbar v_F \tilde{k}_y)^2}, \\ \hbar v_F \tilde{k}_{y1} &= \hbar v_F k_y + m_{x1}, \\ \hbar v_F \tilde{k}_{y2} &= \hbar v_F k_y + m_{x2}, \end{aligned}$$

U_1 and U_2 are the biases applied on the two FMIs, respectively, and $\boldsymbol{m} = \xi \boldsymbol{M}$. Matching the wavefunctions at the boundaries, we get all the coefficients and hence the wavefunction in the whole domain, as follows.

$$t = \frac{Z_5 Z_{10} - Z_6 Z_9}{(Z_4 Z_{10} - Z_6 Z_8) b_0 - (Z_6 Z_7 - Z_3 Z_1 0) a_0},$$

$$r = \frac{(Z_5 Z_7 - Z_3 Z_9) a_0 - (Z_4 Z_9 - Z_5 Z_8) b_0}{(Z_4 Z_{10} - Z_6 Z_8) b_0 - (Z_6 Z_7 - Z_3 Z_{10}) a_0},$$

$$a = \frac{(Y_6 Z_1 - Y_7 Y_{10}) C_0 + (Y_6 Z_2 - Y_8 Y_{10}) d_0}{Y_6 Y_9 - Y_5 Y_{10}} t = a_0 t,$$

$$b = \frac{(Y_6 Y_9 - Y_5 Z_1) C_0 + (Y_8 Y_9 - Y_5 Z_2) d_0}{Y_6 Y_9 - Y_5 Y_{10}} t = b_0 t,$$

$$c = \frac{(X_{10} Y_1 - X_7 Y_4) f_0 + (X_{10} Y_2 - X_8 Y_4) g_0}{X_{10} Y_3 - X_9 Y_4} t = c_0 t,$$

$$d = \frac{(X_7Y_3 - X_9Y_1)f_0 + (X_8Y_3 - X_9Y_2)g_0}{X_{10}Y_3 - X_9Y_4}t = d_0t,$$

$$f = \frac{X_2X_6 - X_3X_5}{X_2X_4 - X_1X_5}t = f_0t,$$

$$g = \frac{X_3X_4 - X_1X_6}{X_2X_4 - X_1X_5}t = g_0t,$$

where th variables X_1-X_{10}, Y_1-Y_{10}, and Z_1-Z_{10} are

$$X_1 \equiv \hbar v_F(\tilde{k}_{y2} + i\tilde{k}_{x2})e^{i(\tilde{k}_{x2}+m_{y2}/\hbar v_F)(L+2d)},$$

$$X_2 \equiv \hbar v_F(\tilde{k}_{y2} - i\tilde{k}_{x2})e^{i(-\tilde{k}_{x2}+m_{y2}/\hbar v_F)(L+2d)},$$

$$X_3 \equiv ie^{-i\theta}e^{ik_F(L+2d)\cos\theta}\sqrt{(E+U_2)(E+U_2-m_{z2})},$$

$$X_4 \equiv (E + U2 - m_{z2})e^{i(\tilde{k}_{x2}+m_{y2}/\hbar v_F)(L+2d)},$$

$$X_5 \equiv (E + U2 - m_{z2})e^{-i(\tilde{k}_{x2}+m_{y2}/\hbar v_F)(L+2d)},$$

$$X_6 \equiv e^{ik_F(L+2d)\cos\theta}\sqrt{(E+U_2)(E+U_2-m_{z2})},$$

$$X_7 = e^{-ik_F(L+d)\cos\theta}\sqrt{(E+U_2)(E+U_2-m_{z2})},$$

$$X_8 \equiv \hbar v_F(\tilde{k}_{y2} - i\tilde{k}_{x2})e^{i(-\tilde{k}_{x2}+m_{y2}/\hbar v_F)(L+d)},$$

$$X_9 \equiv ie^{-i\theta}e^{ik_F(L+2d)\cos\theta}\sqrt{(E+U_2)(E+U_2-m_{z2})},$$

$$X_{10} \equiv -ie^{-i\theta}e^{ik_F(L+2d)\cos\theta}\sqrt{(E+U_2)(E+U_2-m_{z2})},$$

$$X_{10} \equiv -ie^{-i\theta}e^{ik_F(L+2d)\cos\theta}\sqrt{(E+U_2)(E+U_2-m_{z2})},$$

$$Y_1 \equiv (E+U2-m_{z2})e^{i(\tilde{k}_{x2}+m_{y2}/\hbar v_F)(L+d)},$$

$$Y_2 \equiv (E+U2-m_{z2})e^{i(-\tilde{k}_{x2}+m_{y2}/\hbar v_F)(L+d)},$$

$$Y_3 \equiv e^{ik_F(L+d)\cos\theta}\sqrt{(E+U_2)(E+U_2-m_{z2})},$$

$$Y_4 \equiv e^{-ik_F(L+d)\cos\theta}\sqrt{(E+U_2)(E+U_2-m_{z2})},$$

$$Y_5 \equiv \hbar v_F(\tilde{k}_{y1}+i\tilde{k}_{x1})e^{i(\tilde{k}_{x1}+m_{y1}/\hbar v_F)d},$$

$$Y_6 \equiv \hbar v_F(\tilde{k}_{y1}-i\tilde{k}_{x1})e^{i(-\tilde{k}_{x1}+m_{y1}/\hbar v_F)d},$$

$$Y_7 \equiv ie^{-i\theta}e^{ik_Fd\cos\theta}\sqrt{(E+U_1)(E+U_1-m_{z1})},$$

$$Y_8 \equiv -ie^{-i\theta}e^{ik_Fd\cos\theta}\sqrt{(E+U_1)(E+U_1-m_{z1})},$$

$$Y_9 \equiv (E+U1-m_{z1})e^{i(\tilde{k}_{x1}+m_{y1}/\hbar v_F)d},$$

$$Y_10 \equiv (E+U1-m_{z1})e^{i(-\tilde{k}_{x1}+m_{y1}/\hbar v_F)d},$$

$$Z_1 \equiv e^{ik_Fd\cos\theta}\sqrt{(E+U_1)(E+U_1-m_{z1})},$$

$$Z_2 \equiv e^{-ik_Fd\cos\theta}\sqrt{(E+U_1)(E+U_1-m_{z1})},$$

$$Z_3 \equiv \hbar v_F(\tilde{k}_{y1} + i\tilde{k}_{x1}),$$

$$Z_4 \equiv \hbar v_F(\tilde{k}_{y1} - i\tilde{k}_{x1}),$$

$$Z_5 \equiv -Z_6 = ie^{-i\theta}\sqrt{(E + U_1)(E + U_1 - m_{z1})},$$

$$Z_7 \equiv Z_8 = E + U1 - m_{z1},$$

$$Z_9 \equiv Z_{10} = \sqrt{(E + U_1)(E + U_1 - m_{z1})},$$

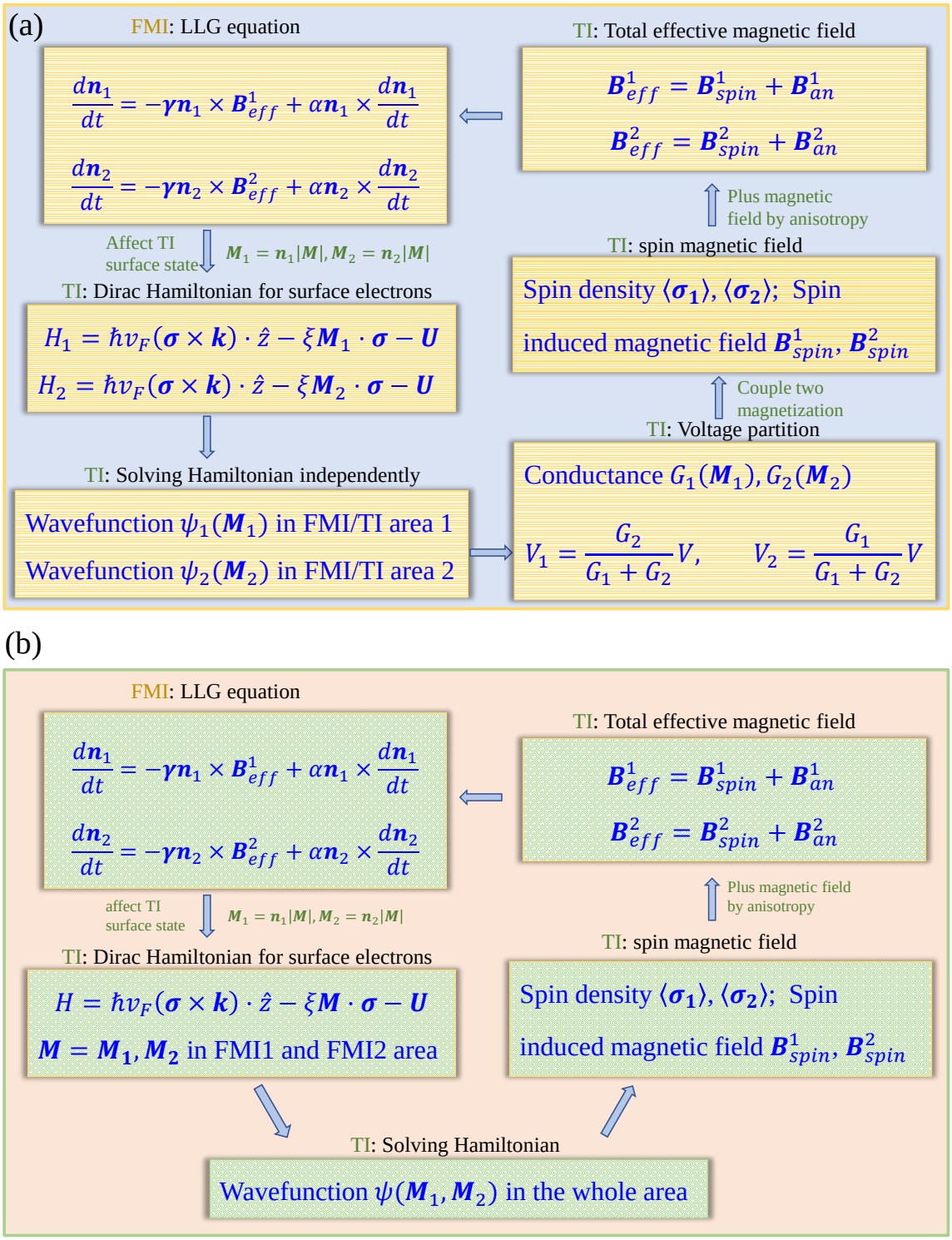

Figure 5.12: Iterative calculation procedure for coupled magnetization dynamics. (a) Current coupled FMIs without quantum interference. (b) Current coupled FMIs with quantum interference.

Chapter 6

SCATTERING OF DIRAC ELECTRONS FROM A SKYRMION: EMERGENCE OF ROBUST SKEW SCATTERING

We study electron scattering from a closed magnetic structure embedded in the top surface of a topological insulator (TI). Outside of the structure there is a uniform layer of ferromagnetic insulator (FMI), leading to a positive effective mass for the Dirac electrons. The mass inside the structure can be engineered to be negative, leading to a skyrmion structure. The geometric shape of the structure can be circular or deformed, leading to integrable and chaotic dynamics in the classical limit. For a circular structure, the relativistic quantum scattering characteristics can be calculated analytically. For a deformed structure, we develop an efficient numerical method, the multiple multipole method, to solve the scattering wavefunctions. We find that, for scattering from a skyrmion, anomalous Hall effect as characterized by skew scattering cross section can arise and is robust against structural deformation, due to the emergence of resonant modes. In the short (long) wavelength regime, the resonant modes manifest themselves as confined vortices (excited edge states). The origin of the resonant states is the spin phase factor of massive Dirac electrons at the skyrmion boundary. In the short wavelength regime, for a circular skyrmion, a large number of angular momentum channels contribute to the resonant modes. In this regime, classical dynamics are relevant, but we find that geometric deformations, even those as severe as leading to fully developed chaos, have little effect on the resonant modes. The vortex structure of the resonant states makes it possible to electrically "charge" the skyrmion, rendering feasible to manipulate its motion through electric means. In the long wavelength regime, only the lowest angular momentum channels con-

tribute to the resonant modes, making the skew scattering sharply directional. These phenomena can be exploited for applications in generating dynamic skyrmions for information storage and in Hall devices.

6.1 Introduction

Previous studies focused on scattering of electrons from radially symmetric skyrmion structures. Deformed skyrmion structure has been studied in recent years. For example, it was found that Majorana modes are robust against skyrmion deformations [287]. Quantum engineering of Majorana fermions in deformed skyrmion structure was also studied [288, 289] and deformed (elongated) skyrmions were used for stabilization and control of Majorana bound states in proximity to an s-wave superconductor [290]. Shape dependent resonant modes have been discovered recently in skyrmions in magnetic nanodisks [291].

The study of deformation also lead to the study of classical chaos in relativistic quantum systems which was recently emerged as an interdisciplinary field of research [292, 293] with applications to Dirac material systems [294, 72]. In contrast to the traditional field of (nonrelativistic) quantum chaos [261, 295] where classical chaos often bears strong signatures in the corresponding quantum systems, such "fingerprints" tend to be weakened in the relativistic quantum counterparts [30, 296]. For example, in scattering (e.g., electronic transport through a quantum dot structure), chaos tends to smooth out fluctuations in scattering matrix elements, quantum transmission, or conductance [297, 298, 299, 300, 301, 302] if the quantum behaviors are governed by the Schrödinger equation. However, in two-dimensional (2D) Dirac materials such as graphene, strong fluctuations of the quantum scattering characteristics can persist to certain extent in spite of classical chaos [303, 304].

In this Chapter, we investigate the Dirac electron skew scattering to a skyrmion

structure residing on top of topological insulator, coupled by the proximity effect. In particular, we consider the setting of a two-dimensional (2D), closed magnetic structure embedded in a uniform layer of ferromagnetic insulating (FMI) materials on the top of a 3D topological insulator (TI). Outside of the structure, due to the FMI layer and the proximity effect, the electrons obey the Dirac equation with a positive mass. The mass of the closed structure can be engineered to be negative, making it a skyrmion [129, 130, 131, 132]. The skyrmion structure can be deformed so that the classical particle motions inside are chaotic. The massive Dirac electrons moving on the surface of the TI are scattered by the structure. The system thus not only provides a setting for exploring new physics associated with scattering of Dirac electrons from a magnetic skyrmion for applications (e.g., in spintronics), but also represents a paradigm to study the effects of classical chaos on relativistic quantum scattering in the presence of magnetism.

More specifically, we investigate electron scattering from a magnetic structure on the top of TI, which can be either of the skyrmion or non-skyrmion type. The structure can simply be a circle, in which case the classical dynamics are integrable, or it can be deformed from the circular shape, e.g., a stadium, where there is fully developed chaos in the classical limit. For a circular structure, the various scattering cross sections can be obtained analytically from the standard partial wave analysis. For a deformed structure, we adopt an efficient method, the multiple multipole (MMP) method in optics, to solving the scattering wavefunctions of the two-component Dirac fermion in the magnetic system. We focus on two regimes: the short wavelength regime where the size of the magnetic structure is larger than the wavelength so that the underlying classical dynamics are relevant, and the long wavelength regime where the structure size is comparable or smaller than the wavelength. There are two main results. Firstly, a skyrmion can lead to strong skew scattering due to the emergence

of resonant modes that manifest themselves as confined vortices inside the skyrmion in the short wavelength regime or confined edge states in the long wavelength regime. The resonant modes are the result of mass sign change across the skyrmion boundary. For a circular skyrmion, in the short wavelength regime, a large number of angular momentum channels contribute to the resonant modes and electron charging arises, providing a way to electrically manipulate the skyrmion motion. In the long wavelength regime, only the lowest angular momentum channels contribute to the resonant states, leading to strongly directional skew scattering with implications in developing Hall devices. The second result is that classical chaos generated by geometrical deformations has little effect on the scattering from a skyrmion. The scattering phenomena uncovered for the circular case are thus robust. The immunity of the scattering dynamics to severe deformation of the skyrmion structure is advantageous for spintronic device applications [305].

6.2 Model and Method

We place an FMI thin film (e.g., Cu_2OSeO_3) on the top of a TI with a single magnetic structure at the center of the thin film, as schematically illustrated in Fig. 6.1. The motions of the surface electrons are affected by the structure with the magnetization vector $\boldsymbol{n}(\boldsymbol{r})$. The Hamiltonian of the system is

$$H = v_F(\hat{\boldsymbol{p}} \times \boldsymbol{\sigma})_z - \Delta_s \boldsymbol{n}(\boldsymbol{r}) \cdot \boldsymbol{\sigma}, \tag{6.1}$$

where v_F is the Fermi velocity, $\hat{\boldsymbol{p}} = -i\nabla$ is the momentum operator, $\boldsymbol{\sigma} = (\sigma_x, \sigma_y, \sigma_z)$ are the Pauli matrices, and $\Delta_s (> 0)$ is the spin-splitting energy from the exchange interaction between the electron and the magnetization. In the polar coordinates $\boldsymbol{r} = (r, \theta)$, for a circular structure, the magnetization vector can be parameterized as

$$\boldsymbol{n}(\boldsymbol{r}) = [-\sin\theta\sqrt{1 - n_z^2(r)}, \cos\theta\sqrt{1 - n_z^2(r)}, n_z(r)]. \tag{6.2}$$

For a deformed magnetic structure, there is swirling spin texture with magnetic moment points up on the edge and down in the center [306]. The out-of-plane component of the magnetic texture $n_z(\boldsymbol{r})$ acts as a Dirac mass term, which opens a gap in the electronic band structure. The in-plane component $\boldsymbol{n}_{||}$ can lead to an emergent magnetic field in the form

$$\boldsymbol{B}(\boldsymbol{r}) = \frac{c\Delta \mathrm{div}\boldsymbol{n}_{||}(\boldsymbol{r})}{e\hbar v_F}.$$

For a swirling skyrmion structure, the emergent magnetic field $\boldsymbol{B}$ is zero and the in-plane component can be gauged away [145, 55]. In this case, the "hard-wall" approximation $n_z(\boldsymbol{r}) = \pm 1$ can be invoked [145, 55], with the point inside and outside of the skyrmion structure taking on the value of minus one and one ($n_1 = 1$, $n_2 = -1$), respectively. In experiments, such a structure can be realized using materials with a strong out-of-plane magnetic anisotropy. In our study, we assume that the magnetic structure is fixed and unaffected by the interface electrons. Experimentally, a skyrmion structure can be stabilized via the Dzyaloshinskii-Moriya (DM) interaction in the FMI [129, 130], where the skyrmion size depends on materials parameters such as the relative strength of the Heisenberg and DM exchange interactions [129, 130]. Our model is valid for skyrmion with a vortical magnetic texture as described. However, for hedgehog skyrmions, the in-plane magnetic field cannot be gauged away due to the emergent magnetic flux and the structure is not as stable as vortical skyrmions [129, 130].

The energy-momentum dispersion for electrons in free space with a uniform magnetic texture (constant mass) is given by

$$E_{\pm} = \pm\sqrt{\hbar^2 v_F^2 (k_x^2 + k_y^2) + \Delta^2 n_z^2}, \tag{6.3}$$

as shown in Fig. 6.1(a). While the energy dispersion curve inside of the skyrmion appears similar to that outside of skyrmion, the spin direction is different for the

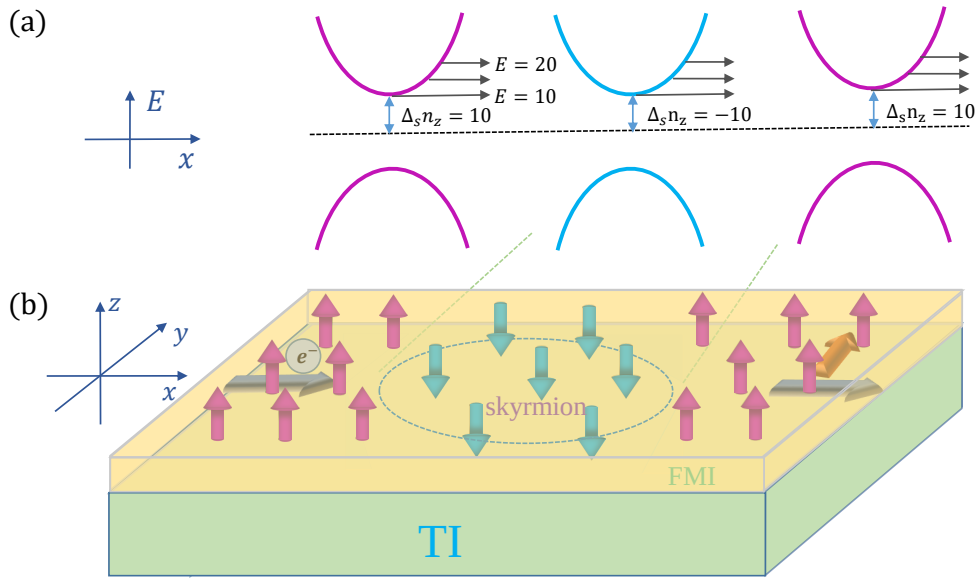

Figure 6.1: Schematic illustration of electron scattering from a skyrmion structure in a thin FMI film deposited on the top of a TI. (a) The band structure of the FMI/TI heterostructure. Outside (inside) of the skyrmion structure, the mass corresponding to the band gap is positive (negative). (b) Illustration of electron scattering behavior from the skyrmion structure. For electronic states outside and inside of the skyrmion, the associated spin direction is different due to the opposite signs of mass.

electronic state due to the opposite signs of mass. An electron will then go through a scattering process in this 2D system. Because of the breaking of the time reversal symmetry, skew scattering will arise.

For a circular magnetic structure, the scattering wavefunction and the related behavior can be solved analytically using the partial-wave decomposition method (Sec. 6.4). For a deformed skyrmion, analytic solutions of the scattering wavefunction are not feasible. We have developed an MMP based method, which has its origin in optics [307, 308, 309, 310, 311] and has recently been extended to scattering of pseudospin-1 particles [30]. The basic idea is to assume two sets of fictitious poles along and in the vicinity of the entire boundary of the magnetic structure: one outside and another inside of the boundary. Each pole emits a wave in the form of Hankel function (spherical wave in the far field). The transmitted wavefunction at each point

inside of the scatterer can be expressed as the superposition of the waves emitted by the poles outside of the scatterer. Similarly, the refracted wavefunction at each point outside of the scatterer can be written as the combination of the waves emitted by the poles inside of the scatterer. The incident plane wave as well as the reflected and transmitted waves are matched on the boundary to enable the poles to be determined, and the expansion coefficients can be obtained by solving the matrix eigenfunctions. (The details of the MMP method adopted to scattering from a magnetic structure are given in Appendix 6.6.1.) We validate the method by comparing the MMP solutions with the analytic solution based on partial wave expansion for a circular skyrmion. Overall, the MMP method is effective and efficient for solving both the near- and far-field scattering problem for a magnetic scatterer of *arbitrary* shape.

In our calculation, we use the dimensionless quantity obtained via considerations of the scales of the physical quantities involved. In particular, the energy scale in the FMI/TI heterostructure is on the order of meV. In free space with zero mass, the wavevector corresponding to the energy of 1 meV is $k \sim 1meV/(\hbar v_F) = 3.04 \times 10^{-3}/nm$. We take the dimensionless radius of the magnetic structure (circular shape) to be $R = 1$, which corresponds to a real structure of size of 100 nm. We then set the dimensionless energy corresponding to 1 meV to be $kR = 0.304$. For $\Delta = 10$, the corresponding energy gap is $10/0.304 \approx 33$ meV.

6.3 Emergence of Robust Resonant States in Scattering from Skyrmion

6.3.1 Short Wavelength Regime - Resonant Vortices and Edge Modes

We concentrate on regime where the wavelength of the incoming Dirac electron is smaller than the size of the magnetic structure so that the classical dynamics inside the structure are relevant. We consider a circular structure as well as a deformed

structure that leads to chaos in the classical limit to identify any effect of chaos on the electron scattering behavior.

Far-field behavior. Far away from the scattering center, for unit incident density the spinor wavefunction can be written as

$$\begin{aligned}\Psi_I &= \Psi_{inc} + \Psi_{ref} \\ &\approx C \begin{pmatrix} 1 \\ i\frac{\hbar v_F k}{E-m_1} \end{pmatrix} e^{ikr\cos\theta} + C \begin{pmatrix} e^{-i\theta} \\ i\frac{\hbar v_F k}{E-m_1} \end{pmatrix} \frac{f(\theta)}{\sqrt{r}} e^{ikr}\end{aligned} \tag{6.4}$$

where C is the normalization factor, $k = \sqrt{k_x^2 + k_y^2}$ is the electron wavevector, $m_1 = \Delta_s n_1$ and $m_2 = \Delta_s n_2$ are the mass terms outside and inside of the magnetic structure, $f(\theta)$ denotes the 2D far-field scattering amplitude in the direction defined by angle θ with the x-axis. For a circular structure, $f(\theta)$ can be obtained analytically. For a chaotic structure, once the reflection function is calculated from the MMP method, $f(\theta)$ can be obtained. The differential cross section is

$$\frac{d\sigma}{d\theta} = |f(\theta)|^2. \tag{6.5}$$

The transport and skew cross sections are defined, respectively, as

$$\sigma_{tr} = \int_0^{2\pi} d\theta |f(\theta)|^2 (1 - \cos\theta) \tag{6.6}$$

and

$$\sigma_{skew} = \int_0^{2\pi} d\theta |f(\theta)|^2 \sin\theta. \tag{6.7}$$

Figures 6.2(a) and 6.2(b) show, respectively, the skew scattering and transport cross sections as a function of incident electron energy, for a skyrmion (negative value of m_2) of circular shape (upper panel) and stadium shape (lower panel) of the same area π in dimensionless units. The stadium shape is chosen because of its mirror symmetry

for the incident plane waves so as to avoid an unnecessary complication: mixing of skew scattering and back-scattering (or reflection). For both skyrmion shapes, there are sharp resonant peaks in the skew cross section in the lower energy range close to the gap - an indication of the emergence of anomalous Hall effect associated with Dirac electron scattering from the skyrmion. As the incident energy is increased, the peak height is reduced but its width becomes larger, as a larger energy value corresponds to less distortion in the energy-momentum dispersion with the mass gap. Note that there is little difference in the skew scattering cross section curves for the two skyrmion shapes, indicating that the nature of the classical dynamics hardly affects the scattering. For the curves of the transport cross section, as shown in Fig. 6.2(b), its value decreases with increasing energy. For low energy values, the valleys in the transport cross section correspond exactly to the skew scattering peaks. Sharp peaks also exist in the backscattering cross section curve. Similar to the skew cross section, the nature of the classical dynamics has no appreciable effect. The results in Fig. 6.2 indicate that skyrmion skew scattering is robust against geometric deformations that are so severe as to change the classical behavior completely: from integrable dynamics to chaos.

Near-field behavior. To understand the origin of the deformation (chaos) independent far-field scattering (transport) behavior, we study the near-field scattering behavior by examining the probability density and the current density distribution associated with some specific energy state. In particular, the probability density is given by $P = \Psi^\dagger\Psi$, where $\Psi = (\psi_1, \psi_2)^T$ is the wavefunction, and the probability current operator is $\hat{J} = \nabla_{\boldsymbol{p}} H = v_F(\sigma_y, -\sigma_x)$. The current density can be obtained as

$$\boldsymbol{J} = (J_x, J_y) = v_F[2(i\psi_1\psi_2^*), -2(\psi_1\psi_2^*)]. \tag{6.8}$$

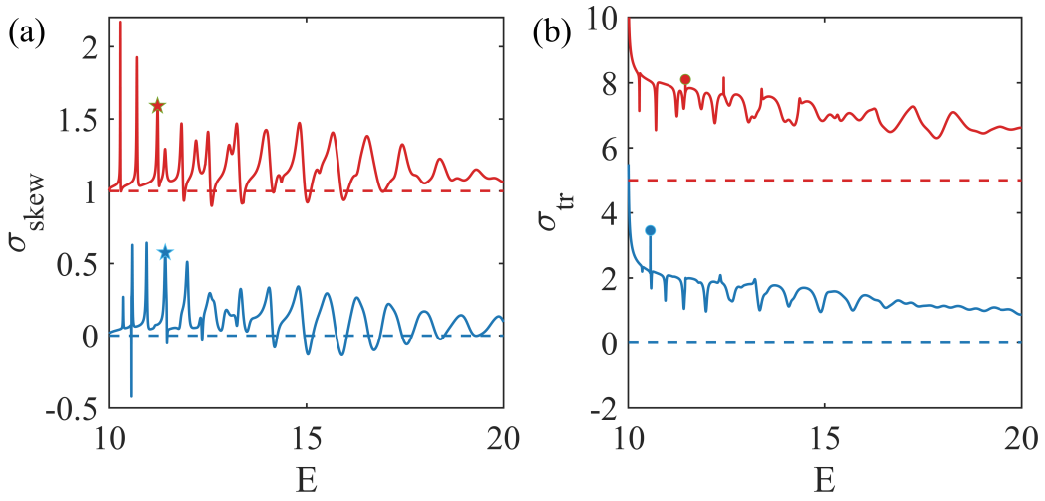

Figure 6.2: Skew scattering and transport cross sections versus incident electron energy in the short wavelength regime. (a) Skew scattering cross section versus the energy. The red and blue curves correspond to a circular and stadium-shaped skyrmion, respectively. The mass values are $m_1 = 10$ and $m_2 = -10$. (b) Backscattering cross section as a function of electron energy for the two skyrmion shapes as in (a). In each panel, the red curve has been shifted upwards by an amount specified by the horizontal red-dashed line for better visualization and comparison with the blue curve.

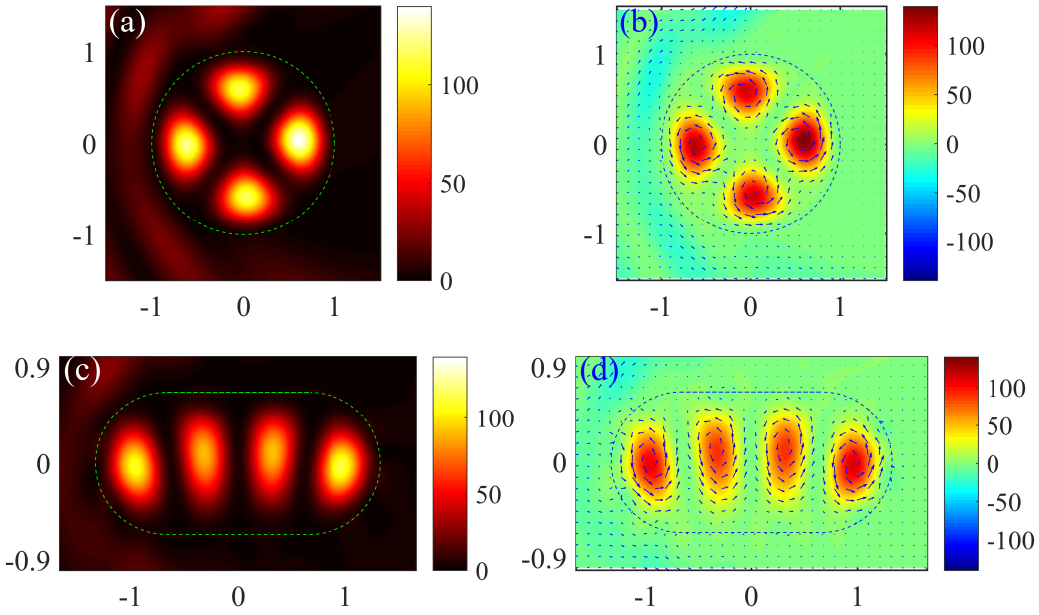

Figure 6.3: Probability and current density distribution for selected vortex states. (a) The probability distribution for scattering from a circular skyrmion for $m_1 = 10$, $m_2 = -10$, and $E = 11.225$. (b) In-plane current (marked as arrows) and spin-z component (color coded) density distribution in the circular skyrmion region. (c,d) The corresponding probability, current and spin distribution for scattering from a stadium-shaped skyrmion for $m_1 = 10$, $m_2 = -10$, and $E = 11.42$.

The probability density distribution of the spin-z component is given by

$$\langle \sigma_z \rangle = |\psi_1|^2 - |\psi_2|^2.$$

We choose a representative energy value corresponding to a skew scattering cross section peak: $E = 11.225$ for the circular skyrmion and $E = 11.42$ for the stadium-shaped skyrmion - marked as the red and blue stars in Fig. 6.2(a), respectively. The probability and the current density distributions are shown in Fig. 6.3. From both skyrmion structures, there are scattering resonant states, as shown in Figs. 6.3(a) and 6.3(c). The resonant patterns correspond to weak backscattering but stronger skew scattering cross sections, indicating that these are effectively quasi-confined states. Further insights into the contribution of the resonant states to skew scattering can be gained by examining the current density distribution (marked as arrows) and the spin-z component density distribution (color coded) in the 2D skyrmion structure, as shown in Figs. 6.3(b) and 6.3(d). We see that the confined resonant states form vortices with counter-clockwise currents. There is also an out-of-plane spin component along the positive z direction. The vortices have an apparent directionality, so they can affect the skew scattering direction and magnitude. The vortices are formed by interference of waves reflected from the boundary and are robust against boundary deformation. As a result, the nature of the classical dynamics, integrable or chaotic, has no significant effect on scattering.

In addition to the confined vortex states inside of the skyrmion structure, another form of confined states arises along the skyrmion boundary, as shown in Figs. 6.4(a) and 6.4(c), for scattering from a circular and a stadium-shaped skyrmion, respectively. There is strong confinement of the scattering wavefunction near the boundary with clockwise current and spin-z component along the negative z axis direction, as shown in Figs. 6.4(b) and 6.4(d). The edge states correspond to sharp resonant peaks in the

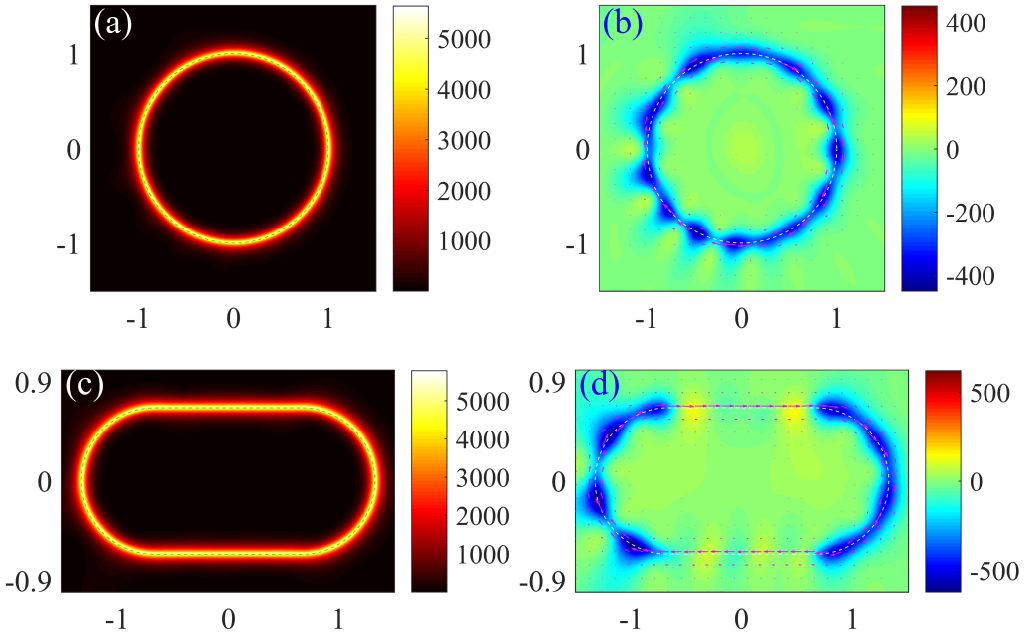

Figure 6.4: Wavefunction probability and current density distribution associated with selected edge states. (a) The probability distribution for scattering from a circular skyrmion for $m_1 = 10$, $m_2 = -10$, and $E = 11.461$. (b) The corresponding in-plane current (marked as arrows) and spin-z component (represented by colors) density distribution. (c,d) The probability and spin distributions associated with scattering from a stadium-shaped skyrmion for $m_1 = 10$, $m_2 = -10$, and $E = 10.564$.

backscattering cross section marked as the filled circles in Fig. 6.2(b). For the circular skyrmion, the edge states have no corresponding sharp peaks in skew scattering. For the stadium-shaped skyrmion, the edges states correspond to sharp valleys in the skew scattering cross section.

6.3.2 Long Wavelength Regime - Resonant Modes Near the Boundary

Far-field behavior. We consider the regime where the skyrmion size is smaller than the electronic wavelength: $R \ll 1/k$. This can be realized by setting the area of the skyrmion structure to be 0.01π for both circular ($R = 0.1$) and stadium-shaped skyrmions. In this long wavelength regime, for a deformed skyrmion structure, the MMP method is still effective for calculating the far-field cross sections and the near-field state distribution. Representative results on the skew scattering and transport

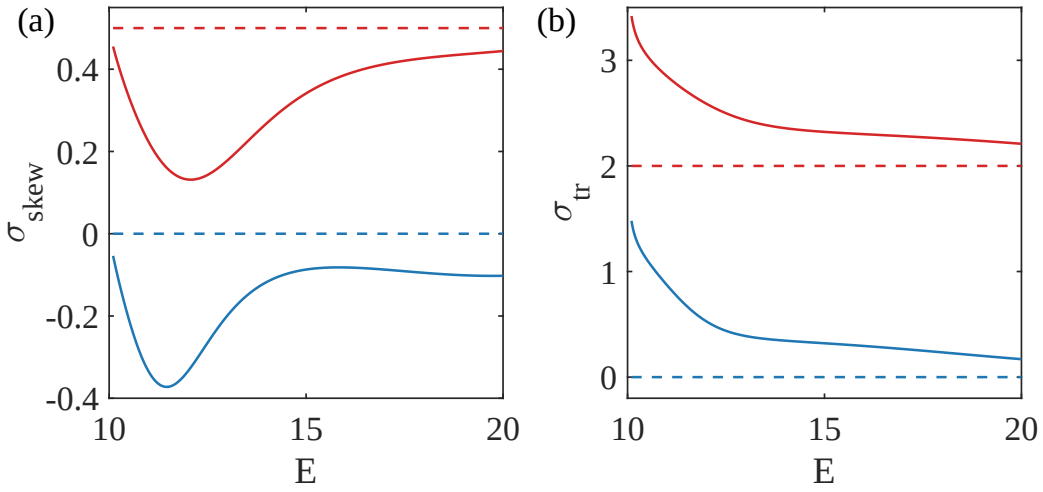

Figure 6.5: Characteristics of Dirac electron scattering from a magnetic skyrmion in the long wavelength regime. (a,b) Skew scattering and backscattering cross sections versus energy, respectively. The red and blue curves correspond to a circular and stadium-shaped skyrmion, respectively. The mass values are $m_1 = 10$ and $m_2 = -10$. In each panel, the red curve has been shifted upward for a proper amount for better visualization and comparison with the blue curve.

cross sections versus the incident energy are shown in Fig. 6.5. Different from the scattering behaviors in the short wavelength regime, the oscillations of the skew scattering cross section with energy are weak. For example, in the energy range $10 < E < 20$, only one smooth peak appears. There is hardly any difference in the scattering characteristics between the two skyrmion structures, which is understandable as any structural differences are not resolved in the long wavelength regime. Because of lack of appreciable oscillations, there is directional skew scattering over a large energy range - a desired feature in Hall device applications.

Near-field behavior. We examine the state associated with the energy value that leads to the lowest skew scattering cross section: $E = 12.072$ for the circular and $E = 11.46$ for the stadium-shaped skyrmion, and the respective probability density distributions are shown in Figs. 6.6(a) and 6.6(c). The states are concentrated in the vicinity of the boundary, which are different from the vortex states observed in the short-wavelength regime. The edge states thus represent a different type of resonant

states with directional current, as shown in Figs. 6.6(b) and 6.6(d). It can be seen that the current direction is downward at the edge, contributing to skew scattering. The spin-z component is along the negative z direction.

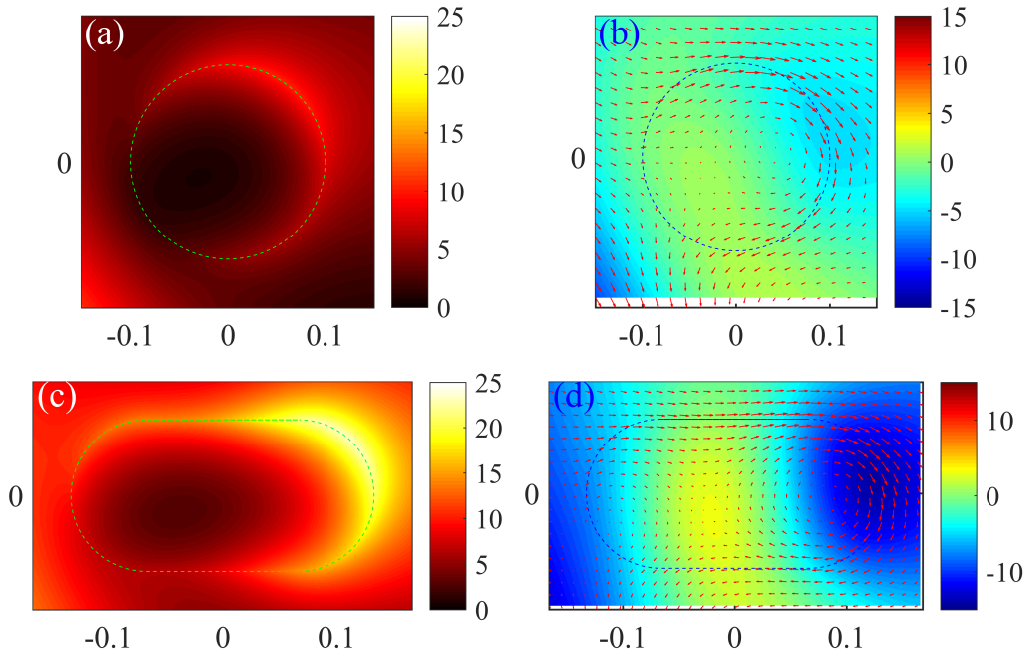

Figure 6.6: Wavefunction probability and current density distributions for selected states for scattering in the long wavelength regime. (a,b) The probability distribution and in-plane current together with the spin-z component density distributions, respectively, for scattering from a circular skyrmion for $m_1 = 10$, $m_2 = -10$, and $E = 12.072$. (c,d) The corresponding results for scattering from a stadium-shaped skyrmion for $m_1 = 10$, $m_2 = -10$, and $E = 11.46$.

6.3.3 Further Demonstration of Strong Skew Scattering from a Skyrmion Structure

To further demonstrate the shape-independent skew scattering behavior of Dirac electrons from a magnetic structure, we study the effects of changing the mass of the skyrmion texture. To be concrete, we set $m_1 > 0$ and choose a set of positive and negative m_2 values. In this setting, there is a skyrmion for $m_2 < 0$ but the magnetic structure is non-skyrmion for $m_2 > 0$.

We first examine the short-wavelength regime to probe into the origin of the

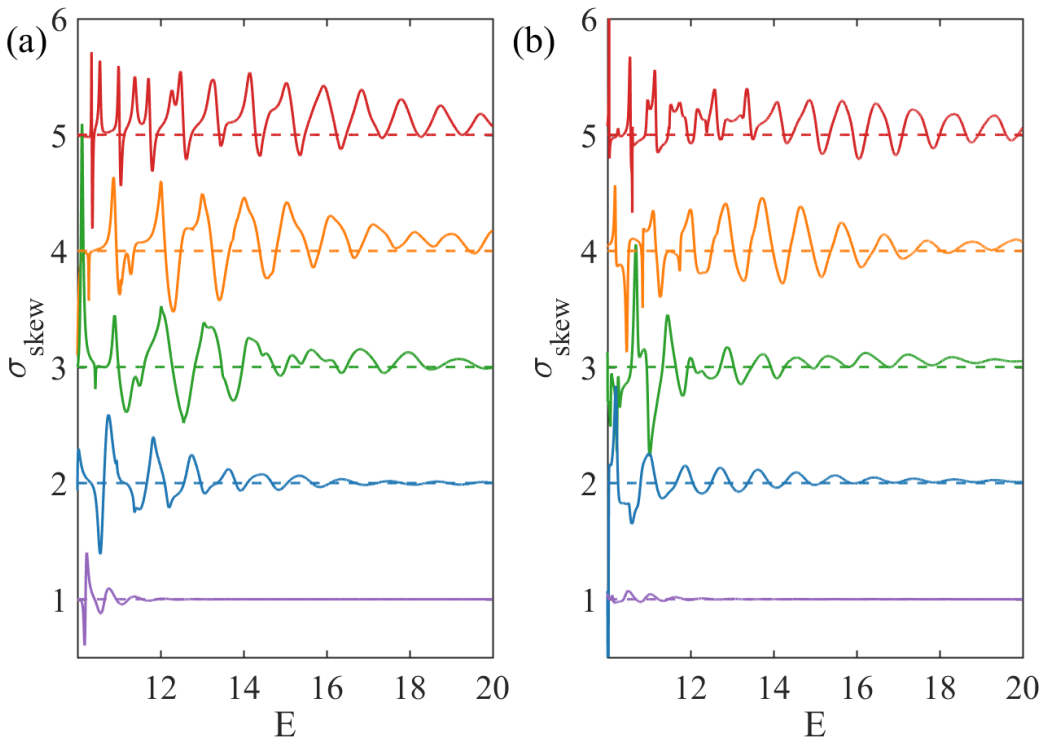

Figure 6.7: Effects of varying mass on Dirac electron scattering in the short wavelength regime. The area of the magnetic structure is π. (a) Skew scattering cross section versus the electron energy for a circular structure for mass values $m_2 = -9, -5, 0, 5, 9$, represented by the red, orange, green, blue and purple solid curves, respectively. In each panel, the curves have been shifted upward for better visualization and comparison, where each horizontal dashed line denotes the zero reference point. The mass outside of the magnetic structure is $m_1 = 10$. (b) The corresponding curves for a stadium-shape structure with the same mass values as in (a).

emerged confined vortex states. Figures 6.7(a) and 6.7(b) show the skew scattering cross sections for the circular and stadium-shaped magnetic structure, respectively, for $m_1 = 10$ and $m_2 = -9, -5, 0, 5, 9$. It can be seen that, among the five cases, the resonant oscillations of the cross section with energy last longer for $m_2 = -9$. On the contrary, for $m_2 = 9$ (non-skyrmion), the oscillations diminish rapidly as the energy is increased. These behaviors hold regardless of whether the underlying classical dynamics are integrable or chaotic. Overall, a large difference between the masses inside and outside of the magnetic structure can lead to stronger and long-lasting resonant

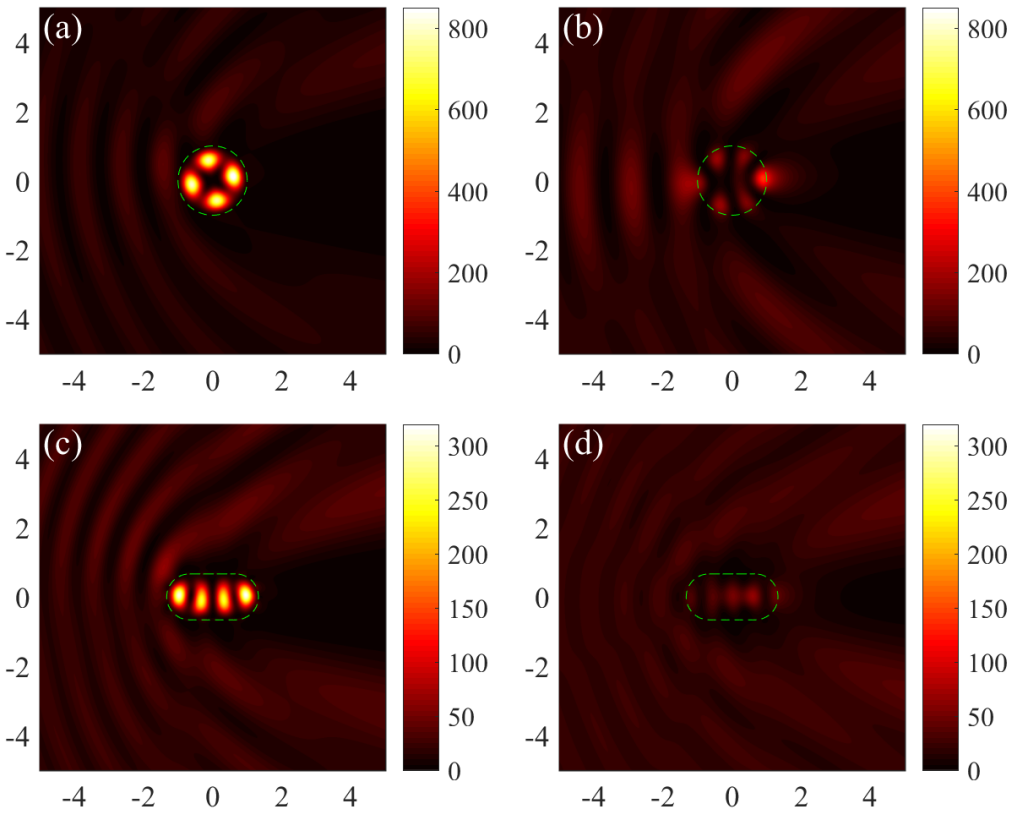

Figure 6.8: Probability density distribution for selected states in the circular and stadium-shaped structure for different masses in the short wavelength regime. (a) Circular skyrmion structure ($m_2 = -9$) for $E = 10.349$, (b) circular non-skyrmion structure ($m_2 = 9$) for $E = 10.234$, (c) stadium-shaped skyrmion ($m_2 = -9$) for $E = 10.552$, and (d) stadium-shaped structure ($m_2 = 9$) for $E = 10.514$.

modes and, consequently, to more pronounced skew scattering. Figures 6.8(a) and 6.8(b) show the probability density distribution for $m_2 = 9$ and $m_2 = -9$, respectively, for the circular magnetic structure. The corresponding results for the stadium-shaped structure are shown in Figs. 6.8(c) and 6.8(d). For both structures, there are resonant modes for $m_2 = -9$ (when the magnetic structure is of the skyrmion type) but not for the case of $m_2 = 9$.

In the long wavelength regime, regardless of the shape of the magnetic structure (circular or stadium-shaped), the skew scattering cross section decreases as the relative mass difference is reduced, as shown in Fig. 6.9 for $m_2 = -9, -5, 0, 5, 9$.

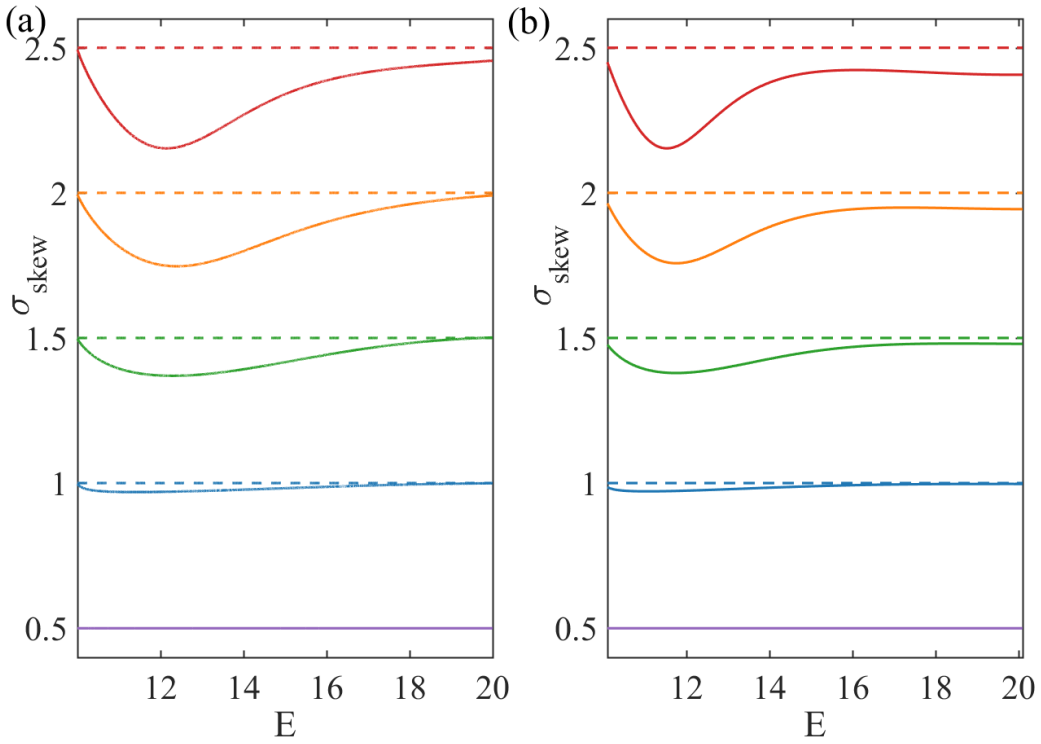

Figure 6.9: Skew scattering for different mass values of the magnetic structure in the long wavelength regime. The area of the structure is $\pi/100$ and the mass outside of the structure is $m_1 = 10$. (a) For a circular structure, skew scattering cross section for $m_2 = -9, -5, 0, 5, 9$, represented by the red, orange, green, blue and purple solid curves, respectively. In each panel, the curves have been shifted upward for better visualization and comparison, with the horizontal dashed lines denoting the zero reference point. (b) The corresponding results for a stadium-shaped magnetic structure.

Figure 6.10 shows representative resonant states for the circular and stadium-shaped structure for $m_2 = \pm 9$. Again, when the magnetic structure is of the skyrmion type, skew scattering is strong, making the scattering electrons directional. However, when the structure is not of the skyrmion type, skew scattering is weak.

6.4 Partial-wave Decomposition Based Analysis

Numerically, we have observed strong skew scattering of Dirac electrons from a skyrmion structure, which is robust against geometric deformation. We now provide an analytic understanding of skew scattering based on the method of partial wave

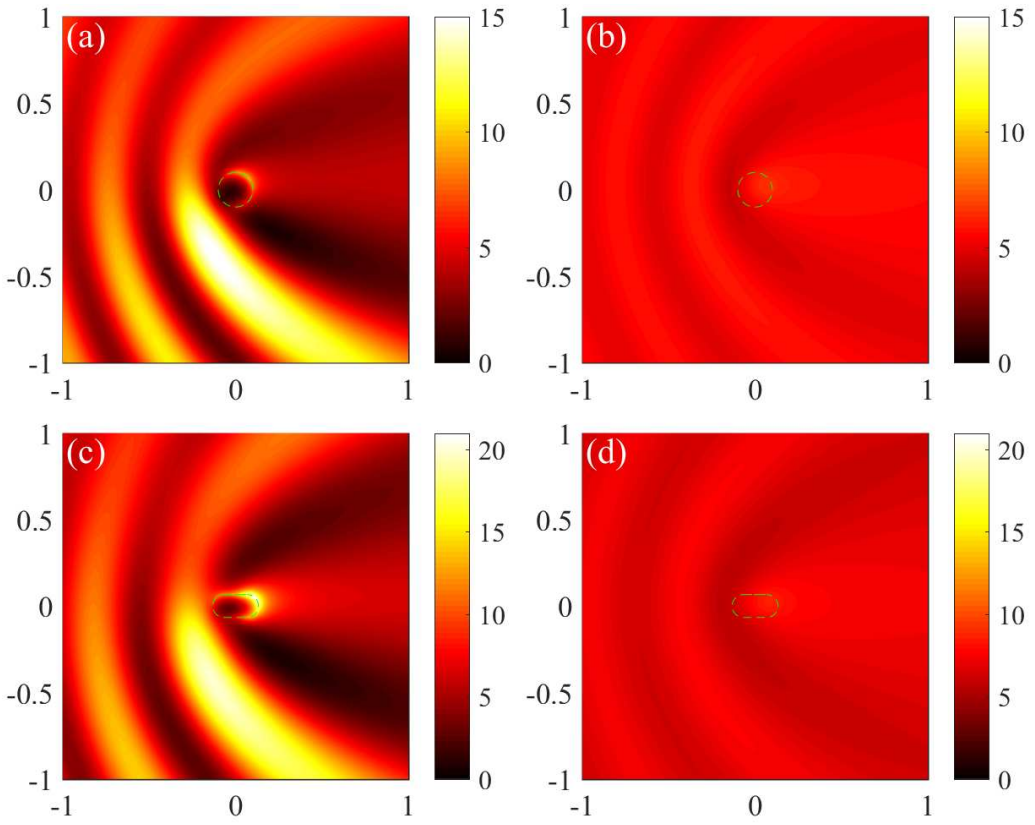

Figure 6.10: Probability density distribution for the states corresponding to the minimum of the skew scattering cross section in circular and stadium-shaped magnetic structures in the long wavelength regime: (a) a circular skyrmion structure for $m_2 = -9$ and $E = 12.152$, (b) a circular non-skyrmion structure for $m_2 = 9$ and $E = 12.317$, (c) a stadium-shaped skyrmion structure for $m_2 = -9$ and $E = 11.53$, and (d) a stadium-shaped non-skyrmion structure for $m_2 = 9$ and $E = 11.72$.

decomposition. Consider a circular skyrmion. Key to pronounced skew scattering is the resonant modes emerged from the scattering process. In the short wavelength regime, a large number of angular momentum components are involved in the scattering, leading to a large number of resonant modes as the result of various combinations of the angular momentum components, which are manifested as peaks in the curve of the cross section with the energy. In the long wavelength regime, typically only a single resonant mode is dominant, implying the involvement of only the lowest several angular momentum components. The asymmetric contribution from different angular momentum channels leads to the observed pronounced skew scattering. Because the

circular and stadium-shaped skyrmion structures generate similar scattering behavior, the analytic results from the circular skyrmion case also provides an understanding of the emergence of strong skew scattering in the stadium-shaped skyrmion.

For a circular skyrmion, the rotational symmetry stipulates conservation of the total angular momentum $\hat{J}_z$: $[\hat{J}_z, H] = 0$, and the partial wave component with total angular momentum j $(= \pm 1/2, \pm 3/2, ...)$ in the polar coordinates (r, θ) can be written as

$$\psi_j(\boldsymbol{r}) = \begin{pmatrix} u_j(r)e^{i(j-1/2)\theta} \\ v_j(r)e^{i(j+1/2)\theta} \end{pmatrix}. \tag{6.9}$$

The Hamiltonian in the polar coordinates is

$$H = \hbar v_F \begin{pmatrix} -\frac{\Delta_s n}{\hbar v_F} & -e^{-i\theta}\frac{\partial}{\partial r} + e^{-i\theta}\frac{i\partial}{r\partial\theta} \\ e^{i\theta}\frac{\partial}{\partial r} + e^{i\theta}\frac{i\partial}{r\partial\theta} & \frac{\Delta_s n}{\hbar v_F} \end{pmatrix}. \tag{6.10}$$

Substituting the partial wave form in Eq. (6.9) into the Hamiltonian Eq. (6.10) leads to an eigenvalue problem and consequently to the explicit expression for the partial waves.

The transmitted wave inside of the skyrmion structure $(r < R)$ can be expanded in terms of the partial waves as

$$\psi^T(r,\theta) = C\sum_{l=-\infty}^{\infty} i^{l-1}B_l \begin{pmatrix} J_{l-1}(k'r)e^{i(l-1)\theta} \\ -\frac{\hbar v_F k'}{E-\Delta_s n'}J_l(k'r)e^{il\theta} \end{pmatrix}, \tag{6.11}$$

and the reflected wave outside of skyrmion $(r > R)$ can be written as

$$\psi^R(r,\theta) = C\sum_{l=-\infty}^{\infty} i^{l-1}A_l \begin{pmatrix} H_{l-1}(kr)e^{i(l-1)\theta} \\ -\frac{\hbar v_F k}{E-\Delta_s n}J_l(kr)e^{il\theta} \end{pmatrix}, \tag{6.12}$$

where C is a normalization factor. We denote n (n') as the magnetic moment and k (k') as the wavevector outside (inside) of the skyrmion structure. For the incident

electron in the free region outside of the skyrmion structure, the wavefunction is

$$\psi^I = C \begin{pmatrix} 1 \\ i\frac{\hbar v_F k}{E-\Delta_s n} \end{pmatrix} e^{ikr\cos\theta}. \tag{6.13}$$

Using the Jacobi-Anger identity:

$$e^{iz\cos\theta} \equiv \sum_{l=-\infty}^{\infty} i^l J_l(z) e^{il\theta}, \tag{6.14}$$

we can expand the plane wave in the form

$$\psi^I = C\sum_l i^{l-1} \begin{pmatrix} J_{l-1}e^{i(l-1)\theta} \\ -\frac{\hbar v_F k}{E-\Delta_s n} J_l(kr) e^{il\theta} \end{pmatrix}. \tag{6.15}$$

Matching the waves at the skyrmion boundary (r = R):

$$\psi^I(R) + \psi^R(R) = \psi^T(R), \tag{6.16}$$

we get, after some algebraic manipulation,

$$A_l = \frac{J_{l-1}(kR)J_l(k'R) - \frac{\tau}{\tau'}J_l(kR)J_{l-1}(k'R)}{\frac{\tau}{\tau'}H_l(kR)J_{l-1}(k'R) - H_{l-1}(kR)J_l(k'R)}, \tag{6.17}$$

and

$$B_l = \frac{J_{l-1}(kR)H_l(kR) - J_l(kR)H_{l-1}(kR)}{H_l(kR)J_{l-1}(k'R) - \frac{\tau'}{\tau}H_{l-1}(kR)J_l(k'R)}, \tag{6.18}$$

where

$$\begin{aligned} \tau &= -\frac{\hbar v_F k}{E-\Delta_s n}, \text{ and} \\ \tau' &= -\frac{\hbar v_F k'}{E-\Delta_s n'}. \end{aligned}$$

Using the explicit formulas for A_l and B_l as given in Eq. (6.17) and (6.18), respectively, we obtain the decomposition coefficients versus the total angular momentum

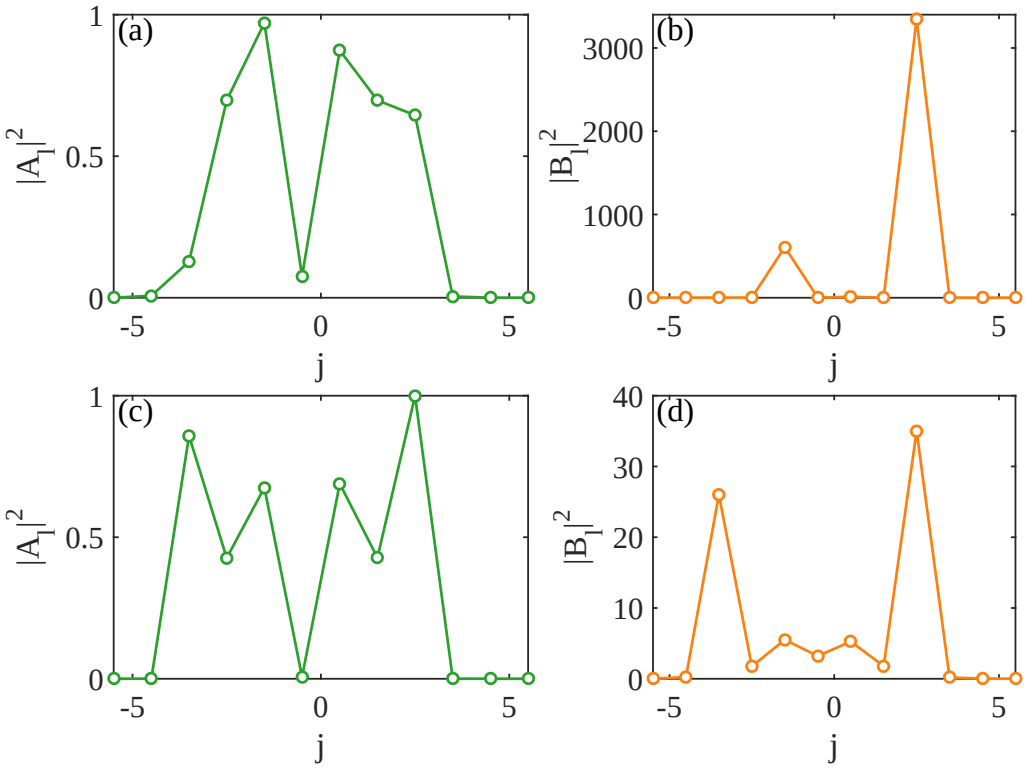

Figure 6.11: Partial wave decomposition coefficients as a function of total angular momentum for a circular magnetic structure in the short wavelength regime. Among the quantities plotted, A_l's are the coefficients for the reflected waves outside of the structure and B_l's are the transmitted wave coefficients. (a,b) For a skyrmion structure ($m_1 = 10$ and $m_2 = -9$), $|A_l|^2$ and $|B_l|^2$ as a function of j, respectively, where the corresponding state is shown in Fig. 6.8(a). (c,d) For a non-skyrmion structure ($m_1 = 10$ and $m_2 = 9$), $|A_l|^2$ and $|B_l|^2$ versus j, respectively, where the corresponding state is shown in Fig. 6.8(b).

for $R = 1$. Figures 6.11(a) and 6.11(b) show, for the case of scattering from a skyrmion structure ($m_1 = 10$ and $m_2 = -9$), the expansion coefficients versus the total angular momentum j. Figures 6.11(c) and 6.11(d) show the corresponding results for a non-skyrmion case ($m_1 = 10$ and $m_2 = 9$). It can be seen that, several angular momentum components contribute to the reflected wave component A_l, and the asymmetric distribution of the angular momentum components about zero leads to skew scattering. For the transmitted wave components, the distribution of the angular components is asymmetric as well, leading to the emergence of resonant vortices. For the B_l coefficients, their values for the non-skyrmion case is much smaller

than those for the skyrmion case, indicating that the skyrmion structure can confine the electrons much more effectively than the non-skyrmion structure.

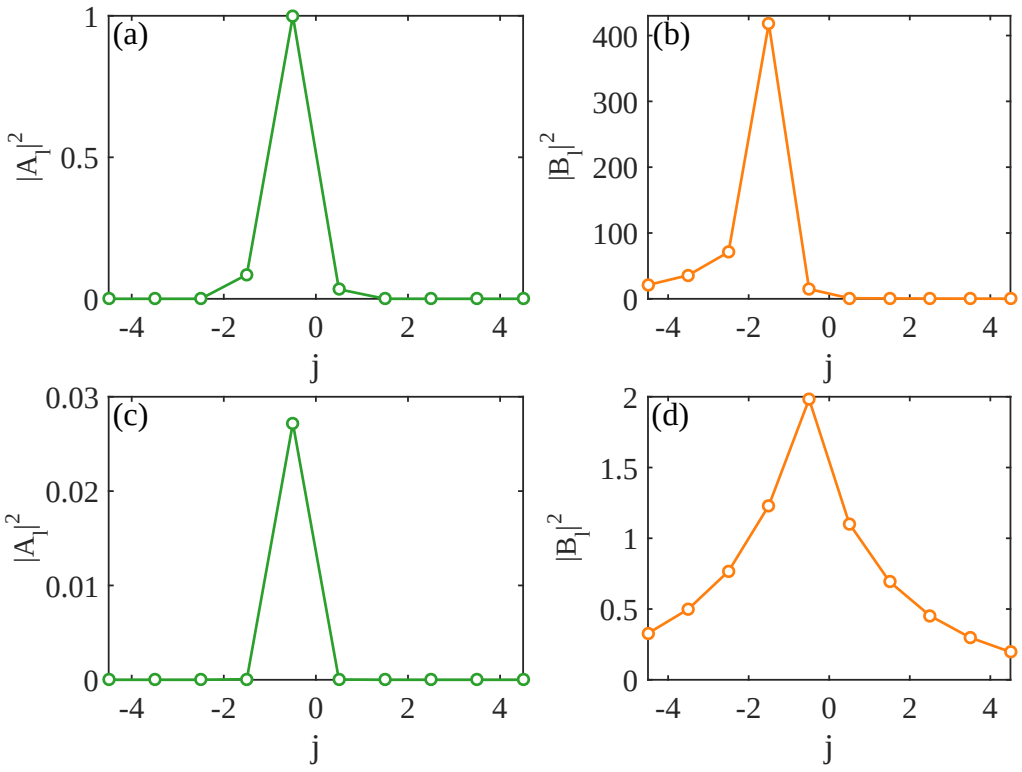

Figure 6.12: Transmitted and reflected partial wave coefficients as a function of the total angular momentum for a circular magnetic structure in the long wavelength regime. The radius of the structure is $R = 0.1$. (a,b) $|A_l|^2$ and $|B_l|^2$ versus j for $m_1 = 10$ and $m_2 = -9$ (skyrmion case), respectively, where the state is the one shown in Fig. 6.10(a). (c,d) $|A_l|^2$ and $|B_l|^2$ versus j for $m_1 = 10$ and $m_2 = 9$ (non-skyrmion case), respectively, where the corresponding state is shown in Fig. 6.10(b).

Setting $R = 0.1$ lands the scattering system in the long wavelength regime. Figures 6.12(a,b) and 6.12(c,d) show the coefficients associated with different angular-momentum components for the skyrmion ($m_1 = 10$ and $m_2 = -9$) and non-skyrmion ($m_1 = 10$ and $m_2 = 9$) cases, respectively. In both cases, only a single angular momentum component contributes to the coefficient A_l, i.e., $j = -1/2$, giving rise to the directionality in the scattering and a slow change in the resonant cross section with the energy. The value of A_l for the non-skyrmion case is much smaller than that of the skyrmion case. For the transmitted coefficient B_l, the angular momentum compo-

nent $j = -3/2$ dominates the skyrmion case and a number of components including $j = -1/2$ have contributions in the non-skyrmion case, and the values of B_l are much larger in the skyrmion than the non-skyrmion case, again implying stronger confinement by resonance and better directionality of scattering in the skyrmion structure as compared with those in the non-skyrmion structure.

6.5 Discussion

We have investigated relativistic quantum scattering of Dirac electrons from a closed magnetic structure embedded in the top surface of a 3D TI. Outside of the structure, there is a uniform FMI layer, leading to a finite but positive mass for the Dirac electron. The mass of the structure itself can be engineered to be negative or positive, where a skyrmion and a non-skyrmion structure arises in the former and latter case, respectively. In the short wavelength regime, the nature of the classical dynamics in the closed structure should be relevant to the quantum scattering dynamics, according to conventional wisdom from the study of quantum chaos [261, 295]. For a perfectly circular structure, the classical dynamics are integrable. For a deformed structure such as one with the stadium shape, there is fully developed chaos in the classical dynamics. Our main findings are two. First, in the short wavelength regime, classical chaos hardly has any effect on the scattering dynamics. In fact, similar behaviors in the scattering characteristics at a *quantitative* level, such as the skew scattering and backscattering cross sections, have arise for the circular and stadium-shaped structures. The diminishing effects of classical chaos on relativistic quantum scattering from a magnetic structure are consistent with previous results on weakened manifestations of chaos in relativistic quantum systems in general [30, 296, 303, 304, 312]. Second, strong skew scattering can arise when the magnetic structure is a skyrmion, regardless of the nature of the classical dynamics.

In the short wavelength regime, the pronounced skew scattering is associated with resonant modes manifested as confined vortices inside of the skyrmion structure, which are originated from the sign change in the mass when the Dirac electrons travel from outside to inside of the skyrmion structure. A partial wave analysis for scattering from a circular skyrmion has revealed that a large number of angular momentum channels contribute to the resonant modes. We have also studied the long wavelength regime, where the geometric details of the magnetic structure are unresolved so naturally the scattering process is expected to be independent of the nature of the classical dynamics. In this regime, resonant states can still emerge as confined edge states inside of the magnetic structure, to which only a single angular momentum channel contributes, leading to highly directional skew scattering.

In the short wavelength regime, the resonant states manifested as confined vortices inside of the skyrmion structure can be exploited for electrically charging the skyrmion structure [144, 145], enabling the surface electrons on the TI to drive skyrmion motion with a low current and high thermal efficiency. In the long wavelength regime, the strong and robust directionality for skew scattering may be exploited for device application based on the anomalous Hall effect.

Note that Our treatment is based on the electron scattering over the skyrmion structure, which is more convenient to get the analytical expression for circular case and utilizing MMP method for deformed case. The cross section can capture the fundamental mechanism of the electron behavior under the influence of a skyrmion structure. For experimental realization, the electron scattering over a skyrmion structure is not easy to control without lead or contact. It is better to set up a device with lead and finite region with skyrmion structure to achieve control of spin skew scattering. Although the boundary may have some effect on electron scattering, as long as the device size is larger compared to the electron wavelength, the basic spin

skew scattering behavior will remain the same.

For the material realization, the evidence of magnetic skyrmions at the interface of ferromagnet/TI (Cr_2Te_3/Bi_2Te_3) heterostructures has been revealed in a recent study [313]. And the inhomogeneous Zeeman coupling is much more easily to be tuned for a ferromagnetic strip with strong out-of-plane magnetic anisotropy [145].

A number of open issues are worth studying, such as using spin transfer torque of the electrons to drive the skyrmion motion, exploitation of skyrmion related switches or oscillators, and scattering from multiple skyrmions that are themselves dynamic with possible phase-locking or anti-phase locking behavior.

6.6 Supplementary Notes

6.6.1 Multiple Multipole (MMP) Method for Scattering of Dirac Electrons on the Top of a TI from a Magnetic Structure

We denote the area outside and inside of the skyrmion structure as regions I and II, respectively. The wavefunction in region II can be written as

$$\Psi^{II}(\boldsymbol{r}) \equiv \begin{pmatrix} \psi_1^I \\ \psi_2^{II} \end{pmatrix} = \sum_{m_I} \sum_{l} \frac{C_l^{m_I}}{\sqrt{2}} \begin{pmatrix} H_{l-1}^{(1)}(k_{II} d_{m_I}) e^{-i\theta_{m_I}} \\ \tau_{II} H_l^{(1)}(k_{II} d_{m_I}) \end{pmatrix} e^{il\theta_{m_I}}, \tag{6.19}$$

where

$$\begin{aligned} k_{II} &= \sqrt{E^2 - \Delta^2 n_{II}^2}/\hbar v_F, \\ \tau_{II} &= -\hbar v_F k_{II}/(E - \Delta n_{II}), \\ d_{m_I} &= |\boldsymbol{r} - \boldsymbol{r}_{m_I}|, \\ \theta_{m_I} &= \text{Angle}(\boldsymbol{r} - \boldsymbol{r}_{m_I}), \end{aligned}$$

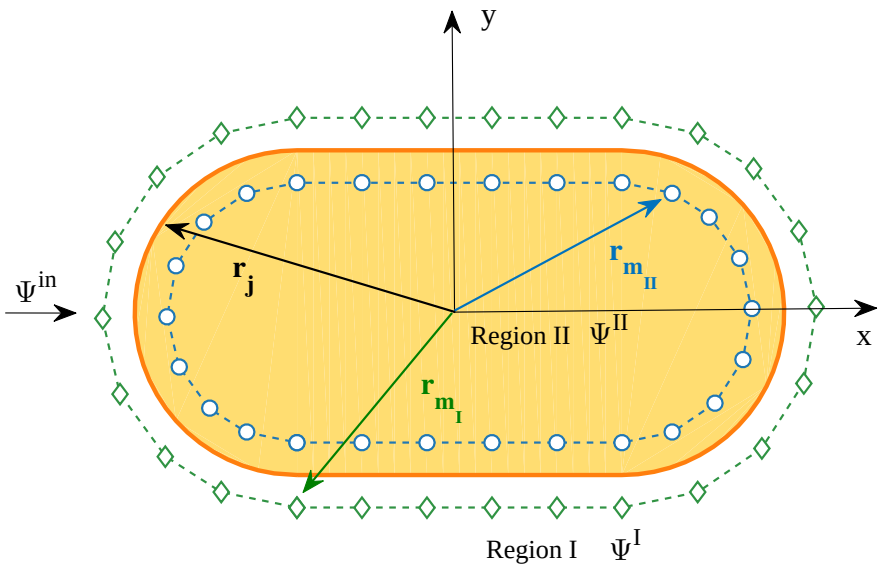

Figure 6.13: A schematic illustration of the basics of the MMP method. Shown is placement of poles (fictitious sources) inside and outside of a magnetic structure of arbitrary shape. The scattering spinor wavefunctions inside (outside) of the structure are determined by the poles outside (inside) of the structure.

and $C_l^{m_I}$ are the expansion coefficients. The scattered wavefunction in region I is

$$\Psi^I(\boldsymbol{r}) \equiv \begin{pmatrix} \psi_1^I \\ \psi_2^I \end{pmatrix} = \sum_{m_{II}} \sum_l \frac{C_l^{m_{II}}}{\sqrt{2}} \begin{pmatrix} H_{l-1}^{(1)}(k_I d_{m_{II}}) e^{-i\theta_{m_{II}}} \\ \tau_I H_l^{(1)}(k_I d_{m_{II}}) \end{pmatrix} e^{il\theta_{m_{II}}}, \tag{6.20}$$

where

$$\begin{aligned} k_I &= \sqrt{(E - \Delta^2 n_I^2}/\hbar v_F, \\ \tau_I &= -\hbar v_F k_I/(E - \Delta n_I), \\ d_{m_{II}} &= |\boldsymbol{r} - \boldsymbol{r}_{m_{II}}|, \\ \theta_{m_{II}} &= \text{Angle}(\boldsymbol{r} - \boldsymbol{r}_{m_{II}}), \end{aligned}$$

and $C_l^{m_{II}}$ are the expansion coefficients. The incident plane wave propagating along the direction defined by an angle β with the x axis in region I is given by

$$\Psi^{in}(\boldsymbol{r}) \equiv \begin{pmatrix} \psi_1^{in} \\ \psi_2^{in} \end{pmatrix} = \frac{1}{\sqrt{2}} \begin{pmatrix} 1 \\ -i\tau_I e^{i\beta} \end{pmatrix} e^{i(k_x r\cos\theta + k_y r \sin\theta)}. \tag{6.21}$$

Matching the boundary conditions

$$(\psi_1^I + \psi_1^{in})|_{r_j\in\Gamma} = \psi_1^{II}|_{r_j\in\Gamma} \tag{6.22}$$

$$(\psi_2^I + \psi_2^{in})|_{r_j\in\Gamma} = \psi_2^{II}|_{r_j\in\Gamma}, \tag{6.23}$$

we get

$$\begin{aligned} & \sum_{m_{II}}\sum_{l} C_l^{m_{II}} \frac{1}{\sqrt{2}} \tau_I H_l^{(1)}(k_I|\boldsymbol{r}_j - \boldsymbol{r}_{m_{II}}|) e^{il\theta_{m_{II}}} \\ - & \sum_{m_I}\sum_{l} C_l^{m_I} \frac{1}{\sqrt{2}} \tau_{II} H_l^{(1)}(k_{II}|\boldsymbol{r}_j - \boldsymbol{r}_{m_I}|) e^{il\theta_{m_I}} \\ = & \frac{i}{\sqrt{2}} \tau_I e^{i\beta} e^{i\boldsymbol{k_I}\boldsymbol{r}} \end{aligned} \tag{6.24}$$

and

$$\sum_{m_{II}}\sum_{l} C_l^{m_{II}} \frac{1}{\sqrt{2}} H_{l-1}^{(1)}(k_I|\boldsymbol{r}_j - \boldsymbol{r}_{m_{II}}|) e^{i(l-1)\theta_{m_{II}}} \tag{6.25}$$

$$\begin{aligned} - & \sum_{m_I}\sum_{l} C_l^{m_I} \frac{1}{\sqrt{2}} H_{l-1}^{(1)}(k_{II}|\boldsymbol{r}_j - \boldsymbol{r}_{m_I}|) e^{i(l-1)\theta_{m_I}} \\ = & -\frac{1}{\sqrt{2}} \tau_I e^{i\beta} e^{i\boldsymbol{k_I}\boldsymbol{r}}, \end{aligned} \tag{6.26}$$

which can be cast in a compact form as

$$\sum_{m_{II}}\sum_{l} {}^j A^I_{lm_{II}} C_l^{m_{II}} - \sum_{m_I}\sum_{l} {}^j A^{II}_{lm_I} C_l^{m_I} = -{}^j\psi^{in}_{II} \tag{6.27}$$

$$\sum_{m_{II}}\sum_{l} {}^j B^I_{lm_{II}} C_l^{m_{II}} - \sum_{m_I}\sum_{l} {}^j B^{II}_{lm_I} C_l^{m_I} = -{}^j\psi^{in}_{I} \tag{6.28}$$

where

$$ {}^{j}A^{I}_{lm_{II}} = \frac{1}{\sqrt{2}}\tau_I H^{(1)}_l(k_I|\boldsymbol{r}_j - \boldsymbol{r}_{m_{II}}|)e^{il\theta_{m_{II}}}, \tag{6.29} $$

$$ {}^{j}A^{II}_{lm_I} = \frac{1}{\sqrt{2}}\tau_{II} H^{(1)}_l(k_{II}|\boldsymbol{r}_j - \boldsymbol{r}_{m_I}|)e^{il\theta_{m_I}}, \tag{6.30} $$

$$ {}^{j}B^{I}_{lm_{II}} = \frac{1}{\sqrt{2}} H^{(1)}_{l-1}(k_I|\boldsymbol{r}_j - \boldsymbol{r}_{m_{II}}|)e^{i(l-1)\theta_{m_{II}}}, \tag{6.31} $$

$$ {}^{j}B^{II}_{lm_I} = \frac{1}{\sqrt{2}} H^{(1)}_{l-1}(k_{II}|\boldsymbol{r}_j - \boldsymbol{r}_{m_I}|)e^{i(l-1)\theta_{m_I}}, \tag{6.32} $$

and

$$ {}^{j}\psi^{in}_2 = -\frac{i}{\sqrt{2}}\tau_I e^{i\beta} e^{i\boldsymbol{k}_I \boldsymbol{r}_j}, \tag{6.33} $$

$$ {}^{j}\psi^{in}_1 = \frac{1}{\sqrt{2}} e^{i\boldsymbol{k}_I \boldsymbol{r}_j}. \tag{6.34} $$

In principle, the set consists of an infinite number of equations with an infinite number of undetermined expansion coefficients $C^{m_{II}}_l$ and $C^{m_I}_l$. To solve the system numerically, finite truncation is necessary. We set the total number of boundary points to be J with M_I and M_{II} poles in regions I and II, respectively, and $l \to [-L, L]$ for all the multipoles. The process leads to the following finite-dimensional matrix equation:

$$ \mathbb{M}_{2J\times N} \cdot C_{N\times 1} = -Y_{2J\times 1}, \tag{6.35} $$

where $N = (2L+1) \times (M_I + M_{II}) = N_I + N_{II}$,

$$C_{N\times 1} = \left(\begin{array}{c} C_{-L}^{1_{II}} \\ \vdots \\ C_{l}^{1_{II}} \\ C_{l}^{2_{II}} \\ \vdots \\ C_{l}^{M_{II}} \\ \vdots \\ C_{L}^{M_{II}} \\ \hline \\ C_{-L}^{1_{I}} \\ \vdots \\ C_{l}^{1_{I}} \\ C_{l}^{2_{I}} \\ \vdots \\ C_{l}^{M_{I}} \\ \vdots \\ C_{L}^{M_{I}} \end{array}\right)_{N\times 1} \quad ; \quad Y_{2J\times 1} = \left(\begin{array}{c} {}^{1}\psi_{2}^{in} \\ \vdots \\ {}^{j}\psi_{2}^{in} \\ \vdots \\ {}^{J}\psi_{2}^{in} \\ \hline \\ {}^{1}\psi_{1}^{in} \\ \vdots \\ {}^{j}\psi_{1}^{in} \\ \vdots \\ {}^{J}\psi_{1}^{in} \end{array}\right)_{2J\times 1} \tag{6.36}$$

and

$$\mathbb{M}_{2J\times N} = \left(\begin{array}{c|c} \mathbb{A}^{(I)} & -\mathbb{A}^{(II)} \\ \hline \mathbb{B}^{(I)} & -\mathbb{B}^{(II)} \end{array}\right) \tag{6.37}$$

with

$$\mathbb{A}^{(\tau)} = \begin{pmatrix} {}^{1}A^{(\tau)}_{-L1_{\overline{\tau}}} & \cdots & {}^{1}A^{(\tau)}_{l1_{\overline{\tau}}} & {}^{1}A^{(\tau)}_{l2_{\overline{\tau}}} & \cdots & {}^{1}A^{(\tau)}_{lM_{\overline{\tau}}} & \cdots & {}^{1}A^{(\tau)}_{LM_{\overline{\tau}}} \\ {}^{2}A^{(\tau)}_{-L1_{\overline{\tau}}} & \cdots & {}^{2}A^{(\tau)}_{l1_{\overline{\tau}}} & {}^{2}A^{(\tau)}_{l2_{\overline{\tau}}} & \cdots & {}^{2}A^{(\tau)}_{lM_{\overline{\tau}}} & \cdots & {}^{2}A^{(\tau)}_{LM_{\overline{\tau}}} \\ \vdots & \cdots & \vdots & \vdots & \cdots & \vdots & \cdots & \vdots \\ {}^{j}A^{(\tau)}_{-L1_{\overline{\tau}}} & \cdots & {}^{j}A^{(\tau)}_{l1_{\overline{\tau}}} & {}^{j}A^{(\tau)}_{l2_{\overline{\tau}}} & \cdots & {}^{j}A^{(\tau)}_{lM_{\overline{\tau}}} & \cdots & {}^{j}A^{(\tau)}_{LM_{\overline{\tau}}} \\ \vdots & \cdots & \vdots & \vdots & \cdots & \vdots & \cdots & \vdots \\ {}^{J}A^{(\tau)}_{-L1_{\overline{\tau}}} & \cdots & {}^{J}A^{(\tau)}_{l1_{\overline{\tau}}} & {}^{J}A^{(\tau)}_{l2_{\overline{\tau}}} & \cdots & {}^{J}A^{(\tau)}_{lM_{\overline{\tau}}} & \cdots & {}^{J}A^{(\tau)}_{LM_{\overline{\tau}}} \end{pmatrix}. \tag{6.38}$$

$$\mathbb{B}^{(\tau)} = \begin{pmatrix} {}^{1}B^{(\tau)}_{-L1_{\overline{\tau}}} & \cdots & {}^{1}B^{(\tau)}_{l1_{\overline{\tau}}} & {}^{1}B^{(\tau)}_{l2_{\overline{\tau}}} & \cdots & {}^{1}B^{(\tau)}_{lM_{\overline{\tau}}} & \cdots & {}^{1}B^{(\tau)}_{LM_{\overline{\tau}}} \\ {}^{2}B^{(\tau)}_{-L1_{\overline{\tau}}} & \cdots & {}^{2}B^{(\tau)}_{l1_{\overline{\tau}}} & {}^{2}B^{(\tau)}_{l2_{\overline{\tau}}} & \cdots & {}^{2}B^{(\tau)}_{lM_{\overline{\tau}}} & \cdots & {}^{2}B^{(\tau)}_{LM_{\overline{\tau}}} \\ \vdots & \cdots & \vdots & \vdots & \cdots & \vdots & \cdots & \vdots \\ {}^{j}B^{(\tau)}_{-L1_{\overline{\tau}}} & \cdots & {}^{j}B^{(\tau)}_{l1_{\overline{\tau}}} & {}^{j}B^{(\tau)}_{l2_{\overline{\tau}}} & \cdots & {}^{j}B^{(\tau)}_{lM_{\overline{\tau}}} & \cdots & {}^{j}B^{(\tau)}_{LM_{\overline{\tau}}} \\ \vdots & \cdots & \vdots & \vdots & \cdots & \vdots & \cdots & \vdots \\ {}^{J}B^{(\tau)}_{-L1_{\overline{\tau}}} & \cdots & {}^{J}B^{(\tau)}_{l1_{\overline{\tau}}} & {}^{J}B^{(\tau)}_{l2_{\overline{\tau}}} & \cdots & {}^{J}B^{(\tau)}_{lM_{\overline{\tau}}} & \cdots & {}^{J}B^{(\tau)}_{LM_{\overline{\tau}}} \end{pmatrix}. \tag{6.39}$$

As the expansions are generally nonorthogonal, more equations are required than the number of unknowns to enable reduction of an overdetermined matrix system with $2J \gg N$, which can be solved by the pseudoinverse algorithm: $\boldsymbol{C} = -\text{pinv}(\mathbb{M} * \boldsymbol{Y})$.

Chapter 7

FANO RESONANCE IN MOLECULAR TRANSPORT

We investigate spin transport through a chiral polyacetylene molecule and uncover the emergence of spin Fano resonances as a manifestation of the chiral induced spin selectivity (CISS) effect. Initializing the electrons through optical excitation, we derive the Fano resonance formula associated with the spin polarization. Computations reveal that quasidegeneracy is common in this complex molecule system. A remarkable phenomenon is the generation of pronounced spin Fano resonances due to the contributions of the two near-degeneracy states. We also find that the Fano resonance width increases linearly with the coupling strength between the molecule and the lead. Our findings lead to new insights into the role of CISS effect in complex molecules from the perspective of transport and resonance of spin polarization, paving the way for chiral molecule based spintronics applications.

7.1 Introduction

In this Chapter, we investigate spin transport through a chiral polyacetylene molecule. Calculating the spin polarization versus the energy, we find the occurrence of a large number of sharp resonances that are characteristic of generalized Fano resonances. To establish this, we derive the Fano formula and test its applicability to the numerically observed resonance profiles. In the conventional Fano formula, typically a resonance occurs at a single energy level. However, the structural complexity of the chiral molecule stipulates that level degeneracy is common where, for instance, two energy levels can be arbitrarily close to each other. Our computations reveal that the quasidegeneracy can lead to large spin polarization manifested as a resonance.

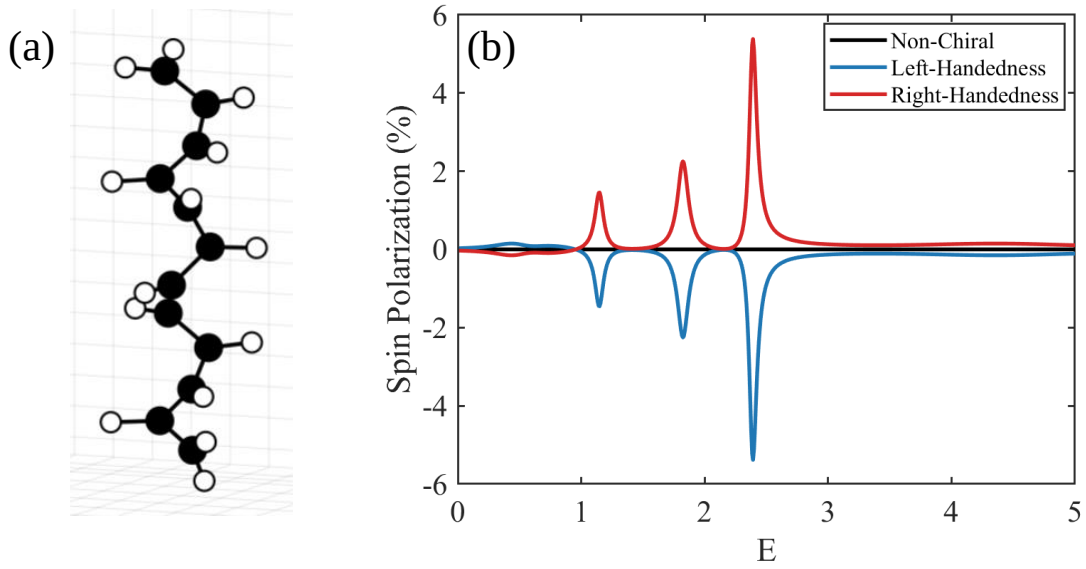

Figure 7.1: A chiral molecule and CISS effect. (a) Illustration of a twisted polyacetylene molecule. (b) Spin polarization with respect to energy for a non-chiral ($\theta = \pi$), a left-handedness ($\theta = \pi/2$), and a right-handedness ($\theta = -\pi/2$) molecule, respectively. The number of carbon atoms is $N = 8$.

We find that, in order to explain the resonant enhancement in the spin polarization, both levels must be taken into account, and this leads to a generalized Fano formula. Instigating proper approximations enables us to calculate the resonance width. Based on the energy level spacing and the resonance width, we obtain a criterion to determine whether one or two energy levels are necessary to account for an observed resonance. To our knowledge, prior to our work, spin Fano resonance associated with spin transport in chiral molecules had not been studied. Our finding of Fano resonance induced and enhanced spin polarization provides new insights into understanding and exploiting CISS in electronic transport through complex molecules.

7.2 Model and Method

We consider a carbohydrate molecule, namely polyacetylene, a flat chain of conjugated carbon atoms that form a helix with a fixed radius, where each atom is oriented

an angle ϕ apart [172]. The pitch of the helix is held fixed so that the geometrical structure of the chain is described by a single parameter: the angle ϕ. An extra hydrogen atom is attached to the carbon atom at both ends. In the limit $\phi \to \pi$, the resulting molecule becomes nonchiral. Each end of the chain is connected to a gold electrode. The starting point is electrons prepared in a localized state in the left lead. A current flows through the molecule while the electrons either pass through the whole molecule to the right lead or is back scattered into the left. A schematic figure of the twisted polyacetylene molecule is shown in Fig. 7.1(a).

We employ the standard tight-binding model for the chiral molecule with the generic set of Slater-Koster hopping parameters [172]. For simplicity, we assume that the leads connect only to the outermost carbon atom in the chain. The carbon atoms are modeled using the four $n = 2$ orbitals: $2s$, $2p_x$, $2p_y$ and $2p_z$, such that the spinless couplings Γ are positive, semidefinite 4×4 matrices. We set the coupling to be diagonal to stipulate that chirality is originated from the molecule, not from the chiral coupling to the lead. In addition, to ensure that the SOC is small in comparison with the coupling to the leads, the diagonal components are set to be 100λ, i.e., a hundred times the atomic SOC of a carbon atom, where $\lambda = 6$ meV.

The general Hamiltonian for the complex molecule can be written as a sum of three terms:

$$\hat{H} = \hat{H}_o + \hat{H}_{SO} + \Sigma, \tag{7.1}$$

where $\hat{H}_o$ is the molecular spinless Hamiltonian, $\hat{H}_{SO}$ is the Hamiltonian for spin-orbit coupling (SOC), and Σ is the lead induced self-energy term. Explicitly, the SOC Hamiltonian can be written as

$$\hat{H}_{SO} = \lambda \boldsymbol{L} \cdot \boldsymbol{\sigma}/\hbar,$$

where $\boldsymbol{L}$ is the orbital angular momentum vector and $\boldsymbol{\sigma}$ is the vector of Pauli matri-

ces. The Hamiltonian $\hat{H}$ preserves the time reversal symmetry and there is Kramers degeneracy with the two-fold degenerate state $|n\rangle$ and its time reversed state $\hat{\Theta}|n\rangle$.

Based on the Hamiltonian, we use the non-equilibrium Green's function (NEGF) method to calculate the charge and spin current [172]:

$$T = \mathrm{Tr}[\frac{1+\boldsymbol{a}\cdot\boldsymbol{\sigma}}{2}\gamma_L G_M^\dagger \Gamma_R G_M], \tag{7.2}$$

$$S = \mathrm{Tr}[\frac{1+\boldsymbol{a}\cdot\boldsymbol{\sigma}}{2}\gamma_L G_M^\dagger \Gamma_R \boldsymbol{\sigma}\cdot\boldsymbol{n} G_M], \tag{7.3}$$

where

$$G_M = \frac{1}{E - H_M + i\Gamma_L/2 + i\Gamma_R/2}. \tag{7.4}$$

The spin polarization is defined as [173]

$$P = \frac{S}{T} = \frac{T_{\uparrow\uparrow} + T_{\uparrow\downarrow} - T_{\downarrow\uparrow} - T_{\downarrow\downarrow}}{T_{\uparrow\uparrow} + T_{\uparrow\downarrow} + T_{\downarrow\uparrow} + T_{\downarrow\downarrow}}. \tag{7.5}$$

We calculate the spin polarization as a function of incident energy E for different twist angles, with a representative example shown in Fig. 7.1(b). When there is no chirality, the spin polarization is zero. However, when the molecule is chiral, there are spin polarization peaks, whose values have opposite signs for the two opposite handedness.

7.3 Spin Fano Resonance in Chiral Molecules

Figure 7.1(b) illustrates that there are resonant peaks in the spin polarization curve, associated with which are relatively values of spin polarization. We now derive the Fano formula for spin polarization based on the NEGF method. Because of the inclusion of the self-energy term Σ, the Hamiltonian is non-Hermitian with complex eigenvalues as well as non-identical left and right eigenstates. The eigenequations for

the right and left eigenstates are

$$\hat{H}|\psi_{\alpha,\mu}\rangle = \epsilon_\alpha|\psi_{\alpha,\mu}\rangle, \tag{7.6}$$

$$\langle\phi_{\alpha,\mu}|\hat{H} = \langle\phi_{\alpha,\mu}|\epsilon_\alpha, \tag{7.7}$$

where $\mu = 1, 2$ denotes the two Kramer's degenerate eigenstates. The eigenstates $|\psi_{\alpha,\mu}\rangle$ and $|\phi_{\alpha,\mu}\rangle$ constitute a biorthonormal basis set under the normalization

$$|\Phi_{\alpha,\mu}\rangle = |\phi_{\alpha,\mu}\rangle/\langle\psi_{\beta,\nu}|\phi_{\alpha,\mu}\rangle. \tag{7.8}$$

The biorthonormal conditions are

$$\langle\Phi_{\alpha,\mu}|\psi_{\beta,\nu}\rangle = \langle\psi_{\alpha,\mu}|\Phi_{\beta,\nu}\rangle = \delta_{\alpha,\beta}\delta_{\mu,\nu}, \tag{7.9}$$

with the completeness relation of the eigenwavefunctions

$$\sum_\mu \sum_\alpha |\psi_{\alpha,\mu}\rangle\langle\Phi_{\alpha,\mu}| = \sum_\mu \sum_\alpha |\Phi_{\alpha,\mu}\rangle\langle\psi_{\alpha,\mu}| = 1. \tag{7.10}$$

Using Eqs. (7.9) and (7.10), we have the Green's function for the molecule as

$$\begin{aligned}
G^R(\boldsymbol{r},\boldsymbol{r}') &= \langle\boldsymbol{r}|\frac{1}{E-\hat{H}_s}|\boldsymbol{r}'\rangle \\
&= \sum_{\alpha,\mu}\sum_{\beta,\nu}\langle\boldsymbol{r}|\psi_{\alpha,\mu}\rangle\langle\Phi_{\alpha,\mu}\frac{1}{E-\hat{H}_s}|\psi_{\beta,\nu}\rangle\langle\Phi_{\beta,\nu}|\boldsymbol{r}'\rangle \\
&= \sum_{\alpha,\mu}\sum_{\beta,\nu}\psi_{\alpha,\mu}(\boldsymbol{r})\frac{1}{E-\epsilon_\beta}\delta_{\alpha,\beta}\delta_{\mu,\nu}\Phi^\dagger_{\beta,\nu}(\boldsymbol{r}') \\
&= \sum_\mu\sum_\alpha \frac{\psi_{\alpha,\mu}(\boldsymbol{r})\Phi^\dagger_{\alpha,\mu}(\boldsymbol{r}')}{E-\epsilon_\alpha} \\
&= \begin{pmatrix} G^R_{\uparrow\uparrow}(\boldsymbol{r},\boldsymbol{r}') & G^R_{\uparrow\downarrow}(\boldsymbol{r},\boldsymbol{r}') \\ G^R_{\downarrow\uparrow}(\boldsymbol{r},\boldsymbol{r}') & G^R_{\downarrow\downarrow}(\boldsymbol{r},\boldsymbol{r}') \end{pmatrix},
\end{aligned} \tag{7.11}$$

where the eigenfunctions are

$$\Phi_{\alpha,\mu}(\boldsymbol{r}') = \begin{pmatrix} \Phi^{\uparrow}_{\alpha,\mu}(\boldsymbol{r}') \\ \Phi^{\downarrow}_{\alpha,\mu}(\boldsymbol{r}') \end{pmatrix}, \tag{7.12}$$

$$\psi_{\alpha,\mu}(\boldsymbol{r}) = \begin{pmatrix} \psi^{\uparrow}_{\alpha,\mu}(\boldsymbol{r}) \\ \psi^{\downarrow}_{\alpha,\mu}(\boldsymbol{r}) \end{pmatrix}. \tag{7.13}$$

The spin-resolved Green's function can be written as

$$G^{R}_{\sigma\sigma'}(\boldsymbol{r},\boldsymbol{r}') = \sum_{\mu=1,2}\sum_{\alpha} \frac{\psi^{\sigma}_{\alpha,\mu}(\boldsymbol{r})\Phi^{\sigma'\dagger}_{\alpha,\mu}(\boldsymbol{r}')}{E-\epsilon_{\alpha}}. \tag{7.14}$$

We use the Fisher-Lee relation to connect the S matrix with the Green's function [178, 314, 315] and then separate the fast from the slow variables. Let E_0 be the energy. If E_0 approaches an eigenenergy of the corresponding closed system, a pole will arise in R, so we can separate the sum into two terms: one term slowly varying and the other rapidly changing, where the former acts effectively as the background and the latter varies rapidly in the small energy interval. Explicitly, we have

$$\begin{aligned} R^{\sigma\sigma'}_{nm} = R^{0,\sigma\sigma'}_{nm} + R^{1,\sigma\sigma'}_{nm} &= \sum_{\mu=1,2}\sum_{\beta\neq\alpha} \frac{\psi^{\sigma}_{\beta n,\mu}(x_r)\Phi^{\sigma'\dagger}_{\beta m,\mu}(x_l)}{E-\epsilon_{\beta}} \\ &+ \sum_{\mu=1,2} \frac{\psi^{\sigma}_{\alpha n,\mu}(x_r)\Phi^{\sigma'\dagger}_{\alpha m,\mu}(x_l)}{E-\epsilon_{\alpha}}. \end{aligned} \tag{7.15}$$

The transmission coefficient is given by

$$\boldsymbol{t}_{\sigma\sigma'} = i\sqrt{V_q} \times R^{\sigma\sigma'} \times \sqrt{V_p}, \tag{7.16}$$

where V_q and V_p are Fermi velocities and we set $V_q = V_p = 1$. The transmission coefficient can be expanded as

$$\boldsymbol{t}_{\sigma\sigma'} = \boldsymbol{t}^{0}_{\sigma\sigma'} + \boldsymbol{t}^{1}_{\sigma\sigma'}. \tag{7.17}$$

For each transmission component, we can write

$$\begin{aligned} T_{\sigma\sigma'} &= \mathrm{Tr}(t_{\sigma\sigma'}t^{\dagger}_{\sigma\sigma'}) \\ &= \mathrm{Tr}[(t^{0}_{\sigma\sigma'}+t^{1}_{\sigma\sigma'})(t^{0\dagger}_{\sigma\sigma'}+t^{1\dagger}_{\sigma\sigma'})] \\ &= \mathrm{Tr}(t^{0}_{\sigma\sigma'}t^{0\dagger}_{\sigma\sigma'})+\mathrm{Tr}(t^{0}_{\sigma\sigma'}t^{1\dagger}_{\sigma\sigma'}) \\ &\quad +\mathrm{Tr}(t^{1}_{\sigma\sigma'}t^{0\dagger}_{\sigma\sigma'})+\mathrm{Tr}(t^{1}_{\sigma\sigma'}t^{1\dagger}_{\sigma\sigma'}) \\ &= T^{00}_{\sigma\sigma'}+T^{01}_{\sigma\sigma'}+T^{10}_{\sigma\sigma'}+T^{11}_{\sigma\sigma'}. \end{aligned} \tag{7.18}$$

We impose the following approximations:

$$T^{00}_{\sigma\sigma'}(E) \approx T^{00}_{\sigma\sigma'}(E_0), \tag{7.19}$$

$$T^{01}_{\sigma\sigma'}(E) = T^{01}_{\sigma\sigma'}(E_0)\frac{E_0-E_\alpha-i\gamma_\alpha}{E-E_\alpha-i\gamma_\alpha} = T^{01}_{\sigma\sigma'}(E_0)\frac{\epsilon_0-i}{\epsilon-i}, \tag{7.20}$$

$$T^{10}_{\sigma\sigma'}(E) = T^{10}_{\sigma\sigma'}(E_0)\frac{E_0-E_\alpha+i\gamma_\alpha}{E-E_\alpha+i\gamma_\alpha} = T^{10}_{\sigma\sigma'}(E_0)\frac{\epsilon_0+i}{\epsilon+i}, \tag{7.21}$$

$$T^{11}_{\sigma\sigma'}(E) = T^{11}_{\sigma\sigma'}(E_0)\frac{(E_0-E_\alpha)^2+\gamma_\alpha^2}{(E-E_\alpha)^2+\gamma_\alpha^2} = T^{11}_{\sigma\sigma'}(E_0)\frac{\epsilon_0^2+1}{\epsilon^2+1}, \tag{7.22}$$

where $\epsilon \equiv (E-E_\alpha)/\gamma_\alpha$ and $\epsilon_0 \equiv (E_0-E_\alpha)/\gamma_\alpha$. For $E_0 = E_\alpha$, we have $\epsilon_0 = 0$. For the spin transmission S, we obtain

$$\begin{aligned} S &= T_{\uparrow\uparrow}+T_{\uparrow\downarrow}-T_{\downarrow\uparrow}-T_{\downarrow\downarrow} \\ &= [T^{00}_{\uparrow\uparrow}+T^{00}_{\uparrow\downarrow}-T^{00}_{\downarrow\uparrow}-T^{00}_{\downarrow\downarrow}] \\ &+ [T^{01}_{\uparrow\uparrow}+T^{01}_{\uparrow\downarrow}-T^{01}_{\downarrow\uparrow}-T^{01}_{\downarrow\downarrow}]\frac{\epsilon_0-i}{\epsilon-i} \\ &+ [T^{10}_{\uparrow\uparrow}+T^{10}_{\uparrow\downarrow}-T^{10}_{\downarrow\uparrow}-T^{10}_{\downarrow\downarrow}]\frac{\epsilon_0+i}{\epsilon+i} \\ &+ [T^{11}_{\uparrow\uparrow}+T^{11}_{\uparrow\downarrow}-T^{11}_{\downarrow\uparrow}-T^{11}_{\downarrow\downarrow}]\frac{\epsilon_0^2+1}{\epsilon^2+1} \\ &= T^{00}_{s}(E)+T^{01}_{s}(E)+T^{10}_{s}(E)+T^{11}_{s}(E) \\ &= T^{00}_{s}(E_0)+T^{01}_{s}(E_0)\frac{\epsilon_0-i}{\epsilon-i}+T^{10}_{s}(E_0)\frac{\epsilon_0+i}{\epsilon+i} \\ &+ T^{11}_{s}(E)\frac{\epsilon_0^2+1}{\epsilon^2+1}. \end{aligned} \tag{7.23}$$

Setting $\epsilon_0 = 0$ and denoting

$$\Delta T_s = T_s^{01}(E_0) + T_s^{10}(E_0) + T_s^{11}(E_0), \tag{7.24}$$

$$q_s = \frac{i}{2}\frac{T_s^{10}(E_0) - T_s^{01}(E_0)}{\Delta T_s}, \tag{7.25}$$

we get

$$\begin{aligned} S &= T_s^{00}(E_0)\frac{(\epsilon + \frac{q_s \Delta T_s}{T_s^{00}})^2 + (1 + \frac{\Delta T_s}{T_s^{00}} - \frac{q_s^2 \Delta T_s^2}{(T_s^{00})^2})}{\epsilon^2 + 1} \\ &= T_s^{00}\frac{(\epsilon + x_s)^2 + y_s}{\epsilon^2 + 1}, \end{aligned} \tag{7.26}$$

where

$$x_s = \frac{q_s \Delta T_s}{T_s^{00}}, \tag{7.27}$$

$$y_s = 1 + \frac{\Delta T_s}{T_s^{00}} - \frac{q_s^2 \Delta T_s^2}{(T_s^{00})^2}. \tag{7.28}$$

Similarly, for spin transmission T, we have

$$\begin{aligned} T &= T_{\uparrow\uparrow} + T_{\uparrow\downarrow} + T_{\downarrow\uparrow} + T_{\downarrow\downarrow} \\ &= [T_{\uparrow\uparrow}^{00} + T_{\uparrow\downarrow}^{00} + T_{\downarrow\uparrow}^{00} + T_{\downarrow\downarrow}^{00}] \\ &+ [T_{\uparrow\uparrow}^{01} + T_{\uparrow\downarrow}^{01} + T_{\downarrow\uparrow}^{01} + T_{\downarrow\downarrow}^{01}]\frac{\epsilon_0 - i}{\epsilon - i} \\ &+ [T_{\uparrow\uparrow}^{10} + T_{\uparrow\downarrow}^{10} + T_{\downarrow\uparrow}^{10} + T_{\downarrow\downarrow}^{10}]\frac{\epsilon_0 + i}{\epsilon + i} \\ &+ [T_{\uparrow\uparrow}^{11} + T_{\uparrow\downarrow}^{11} + T_{\downarrow\uparrow}^{11} + T_{\downarrow\downarrow}^{11}]\frac{\epsilon_0^2 + 1}{\epsilon^2 + 1} \\ &= T_c^{00}(E) + T_c^{01}(E) + T_c^{10}(E) + T_c^{11}(E) \\ &= T_c^{00}(E_0) + T_c^{01}(E_0)\frac{\epsilon_0 - i}{\epsilon - i} + T_c^{10}(E_0)\frac{\epsilon_0 + i}{\epsilon + i} \\ &+ T_c^{11}(E)\frac{\epsilon_0^2 + 1}{\epsilon^2 + 1}. \end{aligned} \tag{7.29}$$

Setting $\epsilon_0 = 0$ and denoting

$$\Delta T_c = T_c^{01}(E_0) + T_c^{10}(E_0) + T_c^{11}(E_0), \tag{7.30}$$

$$q_c = \frac{i}{2}\frac{T_c^{10}(E_0) - T_c^{01}(E_0)}{\Delta T_c}, \tag{7.31}$$

we get

$$T = T_c^{00}(E_0)\frac{(\epsilon + \frac{q_c\Delta T_c}{T_c^{00}})^2 + (1 + \frac{\Delta T_c}{T_c^{00}} - \frac{q_c^2\Delta T_c^2}{(T_c^{00})^2})}{\epsilon^2 + 1}, \tag{7.32}$$

where

$$x_c = \frac{q_c\Delta T_c}{T_c^{00}}, \tag{7.33}$$

$$y_c = 1 + \frac{\Delta T_c}{T_c^{00}} - \frac{q_c^2\Delta T_c^2}{(T_c^{00})^2}. \tag{7.34}$$

The spin polarization can be written as

$$\begin{aligned} P = \frac{S}{T} &= \frac{T_s^{00}}{T_c^{00}}\frac{(\epsilon + x_s)^2 + y_s}{(\epsilon + x_c)^2 + y_c} \\ &= \frac{T_s^{00}}{T_c^{00}}\frac{(\frac{\epsilon + x_c}{\sqrt{y_c}} + \frac{x_s - x_c}{\sqrt{y_c}})^2 + \frac{y_s}{y_c}}{(\frac{\epsilon + x_c}{\sqrt{y_c}})^2 + 1} \\ &= \alpha\frac{(\epsilon_f + q_f)^2 + y_f}{\epsilon_f^2 + 1}, \end{aligned} \tag{7.35}$$

where

$$\alpha = \frac{T_s^{00}}{T_c^{00}}, \tag{7.36}$$

$$\epsilon_f = \frac{\epsilon + x_c}{\sqrt{y_c}}, \tag{7.37}$$

$$q_f = \frac{x_s - x_c}{\sqrt{y_c}}, \tag{7.38}$$

$$y_f = \frac{y_s}{y_c}. \tag{7.39}$$

Equation (7.35) is the Fano resonance formula for spin polarization. To provide numerical validation, we first consider a molecule with eight carbon atoms at the twist angle $\pi/4$. Selecting a peak with energy about $E = 1.68$, we see that the Fano formula (7.35) matches remarkably well with the numerical curve for both the spin polarization and charge transmission, as shown in Figs. 7.2(a) and 7.2(b). From the energy levels in Fig. 7.2(c), we have that the two Kramers degenerate states with real part of the energy about 1.68 contribute to the spin Fano resonance.

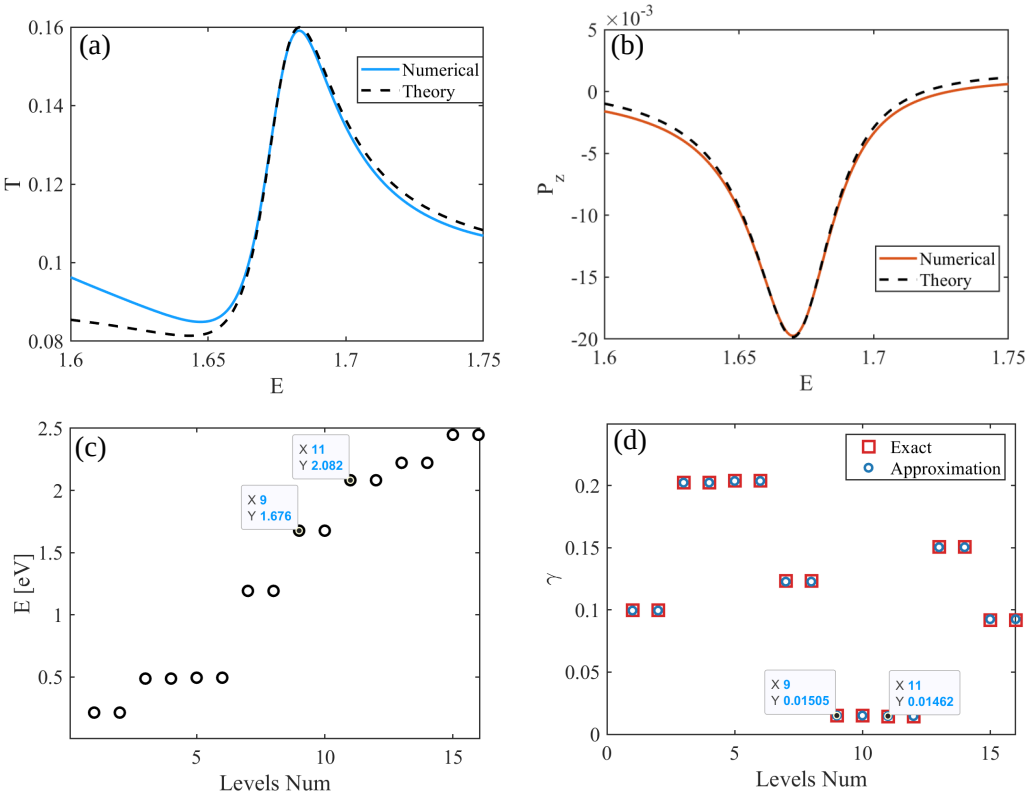

Figure 7.2: Spin Fano resonance in a chiral molecule. (a) Fano resonance curve for electronic transmission, where the blue solid and black dashed curves are numerical and theoretical results, respectively. (b) Spin Fano resonance curve. The red solid and black dashed curves are numerical and theoretical results, respectively. (c,d) Real and imaginary parts of the total eigenenergies in a certain range, respectively. The number of carbon atoms is $N = 8$ and the twist angle is $\theta = \pi/4$.

The width of the Fano resonance peak can also be calculated through a perturbation approach. In particular, with the eigenfunctions in Eqs. (7.12) and (7.13), and treating the self-energy Σ^R as a perturbation, we expand the eigenenergies and the eigenstates as

$$\epsilon_\alpha = \epsilon_{0,\alpha} - \delta_\alpha - i\gamma_\alpha, \tag{7.40}$$

$$|\psi_{\alpha,\mu}\rangle = |\psi_{0\alpha,\mu}\rangle - |\psi_{r\alpha,,\mu}\rangle - i|\psi_{i\alpha,\mu}\rangle. \tag{7.41}$$

Substituting Eqs. (7.40) and (7.41) into Eq. (7.6), we get

$$\begin{aligned}&(\hat{H}_c + \Sigma^R)(|\psi_{0\alpha,\mu}\rangle - |\psi_{r\alpha,\mu}\rangle - i|\psi_{i\alpha,\mu}\rangle)\\ &= (\epsilon_{0,\alpha} - \delta_\alpha - i\gamma_\alpha)(|\psi_{0\alpha,\mu}\rangle - |\psi_{r\alpha,\mu}\rangle - i|\psi_{i\alpha,\mu}\rangle).\end{aligned} \tag{7.42}$$

After some approximations, we obtain

$$\begin{aligned}\delta_\alpha + i\gamma_\alpha &\approx -\sum_\mu \langle\psi_{0\alpha,\mu}|\Sigma^R|\psi_{0\alpha,\mu}\rangle\\ &= -\sum_{\mu,\sigma}\langle\psi^\sigma_{0\alpha,\mu}|\Sigma^R_0|\psi^\sigma_{0\alpha,\mu}\rangle.\end{aligned} \tag{7.43}$$

The resonance width γ_α can be obtained as

$$\gamma_\alpha = -\mathrm{Im}\Big(\sum_{\mu,\sigma}\langle\psi^\sigma_{0\alpha,\mu}|\Sigma^R_0|\psi^\sigma_{0\alpha,\mu}\rangle\Big). \tag{7.44}$$

The width predicted by this formula agrees with the numerical value, as shown in Fig. 7.2(d).

7.4 Degeneracy enhanced spin Fano resonance

The Fano resonances discussed above result from a single energy level (including the case of Kramers' degeneracy of two identical levels). For a complex molecule, the situation can arise where several nearby energy levels collectively contribute to a resonance. This typically occurs for different twist angles when the number of carbon atoms in the molecule is relatively large. To treat such a case, we include more related Green's function terms in the transmission coefficient in Eq. (7.15). The modified form can be written as

$$\begin{aligned}R^{\sigma\sigma'}_{nm} = R^{0,\sigma\sigma'}_{nm} + R^{1,\sigma\sigma'}_{nm} &= \sum_{\mu=1,2}\sum_{\beta\neq\alpha}\frac{\psi^\sigma_{\beta n,\mu}(x_r)\Phi^{\sigma'\dagger}_{\beta m,\mu}(x_l)}{E-\epsilon_\beta}\\ &+\sum_\alpha\sum_{\mu=1,2}\frac{\psi^\sigma_{\alpha n,\mu}(x_r)\Phi^{\sigma'\dagger}_{\alpha m,\mu}(x_l)}{E-\epsilon_\alpha}.\end{aligned} \tag{7.45}$$

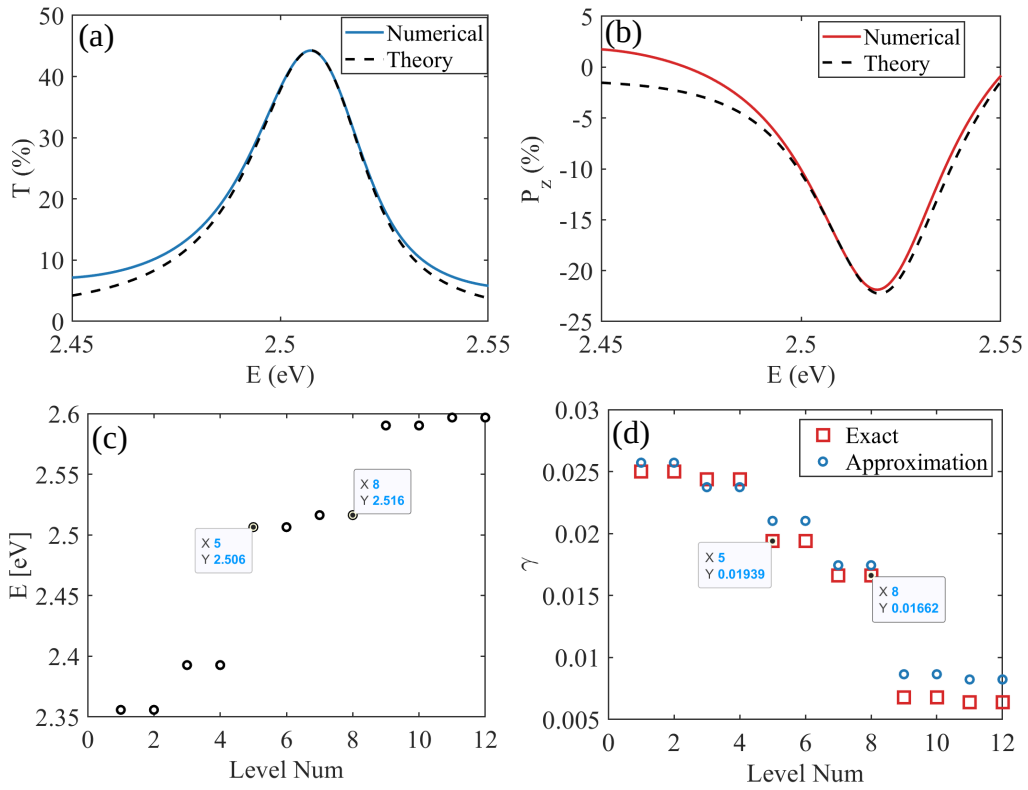

Figure 7.3: Spin Fano resonance in a chiral molecule associated with near degenerate levels. (a) Fano resonance peak for electronic transmission, where blue solid and black dashed curves are numerical and theoretical results, respectively. (b) Spin polarization Fano resonance peak, with red solid and black dashed curves being numerical and theoretical results, respectively. (c,d) Real and imaginary parts of the eigenenergies, respectively, where the red squares and blue circles represent the exact and perturbation results, respectively. The molecule has $N = 27$ carbon atoms and the twist angle is $\theta = \pi/2$.

where the second term contains energy levels that can contribute to the transmission coefficient. A exemplary Fano resonance peak with two contributing levels is shown in Fig. 7.3(a) and 7.3(b) for transmission and spin polarization, respectively. It can be seen that the result from the fast-slow variable approximation fits well with the numerical calculation. In a general sense, this is still a Fano resonance, as the corresponding transmission and spin polarization curves can still be fit by a kind of Fano formula.

A challenging question is, given a resonance, how one can determine if it is con-

tributed by a single energy level or by several. Here we provide a criterion to identify the pertinent states by comparing the resonance peak width γ and the energy level spacing between the levels of the resonance peak and its neighbors. As shown in Fig. 7.3(c), there are two levels which are quite near the Fano resonance peak, with energies $E = 2.506$, $E = 2.516$, and the energy difference $\Delta E = 0.01$. We then check the corresponding peak width γ, as shown in Fig. 7.3(d). We find that the peak width for the two levels are $\gamma \approx 0.02$ and $\gamma \approx 0.015$, which are larger than the level spacing, so both levels ought to be be taken into account when calculating the resonance peak. This peak-width based criterion can be checked in the single level case. Figure 7.2 shows that the resonance peak corresponds to the energy value $E = 1.676$, while the level difference between this level and its nearby levels is about $\Delta E \approx 0.3$. We also have that the peak widths for the three levels are $\gamma = 0.13$, $\gamma = 0.015$, and $\gamma = 0.014$, respectively. These data indicate that there is no significant spin polarization overlap between the central state and its neighboring states, so the resonance is the result of a single energy level.

In comparison with spin Fano resonances due to a single energy level, what effects do nearly degenerate levels have on the resonance? For example, do multiple levels lead to enhanced spin polarization? To address these questions, we focus on the parameter plane of the incident energy E and the twist angle θ, and calculate the spin polarization P_z, the total electron transmission, and the spin z component transmission in the plane, for a relatively large molecule of $N = 28$ carbon atoms. The results are shown in Figs. 7.4(a-c) with coupling strength being one. It can be seen that, near a level crossing point, a large spin polarization component can emerge, where its sign remains unchanged near the level crossing points. This should be compared with the case of a non-degenerate region where there is also larger spin polarization but with opposite directions. We examine the spin polarization about the near degeneracy

point and far from the near-degeneracy point, and find that two levels contribute to the resonance curve in the former while only one level is involved in the latter case.

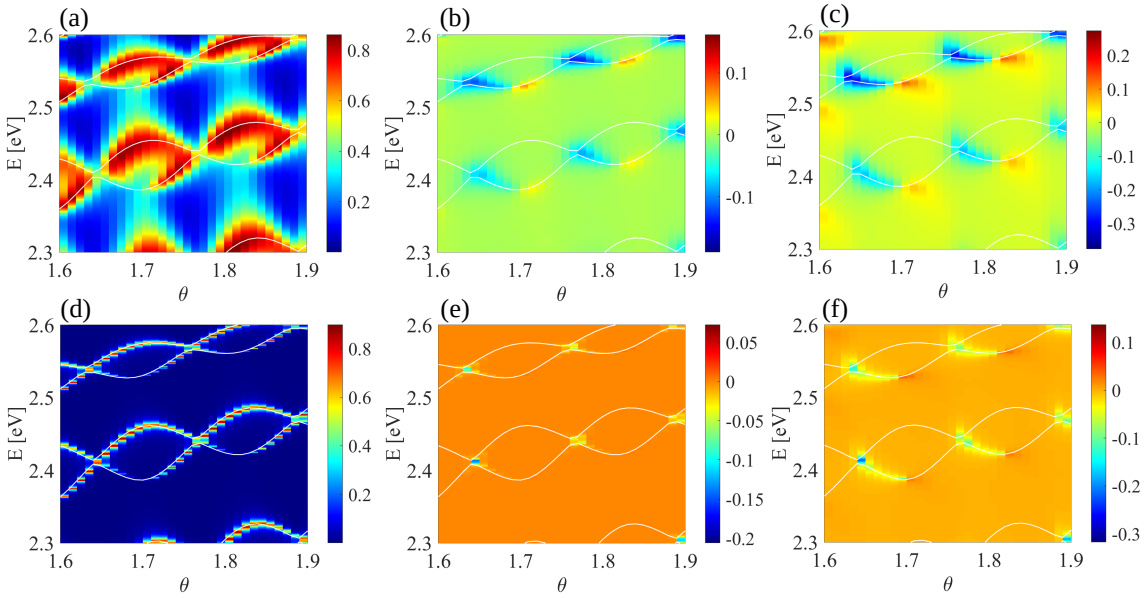

Figure 7.4: Near degeneracy enhanced spin Fano resonance. (a-c) Transmission (T), spin-z transmission (T_z), and spin polarization (P_z) (colors) versus the electron energy E and the twist angle θ for coupling strength one. (d-f) Similar plots as those in (a-c) but for coupling strength 0.1. The number of carbon atoms is $N = 28$.

7.5 Effect of Coupling Strength on Resonance Width

The coupling strength between the molecule and the leads can affect the electron transport behavior and thus the resonance profile. To study this effect, we set the coupling strength to 0.1 and calculate T, T_z, and P_z in the parameter plane (E, θ), as shown in Fig. 7.4(d-f), respectively. Comparing the results in Figs. 7.4(a) and 7.4(d), we see that the transmission area with values above 0.6 is much larger along the energy axis for the case of unity molecule-lead coupling strength as compared with the case of a smaller coupling strength. A similar behavior occurs for the spin transmission, where a larger area of high transmission along the energy axis near a level-crossing point or a non-degenerate lower single level arises for the large coupling

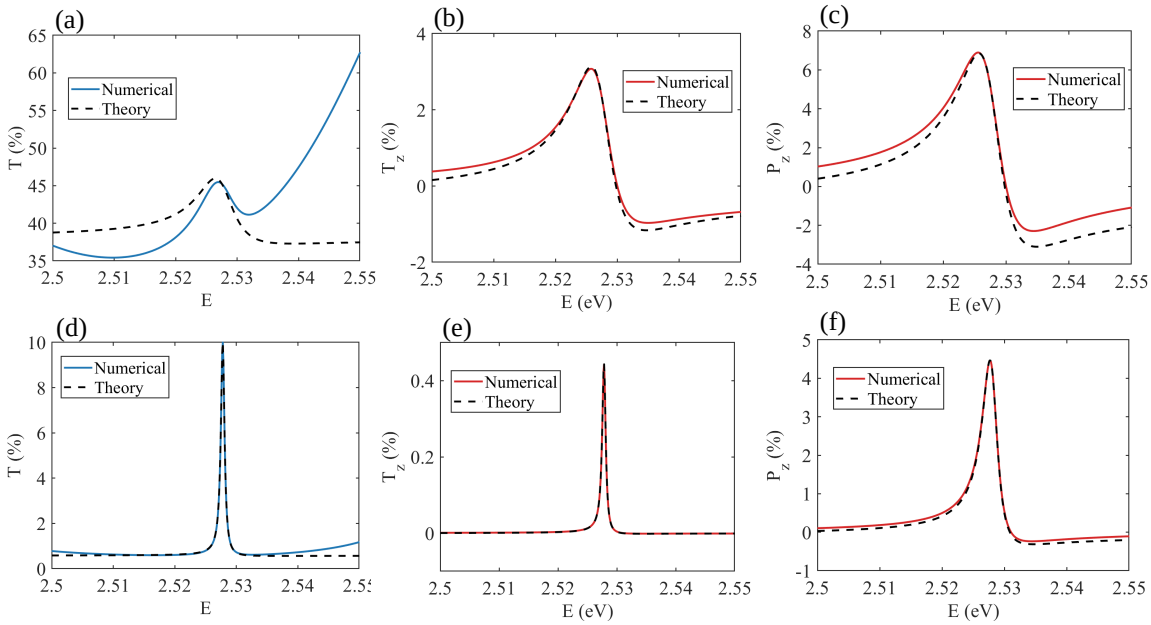

Figure 7.5: Effect of molecule-lead coupling strength on electronic and spin transport. (a-c) Transmission (T), spin-z transmission (T_z), and spin polarization (P_z) versus electron energy E for unity molecule-lead coupling strength. (d-f) The corresponding results for the case of coupling strength 0.1. In both cases, the chain has $N = 28$ carbon atoms and the twist angle is $\theta = 1.69$.

case, as shown in Figs. 7.4(b) and 7.4(e). As the spin polarization is the ratio between the spin and total charge transmission, the areas in which large polarization transport arises are similar in both cases, as shown in Figs. 7.4(c) and 7.4(f).

To further study the transport, we set the twist angle to be $\theta = 1.69$, where the Fano resonance peak value is about $E = 2.528$. Figure 7.5 shows the transmission versus energy about this resonance. We find that the resonance peak is much narrower for the total transmission and spin transmission in the weak molecule-lead coupling case [comparing Figs. 7.5(d,e) with Figs. 7.5(a,b), respectively]. For the spin polarization, the resonance is also narrower in the weak coupling case [comparing Fig. 7.5(f) with Fig. 7.5(c)].

To gain more insights, we calculate the imaginary part of the eigenenergy and the resonance peak width versus the molecule-lead coupling strength, as shown in

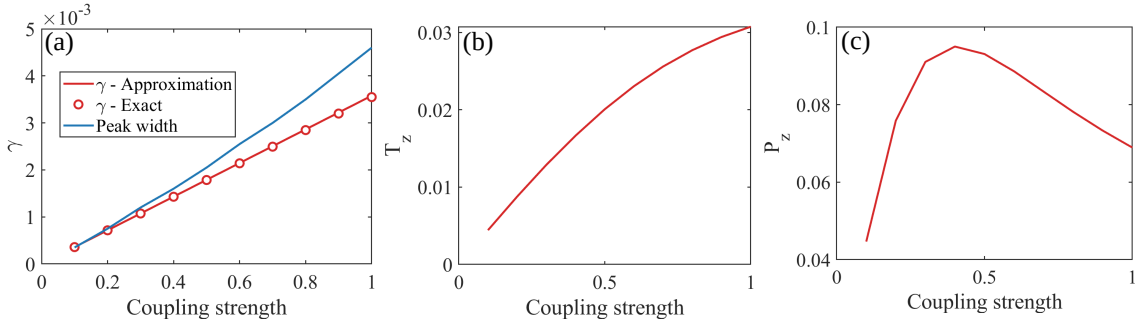

Figure 7.6: Fano resonance width and peak values versus the molecule-lead coupling strength. (a) Resonance peak width (blue curve) and the imaginary part of eigenenergies (red lines and open circles) versus the coupling strength. (b) Resonance peak values of T_z versus the coupling strength. (c) Resonance peak values of P_z versus the coupling strength. The parameter values are $N = 28$ and $\theta = 1.69$. The real part of eigenenergy at the Fano resonance is about $E = 2.528$.

Fig. 7.6(a). It can be seen that the resonance width increases linearly with the coupling strength. The spin transmission also increases with the coupling strength, as shown in Fig. 7.6(b). Due to the distinct increasing behaviors in the electronic and spin transmission, the spin polarization first increase, reaches a maximum, and then decreases with the coupling strength, as shown in Fig. 7.6(c).

7.6 Discussion

Spin-orbit coupling providing a source of magnetic fields for electrons in an atom is a relativistic effect and is thus weak: on the order of a few meV. However, it is still possible to generate a sizable spin polarization through some cumulative effect. For example, for transport through a large molecule, an electron will encounter, visit, and pass through many atoms. At each encounter where the electron orbits the nucleus, the spin-orbit interaction depends on the orbital orientation and will lead to some weak spin polarization. For a chiral molecule such as DNA, there is a preference in the orbital orientation so the effects on electron's spin polarization from the many atoms on the electron's way through will be cumulatively enhanced, leading to the

phenomenon of CISS [150].

At the present, CISS is not well understood. A recent result [172] was that the CISS effect vanishes when all electron states with the same energy are equally likely - a consequence of the Onsager reciprocal principle. The generality of this result means that the CISS effect needs to be understood in terms of the specific experimental settings. Three possible situations were pointed out [172]: the electronic states with the same energy not being equally probable (e.g., for electrons generated optically by a laser), the presence of accidental degeneracy in the molecular spectrum which enhances the spin-orbit coupling, or a magnetic lead. More recently, an analysis based on symmetry in electronic transmission was carried out to gain insights into the origin of CISS [173].

The main contribution of this work is the discovery and analysis of spin Fano resonance associated with transport through a complex molecule. Using chiral polyacetylene molecules of different number of carbon atoms, we find numerically the occurrences of various resonance peaks in the curve of spin polarization versus the electron energy. Extending the recently derived formula of spin Fano resonance for transport through two-dimensional mesoscopic quantum dots [178] to complex molecules, we obtain a general formula for spin Fano resonance in this context of quantum biology. Our formula is more general than any such previously derived formulas in electronic transport through solid-state devices, in the sense that it allows us to include multiple energy levels. This is particularly relevant and important for complex molecules, as quasidegeneracies in the energy levels are ubiquitous. Our formula fits the numerically observed resonance peaks remarkably well for both the straightforward case of one energy level and the more challenging cases where more than one energy level is involved. To our knowledge, for the latter case no existing Fano formulas in the literature are applicable. We also develop a criterion for determining the energy levels

involved in a Fano resonance, based on the resonance width relative to the spacing of neighboring energy levels. Typically, a spin Fano resonance due to more than one energy level is associated with enhanced spin polarization, and this can find potential applications in spintronics based on biological molecules. It should be noted that, at room temperatures, there are atom oscillations that can affect the electron coherent transport. To ensure coherence, the length of the molecular chain cannot be too large.

7.7 Supplementary Notes

7.7.1 Quasidegeneracy and Level Separation for Different Values of the Molecular Twist Angle

To assess the effects of fine-tuning the molecular twist angle on the spin polarization resonance, we choose five slightly different angles: $\theta = 1.61$, 1.63, 1.65, 1.67, and 1.69, and calculate the spin polarization associated with quasidegenerate energy levels and well separated single energy levels, as shown in Fig. 7.7. As the angle increases, there is a change in the contribution to the spin polarization resonance from two-state quasidegeneracy points to well separated single-level points. Take the case $\theta = 1.63$ [Figs. 7.7(b1-b5)] as an example. Figure 7.7(b1) shows the energy levels in a certain range. There is a pair of nearby levels with energy $E = 2.53$ and $E = 2.536$, where each level corresponds to two degenerate states due to Kramer's degeneracy. Figure 7.7(b2) shows that the two quasidegenerate levels correspond to two different imaginary parts of the eigenenergies: $\gamma \approx 0.017$ and $\gamma \approx 0.014$, respectively, which determine the width of the spin Fano resonance peak. Figure 7.7(b3) shows the theoretical result of the spin resonance peak induced by the $E = 2.53$ states, as represented by the black dashed curve, where the red curve is the exact result. The spin resonance peak corresponding to the $E = 2.536$ states is shown as the black

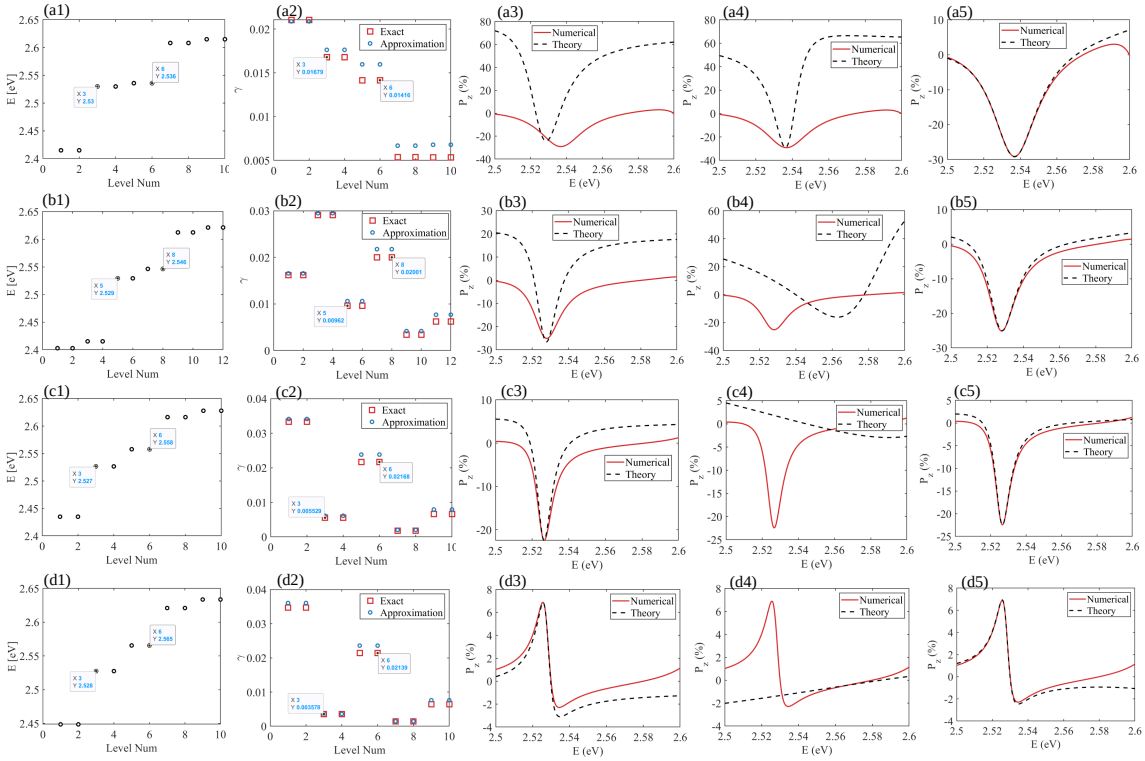

Figure 7.7: Single level or two quasidegenerate levels contributing to a Fano resonance. (a1) The energy levels for a chiral molecule of $N = 28$ carbon atoms with the twist angle $\theta = 1.63$. (a2) Imaginary part of system eigenenergies. (a3,a4) Examples of single-level contribution to spin Fano resonance for $E = 2.53$ [black dashed curve, the lower level in (a1)] and $E = 2.536$ [black dashed curve, the higher level in (a1)], respectively, where the red curves are numerical results from the exact NEGF calculation. (a5) Two-level contribution to spin Fano resonance [black dashed curve, the two levels labeled in (a1)]. The results in panels (b1-b5), (c1-c5), and (d1-d5) are for twist angles $\theta = 1.65$, 1.67, and 1.69, respectively, with the same legends as those in (a1-a5).

dashed curve in Fig. 7.7(b4). It can be seen that all these peaks with contribution from a single energy level cannot match the exact spin resonance peak. Note that the theoretical resonance curve in Fig. 7.7(b3) is wider than that in Fig. 7.7(b4) due to the larger γ value in the former case. We then insert both levels in the fast changing part of the NEGF formula to produce the corresponding theoretical spin resonance curve, as shown by the black-dashed curve in Fig. 7.7(b5). In this case, there is a good fit between the theoretical and numerical resonance curves. For the other four

rows (corresponding to the four other values of the twist angle), the legends are the same as those in Figs. 7.7(b1-b5). In Figs. 7.7(a1-a5), the two target levels are well separated from each other and the exact spin resonance peak is not so sharp. In fact, the theoretical fit from each level or their combination does not produce any result that matches the resonance peak at $E = 2.53$. For $\theta = 1.63$ and $\theta = 1.65$, as shown in Figs. 7.7(b1-b5) and Figs. 7.7(c1-c5), respectively, where the two levels are quite close to each other. While the theoretical resonance curve from each level does not match with the numerical curve, the combination of the two levels produces a spin resonance curve that agrees well with the numerical one. For $\theta = 1.67$ and $\theta = 1.69$, as shown in Figs. 7.7(d1-d5) and Figs. 7.7(e1-e5), respectively, the two levels gradually move away from each other. In both cases, the first level (the lower one) gives the correct resonance curve, while the second level does not contribute significantly to the resonance curve. It can then be concluded that, when there are two nearby levels, they contribute collectively to the spin Fano resonance. However, when the levels are well separated from each other, only one level contributes to the resonance peak.

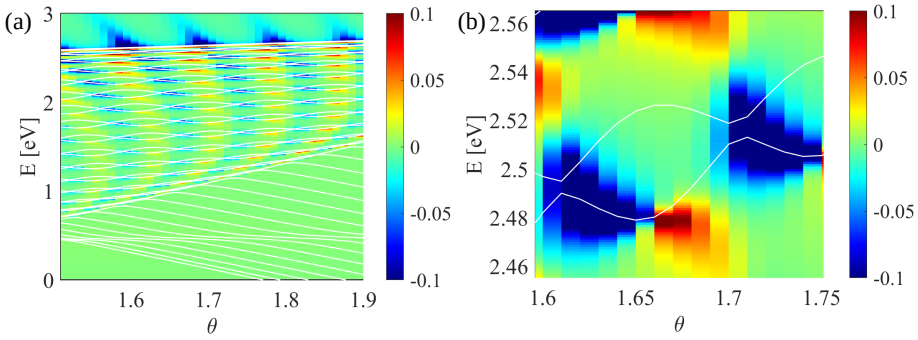

Figure 7.8: Near-degeneracy enhanced spin Fano resonance. (a) Colored-coded spin-polarization value in the parameter plane of electron energy and molecular twist angle. (b) Magnification of part of (a) about a specific degeneracy point. The chiral molecule has $N = 37$ carbon atoms.

Angle	E_1	E_2	$\lvert E_1 - E_2 \rvert$	γ_1	γ_2	levels
1.62	2.523	2.537	0.015	0.0156	0.0155	two
1.63	2.53	2.536	0.006	0.0168	0.0142	two
1.64	2.531	2.54	0.009	0.0123	0.0183	two
1.65	2.529	2.546	0.017	0.0096	0.02	two
1.66	2.528	2.553	0.025	0.0074	0.021	two
1.67	2.527	2.558	0.031	0.0055	0.0217	one
1.68	2.527	2.562	0.035	0.0043	0.0218	one
1.69	2.528	2.565	0.037	0.0036	0.0214	one

Table 7.1: Identification of One or Two-level Contribution to Spin Fano Resonance. The chiral molecule has $N = 28$ carbon atoms.

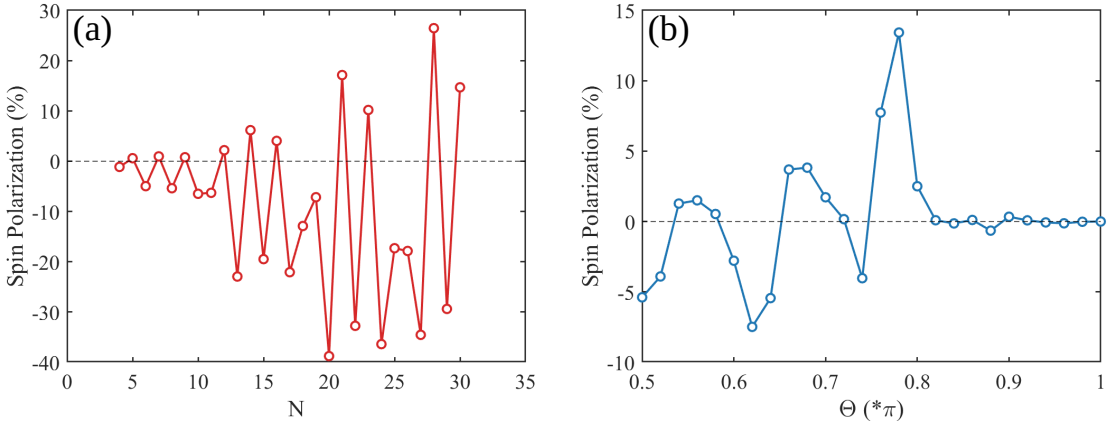

Figure 7.9: Length and angle dependence of the peak value of spin polarization resonance. (a) Peak resonance value versus the carbon atom number for molecule twist angle $\theta = \pi/2$. (b) Peak resonance value versus the twist angle for $N = 8$.

7.7.2 Criteria for Identifying Contribution to Spin Fano Resonance as Due to a Single Level or Two Quasidegenerate Levels

The results in Figs. 7.4 and 7.7 indicate that a pair of nearby levels, e.g., in the vicinity of a level crossing point, can lead to a large spin Fano resonance peak, to which both levels contribute. Away from the crossing point, there can also be large resonance peaks but they are contributed to by a single state. Here we give a general criterion for identifying whether a spin Fano resonance is due to one or two levels in terms of the energy level difference and the imaginary part γ of the eigenenergy. In particular, denoting the energy of the main state as E_1 and the corresponding energy imaginary part as γ_1, we find the energy level that is the closest to E_1 and denote it as E_2 with imaginary part of the eigenenergy as γ_2. If the level difference $|E_1 - E_2|$ is smaller than or comparable to the larger value of γ_1 and γ_2, we deem the second level a contributor to the Fano resonance and include it in the fast changing part of the NEGF formula. Otherwise, we simply choose one level. An example is shown in Table 7.1.

7.7.3 Spin Polarization for a Chiral Molecule of $N = 37$ Carbon Atoms

To provide further support for our finding of near-degeneracy enhanced spin Fano resonance, we calculate the spin polarization in the parameter plane of electron energy and twist angle for a chiral molecule of $N = 37$ carbon atoms, as shown in Fig. 7.8. Near the energy-level crossing points, there is significant spin polarization, so is the case for the well separated single levels. In addition,, the spin polarization has negative values about the quasidegenerate points and is positive about the well separated single levels. These results are consistent with those from a chiral molecule of $N = 28$ carbon atoms in the main text.

7.7.4 Length and Angle Dependence of Peak Spin Polarization Resonance

To confirm the cumulative effect in CISS due to the electron spin-orbit coupling associated with all the atoms in the molecule, we calculate the spin polarization as a function of the carbon atom number N. As shown in Fig. 7.9(a) for $\theta = \pi/2$, the spin polarization increases with N and reaches the value about 30%, in spite of fluctuations. Figure 7.9(b) shows the peak resonance value versus the twist angle θ for $N = 8$. Note that, for $\theta = \pi$, the molecule is no longer chiral. In this case, the spin polarization peak value is approximately zero. As the angle decreases from $\theta = \pi$ to $\theta = \pi/2$, the molecule becomes progressively more chiral, and the spin polarization increases accordingly, indicating the role of chirality in generating spin polarization.

[1] Barry Bradlyn, Jennifer Cano, Zhijun Wang, MG Vergniory, C Felser, RJ Cava, and B Andrei Bernevig. Beyond dirac and weyl fermions: Unconventional quasiparticles in conventional crystals. *Science*, 353(6299):5037, 2016.

[2] Carlo Beenakker. Bringing order to the expanding fermion zoo. *Science*, 353(6299):539–540, 2016.

[3] AH Castro Neto, F Guinea, Nuno MR Peres, Kostya S Novoselov, and Andre K Geim. The electronic properties of graphene. *Rev. Mod. Phys.*, 81(1):109, 2009.

[4] M Zahid Hasan and Charles L Kane. Colloquium: topological insulators. *Rev. Mod. Phys.*, 82(4):3045, 2010.

[5] Xiao-Liang Qi and Shou-Cheng Zhang. Topological insulators and superconductors. *Rev. Mod. Phys.*, 83(4):1057, 2011.

[6] Su-Yang Xu, Ilya Belopolski, Nasser Alidoust, Madhab Neupane, Guang Bian, Chenglong Zhang, Raman Sankar, Guoqing Chang, Zhujun Yuan, Chi-Cheng Lee, et al. Discovery of a weyl fermion semimetal and topological fermi arcs. *Science*, 349(6248):613–617, 2015.

[7] BQ Lv, HM Weng, BB Fu, XP Wang, H Miao, J Ma, P Richard, XC Huang, LX Zhao, GF Chen, et al. Experimental discovery of weyl semimetal taas. *Phys. Rev. X*, 5(3):031013, 2015.

[8] D. Bercioux, D. F. Urban, H. Grabert, and W. Häusler. Massless dirac-weyl fermions in a $\sqcup_3$ optical lattice. *Phys. Rev. A*, 80(6):063603, 2009.

[9] R Shen, LB Shao, Baigeng Wang, and DY Xing. Single dirac cone with a flat band touching on line-centered-square optical lattices. *Phys. Rev. B*, 81(4):041410, 2010.

[10] Daniel F Urban, Dario Bercioux, Michael Wimmer, and Wolfgang Häusler. Barrier transmission of dirac-like pseudospin-one particles. *Phys. Rev. B*, 84(11):115136, 2011.

[11] Balázs Dóra, Janik Kailasvuori, and Roderich Moessner. Lattice generalization of the dirac equation to general spin and the role of the flat band. *Phys. Rev. B*, 84(19):195422, 2011.

[12] Nathan Goldman, DF Urban, and D Bercioux. Topological phases for fermionic cold atoms on the lieb lattice. *Phys. Rev. A*, 83(6):063601, 2011.

[13] D Guzmán-Silva, C Mejía-Cortés, MA Bandres, MC Rechtsman, S Weimann, S Nolte, M Segev, A Szameit, and RA Vicencio. Experimental observation of bulk and edge transport in photonic lieb lattices. *New J. Phys.*, 16(6):063061, 2014.

[14] Weifeng Li, Meng Guo, Gang Zhang, and Yong-Wei Zhang. Gapless mos_2 allotrope possessing both massless dirac and heavy fermions. *Phys. Rev. B*, 89(20):205402, 2014.

[15] Gianluca Giovannetti, Massimo Capone, Jeroen van den Brink, and Carmine Ortix. Kekulé textures, pseudospin-one dirac cones, and quadratic band crossings in a graphene-hexagonal indium chalcogenide bilayer. *Phys. Rev. B*, 91(12):121417, 2015.

[16] Rodrigo A Vicencio, Camilo Cantillano, Luis Morales-Inostroza, Bastián Real, Cristian Mejía-Cortés, Steffen Weimann, Alexander Szameit, and Mario I Molina. Observation of localized states in lieb photonic lattices. *Phys. Rev. Lett.*, 114(24):245503, 2015.

[17] Sebabrata Mukherjee, Alexander Spracklen, Debaditya Choudhury, Nathan Goldman, Patrik Öhberg, Erika Andersson, and Robert R Thomson. Observation of a localized flat-band state in a photonic lieb lattice. *Phys. Rev. Lett.*, 114(24):245504, 2015.

[18] Shintaro Taie, Hideki Ozawa, Tomohiro Ichinose, Takuei Nishio, Shuta Nakajima, and Yoshiro Takahashi. Coherent driving and freezing of bosonic matter wave in an optical lieb lattice. *Sci. Adv.*, 1(10):e1500854, 2015.

[19] Falko Diebel, Daniel Leykam, Sebastian Kroesen, Cornelia Denz, and Anton S Desyatnikov. Conical diffraction and composite lieb bosons in photonic lattices. *Phys. Rev. Lett.*, 116(18):183902, 2016.

[20] Sami Paavilainen, Matti Ropo, Jouko Nieminen, Jaakko Akola, and Esa Rasanen. Coexisting honeycomb and kagome characteristics in the electronic band structure of molecular graphene. *Nano Lett.*, 16(6):3519–3523, 2016.

[21] Liyan Zhu, Shan-Shan Wang, Shan Guan, Ying Liu, Tingting Zhang, Guibin Chen, and Shengyuan A Yang. Blue phosphorene oxide: Strain-tunable quantum phase transitions and novel 2d emergent fermions. *Nano Lett.*, 16(10):6548–6554, 2016.

[22] Angbo Fang, ZQ Zhang, Steven G Louie, and Che Ting Chan. Klein tunneling and supercollimation of pseudospin-1 electromagnetic waves. *Phys. Rev. B*, 93(3):035422, 2016.

[23] J. D. Malcolm and E. J. Nicol. Frequency-dependent polarizability, plasmons, and screening in the two-dimensional pseudospin-1 dice lattice. *Phys. Rev. B*, 93(16):165433, 2016.

[24] Hong-Ya Xu and Ying-Cheng Lai. Revival resonant scattering, perfect caustics, and isotropic transport of pseudospin-1 particles. *Phys. Rev. B*, 94(16):165405, 2016.

[25] Masahisa Tsuchiizu. Three-dimensional higher-spin dirac and weyl dispersions in the strongly isotropic K_4 crystal. *Phys. Rev. B*, 94(19):195426, 2016.

[26] Hongya Xu and Ying-Cheng Lai. Superscattering of a pseudospin-1 wave in a photonic lattice. *Phys. Rev. A*, 95(1):012119, 2017.

[27] A. Fang, Z. Q. Zhang, Steven G. Louie, and C. T. Chan. Anomalous anderson localization behaviors in disordered pseudospin systems. *Proc. Natl. Acad. Sci.*, 114(16):4087–4092, 2017.

[28] D. Bercioux, O. Dutta, and E. Rico. Solitons in one-dimensional lattices with a flat band. *Ann. der Physik*, 529:1600262, 2017.

[29] Chen-Di Han, Hong-Ya Xu, Danhong Huang, and Ying-Cheng Lai. Atomic collapse in pseudospin-1 systems. *Phys. Rev. B*, 99(24):245413, 2019.

[30] Hong-Ya Xu and Ying-Cheng Lai. Pseudospin-1 wave scattering that defies chaos Q-spoiling and Klein tunneling. *Phys. Rev. B*, 99(23):235403, 2019.

[31] Hong-Ya Xu and Ying-Cheng Lai. Anomalous chiral edge states in spin-1 Dirac quantum dots. *Phys. Rev. Research*, 2(1):013062, 2020.

[32] Junpeng Hou, Haiping Hu, and Chuanwei Zhang. Topological phases in pseudospin-1 fermi gases with two-dimensional spin-orbit coupling. *Phys. Rev. A*, 101(5):053613, 2020.

[33] Hong-Ya Xu and Ying-Cheng Lai. Anomalous in-gap edge states in two-dimensional pseudospin-1 Dirac insulators. *Phys. Rev. Research*, 2:023368, Jun 2020.

[34] A Raoux, M Morigi, J-N Fuchs, F Piéchon, and G Montambaux. From dia- to paramagnetic orbital susceptibility of massless fermions. *Phys. Rev. Lett.*, 112(2):026402, 2014.

[35] JT Chalker, TS Pickles, and Pragya Shukla. Anderson localization in tight-binding models with flat bands. *Phys. Rev. B*, 82(10):104209, 2010.

[36] Joshua D Bodyfelt, Daniel Leykam, Carlo Danieli, Xiaoquan Yu, and Sergej Flach. Flatbands under correlated perturbations. *Phys. Rev. Lett.*, 113(23):236403, 2014.

[37] Ramaz Khomeriki and Sergej Flach. Landau-zener bloch oscillations with perturbed flat bands. *Phys. Rev. Lett.*, 116(24):245301, 2016.

[38] Fa Wang and Ying Ran. Nearly flat band with chern number c= 2 on the dice lattice. *Phys. Rev. B*, 84(24):241103, 2011.

[39] Hideo Aoki, Masato Ando, and Hajime Matsumura. Hofstadter butterflies for flat bands. *Phys. Rev. B*, 54(24):R17296, 1996.

[40] Conan Weeks and Marcel Franz. Topological insulators on the lieb and perovskite lattices. *Phys. Rev. B*, 82(8):085310, 2010.

[41] M Lewkowicz and B Rosenstein. Dynamics of particle-hole pair creation in graphene. *Phys. Rev. Lett.*, 102(10):106802, 2009.

[42] B Rosenstein, M Lewkowicz, Hsien-Chung Kao, and Y Korniyenko. Ballistic transport in graphene beyond linear response. *Phys. Rev. B*, 81(4):041416, 2010.

[43] Balázs Dóra and Roderich Moessner. Nonlinear electric transport in graphene: quantum quench dynamics and the schwinger mechanism. *Phys. Rev. B*, 81(16):165431, 2010.

[44] Balázs Dóra and Roderich Moessner. Dynamics of the spin hall effect in topological insulators and graphene. *Phys. Rev. B*, 83(7):073403, 2011.

[45] Szabolcs Vajna, Balázs Dóra, and Roderich Moessner. Nonequilibrium transport and statistics of schwinger pair production in weyl semimetals. *Phys. Rev. B*, 92(8):085122, 2015.

[46] MI Katsnelson, F Guinea, and AK Geim. Scattering of electrons in graphene by clusters of impurities. *Phys. Rev. B*, 79(19):195426, 2009.

[47] József Cserti, András Pályi, and Csaba Péterfalvi. Caustics due to a negative refractive index in circular graphene p- n junctions. *Phys. Rev. Lett.*, 99(24):246801, 2007.

[48] MI Katsnelson and KS Novoselov. Graphene: New bridge between condensed matter physics and quantum electrodynamics. *Solid State Commun.*, 143(1-2):3–13, 2007.

[49] F Guinea. Models of electron transport in single layer graphene. *J. Low Temp. Phys.*, 153(5-6):359–373, 2008.

[50] A Matulis and FM Peeters. Quasibound states of quantum dots in single and bilayer graphene. *Phys. Rev. B*, 77(11):115423, 2008.

[51] Prabath Hewageegana and Vadym Apalkov. Electron localization in graphene quantum dots. *Phys. Rev. B*, 77(24):245426, 2008.

[52] Jens H Bardarson, M Titov, and PW Brouwer. Electrostatic confinement of electrons in an integrable graphene quantum dot. *Phys. Rev. Lett.*, 102(22):226803, 2009.

[53] R. L. Heinisch, F. X. Bronold, and H. Fehske. Mie scattering analog in graphene: Lensing, particle confinement, and depletion of Klein tunneling. *Phys. Rev. B*, 87:155409, Apr 2013.

[54] Jhih-Sheng Wu and Michael M. Fogler. Scattering of two-dimensional massless Dirac electrons by a circular potential barrier. *Phys. Rev. B*, 90:235402, Dec 2014.

[55] Yasufumi Araki and Kentaro Nomura. Skyrmion-induced anomalous hall conductivity on topological insulator surfaces. *Phys. Rev. B*, 96(16):165303, 2017.

[56] Cheng-Zhen Wang, Hong-Ya Xu, and Ying-Cheng Lai. Scattering of Dirac electrons from a skyrmion: Emergence of robust skew scattering. *Phys. Rev. Research*, 2(1):013247, 2020.

[57] Naoto Nagaosa, Jairo Sinova, Shigeki Onoda, Allan H MacDonald, and Nai Phuan Ong. Anomalous Hall effect. *Rev. Mod. Phys.*, 82(2):1539, 2010.

[58] Zhenhua Qiao, Shengyuan A Yang, Wanxiang Feng, Wang-Kong Tse, Jun Ding, Yugui Yao, Jian Wang, and Qian Niu. Quantum anomalous Hall effect in graphene from Rashba and exchange effects. *Phys. Rev. B*, 82(16):161414, 2010.

[59] Zhenhua Qiao, Wei Ren, Hua Chen, L Bellaiche, Zhenyu Zhang, Allan H MacDonald, and Qian Niu. Quantum anomalous Hall effect in graphene proximity coupled to an antiferromagnetic insulator. *Phys. Rev. Lett.*, 112(11):116404, 2014.

[60] Zhiyong Wang, Chi Tang, Raymond Sachs, Yafis Barlas, and Jing Shi. Proximity-induced ferromagnetism in graphene revealed by the anomalous Hall effect. *Phys. Rev. Lett.*, 114(1):016603, 2015.

[61] Guibin Song, Mojtaba Ranjbar, David R Daughton, and Richard A Kiehl. Nanoparticle-Induced Anomalous Hall Effect in Graphene. *Nano Lett.*, 19(10):7112–7118, 2019.

[62] James W McIver, Benedikt Schulte, F-U Stein, Toru Matsuyama, Gregor Jotzu, Guido Meier, and Andrea Cavalleri. Light-induced anomalous Hall effect in graphene. *Nat. phys.*, 16(1):38–41, 2020.

[63] SA Sato, JW McIver, M Nuske, P Tang, G Jotzu, B Schulte, H Hübener, U De Giovannini, L Mathey, MA Sentef, et al. Microscopic theory for the light-induced anomalous Hall effect in graphene. *Phys. Rev. B*, 99(21):214302, 2019.

[64] Aires Ferreira, Tatiana G Rappoport, Miguel A Cazalilla, and AH Castro Neto. Extrinsic spin Hall effect induced by resonant skew scattering in graphene. *Phys. Rev. Lett.*, 112(6):066601, 2014.

[65] W Beugeling, JC Everts, and C Morais Smith. Topological phase transitions driven by next-nearest-neighbor hopping in two-dimensional lattices. *Phys. Rev. B*, 86(19):195129, 2012.

[66] Dmitry Green, Luiz Santos, and Claudio Chamon. Isolated flat bands and spin-1 conical bands in two-dimensional lattices. *Phys. Rev. B*, 82(7):075104, 2010.

[67] EV Gorbar, VP Gusynin, and DO Oriekhov. Electron states for gapped pseudospin-1 fermions in the field of a charged impurity. *Phys. Rev. B*, 99(15):155124, 2019.

[68] Y. Betancur-Ocampo, G. Cordourier-Maruri, V. Gupta, and R. de Coss. Super-Klein tunneling of massive pseudospin-one particles. *Phys. Rev. B*, 96:024304, Jul 2017.

[69] Yong Xu and L.-M. Duan. Unconventional quantum Hall effects in two-dimensional massive spin-1 fermion systems. *Phys. Rev. B*, 96:155301, Oct 2017.

[70] A. K. Geim and K. S. Novoselov. The rise of graphene. *Nat. Mater.*, 6:183–191, 2007.

[71] A. K. Geim and I. V. Grigorieva. Van der waals heterostructures. *Nature*, 499:419–425, 2013.

[72] P. Ajayan, P. Kim, and K. Banerjee. Two-dimensional van der Waals materials. *Phys. Today*, 69(9):38–44, 2016.

[73] S. Pancharatnam. Generalized theory of interference, and its applications. part i. coherent pencils. *Proc. Indian Acad. Sci. A.*, 44:247–262, 1956.

[74] H. C. Longuet Higgins, U. Öpik, M. H. L. Pryce, and R. A. Sack. Studies of the jahn-teller effect ii the dynamical problem. *Proc. R. Soc. A*, 244:1–16, 1958.

[75] M. V. Berry. Quantal phase factors accompanying adiabatic changes. *Proc. R. Soc. A*, 392:45–57, 1984.

[76] Y. B. Zhang, Y. W. Tan, H. L. Stormer, and P. Kim. Experimental observation of the quantum hall effect and Berry's phase in graphene. *Nature*, 438(7065):201–204, 2005.

[77] Pierre Carmier and Denis Ullmo. Berry phase in graphene: Semiclassical perspective. *Phys. Rev. B*, 77:245413, Jun 2008.

[78] G. P. Mikitika and Yu. V. Sharlaib. The berry phase in graphene and graphite multilayers. *Low Temp. Phys.*, 34:794–800, 2008.

[79] E Illes, JP Carbotte, and EJ Nicol. Hall quantization and optical conductivity evolution with variable berry phase in the $\alpha - T_3$ model. *Phys. Rev. B*, 92(24):245410, 2015.

[80] Lucia Duca, Tracy Li, Martin Reitter, Immanuel Bloch, Monika Schleier-Smith, and Ulrich Schneider. An aharonov-bohm interferometer for determining bloch band topology. *Science*, 347(6219):288–292, 2015.

[81] Joaquin F Rodriguez-Nieva and Leonid S Levitov. Berry phase jumps and giant nonreciprocity in dirac quantum dots. *Phys. Rev. B*, 94(23):235406, 2016.

[82] Fereshte Ghahari, Daniel Walkup, Christopher Gutiérrez, Joaquin F Rodriguez-Nieva, Yue Zhao, Jonathan Wyrick, Fabian D Natterer, William G Cullen, Kenji Watanabe, Takashi Taniguchi, et al. An on/off berry phase switch in circular graphene resonators. *Science*, 356(6340):845–849, 2017.

[83] RA Sepkhanov, Johan Nilsson, and CWJ Beenakker. Proposed method for detection of the pseudospin-1 2 berry phase in a photonic crystal with a dirac spectrum. *Phys. Rev. B*, 78(4):045122, 2008.

[84] Shaowen Chen, Zheng Han, Mirza M. Elahi, K. M. Masum Habib, Lei Wang, Bo Wen, Yuanda Gao, Takashi Taniguchi, Kenji Watanabe, James Hone, Avik W. Ghosh, and Cory R. Dean. Electron optics with p-n junctions in ballistic graphene. *Science*, 353(6307):1522–1525, 2016.

[85] M. Sharad, C. Augustine, and K. Roy. Boolean and non-boolean computation with spin devices. In *IEEE International Electron Device Meeting (IEDM)*, volume 52, pages 443–545, San Francisco, 2012. IEEE.

[86] A. Horvath, F. Corinto, G. Csaba, W. Porod, and T. Roska. Synchronization in cellular spin torque oscillator arrays. In *13th International Workshop on Cellular Nanoscale Networks and Their Applications (CNNA)*, Turin Italy, 2012. IEEE.

[87] G. Csaba and W. Porod. Computational study of spin-torque oscillator interactions for non-boolean computing applications. *IEEE Trans. Magnetics*, 49:4447–4451, 2013.

[88] D. E. Nikonov, G. Csaba, W. Porod, T. Shibata, D. Voils, D. Hammerstrom, I. A. Young, and G. I. Bourianoff. Coupled-oscillator associative memory array operation for pattern recognition. *IEEE J. Explor. Solid-State Comp. Dev. Cir.*, 1:85–93, 2015.

[89] D. Fan, S. Maji, K. Yogendra, M. Sharad, and K. Roy. Injection-locked spin hall-induced coupled-oscillators for energy efficient associative computing. *IEEE Trans. Nanotech.*, 14:1083–1093, 2015.

[90] F. Maciá, F. C. Hoppensteadt, and A.D. Kent. Spin wave excitation patterns generated by spin torque oscillators. *Nanotech.*, 25:1045303, 2014.

[91] John C Slonczewski. Current-driven excitation of magnetic multilayers. *J. Magn. Magn. Mater.*, 159(1-2):L1–L7, 1996.

[92] Luc Berger. Emission of spin waves by a magnetic multilayer traversed by a current. *Phys. Rev. B*, 54(13):9353, 1996.

[93] Daniel C Ralph and Mark D Stiles. Spin transfer torques. *J. Magn. Magn. Mater.*, 320(7):1190–1216, 2008.

[94] Arne Brataas, Andrew D Kent, and Hideo Ohno. Current-induced torques in magnetic materials. *Nat. Mater.*, 11(5):372, 2012.

[95] S Il Kiselev, JC Sankey, IN Krivorotov, NC Emley, RJ Schoelkopf, RA Buhrman, and DC Ralph. Microwave oscillations of a nanomagnet driven by a spin-polarized current. *Nature*, 425(6956):380, 2003.

[96] William H Rippard, Matthew R Pufall, S Kaka, Stephen E Russek, and Thomas J Silva. Direct-current induced dynamics in c o 90 f e 10/n i 80 f e 20 point contacts. *Phys. Rev. Lett.*, 92(2):027201, 2004.

[97] IN Krivorotov, NC Emley, JC Sankey, SI Kiselev, DC Ralph, and RA Buhrman. Time-domain measurements of nanomagnet dynamics driven by spin-transfer torques. *Science*, 307(5707):228–231, 2005.

[98] Shehzaad Kaka, Matthew R Pufall, William H Rippard, Thomas J Silva, Stephen E Russek, and Jordan A Katine. Mutual phase-locking of microwave spin torque nano-oscillators. *Nature*, 437(7057):389, 2005.

[99] FB Mancoff, ND Rizzo, BN Engel, and S Tehrani. Phase-locking in double-point-contact spin-transfer devices. *Nature*, 437(7057):393, 2005.

[100] AN Slavin and VS Tiberkevich. Theory of mutual phase locking of spin-torque nanosized oscillators. *Phys. Rev. B*, 74(10):104401, 2006.

[101] J Grollier, V Cros, and A Fert. Synchronization of spin-transfer oscillators driven by stimulated microwave currents. *Phys. Rev. B*, 73(6):060409, 2006.

[102] J Persson, Yan Zhou, and Johan Akerman. Phase-locked spin torque oscillators: Impact of device variability and time delay. *J. Appl. Phys.*, 101(9):09A503, 2007.

[103] B Georges, J Grollier, V Cros, and A Fert. Impact of the electrical connection of spin transfer nano-oscillators on their synchronization: an analytical study. *Appl. Phys. Lett.*, 92(23):232504, 2008.

[104] Dong Li, Yan Zhou, Changsong Zhou, and Bambi Hu. Global attractors and the difficulty of synchronizing serial spin-torque oscillators. *Phys. Rev. B*, 82(14):140407, 2010.

[105] S Sani, J Persson, Seyed Majid Mohseni, Ye Pogoryelov, PK Muduli, Anders Eklund, Gunnar Malm, Mikael Käll, Alexandre Dmitriev, and Johan Åkerman. Mutually synchronized bottom-up multi-nanocontact spin–torque oscillators. *Nat. Comm.*, 4:2731, 2013.

[106] James Turtle, Pietro-Luciano Buono, Antonio Palacios, Christine Dabrowski, Visarath In, and Patrick Longhini. Synchronization of spin torque nano-oscillators. *Phys. Rev. B*, 95(14):144412, 2017.

[107] Hao-Hsuan Chen, Ching-Ming Lee, Zongzhi Zhang, Yaowen Liu, Jong-Ching Wu, Lance Horng, and Ching-Ray Chang. Phase locking of spin-torque nano-oscillator pairs with magnetic dipolar coupling. *Phys. Rev. B*, 93(22):224410, 2016.

[108] Antonio Ruotolo, V Cros, B Georges, A Dussaux, J Grollier, C Deranlot, R Guillemet, K Bouzehouane, S Fusil, and A Fert. Phase-locking of magnetic vortices mediated by antivortices. *Nat. Nanotech.*, 4(8):528, 2009.

[109] Vladislav E Demidov, Sergei Urazhdin, Henning Ulrichs, Vasyl Tiberkevich, Andrei Slavin, Dietmar Baither, Guido Schmitz, and Sergej O Demokritov. Magnetic nano-oscillator driven by pure spin current. *Nat. Mater.*, 11(12):1028, 2012.

[110] Luqiao Liu, Chi-Feng Pai, DC Ralph, and RA Buhrman. Magnetic oscillations driven by the spin hall effect in 3-terminal magnetic tunnel junction devices. *Phys. Rev. Lett.*, 109(18):186602, 2012.

[111] RH Liu, WL Lim, and S Urazhdin. Spectral characteristics of the microwave emission by the spin hall nano-oscillator. *Phys. Rev. Lett.*, 110(14):147601, 2013.

[112] A Giordano, M Carpentieri, A Laudani, G Gubbiotti, B Azzerboni, and G Finocchio. Spin-hall nano-oscillator: A micromagnetic study. *Appl. Phys. Lett.*, 105(4):042412, 2014.

[113] VE Demidov, H Ulrichs, SV Gurevich, SO Demokritov, VS Tiberkevich, AN Slavin, A Zholud, and S Urazhdin. Synchronization of spin hall nano-oscillators to external microwave signals. *Nat. Commun.*, 5:3179, 2014.

[114] Mehrdad Elyasi, Charanjit S Bhatia, and Hyunsoo Yang. Synchronization of spin-transfer torque oscillators by spin pumping, inverse spin hall, and spin hall effects. *J. Appl. Phys.*, 117(6):063907, 2015.

[115] T. Qu and R.H. Victora. Phase-lock requirements in a serial array of spin transfer nano-oscillators. *Sci. Rep.*, 5:11462, 2015.

[116] Yaroslav Tserkovnyak and Daniel Loss. Thin-film magnetization dynamics on the surface of a topological insulator. *Phys. Rev. Lett.*, 108(18):187201, 2012.

[117] Peng Wei, Ferhat Katmis, Badih A Assaf, Hadar Steinberg, Pablo Jarillo-Herrero, Donald Heiman, and Jagadeesh S Moodera. Exchange-coupling-induced symmetry breaking in topological insulators. *Phys. Rev. Lett.*, 110(18):186807, 2013.

[118] Ferhat Katmis, Valeria Lauter, Flavio S Nogueira, Badih A Assaf, Michelle E Jamer, Peng Wei, Biswarup Satpati, John W Freeland, Ilya Eremin, Don Heiman, et al. A high-temperature ferromagnetic topological insulating phase by proximity coupling. *Nature*, 533(7604):513, 2016.

[119] Takehito Yokoyama, Yukio Tanaka, and Naoto Nagaosa. Anomalous magnetoresistance of a two-dimensional ferromagnet/ferromagnet junction on the surface of a topological insulator. *Phys. Rev. B*, 81(12):121401, 2010.

[120] Zhenhua Wu, FM Peeters, and Kai Chang. Electron tunneling through double magnetic barriers on the surface of a topological insulator. *Phys. Rev. B*, 82(11):115211, 2010.

[121] Guang-Lei Wang, Hong-Ya Xu, and Ying-Cheng Lai. Nonlinear dynamics induced anomalous Hall effect in topological insulators. *Sci. Rep.*, 6:19803, 2016.

[122] Guang-Lei Wang, Hong-Ya Xu, and Ying-Cheng Lai. Emergence, evolution, and control of multistability in a hybrid topological quantum/classical system. *Chaos*, 28(3):033601, 2018.

[123] Ion Garate and Marcel Franz. Inverse spin-galvanic effect in the interface between a topological insulator and a ferromagnet. *Phys. Rev. Lett.*, 104(14):146802, 2010.

[124] Takehito Yokoyama, Jiadong Zang, and Naoto Nagaosa. Theoretical study of the dynamics of magnetization on the topological surface. *Phys. Rev. B*, 81(24):241410, 2010.

[125] Takehito Yokoyama. Current-induced magnetization reversal on the surface of a topological insulator. *Phys. Rev. B*, 84(11):113407, 2011.

[126] Yuriy G Semenov, Xiaopeng Duan, and Ki Wook Kim. Voltage-driven magnetic bifurcations in nanomagnet–topological insulator heterostructures. *Phys. Rev. B*, 89(20):201405, 2014.

[127] Xiaopeng Duan, Xi-Lai Li, Yuriy G Semenov, and Ki Wook Kim. Nonlinear magnetic dynamics in a nanomagnet–topological insulator heterostructure. *Phys. Rev. B*, 92(11):115429, 2015.

[128] Papa B Ndiaye, Collins Ashu Akosa, Mark H Fischer, Abolhassan Vaezi, E-A Kim, and Aurelien Manchon. Dirac spin-orbit torques and charge pumping at the surface of topological insulators. *Phys. Rev. B*, 96(1):014408, 2017.

[129] Naoto Nagaosa and Yoshinori Tokura. Topological properties and dynamics of magnetic skyrmions. *Nat. Nanotech.*, 8(12):899, 2013.

[130] Albert Fert, Vincent Cros, and Joao Sampaio. Skyrmions on the track. *Nat. Nanotech.*, 8(3):152, 2013.

[131] Karin Everschor-Sitte, Jan Masell, Robert M Reeve, and Mathias Kläui. Perspective: Magnetic skyrmions - overview of recent progress in an active research field. *J. Appl. Phys.*, 124(24):240901, 2018.

[132] Hector Ochoa and Yaroslav Tserkovnyak. Colloquium: Quantum skyrmionics. *arXiv preprint arXiv:1807.02203*, 2018.

[133] Sebastian Mühlbauer, Benedikt Binz, F Jonietz, Christian Pfleiderer, Achim Rosch, Anja Neubauer, Robert Georgii, and Peter Böni. Skyrmion lattice in a chiral magnet. *Science*, 323(5916):915–919, 2009.

[134] XZ Yu, Yoshinori Onose, Naoya Kanazawa, JH Park, JH Han, Yoshio Matsui, Naoto Nagaosa, and Yoshinori Tokura. Real-space observation of a two-dimensional skyrmion crystal. *Nature*, 465(7300):901, 2010.

[135] Florian Jonietz, Sebastain Mühlbauer, Christian Pfleiderer, Andreas Neubauer, Wolfgang Münzer, Andreas Bauer, T Adams, Robert Georgii, Peter Böni, Rembert A Duine, et al. Spin transfer torques in MnSi at ultralow current densities. *Science*, 330(6011):1648–1651, 2010.

[136] Jiadong Zang, Maxim Mostovoy, Jung Hoon Han, and Naoto Nagaosa. Dynamics of skyrmion crystals in metallic thin films. *Phys. Rev. Lett.*, 107(13):136804, 2011.

[137] XZ Yu, Naoya Kanazawa, WZ Zhang, T Nagai, Toru Hara, Koji Kimoto, Yoshio Matsui, Yoshinori Onose, and Yoshinori Tokura. Skyrmion flow near room temperature in an ultralow current density. *Nature communications*, 3:988, 2012.

[138] S Tsesses, E Ostrovsky, K Cohen, B Gjonaj, NH Lindner, and G Bartal. Optical skyrmion lattice in evanescent electromagnetic fields. *Science*, 361(6406):993–996, 2018.

[139] Gen Yin, Yizhou Liu, Yafis Barlas, Jiadong Zang, and Roger K Lake. Topological spin Hall effect resulting from magnetic skyrmions. *Phys. Rev. B*, 92(2):024411, 2015.

[140] KS Denisov, IV Rozhansky, NS Averkiev, and E Lähderanta. Electron scattering on a magnetic skyrmion in the nonadiabatic approximation. *Phys. Rev. Lett.*, 117(2):027202, 2016.

[141] KS Denisov, IV Rozhansky, NS Averkiev, and E Lähderanta. A nontrivial crossover in topological Hall effect regimes. *Sci. Rep.*, 7(1):17204, 2017.

[142] Papa Birame Ndiaye, Collins Ashu Akosa, and Aurélien Manchon. Topological Hall and spin Hall effects in disordered skyrmionic textures. *Phys. Rev. B*, 95(6):064426, 2017.

[143] KS Denisov, IV Rozhansky, Maria N Potkina, Igor S Lobanov, E Lähderanta, and Valery M Uzdin. Topological Hall effect for electron scattering on nanoscale skyrmions in external magnetic field. *Phys. Rev. B*, 98(21):214407, 2018.

[144] Kentaro Nomura and Naoto Nagaosa. Electric charging of magnetic textures on the surface of a topological insulator. *Phys. Rev. B*, 82(16):161401, 2010.

[145] Hilary M Hurst, Dmitry K Efimkin, Jiadong Zang, and Victor Galitski. Charged skyrmions on the surface of a topological insulator. *Phys. Rev. B*, 91(6):060401, 2015.

[146] Xichao Zhang, Jing Xia, Yan Zhou, Daowei Wang, Xiaoxi Liu, Weisheng Zhao, and Motohiko Ezawa. Control and manipulation of a magnetic skyrmionium in nanostructures. *Phys. Rev. B*, 94:094420, Sep 2016.

[147] Oleksandr V. Pylypovskyi, Denys Makarov, Volodymyr P. Kravchuk, Yuri Gaididei, Avadh Saxena, and Denis D. Sheka. Chiral skyrmion and skyrmionium states engineered by the gradient of curvature. *Phys. Rev. Applied*, 10:064057, Dec 2018.

[148] Brge Göbel, Alexander Schäffer, Jamal Berakdar, Ingrid Mertig, and Stuart Parkin. Electrical writing, deleting, reading, and moving of magnetic skyrmioniums in a racetrack device. *Sci. Rep.*, 9:12119, 08 2019.

[149] Flavio S Nogueira, Ilya Eremin, Ferhat Katmis, Jagadeesh S Moodera, Jeroen van den Brink, and Volodymyr P Kravchuk. Fluctuation-induced Néel and Bloch skyrmions at topological insulator surfaces. *Phys. Rev. B*, 98(6):060401, 2018.

[150] K. Ray, S. P. Ananthavel, D. H. Waldeck, and R. Naaman. Asymmetric scattering of polarized electrons by organized organic films of chiral molecules. *Science*, 283:814–816, 1999.

[151] Zouti Xie, Tal Z Markus, Sidney R Cohen, Zeev Vager, Rafael Gutierrez, and Ron Naaman. Spin specific electron conduction through DNA oligomers. *Nano Lett.*, 11(11):4652–4655, 2011.

[152] B Göhler, V Hamelbeck, TZ Markus, M Kettner, GF Hanne, Z Vager, R Naaman, and H Zacharias. Spin selectivity in electron transmission through self-assembled monolayers of double-stranded DNA. *Science*, 331(6019):894–897, 2011.

[153] Theodore J. Zwang, Sylvia Hürlimann, Michael G Hill, and Jacqueline K. Barton. Helix-dependent spin filtering through the DNA duplex. *J. Am. Chem. Soc.*, 138(48):15551–15554, 2016.

[154] Debabrata Mishra, Tal Z Markus, Ron Naaman, Matthias Kettner, Benjamin Göhler, Helmut Zacharias, Noga Friedman, Mordechai Sheves, and Claudio Fontanesi. Spin-dependent electron transmission through bacteriorhodopsin embedded in purple membrane. *Proc. Natl. Acad. Sci. (USA)*, 110(37):14872–14876, 2013.

[155] Vaibhav Varade, Tal Markus, Kiran Vankayala, Noga Friedman, Mordechai Sheves, David H Waldeck, and Ron Naaman. Bacteriorhodopsin based non-magnetic spin filters for biomolecular spintronics. *Phys. Chem. Chem. Phys.*, 20(2):1091–1097, 2018.

[156] M Kettner, B Göhler, H Zacharias, D Mishra, V Kiran, R Naaman, Claudio Fontanesi, David H Waldeck, Sławomir Sek, Jan Pawłowski, et al. Spin filtering in electron transport through chiral oligopeptides. *J. Phys. Chem. C*, 119(26):14542–14547, 2015.

[157] Albert C Aragonès, Ernesto Medina, Miriam Ferrer-Huerta, Nuria Gimeno, Meritxell Teixidó, Julio L Palma, Nongjian Tao, Jesus M Ugalde, Ernest Giralt, Ismael Díez-Pérez, et al. Measuring the spin-polarization power of a single chiral molecule. *Small*, 13(2):1602519, 2017.

[158] Matthias Kettner, Volodymyr V Maslyuk, Daniel Nürenberg, Johannes Seibel, Rafael Gutierrez, Gianaurelio Cuniberti, Karl-Heinz Ernst, and Helmut Zacharias. Chirality-dependent electron spin filtering by molecular monolayers of helicenes. *J. Phys. Chem. Lett.*, 9(8):2025–2030, 2018.

[159] Vankayala Kiran, Shinto P Mathew, Sidney R Cohen, Irene Hernández Delgado, Jérôme Lacour, and Ron Naaman. Helicenesa new class of organic spin filter. *Adv. Mater.*, 28(10):1957–1962, 2016.

[160] Ai-Min Guo and Qing-feng Sun. Spin-selective transport of electrons in DNA double helix. *Phys. Rev. Lett.*, 108(21):218102, 2012.

[161] Ai-Min Guo and Qing-Feng Sun. Spin-dependent electron transport in protein-like single-helical molecules. *Proc. Nat. Acad. Sci. (USA)*, 111(32):11658–11662, 2014.

[162] R Gutierrez, E Díaz, R Naaman, and G Cuniberti. Spin-selective transport through helical molecular systems. *Phys. Rev. B*, 85(8):081404, 2012.

[163] R Gutierrez, E Díaz, C Gaul, T Brumme, F Domínguez-Adame, and G Cuniberti. Modeling spin transport in helical fields: derivation of an effective low-dimensional Hamiltonian. *J. Phys. Chem. C*, 117(43):22276–22284, 2013.

[164] Shlomi Matityahu, Yasuhiro Utsumi, Amnon Aharony, Ora Entin-Wohlman, and Carlos A Balseiro. Spin-dependent transport through a chiral molecule in the presence of spin-orbit interaction and nonunitary effects. *Phys. Rev. B*, 93(7):075407, 2016.

[165] Ernesto Medina, Luis A González-Arraga, Daniel Finkelstein-Shapiro, Bertrand Berche, and Vladimiro Mujica. Continuum model for chiral induced spin selectivity in helical molecules. *J. Chem. Phys.*, 142(19):194308, 2015.

[166] Ernesto Medina, Floralba López, Mark A Ratner, and Vladimiro Mujica. Chiral molecular films as electron polarizers and polarization modulators. *EPL (Europhys. Lett.)*, 99(1):17006, 2012.

[167] Solmar Varela, Ernesto Medina, Floralba Lopez, and Vladimiro Mujica. Inelastic electron scattering from a helical potential: transverse polarization and the structure factor in the single scattering approximation. *J. Phys. Cond. Matt.*, 26(1):015008, 2013.

[168] Sina Yeganeh, Mark A Ratner, Ernesto Medina, and Vladimiro Mujica. Chiral electron transport: Scattering through helical potentials. *J. Chem. Phys.*, 131(1):014707, 2009.

[169] Shlomi Matityahu, Amnon Aharony, Ora Entin-Wohlman, and Carlos Antonio Balseiro. Spin filtering in all-electrical three-terminal interferometers. *Phys. Rev. B*, 95(8):085411, 2017.

[170] Solmar Varela, Vladimiro Mujica, and Ernesto Medina. Effective spin-orbit couplings in an analytical tight-binding model of DNA: Spin filtering and chiral spin transport. *Phys. Rev. B*, 93(15):155436, 2016.

[171] Volodymyr V Maslyuk, Rafael Gutierrez, Arezoo Dianat, Vladimiro Mujica, and Gianaurelio Cuniberti. Enhanced magnetoresistance in chiral molecular junctions. *J. Phys. Chem. Lett.*, 9(18):5453–5459, 2018.

[172] Sakse Dalum and Per Hedegard. Theory of chiral induced spin selectivity. *Nano Lett.*, 19:5253–5259, 2019.

[173] Martin Sebastian Zöllner, Solmar Varela, Ernesto Medina, Vladimiro Mujica, and Carmen Herrmann. Insight into the origin of chiral-induced spin selectivity from a symmetry analysis of electronic transmission. *J. Chem. Theory Comput.*, 16:2914–2929, 2020.

[174] Ron Naaman, Yossi Paltiel, and David H Waldeck. Chiral molecules and the electron spin. *Nat. Rev. Chem.*, 3(4):250–260, 2019.

[175] Andrey E Miroshnichenko, Sergej Flach, and Yuri S Kivshar. Fano resonances in nanoscale structures. *Rev. Mod. Phys.*, 82(3):2257, 2010.

[176] Liang Huang, Ying-Cheng Lai, Hong-Gang Luo, and Celso Grebogi. Universal formalism of Fano resonance. *AIP Adv.*, 5(1):017137, 2015.

[177] Aldilene Saraiva-Souza, Manuel Smeu, Lei Zhang, Antonio Gomes Souza Filho, Hong Guo, and Mark A Ratner. Molecular spintronics: Destructive quantum interference controlled by a gate. *J. Ame. Chem. Soc.*, 136(42):15065–15071, 2014.

[178] Chen-Rong Liu, Liang Huang, Honggang Luo, and Ying-Cheng Lai. Spin Fano resonances and control in two-dimensional mesoscopic transport. *Phys. Rev. Applied*, 13:034061, 2020.

[179] CJ Lambert. Basic concepts of quantum interference and electron transport in single-molecule electronics. *Chem. Soc. Rev.*, 44(4):875–888, 2015.

[180] Ferdinand Evers, Richard Korytár, Sumit Tewari, and Jan M van Ruitenbeek. Advances and challenges in single-molecule electron transport. *Rev. Mod. Phys.*, 92(3):035001, 2020.

[181] TA Papadopoulos, IM Grace, and CJ Lambert. Control of electron transport through Fano resonances in molecular wires. *Phys. Rev. B*, 74(19):193306, 2006.

[182] Daijiro Nozaki, Hâldun Sevinçli, Stanislav M Avdoshenko, Rafael Gutierrez, and Gianaurelio Cuniberti. A parabolic model to control quantum interference in T-shaped molecular junctions. *Phys. Chem. Chem. Phys.*, 15(33):13951–13958, 2013.

[183] CM Finch, VM Garcia-Suarez, and CJ Lambert. Giant thermopower and figure of merit in single-molecule devices. *Phys. Rev. B*, 79(3):033405, 2009.

[184] Andor Kormanyos, Iain Grace, and CJ Lambert. Andreev reflection through Fano resonances in molecular wires. *Phys. Rev. B*, 79(7):075119, 2009.

[185] Feng Jiang, Douglas I Trupp, Norah Algethami, Haining Zheng, Wenxiang He, Afaf Alqorashi, Chenxu Zhu, Chun Tang, Ruihao Li, Junyang Liu, et al. Turning the tap: Conformational control of quantum interference to modulate single-molecule conductance. *Angew. Chem.*, 131(52):19163–19169, 2019.

[186] Máté Vigh, László Oroszlány, Szabolcs Vajna, Pablo San-Jose, Gyula Dávid, József Cserti, and Balázs Dóra. Diverging dc conductivity due to a flat band in a disordered system of pseudospin-1 dirac-weyl fermions. *Phys. Rev. B*, 88(16):161413, 2013.

[187] Wolfgang Häusler. Flat-band conductivity properties at long-range coulomb interactions. *Phys. Rev. B*, 91(4):041102, 2015.

[188] Thibaud Louvet, Pierre Delplace, Andrei A Fedorenko, and David Carpentier. On the origin of minimal conductivity at a band crossing. *Phys. Rev. B*, 92(15):155116, 2015.

[189] Thomas D Cohen and David A McGady. Schwinger mechanism revisited. *Phys. Rev. D*, 78(3):036008, 2008.

[190] Kenichi L Ishikawa. Nonlinear optical response of graphene in time domain. *Phys. Rev. B*, 82(20):201402, 2010.

[191] Han-Chieh Lee and Tsin-Fu Jiang. Nonlinear optics of graphene in the presence of rabi oscillation. *J. Opt. Soc. Am. B*, 31(10):2263–2272, 2014.

[192] CE Carroll and FT Hioe. Generalisation of the landau-zener calculation to three levels. *J. Phys. A*, 19(7):1151, 1986.

[193] Lih-King Lim, Jean-Noël Fuchs, and Gilles Montambaux. Bloch-zener oscillations across a merging transition of dirac points. *Phys. Rev. Lett.*, 108(17):175303, 2012.

[194] Lih-King Lim, Jean-Noël Fuchs, and Gilles Montambaux. Mass and chirality inversion of a dirac cone pair in stückelberg interferometry. *Phys. Rev. Lett.*, 112(15):155302, 2014.

[195] Yan He, Joel Moore, and CM Varma. Berry phase and anomalous Hall effect in a three-orbital tight-binding Hamiltonian. *Phys. Rev. B*, 85(15):155106, 2012.

[196] Christoph W Groth, Michael Wimmer, Anton R Akhmerov, and Xavier Waintal. Kwant: a software package for quantum transport. *New J. Phys.*, 16(6):063065, 2014.

[197] Bill Sutherland. Localization of electronic wave functions due to local topology. *Phys. Rev. B*, 34:5208–5211, Oct 1986.

[198] Fa Wang and Ying Ran. Nearly flat band with Chern number $c = 2$ on the dice lattice. *Phys. Rev. B*, 84:241103, Dec 2011.

[199] Xueqin Huang, Yun Lai, Zhi Hong Hang, Huihuo Zheng, and C. T. Chan. Dirac cones induced by accidental degeneracy in photonic crystals and zero-refractive-index materials. *Nat. Mater.*, 10:582 EP –, May 2011.

[200] Jun Mei, Ying Wu, C. T. Chan, and Zhao-Qing Zhang. First-principles study of Dirac and Dirac-like cones in phononic and photonic crystals. *Phys. Rev. B*, 86:035141, Jul 2012.

[201] Parikshit Moitra, Yuanmu Yang, Zachary Anderson, Ivan I. Kravchenko, Dayrl P. Briggs, and Jason Valentine. Realization of an all-dielectric zero-index optical metamaterial. *Nat. Photon.*, 7(10):791–795, Oct 2013.

[202] D. Guzmán-Silva, C. Mejía-Cortés, M. A. Bandres, M. C. Rechtsman, S. Weimann, S. Nolte, M. Segev, A. Szameit, and R. A. Vicencio. Experimental observation of bulk and edge transport in photonic Lieb lattices. *New J. Phys.*, 16(6):063061, 2014.

[203] Judit Romhányi, Karlo Penc, and R. Ganesh. Hall effect of triplons in a dimerized quantum magnet. *Nat. Commun.*, 6:6805, 2015.

[204] Yang Li, Shota Kita, Philip Muoz, Orad Reshef, Daryl I. Vulis, Mei Yin, Marko Lonar, and Eric Mazur. On-chip zero-index metamaterials. *Nat. Photon.*, 9(11):738–742, Nov 2015.

[205] Rodrigo A. Vicencio, Camilo Cantillano, Luis Morales-Inostroza, Bastián Real, Cristian Mejía-Cortés, Steffen Weimann, Alexander Szameit, and Mario I. Molina. Observation of Localized States in Lieb Photonic Lattices. *Phys. Rev. Lett.*, 114:245503, Jun 2015.

[206] A. Fang, Z. Q. Zhang, Steven G. Louie, and C. T. Chan. Klein tunneling and supercollimation of pseudospin-1 electromagnetic waves. *Phys. Rev. B*, 93:035422, Jan 2016.

[207] I. C. Fulga and Ady Stern. Triple point fermions in a minimal symmorphic model. *Phys. Rev. B*, 95:241116, Jun 2017.

[208] Motohiko Ezawa. Triplet fermions and dirac fermions in borophene. *Phys. Rev. B*, 96:035425, Jul 2017.

[209] Chengyong Zhong, Yuanping Chen, Zhi-Ming Yu, Yuee Xie, Han Wang, Shengyuan A. Yang, and Shengbai Zhang. Three-dimensional pentagon carbon with a genesis of emergent fermions. *Nature Communications*, 8:15641 EP –, Jun 2017. Article.

[210] Yan-Qing Zhu, Dan-Wei Zhang, Hui Yan, Ding-Yu Xing, and Shi-Liang Zhu. Emergent pseudospin-1 maxwell fermions with a threefold degeneracy in optical lattices. *Phys. Rev. A*, 96:033634, Sep 2017.

[211] Robert Drost, Teemu Ojanen, Ari Harju, and Peter Liljeroth. Topological states in engineered atomic lattices. *Nat. Phys.*, 13:668, 2017.

[212] Marlou R. Slot, Thomas S. Gardenier, Peter H. Jacobse, Guido C. P. van Miert, Sander N. Kempkes, Stephan J. M. Zevenhuizen, Cristiane Morais Smith, Daniel Vanmaekelbergh, and Ingmar Swart. Experimental realization and characterization of an electronic lieb lattice. *Nat. Phys.*, 13:672, 2017.

[213] Xinsheng Tan, Dan-Wei Zhang, Qiang Liu, Guangming Xue, Hai-Feng Yu, Yan-Qing Zhu, Hui Yan, Shi-Liang Zhu, and Yang Yu. Topological maxwell metal bands in a superconducting qutrit. *Phys. Rev. Lett.*, 120:130503, Mar 2018.

[214] F Piéchon, JN Fuchs, A Raoux, and G Montambaux. Tunable orbital susceptibility in $\alpha - T_3$ tight-binding models. *J. Phys. Conf. Ser.*, 603(1):012001, 2015.

[215] E Illes and EJ Nicol. Magnetic properties of the $\alpha - T_3$ model: Magneto-optical conductivity and the hofstadter butterfly. *Phys. Rev. B*, 94(12):125435, 2016.

[216] E Illes and EJ Nicol. Klein tunneling in the $\alpha - T_3$ model. *Phys. Rev. B*, 95(23):235432, 2017.

[217] Áron Dániel Kovács, Gyula Dávid, Balázs Dóra, and József Cserti. Frequency-dependent magneto-optical conductivity in the generalized $\alpha - T_3$ model. *Phys. Rev. B*, 95:035414, Jan 2017.

[218] Vadim V. Cheianov, Vladimir Fal'ko, and B. L. Altshuler. The focusing of electron flow and a Veselago lens in graphene p-n junctions. *Science*, 315(5816):1252–1255, 2007.

[219] Xu Du, Ivan Skachko, Anthony Barker, and Eva Y Andrei. Approaching ballistic transport in suspended graphene. *Nat. Nanotech.*, 3(8):491, 2008.

[220] Andrei V. Shytov, Mark S. Rudner, and Leonid S. Levitov. Klein backscattering and Fabry-Pérot interference in graphene heterojunctions. *Phys. Rev. Lett.*, 101:156804, Oct 2008.

[221] C. W. J. Beenakker, R. A. Sepkhanov, A. R. Akhmerov, and J. Tworzydło. Quantum Goos-Hänchen effect in graphene. *Phys. Rev. Lett.*, 102:146804, Apr 2009.

[222] Ali G. Moghaddam and Malek Zareyan. Graphene-based electronic spin lenses. *Phys. Rev. Lett.*, 105:146803, Sep 2010.

[223] Nan Gu, Mark Rudner, and Leonid Levitov. Chirality-assisted electronic cloaking of confined states in bilayer graphene. *Phys. Rev. Lett.*, 107:156603, Oct 2011.

[224] J. R. Williams, T. Low, M. S. Lundstrom, and C. M. Marcus. Gate-controlled guiding of electrons in graphene. *Nat. Nanotech.*, 6(4):222–225, 2011.

[225] Peter Rickhaus, Romain Maurand, Ming-Hao Liu, Markus Weiss, Klaus Richter, and Christian Schönenberger. Ballistic interferences in suspended graphene. *Nat. Commun.*, 4:2342, 2013.

[226] Bolin Liao, Mona Zebarjadi, Keivan Esfarjani, and Gang Chen. Isotropic and energy-selective electron cloaks on graphene. *Phys. Rev. B*, 88:155432, Oct 2013.

[227] Mahmoud M. Asmar and Sergio E. Ulloa. Rashba spin-orbit interaction and birefringent electron optics in graphene. *Phys. Rev. B*, 87:075420, Feb 2013.

[228] Yue Zhao, Jonathan Wyrick, Fabian D Natterer, Joaquin F Rodriguez-Nieva, Cyprian Lewandowski, Kenji Watanabe, Takashi Taniguchi, Leonid S Levitov, Nikolai B Zhitenev, and Joseph A Stroscio. Creating and probing electron whispering-gallery modes in graphene. *Science*, 348(6235):672–675, 2015.

[229] Peter Rickhaus, Ming-Hao Liu, Peter Makk, Romain Maurand, Samuel Hess, Simon Zihlmann, Markus Weiss, Klaus Richter, and Christian Schonenberger. Guiding of electrons in a few-mode ballistic graphene channel. *Nano Lett.*, 15(9):5819–5825, 2015.

[230] Gil-Ho Lee, Geon-Hyoung Park, and Hu-Jong Lee. Observation of negative refraction of Dirac fermions in graphene. *Nat. Phys.*, 11(11):925–929, Nov 2015. Letter.

[231] Peter Rickhaus, Peter Makk, Klaus Richter, and Christian Schonenberger. Gate tuneable beamsplitter in ballistic graphene. *Appl. Phys. Lett.*, 107(25):251901, 2015.

[232] Jamie D. Walls and Daniel Hadad. The talbot effect for two-dimensional massless Dirac fermions. *Sci. Rep.*, 6:26698, 2016.

[233] Jose Caridad, Stephen Connaughton, Christian Ott, Heiko B. Weber, and Vojislav Krstic. An electrical analogy to Mie scattering. *Nat. Commun.*, 7:12894, 2016.

[234] Christopher Gutiérrez, Lola Brown, Cheol-Joo Kim, Jiwoong Park, and Abhay N Pasupathy. Klein tunnelling and electron trapping in nanometre-scale graphene quantum dots. *Nat. Phys.*, 12(11):1069–1075, 2016.

[235] Juwon Lee, Dillon Wong, Jairo Velasco Jr, Joaquin F. Rodriguez-Nieva, Salman Kahn, Hsin-Zon Tsai, Takashi Taniguchi, Kenji Watanabe, Alex Zettl, Feng Wang, Leonid S. Levitov, and Michael F. Crommie. Imaging electrostatically confined Dirac fermions in graphene quantum dots. *Nat. Phys.*, 12:1032–1036, 2016.

[236] Mikkel Settnes, Stephen R. Power, Mads Brandbyge, and Antti-Pekka Jauho. Graphene nanobubbles as valley filters and beam splitters. *Phys. Rev. Lett.*, 117:276801, Dec 2016.

[237] Ming-Hao Liu, Cosimo Gorini, and Klaus Richter. Creating and steering highly directional electron beams in graphene. *Phys. Rev. Lett.*, 118:066801, Feb 2017.

[238] Arthur W. Barnard, Alex Hughes, Aaron L. Sharpe, Kenji Watanabe, Takashi Taniguchi, and David Goldhaber-Gordon. Absorptive pinhole collimators for ballistic Dirac fermions in graphene. *Nat. Commun.*, 8:15418, 2017.

[239] Yuhang Jiang, Jinhai Mao, Dean Moldovan, Massoud Ramezani Masir, Guohong Li, Kenji Watanabe, Takashi Taniguchi, Francois M. Peeters, and Eva Y. Andrei. Tuning a circular p-n junction in graphene from quantum confinement to optical guiding. *Nat. Nanotech.*, 12:1045–1049, 2017.

[240] Shu-Hui Zhang, Jia-Ji Zhu, Wen Yang, and Kai Chang. Focusing RKKY interaction by graphene p-n junction. *2D Mater.*, 4(3):035005, 2017.

[241] Peter Bãggild, JosÃ© M. Caridad, Christoph Stampfer, Gaetano Calogero, Nick RÃŒbner Papior, and Mads Brandbyge. A two-dimensional Dirac fermion microscope. *Nat. Commun.*, 8:15783, 2017.

[242] H.-Y. Xu, G.-L. Wang, L. Huang, and Y.-C. Lai. Chaos in Dirac electron optics: Emergence of a relativistic quantum chimera. *Phys. Rev. Lett.*, 120:124101, 2018.

[243] J. D. Meiss and E. Ott. Markov-tree model of intrinsic transport in hamiltonian systems. *Phys. Rev. Lett.*, 55:2741–2744, 1985.

[244] Y.-C. Lai, M. Ding, C. Grebogi, and R. Blümel. Algebraic decay and fluctuations of the decay exponent in hamiltonian systems. *Phys. Rev. A*, 45:4661–4669, 1992.

[245] Bodo Huckestein, Roland Ketzmerick, and Caio H. Lewenkopf. Quantum transport through ballistic cavities: Soft vs hard quantum chaos. *Phys. Rev. Lett.*, 84:5504–5507, Jun 2000.

[246] M. Weiss, L. Hufnagel, and R. Ketzmerick. Universal power-law decay in hamiltonian systems? *Phys. Rev. Lett.*, 89:239401, Nov 2002.

[247] G. Cristadoro and R. Ketzmerick. Universality of algebraic decays in hamiltonian systems. *Phys. Rev. Lett.*, 100:184101, May 2008.

[248] Y.-C. Lai and T. Tél. *Transient Chaos: Complex Dynamics on Finite-Time Scales*. Springer, New York, 2011.

[249] J. U. Nöckel, A. D. Stone, and R. K. Chang. Q spoiling and directionality in deformed ring cavities. *Opt. Lett.*, 19:1693–1695, 1994.

[250] A. Mekis, J. U. Nöckel, G. Chen, A. D. Stone, and R. K. Chang. Ray chaos and Q spoiling in lasing droplets. *Phys. Rev. Lett.*, 75:2682–2685, 1995.

[251] Jens U Nöckel, A Douglas Stone, Gang Chen, Helene L Grossman, and Richard K Chang. Directional emission from asymmetric resonant cavities. *Opt. Lett.*, 21(19):1609–1611, 1996.

[252] Jens U Nöckel and A Douglas Stone. Ray and wave chaos in asymmetric resonant optical cavities. *Nature*, 385(6611):45, 1997.

[253] C. Gmachl, F. Capasso, E. E. Narimanov, J. U. Nöckel, A. D. Stone, J. Faist, and D. L. Sivco. High-power directional emission from microlasers with chaotic resonators. *Science*, 280:1556–1564, 1998.

[254] Evgenii E Narimanov, Gregor Hackenbroich, Philippe Jacquod, and A Douglas Stone. Semiclassical theory of the emission properties of wave-chaotic resonant cavities. *Phys. Rev. Lett.*, 83(24):4991, 1999.

[255] Jan Wiersig and Martina Hentschel. Combining directional light output and ultralow loss in deformed microdisks. *Phys. Rev. Lett.*, 100(3):033901, 2008.

[256] Eduardo G Altmann. Emission from dielectric cavities in terms of invariant sets of the chaotic ray dynamics. *Phys. Rev. A*, 79(1):013830, 2009.

[257] X.-F. Jiang, L.-B. Shao, S.-X. Zhang, X. Yi, J. Wiersig, L. Wang, Q.-H. Gong, M. Loncar, L. Yang, and Y.-F. Xiao. Chaos-assisted broadband momentum transformation in optical microresonators. *Science*, 358:344–347, 2017.

[258] L. Yang. Fighting chaos with chaos in lasers. *Science*, 361:1201, 2018.

[259] S. Bittner, S. Guazzotti, Y.-Q. Zeng, X.-N. Hu, H. Yilmaz, K. Kim, S. S. Oh, Q. J. Wang, O. Hess, and H. Cao. Suppressing spatiotemporal lasing instabilities with wave-chaotic microcavities. *Science*, 361:1225–1231, 2018.

[260] Christopher Gutiérrez, Daniel Walkup, Fereshte Ghahari, Cyprian Lewandowski, Joaquin F Rodriguez-Nieva, Kenji Watanabe, Takashi Taniguchi, Leonid S Levitov, Nikolai B Zhitenev, and Joseph A Stroscio. Interaction-driven quantum hall wedding cake–like structures in graphene quantum dots. *Science*, 361(6404):789–794, 2018.

[261] Hans-Jürgen Stöckmann. *Quantum Chaos: An Introduction*. Cambridge University Press, 2007.

[262] Jung-Wan Ryu, Soo-Young Lee, Chil-Min Kim, and Young-Jai Park. Survival probability time distribution in dielectric cavities. *Phys. Rev. E*, 73(3):036207, 2006.

[263] Soo-Young Lee, Sunghwan Rim, Jung-Wan Ryu, Tae-Yoon Kwon, Muhan Choi, and Chil-Min Kim. Quasiscarred resonances in a spiral-shaped microcavity. *Phys. Rev. Lett.*, 93(16):164102, 2004.

[264] Yuki Shiomi, K Nomura, Y Kajiwara, K Eto, M Novak, Kouji Segawa, Yoichi Ando, and E Saitoh. Spin-electricity conversion induced by spin injection into topological insulators. *Phys. Rev. Lett.*, 113(19):196601, 2014.

[265] Praveen Deorani, Jaesung Son, Karan Banerjee, Nikesh Koirala, Matthew Brahlek, Seongshik Oh, and Hyunsoo Yang. Observation of inverse spin hall effect in bismuth selenide. *Phys. Rev. B*, 90(9):094403, 2014.

[266] Mahdi Jamali, Joon Sue Lee, Jong Seok Jeong, Farzad Mahfouzi, Yang Lv, Zhengyang Zhao, Branislav K Nikolic, K Andre Mkhoyan, Nitin Samarth, and Jian-Ping Wang. Giant spin pumping and inverse spin hall effect in the presence of surface and bulk spin- orbit coupling of topological insulator bi2se3. *Nano Lett.*, 15(10):7126–7132, 2015.

[267] J.-C. Rojas-Sánchez, S. Oyarzún, Y. Fu, A. Marty, C. Vergnaud, S. Gambarelli, L. Vila, M. Jamet, Y. Ohtsubo, A. Taleb-Ibrahimi, P. Le Fèvre, F. Bertran, N. Reyren, J.-M. George, and A. Fert. Spin to charge conversion at room

temperature by spin pumping into a new type of topological insulator: α-sn films. *Phys. Rev. Lett.*, 116:096602, Mar 2016.

[268] Yabin Fan, Xufeng Kou, Pramey Upadhyaya, Qiming Shao, Lei Pan, Murong Lang, Xiaoyu Che, Jianshi Tang, Mohammad Montazeri, Koichi Murata, L.-T. Chang, M. Akyol, G.-Q. Yu, T.-X. Nie, K. L. Wong, J. Liu, Y. Wang, Y. Tserkovnyak, and K. L. Wang. Electric-field control of spin–orbit torque in a magnetically doped topological insulator. *Nat. Nanotechnol.*, 11(4):352, 2016.

[269] Yi Wang, Praveen Deorani, Karan Banerjee, Nikesh Koirala, Matthew Brahlek, Seongshik Oh, and Hyunsoo Yang. Topological surface states originated spin-orbit torques in bi 2 se 3. *Phys. Rev. Lett.*, 114(25):257202, 2015.

[270] AR Mellnik, JS Lee, A Richardella, JL Grab, PJ Mintun, Mark H Fischer, Abolhassan Vaezi, Aurelien Manchon, E-A Kim, N Samarth, et al. Spin-transfer torque generated by a topological insulator. *Nature*, 511(7510):449, 2014.

[271] Yabin Fan, Pramey Upadhyaya, Xufeng Kou, Murong Lang, So Takei, Zhenxing Wang, Jianshi Tang, Liang He, Li-Te Chang, Mohammad Montazeri, et al. Magnetization switching through giant spin–orbit torque in a magnetically doped topological insulator heterostructure. *Nat. Mater.*, 13(7):699, 2014.

[272] Anthony Richardella, Abhinav Kandala, and Nitin Samarth. Topological insulator thin films and heterostructures: Epitaxial growth, transport, and magnetism. In *Topological Insulators: Fundamentals and Perspectives*, pages 295–329. John Wiley & Sons, 2015.

[273] Frances Hellman, Axel Hoffmann, Yaroslav Tserkovnyak, Geoffrey SD Beach, Eric E Fullerton, Chris Leighton, Allan H MacDonald, Daniel C Ralph, Dario A Arena, Hermann A Dürr, et al. Interface-induced phenomena in magnetism. *Rev. Mod. Phys.*, 89(2):025006, 2017.

[274] Murong Lang, Mohammad Montazeri, Mehmet C Onbasli, Xufeng Kou, Yabin Fan, Pramey Upadhyaya, Kaiyuan Yao, Frank Liu, Ying Jiang, Wanjun Jiang, et al. Proximity induced high-temperature magnetic order in topological insulator-ferrimagnetic insulator heterostructure. *Nano Lett.*, 14(6):3459–3465, 2014.

[275] A Kandala, A Richardella, DW Rench, DM Zhang, TC Flanagan, and N Samarth. Growth and characterization of hybrid insulating ferromagnet-topological insulator heterostructure devices. *Appl. Phys. Lett.*, 103(20):202409, 2013.

[276] Qi I Yang, Merav Dolev, Li Zhang, Jinfeng Zhao, Alexander D Fried, Elizabeth Schemm, Min Liu, Alexander Palevski, Ann F Marshall, Subhash H Risbud, et al. Emerging weak localization effects on a topological insulator–insulating ferromagnet (bi 2 se 3-eus) interface. *Phys. Rev. B*, 88(8):081407, 2013.

[277] LD Alegria, H Ji, N Yao, JJ Clarke, RJ Cava, and JR Petta. Large anomalous hall effect in ferromagnetic insulator-topological insulator heterostructures. *Appl. Phys. Lett.*, 105(5):053512, 2014.

[278] Hailong Wang, James Kally, Joon Sue Lee, Tao Liu, Houchen Chang, Danielle Reifsnyder Hickey, K Andre Mkhoyan, Mingzhong Wu, Anthony Richardella, and Nitin Samarth. Surface-state-dominated spin-charge current conversion in topological-insulator–ferromagnetic-insulator heterostructures. *Phys. Rev. Lett.*, 117(7):076601, 2016.

[279] YT Fanchiang, KHM Chen, CC Tseng, CC Chen, CK Cheng, SR Yang, CN Wu, SF Lee, M Hong, and J Kwo. Strongly exchange-coupled and surface-state-modulated magnetization dynamics in bi 2 se 3/yttrium iron garnet heterostructures. *Nat. Comm.*, 9(1):223, 2018.

[280] Mingda Li, Cui-Zu Chang, Brian J Kirby, Michelle E Jamer, Wenping Cui, Lijun Wu, Peng Wei, Yimei Zhu, Don Heiman, Ju Li, et al. Proximity-driven enhanced magnetic order at ferromagnetic-insulator–magnetic-topological-insulator interface. *Phys. Rev. Lett.*, 115(8):087201, 2015.

[281] Yang Lv, James Kally, Tao Liu, Protyush Sahu, Mingzhong Wu, Nitin Samarth, and Jian-Ping Wang. Large unidirectional spin hall and rashba-edelstein magnetoresistance in topological insulator/magnetic insulator heterostructures. *arXiv preprint arXiv:1806.09066*, 2018.

[282] A Manchon and Shufeng Zhang. Theory of nonequilibrium intrinsic spin torque in a single nanomagnet. *Phys. Rev. B*, 78(21):212405, 2008.

[283] A Manchon and S Zhang. Theory of spin torque due to spin-orbit coupling. *Phys. Rev. B*, 79(9):094422, 2009.

[284] Ioan Mihai Miron, Gilles Gaudin, Stéphane Auffret, Bernard Rodmacq, Alain Schuhl, Stefania Pizzini, Jan Vogel, and Pietro Gambardella. Current-driven spin torque induced by the rashba effect in a ferromagnetic metal layer. *Nat. Mater.*, 9(3):230, 2010.

[285] Jun-ichiro Inoue, Gerrit EW Bauer, and Laurens W Molenkamp. Diffuse transport and spin accumulation in a rashba two-dimensional electron gas. *Phys. Rev. B*, 67(3):033104, 2003.

[286] Emmanuel I Rashba. Graphene with structure-induced spin-orbit coupling: Spin-polarized states, spin zero modes, and quantum hall effect. *Phys. Rev. B*, 79(16):161409, 2009.

[287] Maxime Garnier, Andrej Mesaros, and Pascal Simon. Topological superconductivity with deformable magnetic skyrmions. *Commun. Phys.*, 2:126, 2019.

[288] Stephan Rachel, Eric Mascot, Sagen Cocklin, Matthias Vojta, and Dirk K Morr. Quantized charge transport in chiral Majorana edge modes. *Phys. Rev. B*, 96(20):205131, 2017.

[289] Eric Mascot, Sagen Cocklin, Stephan Rachel, and Dirk K Morr. Quantum engineering of Majorana fermions. *arXiv preprint arXiv:1811.06664*, 2018.

[290] Utkan Güngördü, Shane Sandhoefner, and Alexey A Kovalev. Stabilization and control of Majorana bound states with elongated skyrmions. *Phys. Rev. B*, 97(11):115136, 2018.

[291] Yizhou Liu, Roger K Lake, and Jiadong Zang. Shape dependent resonant modes of skyrmions in magnetic nanodisks. *J. Mag. Magnet. Mater.*, 455:9–13, 2018.

[292] Ying-Cheng Lai, Hong-Ya Xu, Liang Huang, and Celso Grebogi. Relativistic quantum chaos: An emergent interdisciplinary field. *Chaos*, 28(5):052101, 2018.

[293] Liang Huang, Hong-Ya Xu, Celso Grebogi, and Ying-Cheng Lai. Relativistic quantum chaos. *Phys. Rep.*, 753:1–128, 2018.

[294] A. H. Castro Neto and K. Novoselov. Two-dimensional crystals: Beyond graphene. *Mater. Exp.*, 1:10–17, 2011.

[295] F. Haake. *Quantum Signatures of Chaos*. Springer series in synergetics. Springer-Verlag, Berlin, 3rd edition, 2010.

[296] C.-D. Han, H.-Y. Xu, L. Huang, and Y.-C. Lai. Manifestations of chaos in relativistic quantum systems - a study based on out-of-time-order correlator. *Phys. Open*, 1:100001, Sep 2019.

[297] R. Blümel and U. Smilansky. Classical irregular scattering and its quantum-mechanical implications. *Phys. Rev. Lett.*, 60(6):477–480, 1988.

[298] R. A. Jalabert., H. U. Baranger, and A. D. Stone. Conductance fluctuations in the ballistic regime - a probe of quantum chaos. *Phys. Rev. Lett.*, 65(19):2442–2445, 1990.

[299] Y.-C. Lai, R. Blümel, E. Ott, and C. Grebogi. Quantum manifestations of chaotic scattering. *Phys. Rev. Lett.*, 68(24):3491–3494, 1992.

[300] C. M. Marcus, A. J. Rimberg, R. M. Westervelt, P. F. Hopkins, and A. C. Gossard. Conductance fluctuations and chaotic scattering in ballistic microstructures. *Phys. Rev. Lett.*, 69(3):506–509, 1992.

[301] R. Ketzmerick. Fractal conductance fluctuations in generic chaotic cavities. *Phys. Rev. B*, 54(15):10841–10844, 1996.

[302] R. Yang, L. Huang, Y.-C. Lai, and L. M. Pecora. Modulating quantum transport by transient chaos. *Appl. Phys. Lett.*, 100(9):093105, 2012.

[303] R. Yang, L. Huang, Y.-C. Lai, and C. Grebogi. Quantum chaotic scattering in graphene systems. *Europhys. Lett.*, 94:40004, 2011.

[304] L. Ying, L. Huang, Y.-C. Lai, and C. Grebogi. Conductance fluctuations in graphene systems: The relevance of classical dynamics. *Phys. Rev. B*, 85(24):245448, 2012.

[305] Hongya Xu, Liang Huang, and Ying-Cheng Lai. A robust relativistic quantum two-level system with edge-dependent currents and spin polarization. *EPL (Europhysics Letters)*, 115(2):20005, 2016.

[306] Christoph Schütte and Markus Garst. Magnon-skyrmion scattering in chiral magnets. *Phys. Rev. B*, 90(9):094423, 2014.

[307] Y. Leviatan and A. Boag. Analysis of electromagnetic scattering from dielectric cylinders using a multifilament current model. *IEEE Trans. Anten. Propa.*, 35(10):1119–1127, 1987.

[308] Matthias G. Imhof. Multiple multipole expansions for elastic scattering. *J. Acous. Soc. Am.*, 100(5):2969–2979, 1996.

[309] D. I. Kaklamani and H. T. Anastassiu. Aspects of the method of auxiliary sources (mas) in computational electromagnetics. *IEEE Anten. Propag. Maga.*, 44(3):48–64, 2002.

[310] Esteban Moreno, Daniel Erni, Christian Hafner, and Rüdiger Vahldieck. Multiple multipole method with automatic multipole setting applied to the simulation of surface plasmons in metallic nanostructures. *J. Opt. Soc. Am. A*, 19(1):101–111, Jan 2002.

[311] Gérard Tayeb and Stefan Enoch. Combined fictitious-sources–scattering-matrix method. *J. Opt. Soc. Am. A*, 21(8):1417–1423, Aug 2004.

[312] H.-Y. Xu, L. Huang, Y.-C. Lai, and C. Grebogi. Superpersistent currents and whispering gallery modes in relativistic quantum chaotic systems. *Sci. Rep.*, 5:8963, 2015.

[313] Junshu Chen, Linjing Wang, Meng Zhang, Liang Zhou, Runnan Zhang, Lipeng Jin, Xuesen Wang, Hailang Qin, Yang Qiu, Jiawei Mei, et al. Evidence for magnetic skyrmions at the interface of ferromagnet/topological-insulator heterostructures. *Nano Lett.*, 19(9):6144–6151, 2019.

[314] Supriyo Datta. *Electronic transport in mesoscopic systems*. Cambridge university press, 1997.

[315] Michel Mendoza, Peter A Schulz, Raúl O Vallejos, and Caio H Lewenkopf. Fano resonances in the conductance of quantum dots with mixed dynamics. *Phys. Rev. B*, 77(15):155307, 2008.

APPENDIX A

PUBLICATIONS

Following are the relevant publications on the topics presented in this dissertation

C.-Z. Wang, H.-Y. Xu, L. Huang, and Y.-C. Lai*, Nonequilibrium transport in the pseudospin-1 Dirac-Weyl system, Physical Review B 96, 115440 (2017). [Chapter2]

C.-Z. Wang, H.-Y. Xu, N. D. Rizzo, R. A. Kiehl, and Y.-C. Lai*, Phase Locking of a Pair of Ferromagnetic Nano-Oscillators on a Topological Insulator, Physical Review Applied 10, 064003 (2018). [Chapter3]

C.-Z. Wang, C.-D. Han, H.-Y. Xu, and Y.-C. Lai*, Chaos-based Berry phase detector, Physical Review B 99, 144302 (2019). [Chapter4]

C.-Z. Wang, H.-Y. Xu, and Y.-C. Lai*, Scattering of Dirac electrons from a skyrmion: Emergence of robust skew scattering, Physical Review Research 2, 013247 (2020). [Chapter5]

C.-Z. Wang, H.-Y. Xu, and Y.-C. Lai*, Super skew scattering in two-dimensional Dirac material systems with a flat band, Physical Review B 103, 195439 (2021). [Chapter6]

C.-Z. Wang, V. Mujica, and Y.-C. Lai*, Spin Fano resonances in chiral molecules, to be submitted. [Chapter7]